ΔΙΔΑΚΤΟΡΙΚΗ ΔΙΑΤΡΙΒΗ

Τροποποίηση γραφενίου και σχετικών δι-διάστατων υλικών με οργανικά χρωμοφόρα μόρια

ΕΘΝΙΚΟ ΙΔΡΥΜΑ ΕΡΕΥΝΩΝ
ΙΝΣΤΙΤΟΥΤΟ ΘΕΩΡΗΤΙΚΗΣ ΚΑΙ ΦΥΣΙΚΗΣ ΧΗΜΕΙΑΣ

ΠΑΝΕΠΙΣΤΗΜΙΟ ΚΡΗΤΗΣ
ΤΜΗΜΑ ΧΗΜΕΙΑΣ

Ruben Canton-Vitoria

ΗΡΑΚΛΕΙΟ, ΑΠΡΙΛΙΟΣ 2019

PhD Thesis

Functionalization of graphene and related two-dimensional materials with organic dyes

NATIONAL HELLENIC RESEARCH FOUNDATION
THEORETICAL AND PHYSICAL CHEMISTRY INSTITUTE

UNIVERSITY OF CRETE
DEPARTMENT OF CHEMISTRY

Ruben Canton-Vitoria

HERAKLION, APRIL 2019

Dedicated to my loving family

«*The science of today is the technology of tomorrow*».

Edward Teller

EXAMINATION COMMITTEE

Haralambos E. Katerinopoulos, Professor
Department of Chemistry, University of Crete

Nikos Tagmatarchis, Director of Research (Supervisor)
Theoretical and Physical Chemistry Institute, National Hellenic Research Foundation

Ioulia Smonou, Associate Professor
Department of Chemistry, University of Crete

Georgios Vassilikogiannakis, Professor
Department of Chemistry, University of Crete

Manolis Stratakis, Professor
Department of Chemistry, University of Crete

Athanassios G. Coutsolelos, Professor
Department of Chemistry, University of Crete

Georgios Frudakis, Professor
Department of Chemistry, University of Crete

ΕΛΛΗΝΙΚΗ ΔΗΜΟΚΡΑΤΙΑ
ΠΑΝΕΠΙΣΤΗΜΙΟ ΚΡΗΤΗΣ

ΣΧΟΛΗ ΘΕΤΙΚΩΝ & ΤΕΧΝΟΛΟΓΙΚΩΝ ΕΠΙΣΤΗΜΩΝ
ΤΜΗΜΑ ΧΗΜΕΙΑΣ

ΠΡΑΚΤΙΚΟ ΕΠΤΑΜΕΛΟΥΣ ΕΞΕΤΑΣΤΙΚΗΣ ΕΠΙΤΡΟΠΗΣ ΓΙΑ ΤΗΝ ΕΞΕΤΑΣΗ ΔΙΔΑΚΤΟΡΙΚΗΣ ΔΙΑΤΡΙΒΗΣ

Η Επταμελής Εξεταστική Επιτροπή της Διδακτορικής Διατριβής του κ. Canton - Vitoria Ruben, η οποία ορίσθηκε στην από 19/02/2019 συνεδρία της Σ.Τ., συνεδρίασε σήμερα Δευτέρα **08 Απριλίου 2019** να εξετάσει τη διατριβή του υποψήφιου με τίτλο:
«Functionalization of graphene and related two-dimensional materials with organic dyes»

Τα παρόντα μέλη της Επταμελούς Εξεταστικής Επιτροπής εκφράζουν ομόφωνα την πλήρη ικανοποίησή τους για την υψηλή ποιότητα του περιεχομένου και της υποστήριξης της Διατριβής.

Τα Ερευνητικά αποτελέσματα της εργασίας του κ. Canton -Vitoria Ruben είναι σημαντικά, πρωτότυπα και διευρύνουν το πεδίο της έρευνας στον Τομέα Οργανικής Χημείας.

Ως εκ τούτου η Επταμελής Εξεταστική Επιτροπή προτείνει ομόφωνα την απονομή του Διδακτορικού Διπλώματος στον κύριο Canton - Vitoria Ruben.

Τα μέλη της Επταμελούς Εξεταστικής Επιτροπής για την Αξιολόγηση της Διδακτορικής Διατριβής του κυρίου Canton - Vitoria Ruben :

1. **Κατερινόπουλος Χαράλαμπος (Επιβλέπων)**
   Καθηγητής
   Τμήματος Χημείας Πανεπιστημίου Κρήτης
2. **Ταγματάρχης Νικόλαος**
   Διευθυντής Ερευνών
   Εθνικό Ίδρυμα Ερευνών
3. **Σμόνου Ιουλία**
   Αναπληρώτρια Καθηγήτρια
   Τμήματος Χημείας Πανεπιστημίου Κρήτης
4. Βασιλικογιαννάκης Γεώργιος
   Καθηγητής
   Τμήματος Χημείας Πανεπιστημίου Κρήτης
5. Στρατάκης Εμμανουήλ
   Καθηγητής
   Τμήματος Χημείας Πανεπιστημίου Κρήτης
6. Κουτσολέλος Αθανάσιος
   Καθηγητής
   Τμήματος Χημείας Πανεπιστημίου Κρήτης
7. Φρουδάκης Γεώργιος
   Καθηγητής
   Τμήματος Χημείας Πανεπιστημίου Κρήτης

Τ.Θ.2208, Τ.Κ.71003 Βούτες,
Ηράκλειο, Κρήτη
Tel. +30 2810 545131, 545133, 545136, 545138

P.O. BOX 2208, 71003 Voutes,
Heraklion, Crete, Greece
Fax: +30 2810 545166, 545164

e-mail: pantelidaki@chemistry.uoc.gr, nbouranta@chemistry.uoc.gr, tsolis@uoc.gr

ACKNOWLEDGEMETS

First and foremost, I would like to express my sincere gratitude to my supervisor, Dr. Nikos Tagmatarchis. Beginning with the opportunity to do my Ph.D. with him in his group, followed by his continuous support and guidance throughout my time in the laboratory, up to many possibilities he gave me to work in great collaborations. I am truly thankful for his inspirational mentorship that influenced my scientific development over the past 3 and half years, fulfilling my biggest dream to become a great scientist.

Besides my advisor I would like to express my appreciation to the rest of my committee members; Prof. H. E. Katerinopoulos, Dr. N. Tagmatarchis, Prof. I. Smonou, Prof. G. Vassilikogiannakis, Prof. M. Stratakis, Prof. A. G. Coutsolelos and Prof. G. Frudakis for their kind advises they gave me.

I am indebted to all the past and current members of our group, Dr. Theodosis Skaltsas, Dr. Anastasios Stergiou, Dr. Christina Stangel, Ms. Antonia Kagkoura, Ms. Malamatenia Koklioti, and Mr. Dimitris Perivoliotis for being friendly and supportive lab mates. Also, for providing an excellent atmosphere and making the times that we spent together in and out of the lab very special. Additionally, I would like to thank Mr. Athanasios Skandalis, Dr. George Mousdis and Dr. Constantinos Tsiantos for their useful help.

The completion of the work presented herein would not have been possible without the valuable efforts of many collaborators, thus I would like to thank all the co-authors who contributed to the publications presented in this dissertation.

I wish to thank all members from Enabling excellence network, especially Mr. Edward Goldwyn and Dr. Chris Ewels, without them ChemiProject would not have been possible. In addition, I would like to thank my collaborators of Carboquimica and from University of Zaragoza, Dr. Raul Arenal, Dr. Ana Benito, Dr. Wofgang Maser, Dr. Lorenzo Vallen, Dr. Emin Istif, Mr. Mario Pelaez Fernandez, Ms. Ana Santidrian and Dr. Esteban Urriolabeitia. Thanks to my collaborators in the IMN, Mr. Yuman Sayed-Ahmad-Baraza, Dr. Daniel Funes Fernando. Thanks to the University of Sussex, Dr. Alan Dalton, Dr. Sean P. Ogilvie, Dr. Matthew J. Large, Ms.

Manuela Meloni, Mr. Giuseppe Fratta, Dr. Florian Massuyeau, Dr. Alice King and Dr. Sebastion Nufer.

I would like also to thank all colleagues and scientific collaborators; Dr. Habtom B. Gobeze, Dr. Youngwoo Jang, and Prof. Francis D'Souza, from University of North Texas, USA; Dr. Carla Bittencourt from Mons University, Belgium, Mr. Fernando Ruipérez, Dr. Jon M. Matxain from San Sebastian University, Spain; Dr. Vicente M. Blas-Ferrando, Dr. Javier Ortiz, Dr. Fernando Fernández-Lázaro and Dr. Ángela Sastre-Santos from Miguel Hernández University, Spain; Dr. Yusuke Nakanishi and Dr. Hisanori Shinohara from Nagoya University, Japan, and Dr. Kyriakos C. Prousis, Ms. Maria Goulielmaki, Dr. Vassilis Zoumpourlis and Dr. Theodora Calogeropoulou from National Hellenic Research Foundation, Institute of Biology, Medicinal Chemistry & Biotechnology, Greece.

I am grateful to my whole family and my friends who always supported me and help me to kill the feeling of loneliness. Mom, father, brothers and sister, still you don't understand what I was doing during my Ph.D., but anyway, you always you helped me in everything. I have no words in any language that could express my gratitude; I will always have you in my heart. Os quiero.

The research fellowship programme "Research and innovation Marie Sklodowska-Curie grant actions," offered by EC H2020, agreement No 642742, is greatly acknowledged.

CURRICULUM VITAE

Personal Details

First name: Ruben

Surname: Canton

Second surname: Vitoria

Date of birth: 28/04/1990

Place of birth: Valencia/Spain

Citizenship: Spain

Institution Address

Theoretical and Physical Chemistry Institute (TPCI), National Hellenic Research Foundation (NHRF), 48 Vassileos Constantinou Avenue, 11635 Athens, Greece

E-mail: canton@eie.gr

Education

10/2015-4/2019 **Ph.D. in Chemistry**, Theoretical and Physical Chemistry Institute (TPCI), National Hellenic Research Foundation (NHRF)

2013-2014 **MSc in Organic Chemistry**, University of Valencia.

2009-2013 **BSc in Chemistry**, University of Valencia

Awards

- PhD Fellowship "**Marie Skłodowska-Curie**", H2020 ITN. Action Acronym: Enabling Excellence, Action Title: "Graphene-based nanomaterials for touchscreen technologies: Comprehension, Commerce and Communication" Grant agreement no: 642742
- Marie Curie ITN Fellow of the Week, March 2018.

Projects / Research Experience

- **2019**, **Ph.D. Thesis**: "*Functionalization of graphene and related two-dimensional materials with organic dyes.*" Theoretical and Physical Chemistry Institute (TPCI), National Hellenic Research Foundation (NHRF), Athens, Greece.
- **2014**, **Master Thesis**: "*Enantioselective addition of naphtols to benzoxatiazines through cupreine derivative catalyst.*" Organic chemistry department, Valencia University, Valencia, Spain.
- **2013**, **Undergraduate research project**: "*Antibody monoclonal characterization vs mepanipyrim and pyrimetainl conjugated.*"- Instituto de Agroquímica y Tecnología de Alimentos. Valencia University, Valencia, Spain.
- **2012**, **Undergraduate research project**: "Sinthesis and reactivity of phosphine derivatives" Organic chemistry department, Valencia University, Valencia, Spain.

Scientific communication activities

- **2018**, Develop and commercialization of ChemiProject. A STEM game about chemistry. Amazon.es ASIN: B07G9JLPPW
- **2018**, Expociencia, University of Valencia. Lola Cantón-Vitoria, Alejandro Cantón-Vitoria, Rubén Cantón Vitoria. *ChemiProject joga y apren.*
- **2018**, Euroscience Open forum, ESOF, July 9-14, Ruben Canton-Vitoria, Nikos Tarmatarchis, *Educational chemistry game: ChemiProject. Enjoy, play and learn!*
- **2018**, 8-9 November, Ciencia Astea. San Sebastian University. *Tabakalera,* Rubén Cantón Vitoria, Loca Cantón-Vitoria. *ChemiProject: jolastu eta ikasi!*

Technical Knowledge

- NMR, UV-Vis, FTIR, Fluorescence, Raman, TGA, HPLC, Electrochemistry, Time - Resolved Fluorescence.

Publications

1. **R. Canton-Vitoria**, H. B. Gobeze, V. M. Blas-Ferrando, J. Ortiz, Y. Jang, F. Fernández-Lázaro, Á. Sastre-Santos, Y. Nakanishi, H. Shinohara, F. D'Souza, N. Tagmatarchis, "Excited state charge transfers in covalently functionalized MoS_2 with zinc phthalocyanine donor-acceptor hybrid", *Angew. Chem. Int. Ed.* **2019**, *58*, 5712.
2. **R. Canton-Vitoria**, Y. Sayed-Ahmad-Baraza, R. Arenal, C. P. Ewels, N. Tagmatarchis, "Non-covalent immobilization of pyrene onto transition metal dichalcogenides for photoinduced charge-transfer processes and protection from photooxidation", **2019**, *Submitted*.

3. K. C. Prousis,[#] **R. Canton-Vitoria**,[#] G. Pagona, M. Goulielmaki, V. Zoumpourlis, N. Tagmatarchis, T. Calogeropoulou, "Cyanine-graphene hybrid materials for bioimaging applications", **2019**, *Submitted*.

   [#] Equally contributed.

4. **R. Canton-Vitoria**, E. Istif, J. Hernández-Ferrer, E. P. Urriolabeitia, A. M. Benito, W. K. Maser, N. Tagmatarchis, "Integrating water-soluble polythiophene with transition metal dichalcogenides for managing photoinduced processes", *ACS Appl. Mater. Interfaces* **2019**, *11*, 5947-5956.

5. **R. Canton-Vitoria**, N. Tagmatarchis, Y. Sayed-Ahmad-Baraza, C. Ewels, D. Winterauer, T. Batten, A. Brunton, S. Nufer, "Gas sensing using monolayer MoS_2", in Book: Nanoscale Materials for Warfare Agent Detection: Nanoscience for Security, Eds: C. Bittencourt, C. Ewels, E. Llobet, *Springer Nature B. V.* **2019**, Chapter 5, 71-96.

6. **R. Canton-Vitoria**, C. Stangel, N. Tagmatarchis, "Electrostatic association of ammonium-functionalized layered-transition-metal dichalcogenides with an anionic porphyrin", *ACS Appl Mater Interfaces* **2018**, *10*, 23476-23480.

7. **R. Canton-Vitoria**, L. Vallan, E. Urriolabeitia, A. M. Benito, W. K. Maser, N. Tagmatarchis, "Electronic interactions in illuminated carbon Dot/MoS_2 ensembles and electrocatalytic activity towards hydrogen evolution", *Chem. Eur. J.* **2018,** *24*, 10468-10474.

8. L. Vallan, E. P. Urriolabeitia, F. Ruipérez, J. M. Matxain, **R. Canton-Vitoria**, N. Tagmatarchis, A. M. Benito, W. K. Maser, "Supramolecular-enhanced charge transfer within entangled polyamide chains as the origin of the universal blue fluorescence of polymer carbon dots", *J. Am. Chem. Soc.* **2018**, *140*, 12862-12869.

9. L. Vallan,[#] **R. Canton-Vitoria**,[#] H. B. Gobeze, Y. Jang, R. Arenal, A. M. Benito, W. K. Maser, F. D'Souza, N. Tagmatarchis, "Interfacing transition metal dichalcogenides with carbon nanodots for managing photoinduced energy and charge-transfer processes", *J. Am. Chem. Soc.* **2018**, 140, 13488-13496.

   [#] Equally contributed.

10. S. P. Ogilvie, M. J. Large, G. Fratta, M. Meloni, **R. Canton-Vitoria**, N. Tagmatarchis, F. Massuyeau, C. P. Ewels, A. A. K. King, A. B. Dalton, "Considerations for spectroscopy of liquid-exfoliated 2D materials: emerging photoluminescence of N-methyl-2-pyrrolidone", *Sci. Rep.* **2017**, *7*,16706-16713.

11. **R. Canton-Vitoria**, Y. Sayed-Ahmad-Baraza, M. Pelaez-Fernandez, R. Arenal, C. Bittencourt, C. P. Ewels, N. Tagmatarchis, "Functionalization of MoS_2 with 1, 2-dithiolanes: toward donor-acceptor nanohybrids for energy conversion", *npj 2D Mater. Appl.* **2017**, *1*, 1-13.
12. M. Montesinos-Magraner, C. Vila, **R. Cantón**, G. Blay, I. Fernández, M. C. Muñoz, J. R. Pedro, "Organocatalytic asymmetric addition of naphthols and electron-rich phenols to isatin-derived ketimines: highly enantioselective construction of tetrasubstituted stereocenters", *Angew. Chem. Int. Ed.* **2015**, *54*, 6320-6324.
13. M. Montesinos-Magraner, **R. Canton**, C. Vila, G. Blay, I. Fernandez, M. C. Muñoz, J. R. Pedro, "Organocatalytic enantioselective aza-Friedel–Crafts reaction of 2-naphthols with benzoxathiazine 2,2-dioxides", *RSC Adv.* **2015**, *54*, 60101-60105.

Conferences

1. **R. Canton-Vitoria**, N. Targmatarchis, "Covalent 1,2-dithiolane functionalization of layered transition metal dichalcogenides", *NanoteC18 – Carbon Nanoscience and Nanotechnology*, Brighton, United Kingdom, **2018** (Oral).
2. L. Vallan, E. P. Urriolabeitia, F. Ruipérez, J. M. Matxain, **R. Canton-Vitoria**, N. Tagmatarchis, A. M. Benito, W. K. Maser, "Fluorescence in non-conjugated polymeric carbon dots", *NanoteC18 – Carbon Nanoscience and Nanotechnology*, Brighton, United Kingdom, **2018** (Oral).
3. Y. Sayed-Ahmed Baraza, C. Ewels, **R. Canton-Vitoria**, M. Pelaez-Fernandez, R. Arenal, C. Bittencourt, N. Tagmatarchis, "MoS_2: phases, edges and functionalization", *NanoteC18 – Carbon Nanoscience and Nanotechnology*, Brighton, United Kingdom, **2018** (Poster).
4. Y. Sayed-Ahmad-Baraza, M. Palaez Fernandez, P. Briddon, **R. Canton-Vitoria**, N. Tagmatarchis, C. Ewels, "Experimental and DFT studies of functionalisation in MoS_2 and Graphene Oxide", *ChemOnTubes*, Biarritz, France, **2018** (Oral).
5. **R. Cantón-Vitoria**, C. Stangel, N. Tagmtarchis, "Transition metal dichalcogenides functionalized with porphyrins for energy conversion", *HeteroNanoCarb2017*, Benasque, Spain, **2017** (Oral).

6. Y. Sayed-Ahmad-Baraza, **R. Canton-Vitoria**, M. Pelaez-Fernandez, B. Anothumakkool, C. Bittencourt, J. Gaubicher, R. Arenal, B. Humbert, N. Tagmatarchis, C. P. Ewels, "Experimental and DFT studies on the functionalisation of 2D nanomaterials with pyrene derivatives", *HeteroNanoCarb2017*, Benasque, Spain, **2017** (Oral).
7. **R. Canton-Vitoria**, K. Proussis, T. Calogeropoulou, N. Tagmatarchis, "Functionalization of graphene with cyanine dyes", *NanoteC17 – Carbon Nanoscience and Nanotechnology*, Nantes, France, **2017.** (Oral)
8. Y. Sayed-Ahmad-Baraza, **R. Canton-Vitoria**, M. Pelaez-Fernandez, N. M. Seck, B. Humbert, N. Tagmatarchis, C. P. Ewels, "Combined DFT and experimental study of pyrene functionalized 2D-MoS_2 layers", *Annual meeting of the GDR-I GNT*, Saint Pierre d'Oléron, France, **2016** (Poster).
9. **R. Canton-Vitoria**, Y. Sayed-Ahmad-Baraza, M. Pelaez-Fernandez, C. Bittencourt, R. Arenal, C. P. Ewels, N. Tagmatarchis, "Covalent functionalization of semiconducting tmds via lipoic acid derivates with photophisic properties", *Annual meeting of the GDR-I GNT*, Saint Pierre d'Oléron, France, **2016** (Poster).
10. **R. Canton-Vitoria**, Y. Sayed-Ahmad-Baraza, M. Pelaez-Fernandez, C. Bittencourt, R. Arenal, C. P. Ewels, N. Tagmatarchis, "Functionalization of transition metal dichalcogenides with 1,2-dithiolanes", *NanoteC16 – Carbon Nanoscience and Nanotechnology*, Dublin, Ireland, **2016** (Poster).
11. Y. Sayed-Ahmad-Baraza, **R. Canton-Vitoria**, M. Pelaez-Fernandez, N. M. Seck, B. Humbert, N. Tagmatarchis, C. P. Ewels, "Combined DFT and experimental study of pyrene functionalized 2D-MoS_2 layers", *NanoteC16 – Carbon Nanoscience and Nanotechnology,* Dublin, Ireland, **2016** (Poster).
12. C. Vila, M. Montesinos-Magraner, **R. Cantón**, G. Blay, I. Fernández, J. R. Pedro, "Organocatalytic enantioselective friedel-crafts reactions of naphthols and electron-rich phenols", *XXXV Reunion Bineal RSEQ*, Coruña, Spain, **2015** (Oral).
13. M. Montesinos-Magraner, C. Vila, **R. Cantón**, G. Blay, I. Fernández, J. R. Pedro, "Quinine-derived thiourea-catalyzed enantioselective addition of naphthols and activated phenols to isatin-derived ketimines", *XXXV Reunion Bineal RSEQ*, Coruña, Spain, **2015** (Oral).

14. M. Montesinos-Magraner, **R. Cantón-Vitoria**, I. Fernández, J. R. Pedro, "Organocatalytic enantioselective Friedel-Crafts reaction of naphthols with cyclic imines", *Simposio de Investigadores Jovenes*, Basque Country, Spain, **2014** (Oral).

Workshop and secondment

1. International European-Japanese Workshops, Tokyo-Nagoya-Osaka, Japan, 21-30/5/2018
2. Nanocharacterization of structures, Training Workshop, Bristol, UK, 20-24/3/2017
3. Secondment - Prototype devices, Sussex University, Brighton, UK, 23-29/7/2017
4. Secondment - Prototype devices M-Solv, Oxford, UK, 28/6/2017 - 23/7/2017
5. Secondment - Training on imaging techniques, Zaragoza, Spain, 13/5/2017 - 4/6/2017
6. Secondment - Training on computation and theoretical studies, Nantes, France, 5/9/2017 - 5/10/2017
7. Commerce Training Workshop, Dublin, Ireland, 3-4/09/2016
8. Graphene Nanobuilding Blocks Training Workshop, Larnaca, Cyprus, 2-7/5/2016
9. Graphene Communication Training Workshop, Hinxton, UK, 29/11/2015 - 4/12/2015

Computer Skills

- Operating Systems: MS Windows XP/Vista, Linux.
- Microsoft Office: Word, Excel, Power Point, Access, Front Page.
- Chemistry/Scientific Programs: ChemOffice, Chem3D, Draw, Mestrenova, EndNote, Origin.

Foreign Languages

- English, Portuguese, Catalan.

ΠΕΡΙΛΗΨΗ

Η παρούσα διδακτορική διατριβή αφορά στη χημική τροποποίηση φύλλων γραφενίου καθώς και σχετικών δισδιάστατων αναλόγων του που βασίζονται στα διχαλκογενίδια μετάλλων μετάπτωσης MoS_2 και WS_2, με στόχο την παρασκευή υβριδικών υλικών για ενεργειακές εφαρμογές. Αναλυτικότερα, χρησιμοποιήθηκαν μέθοδοι τόσο ομοιοπολικής χημικής τροποποίησης όσο και τεχνικές υπερμοριακής χημείας για την πρόσδεση/αλληλεπίδραση οργανικών χρωμοφόρων μορίων στο πλέγμα του γραφενίου και των MoS_2 και WS_2.

Πιο συγκεκριμένα, στο πρώτο μέρος της διατριβής επιτεύχθηκε η ομοιοπολική πρόσδεση (α) 4,4-διφθορο-4-βορανο-3α,4α,8-τριαζο-*s*-ινδακενίων (boron azadipyrromethenes – azaBDPs) σε αποφλοιωμένο γραφένιο το οποίο αρχικά είχε τροποποιηθεί κατάλληλα μέσω αντίδρασης με in-situ σχηματιζόμενα άρυλο-διαζωνιακά άλατα ώστε να φέρει ομάδες αλκυνίου, οι οποίες ακολούθως αντέδρασαν μέσω χημείας “click” με παράγωγα azaBDP που έφεραν ομάδες αζιδίου, και (β) κυανινών (cyanines) ακολουθώντας τη μεθοδολογία χημικής τροποποίησης με in-situ σχηματιζόμενα άρυλο-διαζωνιακά άλατα που είτε έφεραν εξ’αρχής τις κυανίνες ως μέρος της δομής τους, είτε χρησιμοποιήθηκαν για περαιτέρω σύζευξη με τις κυανίνες μέσω αντιδράσεων συμπύκνωσης πάνω στο πλέγμα του ήδη τροποποιημένου γραφενίου.

Στο δεύτερο μέρος της διατριβής αναπτύχθηκε μεθοδολογία για τη χημική τροποποίηση των δισδιάστατων και φυλλόμορφων διχαλκογενιδίων μετάλλων μετάπτωσης MoS_2 και WS_2 η οποία ακολούθως εφαρμόσθηκε για την παρασκευή υβριδικών υλικών. Συγκεκριμένα, βρέθηκε ότι 1,2-διθειολάνια προσδένονται σε ατέλειες των Mo και W που οφείλονται σε κενές θέσεις S και βρίσκονται στις άκρες του πλέγματος των MoS_2 και WS_2. Οι εν λόγω ατέλειες σχηματίζονται κατά τη διαδικασία αποφλοίωσης των MoS_2 και WS_2 από τα αντίστοιχα υλικά βάσης (bulk materials) αναδεικνύοντας την ευκολία και ευχρηστία της μεθόδου. Παράλληλα, μελετήθηκε η σταθερότητα του διαλύτη *N*-μέθυλοπυρρολιδόνη που χρησιμοποιείται ευρέως σε μεθόδους υγρής αποφλοίωσης τόσο γραφενίου όσο και των MoS_2 και WS_2 και διερευνήθηκε η επίδραση και οι περιορισμοί του στο υλικά που παράγονται.

Ακολούθως, παρασκευάσθηκαν υβριδικά υλικά βασισμένα σε MoS_2 και WS_2 που φέρουν ομοιοπολικά προσδεμένες χρωμοφόρες ομάδες (α) πυρενίου, (β) πορφυρίνης, (γ) φθαλοκυανίνης του ψευδαργύρου, και (δ) «τελειών» άνθρακα (carbon dots). Επιπρόσθετα, παρασκευάσθηκαν

υβριδικά υλικά στα οποία τα διχαλκογενίδια των μετάλλων μετάπτωσης έχουν τροποποιηθεί έτσι ώστε να φέρουν αμμωνιακά άλατα. Στην συνέχεια, τα θετικά φορτία των αμμωνιακών αλάτων χρησιμοποιήθηκαν για την ηλεκτροστατική σύμπλεξη αρνητικά φορτισμένων χρωμοφόρων ομάδων (α) πορφυρίνης, (β) πολυθειοφαινείου, και (γ) «τελειών» άνθρακα προς σχηματισμό νέων υπερμοριακών υβριδικών υλικών. Επίσης, πραγματοποιήθηκε υπερμοριακή αλληλεπίδραση αποφλοιωμένου MoS_2 και WS_2 με πυρένιο μέσω ανάπτυξης πολλαπλών S-π δυνάμεων ανάμεσα στα δύο συστατικά του υβριδικού υλικού.

Όλα τα υβριδικά υλικά χαρακτηρίστηκαν δομικά με συμπληρωματικές φασματοσκοπικές και θερμικές τεχνικές, ενώ μελετήθηκε η μορφολογία τους με ηλεκτρονιακή μικροσκοπία, επιβεβαιώνοντας την επιτυχή παρασκευή τους. Επιπλέον, μελετήθηκαν ενδελεχώς οι φωτοφυσικές, ηλεκτροχημικές και ηλεκτροκαταλυτικές ιδιότητες των νέων υβριδικών υλικών γραφενίου και MoS_2 και WS_2 αποκαλύπτωντας τη δυνατότητα εφαρμογής τους σε συστήματα μετατροπής και διατήρησης ενέργειας.

Λέξεις κλειδιά : γραφένιο, MoS_2, WS_2, χρωμοφόρα, χημική τροποποίηση, υβριδικά υλικά, μεταφορά ηλεκτρονίων.

ABSTRACT

This PhD thesis deals with the chemical functionalization of graphene sheets and related two-dimensional analogues based on transition metals dichalcogenides, e.g. MoS_2 and WS_2, focusing on the development of hybrid materials for energy conversion applications. More specifically, both covalent and supramolecular functionalization methodologies were employed for interaction of organic chromophores with graphene, MoS_2 and WS_2 sheets.

The first part focuses on the covalent attachment of (a) 4,4-difluoro-4-boron-3a,4a,8-triazo-s-indacene (boron azadipyrromethenes – azaBDP) on exfoliated graphene, which it was prior chemically functionalized with *in situ* aryl-diazonium salts carrying alkyne groups that subsequently reacted by "click" chemistry with azaBDP derivatives bearing azide groups; and (b) cyanines following the chemical functionalization methodology with *in situ* formed aryl-diazonium salts which either brought already the cyanines as part of their structure or used for further coupling with cyanines via condensation reactions onto the already modified graphene sheets.

The second part of this thesis provides a methodology for the chemical functionalization of the two-dimensional transition metal dichalcogenides, e.g. MoS_2 and WS_2, which it was then applied for the preparation of hybrid materials. In particular, it has been found that 1,2-dithiolane units possess high affinity to Mo and W atoms due to sulfur vacancy sites that are located at the edges of the MoS_2 and WS_2 sheets. These defects are introduced during the exfoliation process of MoS_2 and WS_2 from their respective bulk materials, highlighting the versatility and wide utility of the proposed procedure. In parallel, the stability of the N-methyl pyrrolidone (NMP) solvent, which is widely used in graphene as well as MoS_2 and WS_2 liquid exfoliation processes, was investigated and its effects and limitations on the developed materials were examined.

Next, MoS_2 and WS_2-based hybrid materials bearing covalently bonded chromophore groups of (a) pyrene, (b) porphyrin, (c) zinc phthalocyanine, and, (d) carbon dots were prepared. Additionally, hybrid materials were developed in which the transition metal dichalcogenides were suitably modified to carry ammonium salts. The positive charges of the ammonium salts

were then used to electrostatically interact with negatively charged chromophore groups of (a) porphyrin, (b) polythiophene, and (c) carbon dots to construct new supramolecular hybrid materials. Moreover, supramolecular interactions of exfoliated MoS_2 and WS_2 sheets with pyrene were developed attributable to multiple S-π forces between the two components of the hybrid material.

All hybrid materials were structurally characterized by complementary spectroscopic and thermal techniques, while their morphology was studied by electron microscopy, confirming their successful preparation. In addition, the photophysical, electrochemical and electrocatalytic properties of newly prepared graphene, MoS_2 and WS_2-based hybrid materials have been thoroughly investigated, revealing their applicability in energy conversion systems.

Key words: graphene, MoS_2, WS_2, chromophore molecules, chemical functionalization, hybrid materials, electron transfer

CONTENTS

ABBREVIATIONS

^{1}H NMR: Proton Nuclear Magnetic Resonance

^{13}C NMR: Carbon Nuclear Magnetic Resonance

2D: Two-dimensional

ATR-IR: Attenuated Total Reflectance Infra-Red

azaBDP: Aza-boron-dipyrromethene

BDP: Boron-dipyrromethene

BOC: *Tert*-butyl carbamate

DCM: Dichloromethane

DMF: Dimethyl formamide

DMAP: 4-Dimethylaminopyridine

DMSO: Dimethyl sulfoxide

DSSC: Dye Sensitized Solar Cell

CDs: Cabon dots

CNDs: Carbon nanodots

CS: Charge separation

EDCI: N-(3-Dimethylaminopropyl)-N′-ethylcarbodiimide hydrochloride

EELS: Electron energy loss spectroscopy

EDX: Energy-dispersive X-ray

ET: Electron transfer

FE-SEM: Field emission scanning electron microscopy

HAADF: High-angular annular dark-field

HER: Hydrogen evolution reaction

HOMO: Highest occupied molecular orbital

HRTEM: High-resolution transmission electron microscopy

LH: Light Harverster

LUMO: Lowest unoccupied molecular orbital

MoS_2: Molybdenum disulfide

MALDI-TOF: Matrix-assisted laser desorption/ionization-time of flight

NIR: Near-infra-red

NMP: 1-Methyl pyrrolidine

o-DCB: Ortho-dichlorobenzene

OTE: Optical transparent electrode

PCE: Power conversion efficiency

PTFE: Polytetrafluoroethylene

TCSPC: Time-correlated-single-photon-counting

TEM: Transmission electron microscopy

TGA: Thermogravimetric analysis

TMDs: Transition-metal dichalcogenides

SEM: Scanning electron microscopy

STEM: Scanning transmission electron microscopy

UV-Vis: Ultraviolet-Visible

XPS: X-ray photoelectron spectroscopy

WS_2: Tugnsten disulfide

CHAPTER 1

Graphene and transition metal dichalcogenides

ABSTRACT

The chapter deals with the properties of graphene and focuses on its covalent and non-covalent functionalization with organic compounds and chromophores. Covalent strategies employing for example addition reactions based on aryl diazonium salts and azomethine ylides among others chemical reactions, as well non-covalent interactions such as π–π interactions are discussed. The main objective is to highlight widely employed modification routes for graphene and present interesting hybrid materials potentially suitable for energy-related applications. Standard characterization techniques, spectroscopic, thermal and microscopy imaging, for proving the functionalization of graphene are also discussed.

Complementing graphene, the most studied two-dimensional materials are those belonging to the wider family of layered transition metal dichalcogenides (TMDs), with most examined representatives those of MoS_2 and WS_2. The TMDs have attracted significant scientific interest due to their intriguing electronic and optical properties, and herein we highlight the main structural features and physicochemical properties of TMDs. In addition, exfoliation methodologies yielding single or oligolayered TMD nanosheets are presented and functionalization strategies developed are discussed.

1.1 GRAPHENE

Graphene is without a doubt the most studied two-dimensional (2D) nanomaterial. It is defined by IUPAC as a single carbon layer of graphite structure, analogous to a polycyclic aromatic hydrocarbon of quasi-infinite size. The atomic layer of graphene is formed by sp^2-hybridized carbons arranged in a honeycomb structure, with a C-C distance of 0.142 nm and energy of 112 kcal/mol. However, this definition is frequently expanded to include multiple layers of graphene. Graphene's high tensile strength measured at 130 GPa, Young's modulus of 1.0 TPa, and also a (hypothetical) density of 0.77 mg/m^2 renders it one of the strongest materials. Pristine graphene is practically transparent, absorbing, on average, 2,3 % of all incident light.[1] Also, graphene presents remarkable electronic properties,[2] with a mobility value as high as 200,000 cm^2/V s. Thanks to these extraordinary and superior properties, graphene has already revealed a large number of potential applications with possible uses in touch screens, capacitors, spintronics devices, fuel cells, batteries, sensors, transparent conductive films, high frequency circuits, elimination of toxic material, and flexible electronics.[3] However, one the major drawbacks is the low solubility due to π-π staking and van deer Waals interactions between the different graphene layers.

Graphene oxide (GO) is the highly oxidized form of graphene, typically obtained after chemical treatment under hard oxidation conditions from graphite. Hummer method is without any doubt, the methodology mostly used to produce GO. Typically, graphite is exfoliated and chemically modified upon treatment with sodium nitrate, potassium permanganate, sulfuric acid and hydrogen peroxide, resulting on the incorporation of several oxygen-based groups (e.g., hydroxyl, carboxyl, and epoxy) onto the graphitic framework. One of the main advantages of GO compared to pristine graphene, is that it can be easily dissolved in organic solvents and even in water due to the presence of the polar oxygen functional groups that generate repulsion forces between layers. However, the honeycomb lattice of GO exhibits a discontinuous sp^2 system, featuring sp^3 carbons, holes and defects, which in turn reduce drastically the electronic properties. The latter can be improved by reducing GO to reduced graphene oxide (rGO) and healing the sp^2 system. This process can be done with several ways, including thermal annealing or chemical reduction reaction with hydrazine. Apparently, not all the electronic properties of graphene can be recovered since several defects such as vacancies and oxygen related groups (i.e. COOH at the edges) still remain on the lattice.

Production of graphene occurs by various different approaches, including liquid exfoliation, chemical vapor deposition, epitaxial mechanical exfoliation or synthesis through molecular assembly. From a chemist's standpoint, some methods appear significantly more attractive than others. Liquid and chemical exfoliation, offer chemists significant amounts of starting material as a blank canvas to decorate and functionalize graphene sheets towards the realization of functional hybrid materials. So far the easiest method that seems to produce graphene of sufficient quality is liquid exfoliation.

During liquid exfoliation, graphite is dispersed in a specific solvent, followed by sonication and finally purification of the exfoliated graphene. The exfoliation effect depends on the power and time of sonication, the stability of the liquid medium, and the purification progress. Generally, the time and sonication power are inversely related with the length and defects of the flake and they can be easily studied.[4] The suitable liquid media are chosen in order to provide an environment that allows the formation of stable graphene dispersions during sonication. Coleman and co-workers[5] realized that closer surface energies between graphene and solvent favors the exfoliation, with the optimal surface tension (γ) being 40-50 mJ/m^2. Typically, N-methyl-pyrrolidone (NMP), dimethylformamide (DMF) and 1,2-dichlorobenzene (o-DCB) having a high interfacial tension, 40.0, 37.0 and 37.1, respectively, are selected as appropriate solvents. These solvents are introduced between graphene layers, hence reducing the π-π staking interactions between layers and stabilizing single layers of graphene.[6] However, even when the sonication protocol produces pristine graphene of high quality and in amounts suitable for laboratory experiments, the concentration of the graphene dispersions obtained does not exceed 0.01 mg/mL, which is not suitable for real applications.

1.2 FUNCTIONALIZATION OF GRAPHENE

To further modify the properties, fully harness their capabilities, and even broaden the application of graphene, chemical functionalization of such material is an absolute necessity. Functionalization of graphene can take place either via covalently linked organic species or via non-covalent interactions. Non-covalent modification of graphene is usually performed in liquid media through simple mixture. However, the forces that maintain together the organic species with graphene to yield the functionalized material only are weak interactions of van der Waals,

columbic or π-π staking. The later are the more studied because the majority of the photoactive molecules, e.g. porphyrin, pyrenes or perylenes have planer and aromatic structures with an extended sp^2 system that excellently interact with the surface of graphene through orbital overlapping. In fact, π-π staking interactions with organic dyes not only ensure the functionalization but also weaken the interactions between layers enhancing the level of exfoliation. In general, non-covalent functionalization has low stabilization energies of 2-3 kcal/mol, meaning that the organic compounds onto graphene are easily separated, being an advantage in some fields like bioimaging but also a disadvantage for accurate photo-electronic studies in liquid media, wherein detaching of organic dyes, cannot be abolished, masking the real results.

On the other hand, covalent bonds have energies around 100 kcal/mol, ensuring a robust linkage between the dyes and graphene, which is easily purified of contaminants and starting materials without any risk of desorption. Covalent functionalization normally has a shorter distance between graphene and the photoactive molecules in comparison with non-covalent functionalization. Those short distances are desired for electron donor-acceptor systems. In fact, the probability to have electron transfer between graphene and one photoactive molecule is inversely related with the distance. Additionally, covalent functionalization has the advantage over non covalent to attach species that have no columbic or π-π interaction, reaching the formation of new hybrids. Generally, basal functionalization introduces groups that reduce the attractive forces between layers of graphene and help to the exfoliation. Such effect is more evident when the dyes employed for the functionalization has steric groups or charged species that induce repulsions forces. However, the reactivity of graphene is low and ensuring covalent functionalization is very challenging. On the other hand, the main drawback of covalent functionalization is that it changes the hybridization of the graphene carbon atoms from sp^2 to sp^3. This process can be considered formally as an introduction of defects reducing the electronic properties of graphene.[7]

In order to confirm the functionalization of graphene, spectroscopy, thermal and microscopy imaging techniques are normally used. Spectroscopy techniques include Raman, attenuated-total-reflectance infra-red (ATR-IR) and UV-Vis. Further, thermal analysis includes

thermogravimetric analysis (TGA) and microscopy techniques involve high-resolution transmission electron microscopy (TEM) imaging.

Raman spectroscopy is a well stablished spectroscopic technique for characterizing graphene. Specifically, graphene shows 3 characteristic modes at ~1350 cm^{-1}, 1590 cm^{-1} and 2700 cm^{-1} which corresponds to D, G and 2D bands respectively. The G-band is attributed to vibrations due to sp^2 hybridized carbon atoms, while the D-band is ascribed to vibrations due to defect sites and sp^3 hybridized carbon atoms. The shape and frequency of the 2D band is sensitive to the number of graphene sheets. Covalent functionalization of graphene can be monitored by Raman technique because perturbs the graphene's honeycomb from sp^2 to sp^3 and moreover enhances the intensity of D band proportionally with the range of functionalization.

The ATR-IR spectroscopy is usually employed to determine the functional groups owned to the attached organic components. While no significant peaks were found in graphene beyond the C=C moiety at ~1600 cm^{-1}, for graphene-based hybrids sharp characteristic peaks related with specific functional groups such as carbonyls (1630-1750 cm^{-1}), azides (2000-2100), alcohols (3000-3300) among others are found. Hence, ATR-IR allows the qualitative identification of the organic addends in graphene-modified materials.

Functionalization of graphene layers enhances the solubility and allows the study of their properties in liquid media. UV-Vis shows graphene's characteristic continuous absorption in the NIR region. In addition, photoactive dyes in modified graphene-based materials exhibit characteristic absorption bands owed to the presence of the organic dyes.

TGA allows establishing the amount of functional groups by calculating the mass loss occurred upon increasing temperature. Graphene is a stable material at high temperatures under inert conditions, e.g. nitrogen atmosphere; however, organic materials tend to decompose between 200-550 ºC. Hence, in a typical TGA graph of graphen-based hybrid materials, the loading of the molecules added onto graphene sheets can be quantitatively calculated.

Transmission electron microscopy (TEM) imaging provides information about the lattice of graphene showing images of the atomic layers. Firstly, TEM sheds light of the honeycomb of graphene, providing interesting information about the average of size and the number of layers of

the material as well as the presence of defects. Furthermore, TEM is usually complemented for spectroscopic characterization, typically, energy dispersive X-ray (EDX) that identify the atomic composition not only of graphene, but also of the functional hybrid materials. Additionally, a more sophisticated electron loss energy spectroscopy (EELS) shows the presence of the atoms and gives information about the chemical bonding.

Several strategies have been developed for the covalent functionalization of graphene. The main ones involve addition reactions, such as addition of *in-situ* generated aryl diazonium salts, addition of malonates (Bingel-Hirsch), Diels-Alder cycloaddition, 1,3-dipolar cycloaddition of *in-situ* generated azomethine ylides, as well as click-chemistry and condensation reactions onto GO.

The Bingel-Hirsch reaction is a [1+2] cycloaddition that use malonate derivatives furnishing cyclopropane rings onto the basal plane of graphene. This versatile strategy involves the generation of reactive carbanions from α-halo esters and their subsequent addition to a double bond of graphene, followed by the elimination of halogen. In general, the addition takes place on double bonds of the honeycomb of graphene furnishing cyclopropane rings. This strategy of covalent modification of graphene has been widely studied thanks to the easily synthesis of malonate derivatives. In fact, malonic acid allows the functionalization with different organic structures bearing hydroxyls, forming esters who are capable to react with graphene (Figure 1).[8]

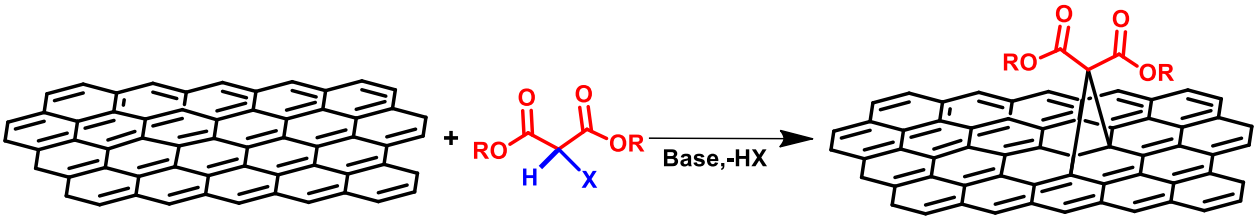

Figure 1. General example of chemical modification of graphene through [1+2] Bingel cycloaddition.

Haddon and coworkers described the application of the Diels-Alder reaction in the functionalization of graphene. This [4+2] cycloaddition has been a long-standing tool in the synthetic arsenal of synthetic chemists focused in total synthesis,[9] fullerene[10] and SWNT[11]

functionalization. Such cycloaddition reaction tests organic molecules bearing dienophiles (alkenes) and dienophile (four consecutive sp^2 carbons) of graphene, furnishing rings of 6 members in the basal plane. In addition, the alkenes present in graphene also act as the dienophile in presence of diene derivatives. Diels-Alder reaction can be performed employing a widely variety of alkenes or dienes bearing different groups, including electron donors such as ethers and electron acceptors e.g. nitriles or even aromatics structures as naphthols.[12] Finally, Diels-Alder reaction is reversible under middle-high-temperatures (100-160ºC) being a powerful strategy to produce hybrids and tune of the electronic properties of graphene under mild conditions (Figure 2).

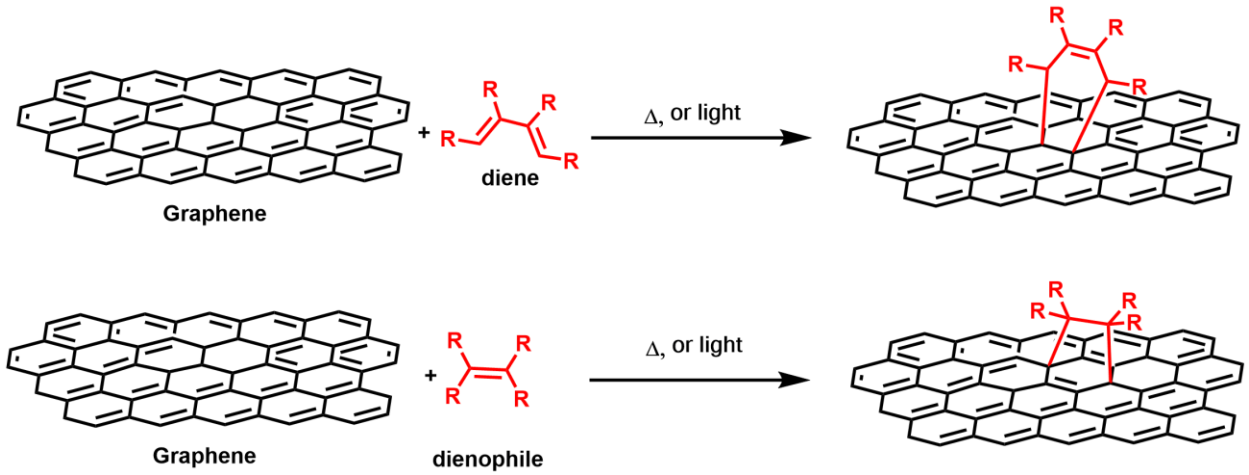

Figure 2. General example of chemical modification of graphene through Diels-Alder reaction. Graphene can react with dienes (upper panel) or with dienophiles (lower panel).

The aryl diazonium salt reaction introduces aromatic species on the basal plane of graphene. Functionalization of graphene through diazonium salt reaction is obtained in situ, by its corresponding aniline together with sodium nitrite or isoamyl nitrite. During the functionalization one electron is transfer from graphene to aryl diazonium salt derivative, resulting in the formation of the corresponding radical aryl unit, which reacts with a sp^2-carbon on the lattice of graphene. Aniline derivatives employed can bear different functional groups usually in *para*-position or even photoactive molecules (Figure 3).[13]

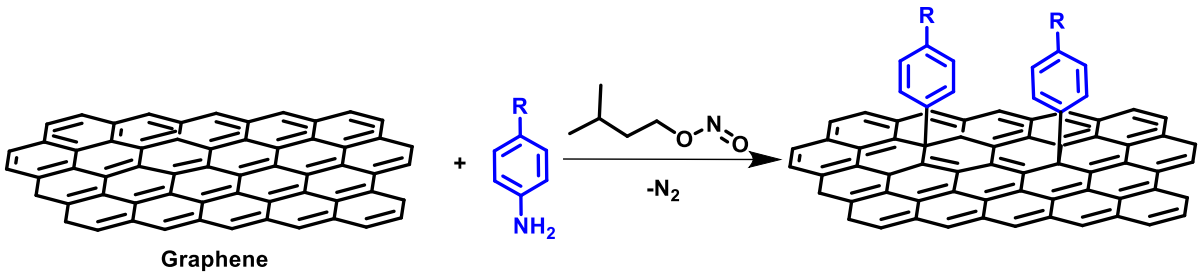

Figure 3. General example of chemical modification of graphene through in-situ generated aryl diazonium salt reaction.

Azomethine ylides react through 1,3-dipolar cycloaddition with graphene to introduce fused pyrrolidine rings on the lattice of graphene. Azomethine ylides are very reactive intermediate, obtained from decarboxylation of an α-amino acid and a carbonyl species under heating conditions. The 1,3-dipolar cycloaddition reaction is very versatile, yielding in this way a large range of functional groups bound onto the graphene surface by employing diverse aldehydes or substituted α-amino acids (Figure 4).[14]

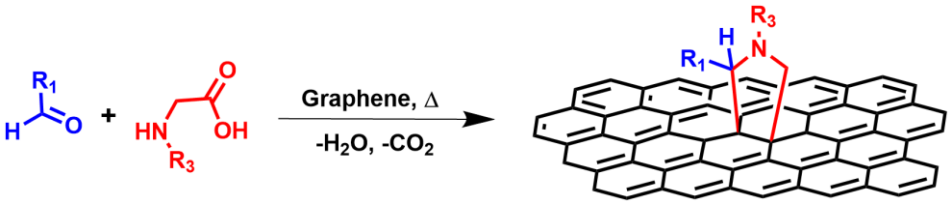

Figure 4. General example of chemical modification of graphene through 1,3-dipolar cycloaddition reaction.

Another functionalization reaction for graphene modification is the addition of azides which form aziridine adducts onto the honeycomb of graphene. The particular functionalization proceeds via nitrenes as generated upon the thermal or photochemical N_2 decomposition of aryl azides. The addition of specific dyes employing this reaction is possible employing the specific aryl azide derivatives (Figure 5).[15]

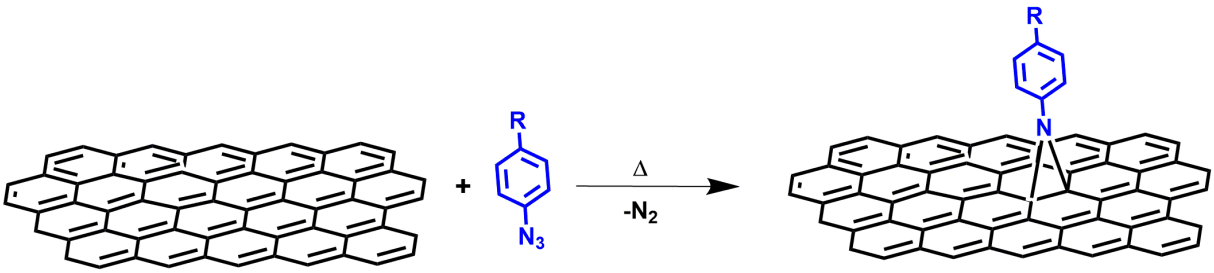

Figure 5. General example of chemical modification of graphene through direct addition of azides.

Condensation reactions are usually employed for the covalent functionalization of GO. In such reactions alcohols, amines or thiols can easily react under soft conditions with acids of graphene oxide. The reaction needs coupling agents or forming the acyl halide with e.g. thionyl chloride in order catalyst the reaction in ambient conditions. The condensation reaction does not disrupt the honeycomb of GO because the sp^2 carbons of the honeycomb of GO are not involved. Notably, such functionalization reaction can involve an infinite range of functional groups or even photoactive molecules bearing in the reactants (Figure 6).[16]

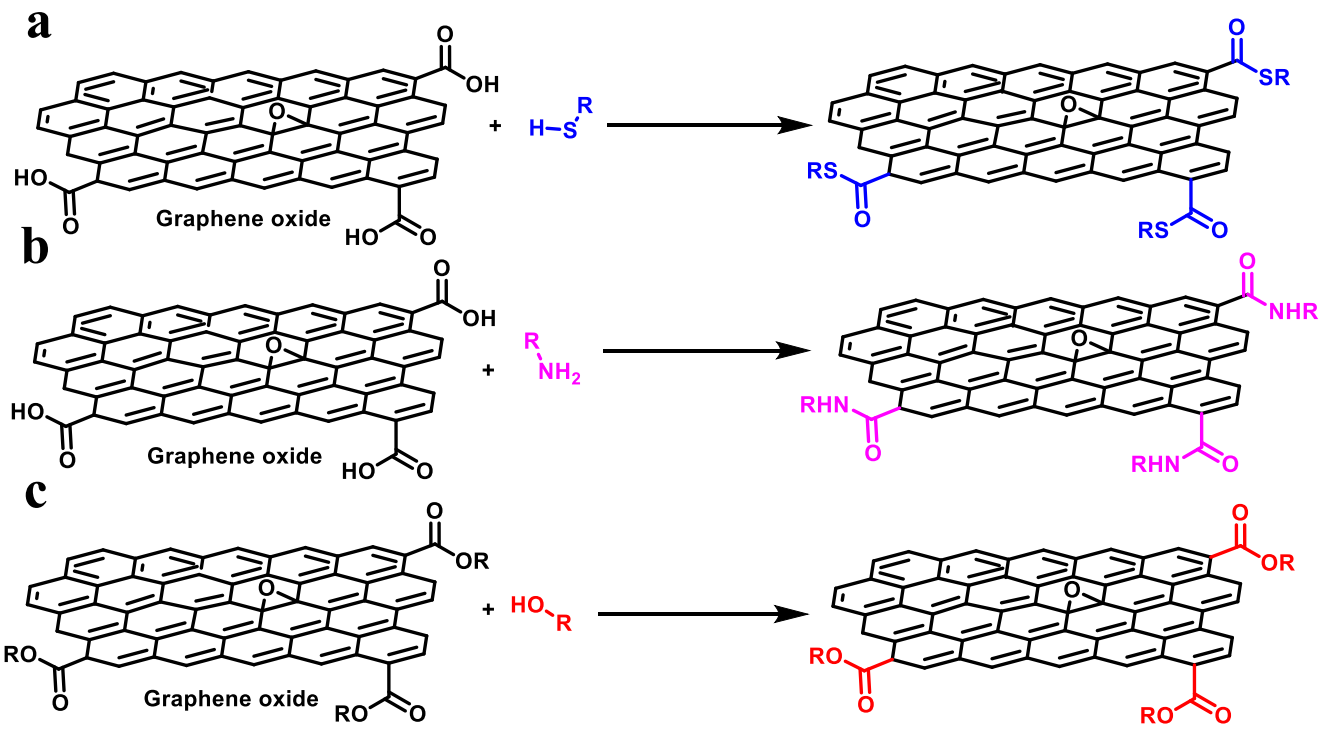

Figure 6. General examples of chemical modification of GO through condensation reactions with (a) thiols, (b) amines, and (c) alcohols.

Common examples of noncovalent functionalization with graphene include π−π, electrostatic and van der Waals interactions. This allows stable functionalization with molecules that have extended sp^2 systems, including chromophores e.g. porphyrins, phthalocyanines and pyrenes. In addition, the basal plane of GO has functional groups such as epoxides, hydroxides or carboxylic acid in its structure, for this reason, GO also has hydrogen-bonds interaction.

1.3 GRAPHENE-BASED HYBRID MATERIALS FEATURING ORGANIC CHROMOPHORES

Due to simplicity, for the non-covalent functionalization of graphene naphthalene, anthracene, pyrene, coronene, porphyrins and their derivatives have been employed. Nowadays, more complex structures are studied. For example, bifunctional compounds that strongly enhance the solubility and at the same time induce energy transfer has recently described. In a recent example, Brunneti et. al, synthesizes and advanced diimideperylene bearing bolaamphiphiles which is able to stabilize graphene nanosheets of microns in liquid media and reduce at the same time the strong perylene emission, indicating a pronounced electronic communication with graphene.[17]

The possibility of attaching multiple porphyrins to graphene was also studied.[18] In this approach, firstly, an anionic porphyrine (hemo-porphyrin) was selected to stabilize graphene in liquid media though non-covalent π-π staking interactions. Afterwards the modified graphene was combined with a cationic porphyrin (tetra aryl ammonium porphyrin) via columbic interactions, producing a porphyrin/porphyrin/graphene modified material. Electronic communication was evident by the emission quenching and faster fluorescence lifetimes.

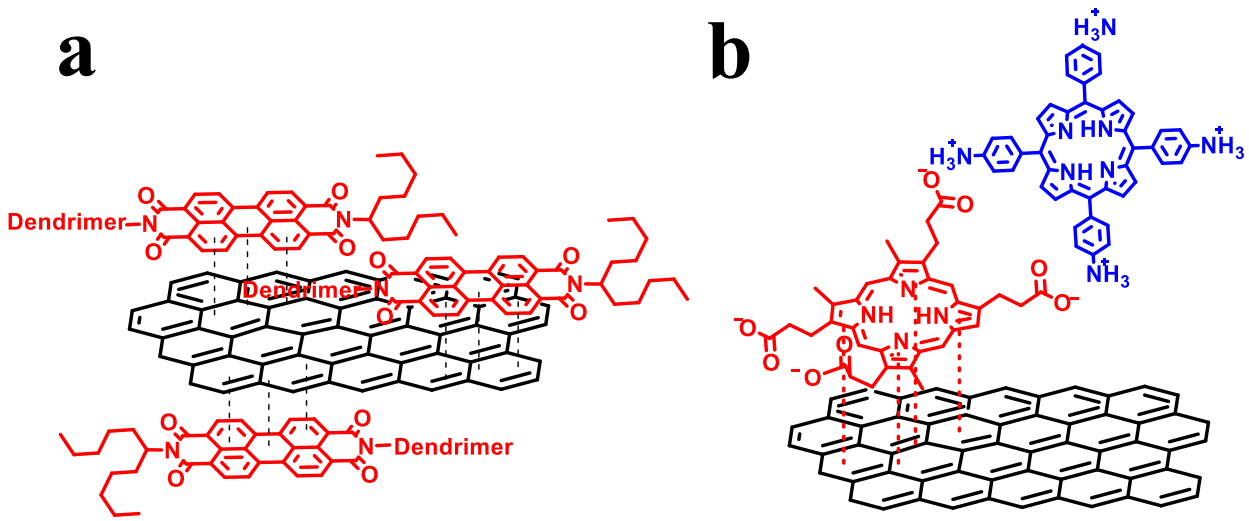

Figure 7. General example of non-covalent chemical modification of graphene with photoactive molecules of (a) perylene and (b) porphyrin derivatives.

Additionally, pyrene bearing anionic heptamethine cyanine was employed for managing electronic interactions with graphene through π-π staking. In this example, pyrene has strong affinity for graphene, being responsible of the non-covalent functionalization without appreciable desorption and carrying the cyanine moiety to graphene. Cyanines are photoactive NIR dyes with strong quantum yields. In graphene/cyanine ensembles, red-shift in UV-Vis and fluorescence emission studies ensure appreciable electronic communication in ground and excited state, and, in addition, charge transfer from cyanine to graphene (Figure 8).[19]

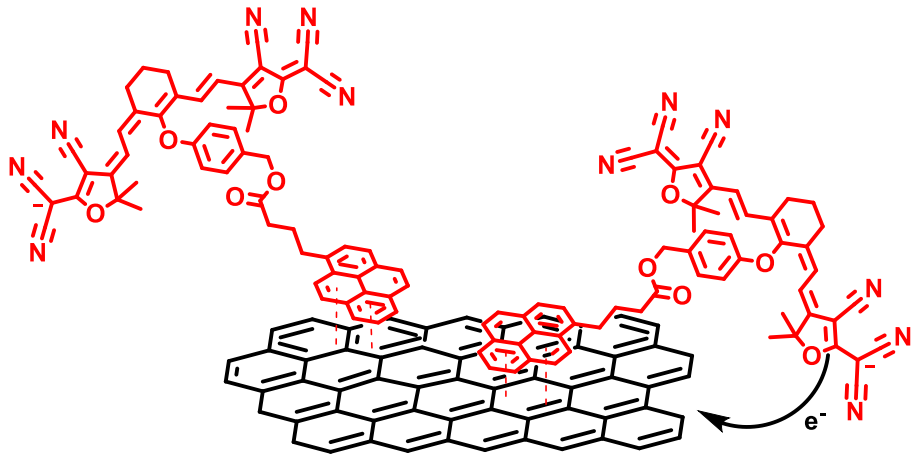

Figure 8. Non-covalent chemical modification of graphene with pyrene bearing a cyanine moiety.

The covalent functionalization of graphene featuring dyes such as porphyrins or phthalocyanines and exfoliated graphene has been extensively studied during the last decade.[20] In a representative example described by Karousis et. al, the fluorescence of the Zn-phthalocyanine resulted in efficient quenching in the Zn-phthalocyanine–graphene hybrid material. In fact, photoinduced events occurs from the photoexcited phthalocyanine to exfoliated graphene evidenced by femtosecond transient absorption spectroscopy revealed the formation of transient species such as Zn-phthalocyanine$^{\bullet+}$, yielding the charge-separated state Zn-phthalocyanine$^{\bullet+}$–graphene$^{\bullet-}$. In fact, Zn-phthalocyanine–graphene can be integrated into a photoactive electrode of an optical transparent electrode (OTE), exhibiting stable and reproducible photocurrent responses.[21]

In 2014, Torres and co-workers reported the first example of exfoliated graphene covalently connected with electron accepting Zn-phthalocyanines. Steady-state and time-resolved spectroscopy experiments demonstrated photoinduced electron transfer from the graphene to the electron-accepting phthalocyanines with a lifetime of 1.0±0.5 ps. Functionalization was accomplished in two steps. First, graphene was modified through diazonium salt reaction with an alkyl aniline derivative followed by alkyne–azide "click chemistry" reaction (Figure 9a). The conclusions of this study is relevant for photoelectronic applications.[22]

Hirsch et. al, synthesized a novel graphene–porphyrin hybrid with a direct covalent linkage between the graphene carbon network and amine porphyrin through the aryl diazonium salt approach. Interestingly, the porphyrin is linked in a perpendicular orientation by a single σ-bond to the graphene lattice, producing an uncommon orbital overlapping of graphene with porphyrin. The red-shift observed in UV-Vis and PL suggested interesting electronic communications between the orbitals of both, graphene and porphyrin. In fact, this type of covalently coupled hybrid material has the potential to become an integral part in solar energy conversion and electronic devices (Figure 9b).[23]

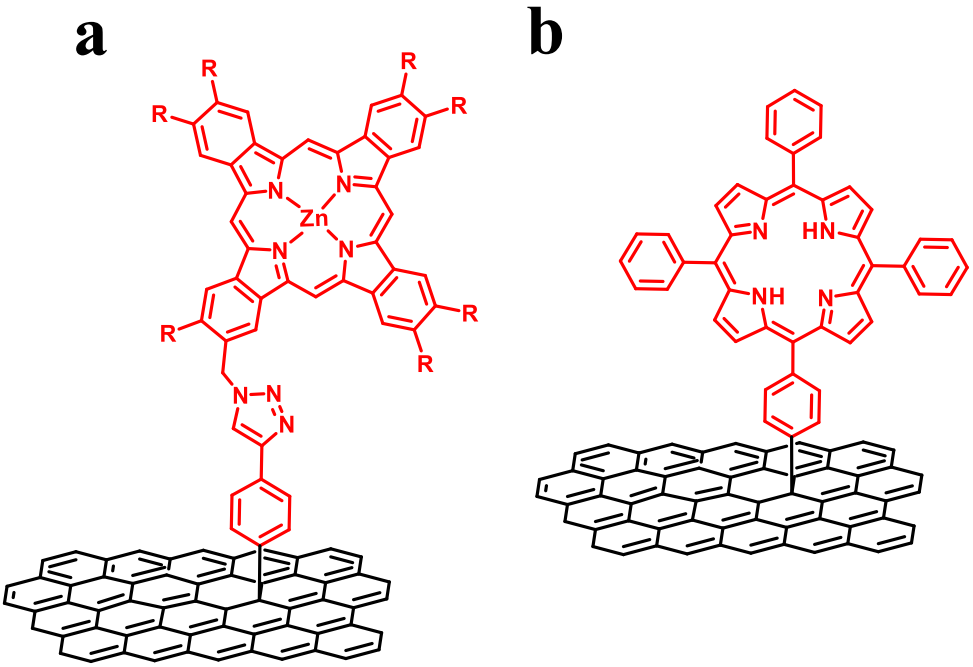

Figure 9. (a) Electron donor-acceptor systems of Zn-phthalocyanine-graphene, and (b) porphyrin-graphene directly connected through a single σ-bond.

Additional perylene diimide was covalently attached to graphene (Figure 10a). The electronic communication of perylene in the ground state was evident based in substantial shift of the fluorescence emission of the dye, and the energy transfer was employed to enhance the hydrogen catalytic production in methanol even in the absence of a sacrificial donor.[24]

Boron azadipyrromethenes (BDPs) are dyes that absorb in the near-IR region and with high quantum yields related with a push-pull system as well as the rigidity of the structure that boron confers. Electronic interactions between graphene and BDP have been studied in recent years. In 2014 Yadav et. al, found electronic communication in the ground states of BDP within a BDP-graphene nanomaterial. An electron transfer mechanism was evident through photocurrent measurements, in which the BDP-graphene nanomaterial has a current density of 7.5 $\mu A/cm^2$.[25] Afterwards, in 2018, Durmuş et. al, optimized the device to produce a current density of 5.51 mA/cm^2 with a power conversion efficiency (PCE) of 1.16% (Figure 10b).

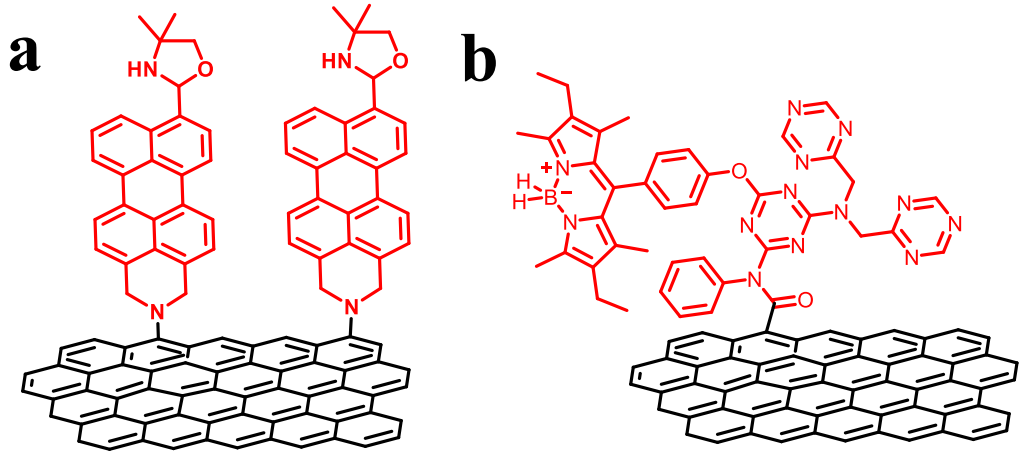

Figure 10. Covalent functionalization of photoactive spices of (a) perylenes and (b) BDP derivatives.

1.4 TRANSITION METAL DICHALCOGENIDES

Transition-metal dichalcogenides (TMDs) are layered materials of similar structure to graphite, while individual 2D layers of TMDs can be isolated in close similarity to graphene. In fact, TMDs are the most studied 2D materials beyond graphene. The thickest layer of TMDs usually consists of a distribution of M in a plane sandwiched between two atomic planes of X in which M is a transition metal, typically from groups 4–7 (M = Ti, Nb, Ta, Mo, or W) and X is a chalcogen (X=S, Se and Te), meaning that a single layer of TMDs have a height of only 3 atoms, typically, between 0.6 and 1 nm. Due to the combination of the different metals and chalcogens more than 40 different layered TMDs have been identified until today, however, the most studied, stable and commonly representative TMDs are those of MoS_2 and WS_2 followed by $MoSe_2$ and WSe_2. In fact, MoS_2 and WS_2 are the most investigated among the TMDs due to their economic availability and well-established obtaining processes. The TMDs are attractive because the electronic switch ratio, e.g. MoS_2 has a value of I_{on}/I_{off} ~10^8, the thickness of 0.65 nm and the hypothetically infinite size that provide a high surface-area-to-volume ratio, their stability upon ambient conditions and the charge density of 200 cm/Vs. Hence, TMDs are useful in electronic, sensors and nanotechnology fields. Markedly, the value of charge density of TMDs is 1000 times smaller than that of graphene, however, this value is higher than that of other semiconductors such as monocrystals of silicon (120 cm/Vs) employed in common solar cells. In fact, TMDs have been already employed as components in an extensive number of devices such as

photodetectors transistors (FETs) and solar cells, and proposed as potential alternatives to silicon in nanotechnology.[26] In addition, mono or few layered TMDs are intensively investigated for applications in diodes, electronic switches, informatics, transistors, detectors and other devices.[27]

Transition metals are covalently bonded with dichalcogenides in TMDs with energies between 1–10 eV per atom, whereas adjacent sheets interact only with van der Waals forces that are few tens of meV per atom.[28] Different distribution of M and X confers specific phases such as hexagonal, with trigonal prismatic (D_{3h}) coordination, or tetragonal with octahedral (O_h) coordination, which are important for the electronic properties of the materias.[29] In nature, the semiconducting H phase is mostly available in bulk (3D) TMDs crystals. Bulk TMDs normally have an indirect band gap that depends of the number of layers, however semiconducting monolayers of TMDs also have a sharp direct band gap, thus enhancing the emission of the photoluminescence excitons growing by 4 orders of magnitude.[30] In addition, a single TMD monolayer can absorb between the 5-20% of all the visible light, being more prominent in the semiconducting phases, which have specific absorption bands related with the band gap.

1.5 EXFOLIATION

The main production methods of TMDs include chemical vapor deposition and exfoliation. Focusing in exfoliation, three different ways to obtain few layered TMDs from bulk exist, namely, chemical exfoliation with butyl lithium (BuLi), super acid exfoliation and liquid exfoliation.

The chemical exfoliation is performed by intercalation of lithium obtaining monolayers of metallic MoS_2 from the semiconducting bulk TMDs with substantial yield.[31] Lithium is a small metal with a reduced electronegative value that can intercalated between the different layers of TMDs and transfer electrons to the layers of TMDs, forming Li^+ and negative charges onto TMDs. Columbic repulsions between the layers of TMDs promote the separation between the nanosheets that are only kept by weak Van der Waal forces.[32] This methodology can produce monolayers of TMDs, however, chemical modification with lithium also change the phase from semiconducting to metallic due to the hard conditions and the elevated number of electron transfer. More recently, in 2011 Eda et. al, discovered that a defective semiconducting phase can

be partially recovered though annealing, phenomena that deplete the excess of electrons of the material.[33]

Chlorosulfonic acid is an alternative to BuLi that keeps the desirable semiconducting phase of TMDs unaltered upon exfoliation. In this process, chlorosulfonic acid intercalates between the layers of the TMDs with the lone of electrons of sulfur placed in the TMDs. Basal sulfur acts as a weak base, which can be protonated by chlorosulfonic acid, however, without being oxidized. Protonation of TMDs is the initial step toward exfoliation due to the excess of positive charges and repulsive electrostatic forces separate the layers of TMDs. Notably, deprotonation can take place in the presence of a competing base such as water, which in addition, exoterically reacts with the chlorosulfonic acid yielding sulfuric acid and HCl gas further that expand the layers and contribute to the exfoliation. This methodology yields few and even monolayers of TMDs with sizes of hundreds of nanometers. The major advantage of exfoliation with chlorosulfonic acid is that it preserves all the properties of the semiconducting phase, as compared with e.g. BuLi. This unprecedented outcome will facilitate and enable charge-transfer phenomena within exfoliated TMD-based hybrid materials and electrodes.[34] In fact, chlorosulfonic acid has advantages with respect to simple liquid exfoliation. However, liquid exfoliation still has an important role in the production of high quality TMDs and must be explained. Typically, solvents like NMP have been employed[35] to separate the layers with the assistance of ultra-sonication, yielding single or few-layers from bulk TMDs (Figure 11). During this procedure the solvent passes between layers weakening the van deer Waals interactions, and stabilizing the dispersion of single or few layers through London dispersion forces or polar interactions. Liquid exfoliation requires strong energy during the sonication, breaking the layers in small sizes and introducing additional defects.

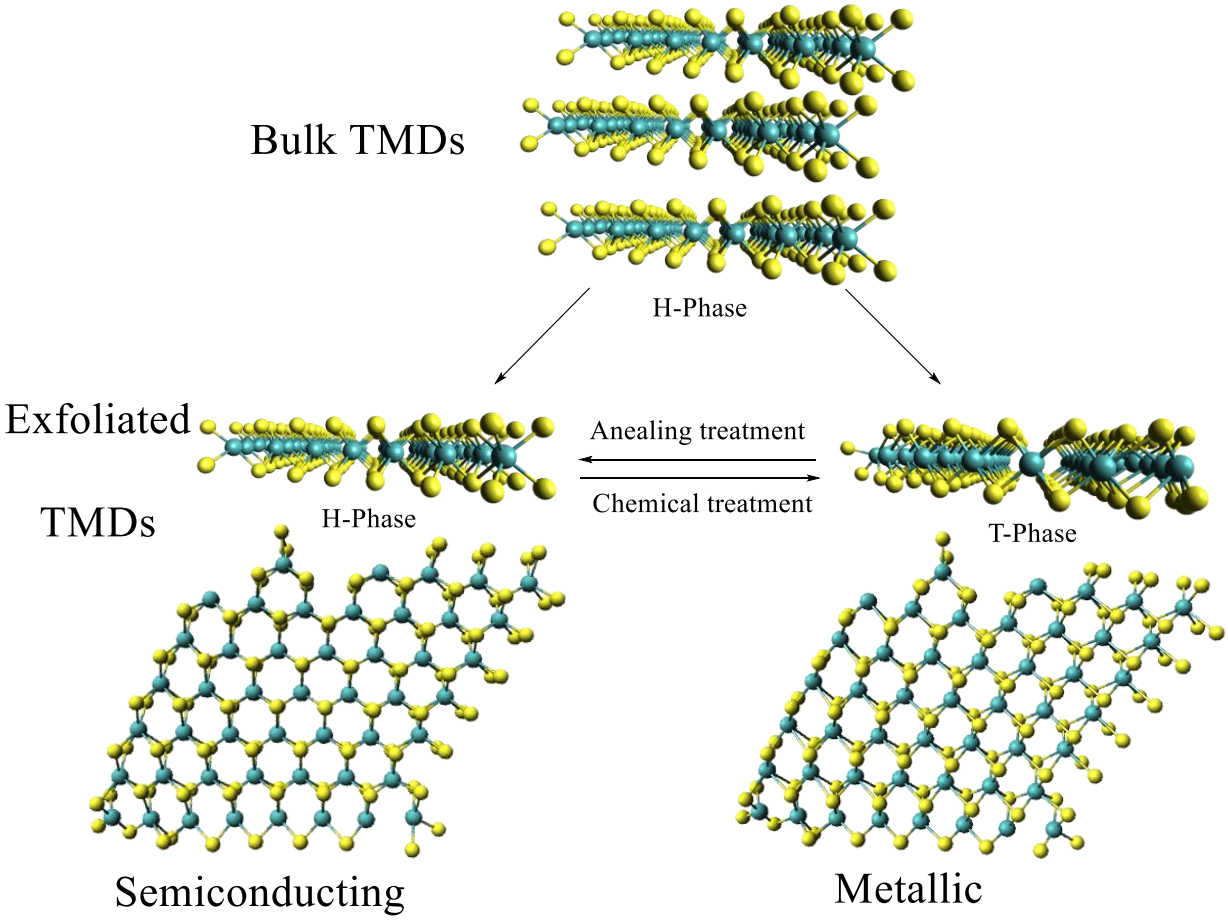

Figure 11. Route for synthesis of the two different phases of TMDs through exfoliation.

In exfoliated TMDs, defects are mostly generated during the sonication process, and they are concentrated at the edges, based in the vacancies of any of the M or X atoms.[36] In fact, such vacancies are common in mono and few layered TMDs and have been found in a wide variety of techniques.[37] For example, TEM images of MoS_2 single layers showed that basal sulfur vacancies are the most abundant type of defects with densities of the order of ~1.2 10^{17} m^2 in both exfoliated and CVD-grown MoS_2. However, double sulfur basal plane vacancies were found principally in exfoliated MoS_2 in the range of ~10^{16} m^2.[38] The densities of single and double vacancies are corresponding to ~10 and 1 per every 1100 MoS_2 units, assuming that the basal plane defects still provide a good quality of sheets. On the other hand, at the edges, are full of Mo and single or double S defects (Figure 12).

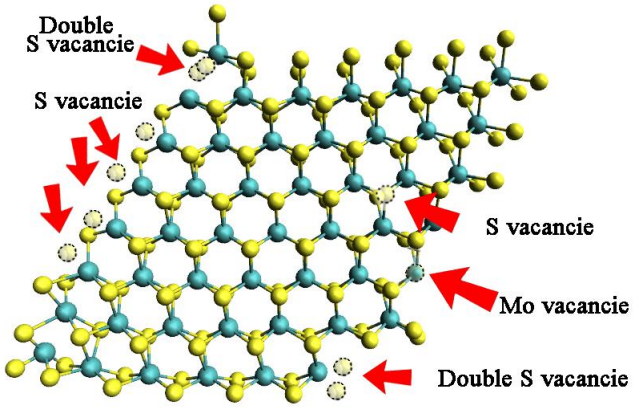

Figure 12. Representative defects of monolayer of MoS_2.

1.6 FUNCTIONALIZATION OF TMDS

The scientific community got a tremendous interest to conduct covalent and non-covalent functionalization of TMDs during the last years. Similarly to graphene, functionalization of TMDs modify their properties, take full advantage of their capabilities, and even broaden their application, hence, chemical functionalization of single and layered TMD materials is an absolute necessity. In fact, functionalization of exfoliated TMDs can enhance the emission of band gap and prevents re-staking. Other advantage of functionalization is the passivation of TMDs, protecting for undesired effects such as oxidation. In the last years, doping of TMDs has been widely studied due to the tuning of the optical properties. In fact, doping of TMDs with electro-active species via electron donor (adding electrons) or electron acceptor (adding holes), modify the charge-carrier density, acquire tremendous interest in as a component in transistors an in solar cells.[29,39] Unfortunately, TMDs tend to be rather inert to chemical functionalization, being challenging the production of functionalized modified TMDs materials.

Briefly, the main advantage of non-covalent functionalization of TMDs with organic dyes is that, in principle, such functionalization preserves the optical and electronic properties of TMDs that are remarkably precious in the semiconducting phase. Predominantly, the forces that keep in contact a non-covalent functionalization are van der Waals, hydrophobic and π-S interactions. Those forces are very week, hence, non-covalently interacting moieties with TMDs can be easily

detached, recovering pristine TMDs material and making accurate studies in liquid media difficult.[40]

In fact, the weak interactions in non-covalent functionalization of TMDs, requests to develop covalent strategies to produce stable chemically modified TMD-based materials in order to enhance their utility in technological applications. Covalent attachment results on strong bonding to TMDs, ensuring strong and close contact, which is not obtained in non-covalent interactions. Covalent functionalization of TMDs has been performed in both the semiconducting and metallic phases. Despite the lack of reactivity, different strategies have been developed to perform stable covalent functionalization. Functionalization depends on the phase, being more reactive the T-phase because it has more distortion areas and is reach in electrons, allowing nucleophilic reactions to occur, however in the last years several studies have been performed aiming the covalent functionalization of TMDs with H-phase. In this frame, thiol functionalization, diazonium salt reaction and chemical coordination with metals are the main strategies employed.

The nature of TMDs and functionalized modified TMDs can be studied through spectroscopy, thermal and microscopy imaging techniques. Spectroscopy techniques that are used in order to study TMDs are usually Raman, ATR-IR, UV-Vis and photoluminescence (PL) emission, while thermal analysis include TGA, and microscopy imaging is mainly based onTEM.

TMDs have sharp modes in Raman spectroscopy. Metallic phase of MoS_2 is more rich than semiconducting, having additional signals, the so-called J_1, J_2 and J_3 modes at 150, 225 and 325 cm^{-1}, respectively.[41] In addition, the bands A_{1g} at ~379 cm^{-1}, E^1_{2g} at ~403 cm^{-1} and 2LA(M) at ~451 cm^{-1} shed light about, the out-of-plane vibrations of S atoms, the in-plane vibrations of S and the defects present in the nanosheets of MoS_2, respectively. Additionally, the frequency difference between the E^1_{2g} and A_{1g} modes, ranging between 21-28 cm^{-1}, has been related with the number of layers, of TMDs, being lower the number of layers at higher frequencies.[42] The range of covalent functionalization can be controlled through 2LA(M) node, in fact, addition of defects on the basal plane of TMDs perturbs the nature of sulfur atoms, enhancing the 2LA(M) node. On the other hand, reduction of the 2LA(M) band is related with the reduction of the defects, for example, as occurred by sulfur vacancies healing. Along similar lines is the situation

with the Raman spectrum for others TMDs, e.g. the Raman spectrum of exfoliated WS_2 shows the 2LA(M) at 348 cm^{-1}, the E^1_{2g} at 353 cm^{-1} and the A_{1g} at 419 cm^{-1}.

Similar to graphene, the ATR-IR spectroscopy of functionalized TMDs is employed to determine the functional groups due to the presence of organic units carried in the functionalized TMDs. While no significant peaks were found in any TMDs, organic molecules possess sharp characteristic peaks related with specific functional groups such as alcohols, (2500-3100), N-H (3500-3300) carbonyls (1630-1750 cm^{-1}), among others.

The electronic absorption spectrum at the region UV-Vis shows in semiconducting phase of few or mono-layers the excitonic bands of MoS_2 at ~ 629 and 685 nm and the indirect excitons at ~ 481 and 523 nm. In WS_2, the direct exciton is found at ~ 640 nm and the indirect excitonic bands are at ~ 426, 481 and 566 nm. Those bands provide useful information about the nature of the bonds. In fact Coleman et. al. correlated the position of the bands ~ 685 nm in MoS_2 and ~ 640 nm in WS_2, with the number of layers in the material.[43] In opposite, metallic phases in both MoS_2 and WS_2 have different morphology, without no characteristic bands in the excitonic spectra. Once TMDs are functionalized with photoactive molecules, additional bands associated with the organic dyes are distinguishable. In fact, shift of those signals are associated with electronic communications of the bands of TMDs and the ground state of the organic dye.

PL emission is without any doubt, a powerful tool that sheds light to the nature of TMDs. Only the semiconducting phase has a direct band gap. However, the emission is thickness dependent. Due to the strong hybridisation between the d-orbitals of transition metal an indirect band-gap exists, which strongly depends on the number of layers. Conversely, the direct band-gap of TMDs is unaffected by interlayer interactions. The photoluminescence originating from the direct band-gap transition (A exciton) is observed stronger and more intense by orders of magnitude in monolayer than in oligolayered and bulk material. Notably, although the photoluminescence energy due to the A exciton only slightly blue-shifts with decreasing thickness, the presence of large blue-shifts originating from the indirect band-gap transition, indicate strong and weak interlayer coupling for the indirect and direct transition, respectively.[44]

TGA allows establishing the amount of functional groups attached on the functionalized TMDs by calculating the mass loss occurred while increasing the temperature. TMDs are stable at high

temperatures under inert conditions, e.g. nitrogen atmosphere, with small mass loss occurring at temperature higher than 550 ºC, due to the presence of defects. Therefore, the mass loss of functionalized TMDs between 200-550 ºC corresponds to the thermal decomposition of the organic addends.

Similarly with graphene, TEM microscopy imaging is employed to confirm the presence of TMDs in the functionalized material and as well as to give information about the morphology, defects and phases. EELs or EDX, provide information about the functionalized materials, in which carbon species are easily distinguishable from the transition metals and dichalcogenides.

Photoactive species such as metal-phthalocyanines have been non-covalently interacted with layered TMDs, tuning the transition-metal dichalcogenides properties such as charge-carrier density. Once an electron is photoexcited in the conduction band of $MoSe_2$, it is transferred to Ni-phthalocyanines, but this does not happen in the case of MoS_2 because the conduction band of MoS_2 is less energetic that the excited states of the $MoSe_2$.[40c] Similarly, physisorbed Mg-phthalocyanines or Ni-phthalocyanines can accept electrons for WSe_2.

Typically, thiol derivatives have been explored for the covalent functionalization of defective TMDs in both semiconducting and metallic phase.[45] During the functionalization, sulfur coordinates with the metal of TMDs at chalcogen vacancies. However, ligand conjugation of thiols to Mo atoms of TMDs,[45b, 46] is a rather debatable route of functionalization, since thiols can convert to the corresponding disulfides (Figure 13) in a catalytic reaction activated by the presence of MoS_2, which eventually physisorb onto the basal plane of TMDs.[47]

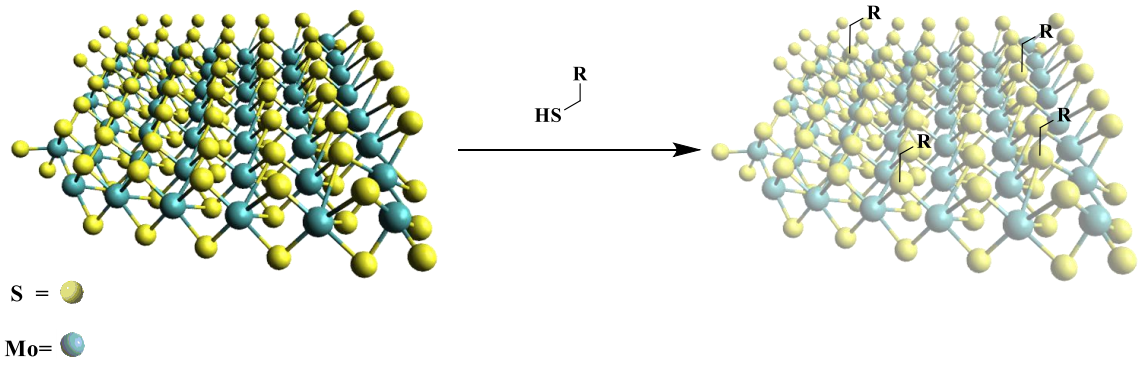

Figure 13. General example of chemical modification of semiconducting or metallic TMDs through thiol functionalization.

In 2015, a reaction was described between metallic TMDs[48] and organohalides such as methyl iodide or iodoacetamide resulting in the formation of covalent C-S bond. During this reaction, rich-in-electron metallic MoS_2 acts as a nucleophilic in a S_{N2} reaction that attacks the organohalides, being the halogen the leaving group. In fact this reaction can be performed in semiconducting phase employing tetrakis(triphenylphosphine)palladium(0) ($Pd(PPh_3)_4$) as a catalyst, wherein aryl-halides derivatives of pyrene, coumarin and porphyrin show stable basal functionalization.[49] Such reaction can tune the optical properties of the TMDs and have applications in optoelectronics. However, the method described above disrupts the basal plane, by adding distortions, and a significant reduction of the charge carrier density is expected (Figure 16).

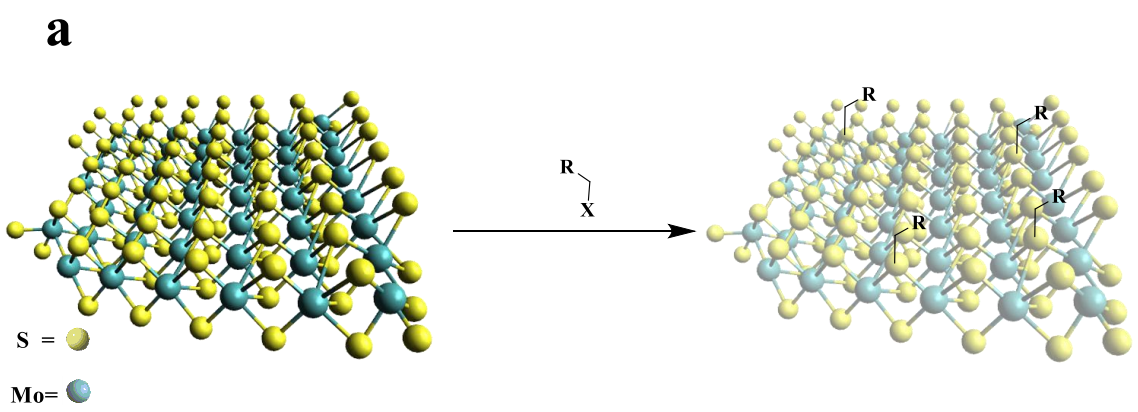

Figure 16 General example of chemical modification of metallic TMDs through halide derivatives.

Next, metallic MoS_2 can react with aryl diazonium salt by covalent functionalization at the basal plane.[50] During the reaction aryl radical is obtained though electron transfer from MoS_2 to the aryl diazonium salt derivative. The basal functionalization route is obtained through radical recombination between the species involved. Varying the reactant amounts, time and temperature was possible to transform the metallic MoS_2 to semiconducting. Such methodology allows further functionalization, for example chemically modified TMDs were further functionalized with cobaloxime[51] or $Ru(II)(bpy)_2Cl_2$[52] compounds though chemical coordination.

However due to the non-well characterized metallic/semiconducting phase, their use in optoelectronics could be problematic (Figure 17).

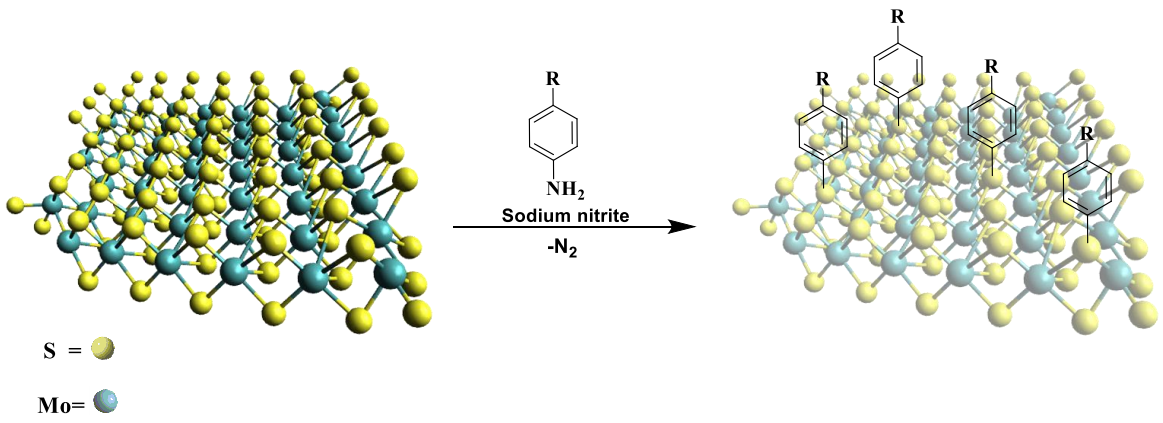

Figure 17. General example of chemical modification of metallic TMDs through with diazonium salt reaction.

At this point it is clearly stated that performing a basal functionalization of semiconducting TMDs without disrupting the electronic properties is challenging. In 2015, Bakes et. al, achieved an additional basal functionalization by cationic metal complexes using the rich-chalcogens surface of TMDs as ligands in a Lewis acid–base type of coordination chemistry.[53] Metals such as Cu^{2+}, Zn^{+} and Ni^{2+} ions were identified as suitable anchors to the TMD chalcogens. The functionalized materials had good solubility and UV-Vis spectra showed no alteration of the optoelectronic properties of TMDs. However, this functionalization has no any physical application beyond p-type doping in covalent functionalization (Figure 18).

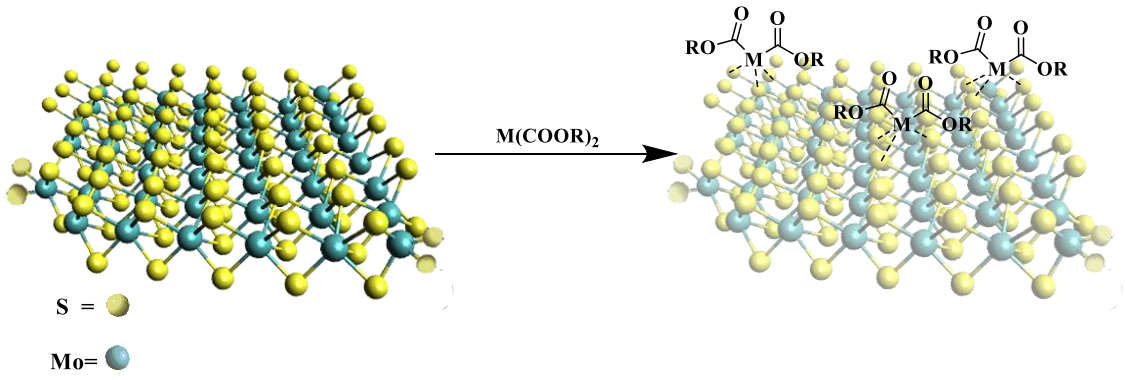

Figure 18. Representative example of basal functionalization of semiconducting TMDs through coordination reaction of cationic metal complexes.

1.7 REFERENCES

1. K. F. Mak, M. Y. Sfeir, Y. Wu, C. H. Lui, J. A. Misewich and T. F. Heinz. Measurement of the Optical Conductivity of Graphene. *Phys. Rev. Lett*. **2008**, *101*, 196405-196409.

2. F. Bonaccorso, Z. Sun, T. Hasan and A. C. Ferrari. Graphene photonics and optoelectronics. *Nature Photon*. **2010**, *4*, 611-622; (b) K. I. Bolotin, K. J. Sikes, Z. Jiang, M. Klima, G. Fudenberg, J. Hone, P. Kim and H. L. Stormer. Ultrahigh electron mobility in suspended graphene. *Solid State Commun*. **2008**, *146*, 351-355; (c) K. I. Bolotin, K. J. Sikes, Z. Jiang, M. Klima, G. Fudenberg, J. Hone, P. Kim, and H. L. Stormer. Ultrahigh electron mobility in suspended graphene. *Solid State Commun*. **2008**, *146*, 351-355.

3. V. Georgakilas, M. Otyepka, A. B. Bourlinos, V. Chandra, N. Kim, K. C. Kemp, P. Hobza, R. Zboril and K. S. Kim, Functionalization of Graphene: Covalent and Non-Covalent Approaches, Derivatives and Applications. *Chem. Rev*. **2012**, *112*, 6156-6214.

4. Y. Xu, H. Cao, Y. Xue, B. Li and W. Cai. Nanomaterials Liquid-Phase Exfoliation of Graphene: An Overview on Exfoliation Media. *Techniques, and Challenges, Basel*, **2018**, *8*, 942-974.

5. Y. Hernandez, V. Nicolosi, M. Lotya, F. M. Blighe, Z. Sun, S. De, I. T. McGovern, B. Holland, M. Byrne, Y. K. Gun'Ko, J. J. Boland, P. Niraj, G. Duesberg, S. Krishnamurthy, R. Goodhue, J. Hutchison, V. Scardaci, A. C. Ferrari and J. N. Coleman. High-yield production of graphene by liquid-phase exfoliation of graphite. *Nat. Nanotechnol.* **2008**, *3*, 563-568.

6. M. Lotya, Y. Hernandez, P. J. King, R. J. Smith, V. Nicolosi, L. S. Karlsson, F. M. Blighe, S. De, Z. Wang, I. T. McGovern, G. S. Duesberg and J. N. Coleman. Liquid Phase Production of Graphene by Exfoliation of Graphite in Surfactant/Water Solutions. *J. Am. Chem. Soc*. **2009**, *131*, 3611-3620.

7. G. Bottari, H. MÁ, L. Wibmer, M. Volland, L. Rodríguez-Pérez, D.M. Guldi, A. Hirsch, N. Martín F. D'Souza and T. Torres. Chemical functionalization and characterization of graphene-based materials. *Chem Soc Rev*. **2017**, *46*, 4464-4500.

8. B. Jin, J. Shen, R. Peng, C. Chen, Q. Zhang, X. Wang and S. Chu Ind. DMSO: an efficient catalyst for the cyclopropanation of C_{60}, C_{70}, SWNTs and graphene through the Bingel reaction. *Eng. Chem. Res*. **2015**, *54*, 2879-2885.

9. (a) M. M. Heravi and V. F. Vavsari. Recent applications of intramolecular Diels-Alder reaction in total synthesis of natural products. *RSC Advances.* **2015**, *5*, 50890-50912. (b) K. C. Nicolaou, S. A. Snyder, T. Montagnon and G. Vassilikogiannakis. The Diels–Alder Reaction in Total Synthesis. *Angew. Chem., Int. Ed.* **2002**, *41*, 1668-1698.

10. A. Isakova, C. Burton, D. J. Nowakowski and P. D. Topham. Diels-Alder cycloaddition and RAFT chain end functionality: an elegant route to fullerene end-capped polymers with control over molecular mass and architecture. *Polym. Chem.* **2017**, *8*, 2796-2805.

11. D. Mata, M. Amaral, A. J. S. Fernandes, B. Colaco, A. Gama, M. C. Paiva, P. S. Gomes, R. F. Silva and M. H. Fernandes. Diels-Alder functionalized carbon nanotubes for bone tissue engineering: in vitro/in vivo biocompatibility and biodegradability. *Nanoscale* **2015**, *7*, 9238-9251; (b) J. L. Delgado, P. de la Cruz, F. Langa, A. Urbina, J. Casado and J. T. Lopez-Navarrete. Microwave-assisted sidewall functionalization of single-wall carbon nanotubes by Diels-Alder cycloaddition. *Chem. Commun*. **2004**, 1734-1735; (c) S. Munirasu, J. Albuerne, A. Boschetti-de-Fierro and V. Abetz. Functionalization of Carbon Materials using the Diels-Alder Reaction. *Macromol*. *Rapid Commun*. **2010**, *31*, 574-579.

12. (a) J. Li, M. Li, L.-L. Zhou, S.-Y. Lang, H.-Y. Lu, D. Wang, C.-F. Chen and L.-J. Wan. Click and Patterned Functionalization of Graphene by Diels–Alder Reaction. *J. Am. Chem. Soc.* **2016**, *138*, 7448; (b) S. Sarkar, E. Bekyarova, S. Niyogi and R. C. Haddon. Diels−Alder Chemistry of Graphite and Graphene: Graphene as Diene and Dienophile *J. Am. Chem. Soc.* **2011**, *133*, 3324–3327.

13. J. Greenwood, T. H. Phan, Y. Fujita, Z. Li, O. Ivasenko, W. Vanderlinden, H. Van Gorp, W. Frederickx, G. Lu, K. Tahara, Y. Tobe, H. Uji-i, S. F. L. Mertens and D. S. Feyter. Covalent Modification of Graphene and Graphite Using Diazonium Chemistry: Tunable Grafting and Nanomanipulation. *ACS Nano.* **2015**, *9*, 5520-5535.

14. M. Quintana K. Spyrou M. Grzelczak W.R. Browne P. Rudolf and M Prato. Functionalization of graphene via 1,3-dipolar cycloaddition. *ACS Nano.* **2010**, *4*,3527–33.

15. L.-H. Liu and M. Yan, Functionalization of pristine graphene with perfluorophenyl azides. *J. Mater. Chem.* **2011**, *21*, 3273–3276.

16. Z. Du, W. Ai, L. Xie and W. Huang. Organic radical functionalized graphene as a superior anode material for lithium-ion batteries. *J. Mater. Chem. A* **2014**, *2*, 9164-9168; (b) M. M. Stylianakis, D. Konios, G. Kakavelakisa, G. Charalambidisd E. Stratakis, A. G. Coutsolelos, E. Kymakis and S. H. Anastasiadis. Efficient ternary organic photovoltaics incorporating a graphene-based porphyrin molecule as a universal electron cascade material. *Nanoscale* **2015**, *7*, 17827-17835.

17. F. G. Brunetti, H. Isla, J. Arago, E. Ortı, E. M. Perez and N. Martın. Exploiting Multivalent Nanoparticles for the Supramolecular Functionalization of Graphene with a Nonplanar Recognition Motif. *Chem.-Eur. J,* **2013**, *19*, 9843-9848.

18. S. P. Economopoulos and N. Tagmatarchis. Multichromophores Onto Graphene: Supramolecular Non-Covalent Approaches for Efficient Light Harvesting. *J. Phys. Chem. C* **2015**, *119*, 8046–8053.

19. A. Roth, C. Schierl, A. Ferrer-Ruiz, M. Minameyer, L. Rodríguez-Pérez C. Villegas, M. Ángeles-Herranz, N. Martín and D. M.Guldi. Low-Dimensional Carbon Allotropes: Ground- and Excited-State Charge Transfer with NIR-Absorbing Heptamethine Cyanine. *Chem.* **2017**, 164-173.

20. A. Wang, J. Ye, M. G. Humphrey, and C. Zhang. Graphene and Carbon-Nanotube Nanohybrids Covalently Functionalized by Porphyrins and Phthalocyanines for Optoelectronic Properties. *Adv Mater*. **2018**, *17*, 1705704- 1705713.

21. Zinc phthalocyanine–graphene hybrid material for energy conversion: synthesis, characterization, photophysics, and photoelectrochemical cell preparation. N. Karousis, J. Ortiz, K. Ohkubo, T. Hasobe, S. Fukuzumi, Á. Sastre-Santos, N. Tagmatarchis, *J. Phys. Chem.* C **2012**, *116*, 20564-20573.

22. M. E. Ragoussi, G. Katsukis, A. Roth, J. Malig, G. de la Torre, D. M. Guldi, T. Torres. Electron-Donating Behavior of Few-Layer Graphene in Covalent Ensembles with Electron-Accepting Phthalocyanines. *J. Am. Chem. Soc*. **2014**, *136*, 4593-4598.

23. D. Dasler, R. A. Schäfer, M. B. Minameyer, J. F. Hitzenberger, F. Hauke, T. Drewello and A. Hirsch. Direct Covalent Coupling of Porphyrins to Graphene. *J. Am. Chem. Soc*. **2017**, *139*, 11760- 11765.

24. K. Abinaya, S. Karthikaikumar, K. Sudha, S. Sundharamurthi, A. Elangovan and P. Kalimuthu. Efficient visible light driven hydrogen generation using 9-(3,3-dimethyl-1,2-

oxazetidine-N-yl) perylene-3,4-dicarboximide functionalized amino graphene. *Appl Catal B.* **2019**, *242*, 293-301.

25. R. K. Yadav, J.-O. Baeg, A. Kumar, K.-j. Kong, G. H. Oha and N.-J. Park. Graphene–BODIPY as a photocatalyst in the photocatalytic–biocatalytic coupled system for solar fuel production from CO_2. *J. Mater. Chem. A* **2014**, *2*, 5068-5076.

26. S. Bertolazzi, M. Gobbi, Y. Zhao, C. Backes, and P. Samorì. Molecular chemistry approaches for tuning the properties of two-dimensional transition metal dichalcogenides. *Chem. Soc. Rev.* **2018**, *47*, 6845-6888.

27. K. F. Mak and J. Shan. Photonics and optoelectronics of 2D semiconductor transition metal dichalcogenides. *Nat. Photonics* **2016**, *10*, 216.

28. (a) D. L. Duong, S. J. Yun and Y. H. Lee. van der Waals Layered Materials: Opportunities and Challenges. *ACS Nano*. **2017**, *11*, 11803-11830; (b) P. Miro, M. Audiffred and T. Heine. An atlas of two-dimensional materials. *Chem. Soc. Rev*. **2014**, *43*, 6537-6554; (c) A. C. Ferrari, F. Bonaccorso, V. Falko, K. S. Novoselov, S. Roche, P. Boggild, S. Borini, F. H. L. Koppens, V. Palermo, N. Pugno, J. A. Garrido, I. A. Kinloch, T. Seyller, E. Quesnel, X. L. Feng, K. Teo, N. Rupesinghe, P. Hakonen, S. R. T. Neil, Q. Tannock, T. Lofwander and J. Kinaret. Science and technology roadmap for graphene, related two-dimensional crystals, and hybrid systems. *Nanoscale* **2015**, *7*, 4598-4810; (d) M. Chhowalla, H. S. Shin, G. Eda, L. J. Li, K. P. Loh and H. Zhang. The chemistry of two-dimensional layered transition metal dichalcogenide nanosheets. *Nat. Chem.* **2013**, *5*, 263-275.

29. A. Kuc and T. Heine. The electronic structure calculations of 2D TMDs in the presence of external electric and magnetic fields. *Chem. Soc. Rev*. **2015**, *44*, 2603-2614; (b) F. A. Rasmussen and K. S. Thygesen. Computational 2D Materials Database: Electronic Structure of TMDs and Oxides. *J. Phys. Chem. C* **2015**, *119*, 13169- 13183; (c) C. Ataca, H. Sahin and S. Ciraci, Stable, Single-Layer MX_2 Transition-Metal Oxides and Dichalcogenides in a Honeycomb-Like Structure *J. Phys. Chem. C* **2012**, *116*, 8983-8999.

30. D. Jariwala, V. K. Sangwan, L. J. Lauhon, T. J. Marks and M. C. Hersam. Emerging Device Applications for Semiconducting Two-Dimensional TMDs. *ACS Nano*. **2014**, *8*, 1102-1120.

31. P. Joensen, R. Frindt and S. R. Morrison. Single-layer MoS_2. *Mater. Res. Bull*. **1986**, *21*, 457-461.

32. H. Fang, M. Tosun, G. Seol, T. C. Chang, K. Takei and J. G. Javey. Degenerate n-Doping of Few-Layer Transition Metal Dichalcogenides by Potassium. A. *Nano Lett*. **2013**, *13*, 1991-1995.

33. G. Eda, H. Yamaguchi, D. Voiry, T. Fujita, M. Chen, M. Chhowalla. Photoluminescence from Chemically Exfoliated MoS_2. *Nano Lett*. **2011**, *11*, 5111-5116.

34. G. Pagona, C. Bittencourt, R. Arenal, and N. Tagmatarchis. Exfoliated semiconducting pure 2H-MoS_2 and 2H-WS_2 assisted by chlorosulfonic acid. *Chem. Com*mun. **2015**, *15*, 12950-12953.

35. J. N. Coleman, M. Lotya, A. O'Neill, S. D. Bergin, P. J. King, U. Khan, K. Young, A. Gaucher, S. De and J. R. Smith. Two-Dimensional Nanosheets Produced by Liquid Exfoliation of Layered Materials. *Science* **2011**, *331*, 568-571; (b) G. Cunningham, M. Lotya, C. S. Cucinotta, S. Sanvito, S. D. Bergin, R. Menzel, M. S. Shaffer and J. N. Coleman. Solvent Exfoliation of Transition Metal Dichalcogenides: Dispersibility of Exfoliated Nanosheets Varies Only Weakly between Compounds. *ACS Nano.* **2012**, *6*, 3468- 3480; (c) A. O'Neill, U. Khan and J. N. Coleman. Preparation of High Concentration Dispersions of Exfoliated MoS_2 with Increased Flake Size. *Chem. Mater*. **2012**, *24*, 2414-2421.

36. (a) M. Yi and Z. G. Shen. A review on mechanical exfoliation for the scalable production of graphene. *J. Mater. Chem. A*, **2015**, *3*, 11700- 11715; (b) M. Eredia, S. Bertolazzi, T. Leydecker, M. E. Garah, I. Janica, G. Melinte, O. Ersen, A. Ciesielski and P. Samorı. Morphology and Electronic Properties of Electrochemically Exfoliated Graphene. *J. Phys. Chem. Lett.* **2017**, *8*, 3347-3355.

37. Z. Lin, B. R. Carvalho, E. Kahn, R. T. Lv, R. Rao, H. Terrones, M. A. Pimenta and M. Terrones. Defect engineering of two-dimensional transition metal dichalcogenides. *2D Mater.* **2016**, *3*, 022002-022024.

38. J. Hong, Z. Hu, M. Probert, K. Li, D. Lv, X. Yang, L. Gu, N. Mao, Q. Feng, L. Xie, J. Zhang, D. Wu, Z. Zhang, C. Jin, W. Ji, X. Zhang, J. Yuan and Z. Zhang. Exploring atomic defects in molybdenum disulphide monolayers. *Nat. Commun.* **2015**, *6*, 6293-6391.

39. C. Li, Q. Cao, F. Wang, Y. Xiao, Y. Li, J.-J. Delaunay and H. Zhu. Engineering graphene and TMDs based van der Waals heterostructures for photovoltaic and photoelectrochemical solar energy conversion. *Chem. Soc. Rev*. **2018**,*47*, 4981-5037.

40. (a) S. Kaushika, U. K. Tiwaria, S. S. Pala and R. K. Sinhaa. Rapid detection of Escherichia coli using fiber optic surface plasmon resonance immunosensor based on biofunctionalized Molybdenum disulfide (MoS_2) nanosheets. *Biosens. Bioelectron.* **2019**, *126*, 501-509; (b) E. P. Nguyen, B. J. Carey, C. J. Harrison, P. Atkin, K. J. Berean, E. D. Gaspera, J. Z. Ou, R. B. Kaner, K. Kalantar-zadeh and T. Daeneke. Excitation dependent bidirectional electron transfer in phthalocyanine-functionalised MoS_2 nanosheets. *Nanoscale* **2016**, *8*, 16276-16283; (c) J. Choi, H. Zhang and J. H. Choi. Modulating Optoelectronic Properties of Two-Dimensional Transition Metal Dichalcogenide Semiconductors by Photoinduced Charge Transfer. *ACS Nano*. **2016**, *10*, 1671-1680; (d) T. R. Kafle, B. Kattel, S. D. Lane, T. Wang, H. Zhao and W-L. Chan. Charge Transfer Exciton and Spin Flipping at Organic-Transition-Metal Dichalcogenide Interfaces. *ACS Nano*. **2017**, *11*, 10184-10192.

41. (a) B. Chakraborty, A. Bera, D. V. S. Muthu, S. Bhowmick, U. V. Waghmare and A. K. Sood. Symmetry-dependent phonon renormalization in monolayer MoS_2. *Phys. Rev. B: Condens. Matter*. **2012**, *85*, 161403-161409; (b) Y. Shi, J.-K. Huang, L. Jin, Y.-T. Hsu, S. F. Yu, L.-J Li and H. Y. Yang. Selective decoration of Au nanoparticles on monolayer MoS_2 single crystals. *Sci. Rep*. **2013**, *3*, 1839-1846.

42. H. Li, Q. Zhang, R. Y. C. Chong, K. T. Beng, T. E. T. Hang, A. Olivier and D. Baillargeat. From bulk to monolayer MoS_2: Evolution of Raman scattering. *Adv. Funct. Mater*. **2012**, *22*, 1385-1390.

43. (a) C. Backes, B. M. Szydłowska, A. Harvey, S. Yuan, V. Vega-Mayoral, B. R. Davies, P.-L. Zhao, D. Hanlon, E. J. G. Santos, M. I. Katsnelson, W.J. Blau, C. Gadermaier and J. N. Coleman. Production of highly monolayer enriched dispersions of liquid-exfoliated nanosheets by liquid cascade centrifugation. *ACS Nano* **2016**, 10, 1589-1601.

44. (a) W. S. Yun, S. W. Han, S. C. Hong, I. G. Kim and J. D. Lee. Thickness and strain effects on electronic structures of transition metal dichalcogenides: 2H-MX_2 semiconductors (M = Mo, W; X= S, Se, Te). *Phys. Rev. B* **2012**, *85*, 033305-033310; (b) K. F. Mak, C. Lee, J. Hone and J. Shan, T. F. Heinz. Atomically Thin MoS_2: A New Direct-Gap Semiconductor. *Phys. Rev. Lett*. **2012**, *105*, 136805-136809; (c) P. Tonndorf, R. Schmidt, P. Bottger, X. Zhang, J. Borner, A. Liebig, M. Albrecht, C. Kloc, O. Gordan, D. R. T. Zahn, S. M. De Vasconcellos and R. Bratschitsch. Photoluminescence emission and Raman response of monolayer MoS_2, $MoSe_2$, and WSe_2. *Opt. Express* **2013**, *21*, 4908-4916.

45. (a) S. Bertolazzi, S. Bonacchi, G. J. Nan, A. Pershin, D. Beljonne and P. Samorı. Engineering Chemically Active Defects in Monolayer MoS_2 Transistors via Ion-Beam Irradiation and Their Healing via Vapor Deposition of Alkanethiols. *Adv. Mater*. **2017**, *29*, 1606760-1606767; (b) K. Cho, M. Min, T.-Y. Kim, H. Jeong, J. Pak, J.-K. Kim, J. Jang, S. J. Yun, Y. H. Lee, W.-K. Hong and T. Lee. Electrical and Optical Characterization of MoS_2 with Sulfur Vacancy Passivation by Treatment with Alkanethiol Molecules. *ACS Nano*. **2015**, *9*, 8044-8053.

46. S. S. Chou, M. De, J. Kim, S. Byun, C. Dykstra, J. Yu, J. Huang and V. P. Dravid. Ligand Conjugation of Chemically Exfoliated MoS_2. *J. Am. Chem. Soc.* **2013**, *135*, 4584-4587; (b) L. Zhou, B. He, Y. Yang and Y. He. Facile approach to surface functionalized MoS_2 nanosheets. *RSC Adv.* **2014**, *4*, 32570-32578; (c) R. Anbazhagan, H.-J. Wang, H.-C. Tsai and R.-J. Jeng. Highly concentrated MoS_2 nanosheets in water achieved by thioglycolic acid as stabilizer and used as biomarkers. *RSC Advances* **2014**, *4*, 42936-42941; (d) J.-S. Kim, H.-W. Yoo, H. O. Choi, H.-T. Jung. Tunable Volatile Organic Compounds Sensor by Using Thiolated Ligand Conjugation on MoS_2. *Nano Lett.* **2014**, *14*, 5941-5947; (e) T. Liu, S. Shi, C. Liang, S. Shen, L. Cheng, C. Wang, X. Song, S. Goel, T. E. Barnhart, W. Cai, Z. Liu. Iron Oxide Decorated MoS_2 Nanosheets with Double PEGylation for Chelator-Free Radiolabeling and Multimodal Imaging Guided Photothermal Therapy. *ACS Nano* **2015**, *9*, 950-960; (f) E. P. Nguyen, B. J. Carey, J. Z. Ou, J. van Embden, E. D. Gaspera, A. F. Chrimes, M. J. S. Spencer, S. Zhuiykov, K. Kalantar-zadeh, T. Daeneke. Electronic Tuning of 2D MoS_2 through Surface Functionalization. *Adv. Mater*. **2015**, *27*, 6224-6229.

47. X. Chen, N. C. Berner, C. Backes, G. S. Duesberg, A. R. McDonald. Functionalization of Two-Dimensional MoS_2: On the Reaction Between MoS_2 and Organic Thiols. *Angew. Chem. Int. Ed*. **2016**, *55*, 5803-5908.

48. (a) M. A. Khan, M. Erementchouk, J. Hendrickson and M. N. Leuenberger. Plasmonics in graphene at infrared frequencies. *Phys. Rev. B.* **2017**, *95*, 245435-245447; (b) Y. Guo, D. Liu and J. Robertson. Defect induced gap states in monolayer MoS_2 control the Schottky barriers of Pt-mMoS_2 interfaces. *Appl. Phys. Lett*. **2015**, *106*, 173106-173111.

49. (a) P. Vishnoi, A. Sampath, U. V. Waghmare and C. N. R. Rao. Covalent Functionalization of Nanosheets of MoS_2 and $MoSe_2$ by Substituted Benzenes and Other Organic Molecules. *Chem.-Eur. J*. **2017**, *23*, 886-895.

50. K. C. Knirsch, N. C. Berner, H. C. Nerl, C. S. Cucinotta, Z. Gholamvand, N. McEvoy, Z. Wang, I. Abramovic, P. Vecera, M. Halik, S. Sanvito, G. S. Duesberg, V. Nicolosi, F. Hauke, A. Hirsch, J. N. Coleman and C. Backes. Basal-Plane Functionalization of Chemically Exfoliated Molybdenum Disulfide by Diazonium Salts. *ACS Nano*. **2015**, *9*, 6018-6030.

51. M. Cai, F. Zhang, C. Zhang, C. Lu, Y. He, Y. Qu, H. Tian, X. Feng and X. Zhuang. Cobaloxime anchored MoS_2 nanosheets as electrocatalysts for the hydrogen evolution reaction. *J. Mater. Chem. A* **2018**, *6*, 138-144.

52. X. Chen, D. McAteer, C. McGuinness, I. Godwin, J. N. Coleman and A. R. McDonald. RuII Photosensitizer-Functionalized Two-Dimensional MoS_2 for Light-Driven Hydrogen Evolution. *Chem.-Eur. J*. **2018**, *24*, 351-355.

53. (a) C. Backes, N. C. Berner, X. Chen, P. Lafargue, P. LaPlace, M. Freeley, G. S. Duesberg, J. N. Coleman and A. R. McDonald. Functionalization of Liquid-Exfoliated Two-Dimensional 2H-MoS_2. *Angew. Chem. Int. Ed*. **2015**, *54*, 2638.

CHAPTER 2

Scope of research

The strategic objective of the PhD thesis is the development of novel hybrid materials, based on graphene and TMDs featuring organic photo- and/or electro-active components, with interesting photophysical and redox properties, potentially suitable to be employed in energy-related processes. The scope of the conducted research to accomplish the objective is two-fold, namely to (a) covalently incorporate organic dyes with absorption in the NIR region onto graphene sheets, and (b) functionalize transition metal dichalcogenides (TMDs), MoS_2 and WS_2, as related two-dimensional analogues of graphene, with chromophore moieties.

In **Chapter 3**, the covalent functionalization of exfoliated graphene sheets with 4,4-difluoro -4-boron-3a,4a,8-triazo-s-indacene (boron azadipyrromethenes – azaBDP) derivatives was accomplished. The exfoliated graphene was initially modified upon reaction with in-situ generated aryl diazonium salts to carry terminal alkyne chains. In parallel, azaBDP derivatives, specifically designed to feature azide units, were synthesized following a multi-step synthetic approach and then reacted with the pre-modified graphene sheets via “click-chemistry” conditions. In addition, graphene sheets were functionalized with aryl diazonium salts bearing cyanine derivatives as part of their structure as well as amine moieties which were subsequently employed in condensation reactions with cyanines possessing a free carboxylic acid group. Of particular importance was the incorporation of ethylene glycol chain as part of the azaBDP structure to enhance the solubility of the graphene-based hybrid materials. The structures of the graphene-based hybrid materials featuring azaBDPs and cyanines as addends are collectively presented in Figure 1. All hybrid materials were comprehensively characterized by complementary spectroscopic, thermal and microscopy imaging techniques, while the optical and redox properties were assessed by electronic absorption, fluorescence emission and electrochemistry. Overall, upon photoexcitation electron/energy transfer processes from the dyes to graphene acting as acceptor were observed. Due to these processes the newly prepared graphene-based hybrid materials are expected to find interesting applications in the energy-related field.

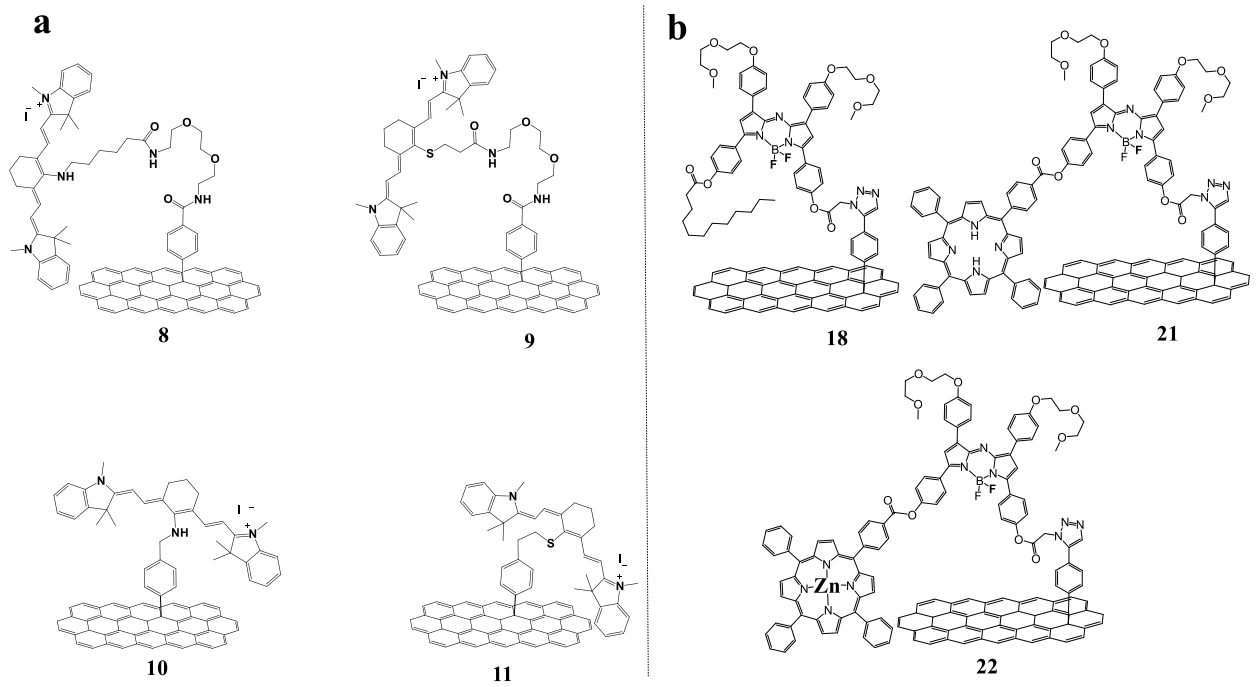

Figure 1. Graphene-based hybrid materials featuring (a) azaBDPs, and (b) cyanines as addends.

In **Chapter 4**, a new methodological approach developed for the covalent functionalization of MoS_2 and WS_2 is presented. Specifically, it was found that 1,2-dithiolanes can efficiently bind at the edges of MoS_2 and WS_2 at sulfur vacant sites of defected Mo and W (Figure 2). Those defects are formed during the exfoliation procedure from the bulk. In parallel, the stability of N-methyl pyrrolidone (NMP), which is widely employed as solvent in wet exfoliation approaches for both graphene and TMDs was studied. Furthermore, the effect and implications of NMP in the exfoliated materials were assessed.

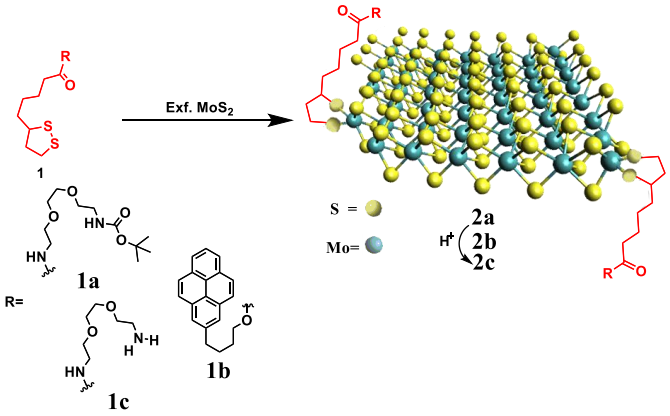

Figure 2. Functionalization of TMDs based on the addition of 1,2-dithiolanes.

In **Chapter 5**, building on the functionalization of TMDs with 1,2-dithiolanes, covalently modified TMDs with (a) carbon dots, (a) porphyrin, and (c) zinc phthalocyanine, according to Figure 3, were prepared. The newly developed hybrid materials were fully characterized by complementary spectroscopic, thermal and microscopy imaging techniques. The photophysical and electrochemical properties of the hybrid materials were assessed and interesting properties based on photoinduced charge-transfer interactions were identified. In addition to the aforementioned covalently formed hybrid materials, modified TMDs featuring ammonium moieties were also prepared.

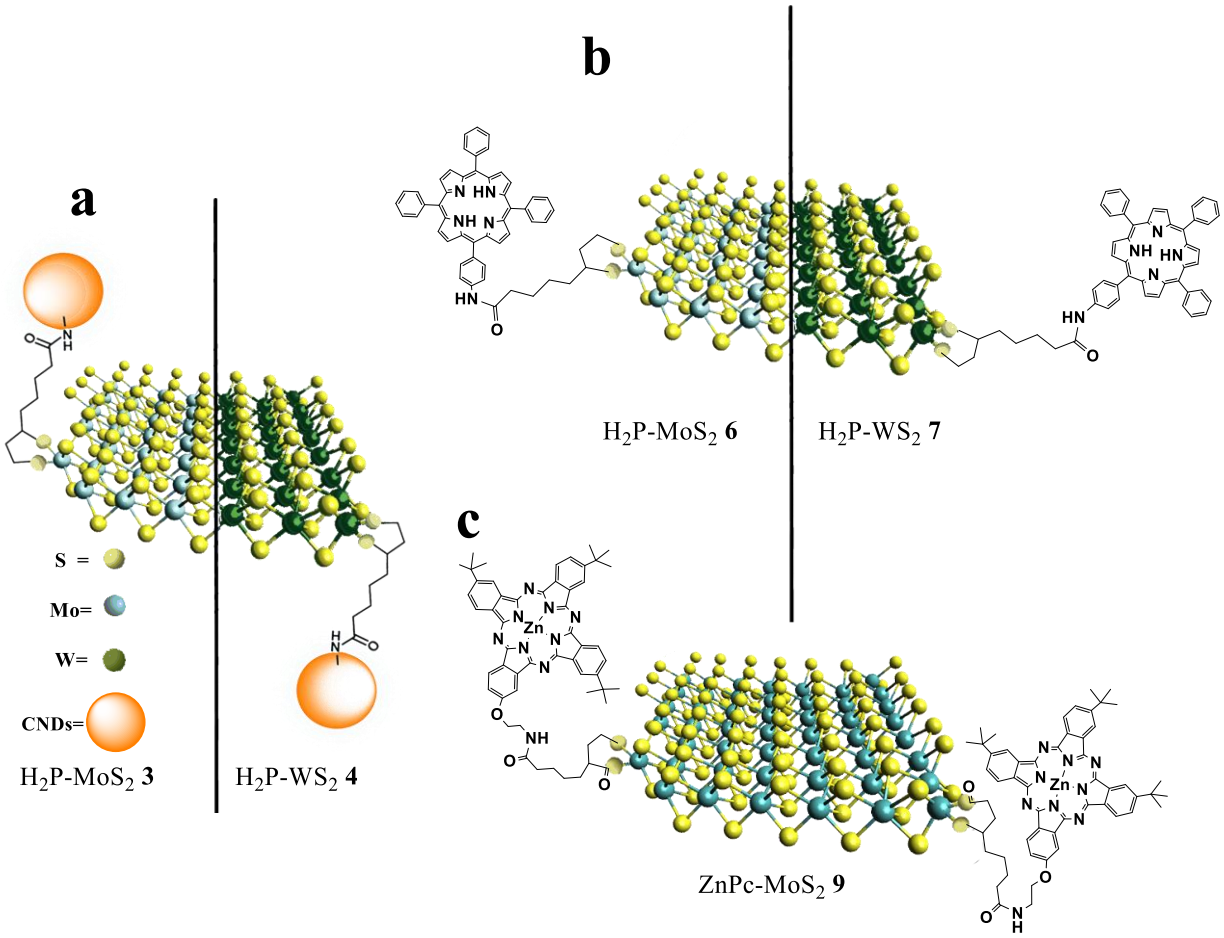

Figure 3. Covalently incorporated (a) pyrene, (b) porphyrin, (c) zinc phthalocyanine, and (d) carbon dots onto TMDs.

In **Chapter 6**, the positive charges due to the presence of ammonium moieties on modified TMDs were exploited to electrostatically associate negatively charged chromophore species of (a) porphyrin, (b) polythiophene, and (c) carbon dots. The latter approach allowed preparing TMD-based ensembles in which the organic dyes were non-covalently associated. In addition, the supramolecular immobilization of pyrene via multiple π-S interactions with exfoliated MoS_2 and WS_2 sheets was accomplished. All ensembles were fully structurally characterized and their morphology was imaged with electron microscopy, proving their successful preparation. Furthermore, the photophysical, electrochemical and electrocatalytic properties of the new materials were evaluated, revealing high prospects for applications in energy-related schemes.

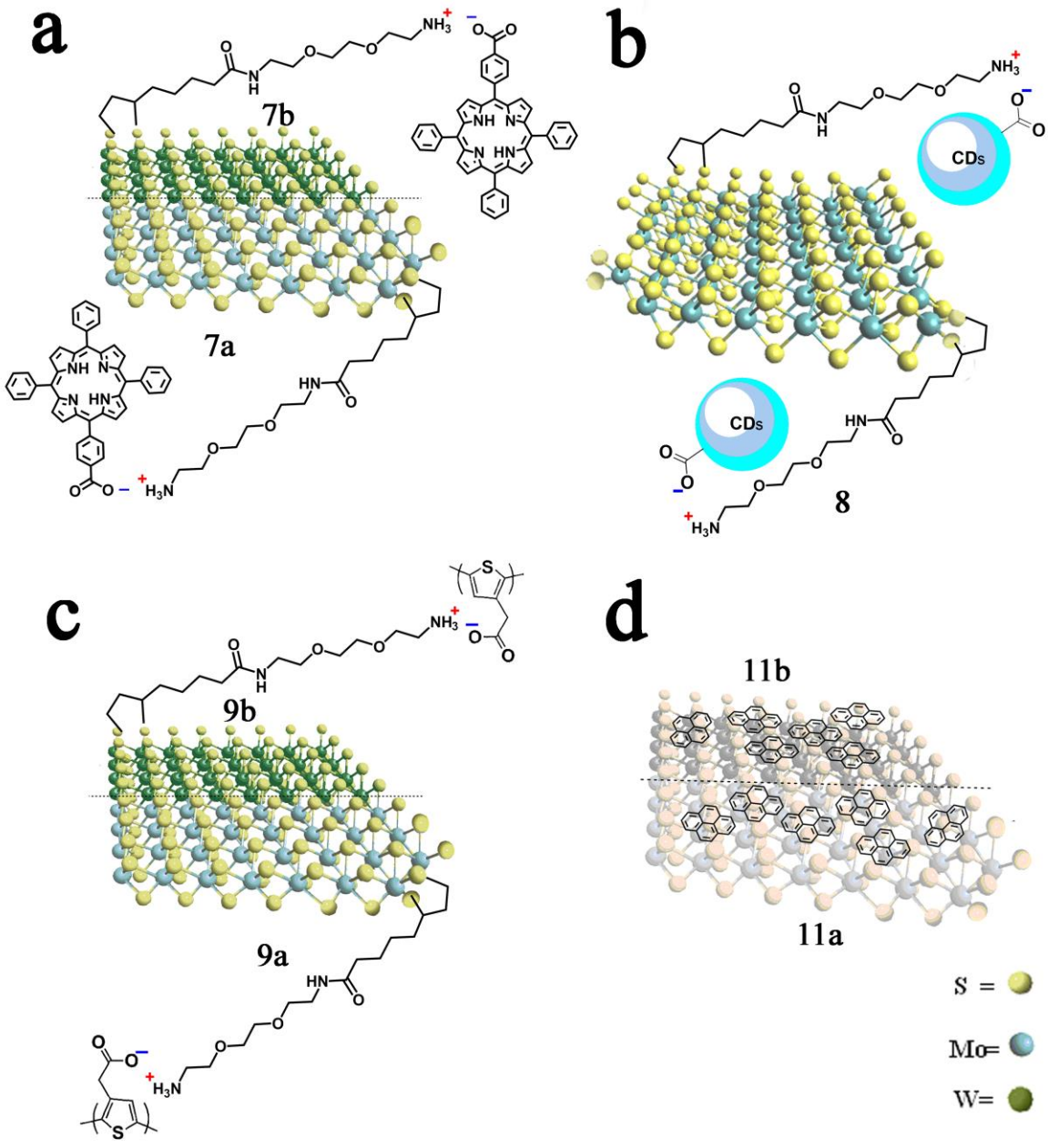

Figure 4. (a) Electrostatically associated (a) porphyrin, (b) polythiophene, and (c) carbon dots, with TMDs and (d) supramolecularly immobilized pyrene on MoS_2 and WS_2.

CHAPTER 3

Functionalization of graphene

ABSTRACT

Exfoliated graphene has attracted increased attention for the development of donor-acceptor materials towards improved energy conversion applications. The development of novel donor-acceptor systems consisting of cyanine or azabodipy dyes and graphene has been accomplished. Cyanines and azabodipy are attractive dyes possessing remarkable optical properties in the NIR region. In fact, the characteristic fluorescence emission of the dyes is quenched once are covalently attached to graphene, revealing photoinduced intra-ensemble energy and/or electron transfer from the dyes to graphene. On the other hand, the presence of charged cyanines and ethyleneglycol chains in the hybrid materials enhances their solubility in various solvents. These findings highlight the importance of graphene covalent functionalization aiming at the creation of novel donor-acceptor graphene hybrids for advanced optoelectronic applications.

3.1 INTRODUCTION

Graphene is a 2D material with a sp^2-hybridized carbons atoms arranged in a honeycomb structure, with a C-C distance of 0.142 nm, being one of the most investigated materials during the last 10 years. Its intrinsic properties such as excellent electrical and thermal conductivity combined with high strength and stiffness render it an excellent material for advanced technological applications.[1] In this context, graphene bears the potential to emerge as an indispensable material in nanotechnology, acquiring special interest for the next generation of ultrafast transistors,[2] or energy conversion[3] in which highly efficient photocurrent[4] have been recorded. Unfortunately, the large and inexpensive production of monolayer and defect free honeycomb of graphene still is a handicap, reducing its practical uses.

Alternatively, sonochemical exfoliation of graphite is regarded as a scalable and relatively cheap approach for the production of mono- and few layers of graphene, preserving the electronic properties. [5] Usually, ultra-sonication of graphene is performed in specific solvents providing enough energy to break the π–π interactions onto the lattice of each layer, expanding and even insolating single layers of graphene.[6]

The exfoliated graphene could be functionalized through covalent and non-covalent interactions. The covalent attachment of organic moieties involves chemical reaction with the C=C of graphene and results in strong bonding of two species, whereas non-covalent functionalization occurs through physisorption, mainly via van der Waals or π-π staking interactions. Then, the strong covalent bond allows the efficient purification of the functionalized graphene by filtration, which is not possible for non-covalently interacting species with graphene. In fact, functionalization with photoactive molecules confers potential applications for solar energy conversion,[7] especially when the photoactive molecule possesses an extended planar π-π system such as in the case of pyrenes,[8] or porphyrins.[9] However, only few examples combine graphene with photoactive molecules possessing absorption in the near-infrared (NIR) region, which constitutes a significant portion of the solar spectrum. In particular, cyanines represent an interesting class of ionic light harvester dyes, showing an intense NIR absorption that spans from 750 to 900 nm.[10] In addition, new fluorophores based in azaborondipyrromethenes (azaBDPs)

acquired importance because they possess near-IR absorption and emission with quantum yield higher than 40%, thus making them attractive materials to participate in electron donor-acceptor systems,[11] bio-imaging or sensing.[12]

On the other hand, one of the main drawbacks of graphene is related with its low solubility, making rather challenging a proper study in liquid media. Lack of solubility is mainly due to attractive forces van der Waals forces as well as π-π staking between layers. However, several ways have been proposed to enhance the solubility of graphene, comprising its covalent functionalization with *tert*-butyl steric groups, positive or negative charged as well as the addition of soluble species (i.e. ethylene-glycol).[13] In fact, hybridization of graphene with cyanines or azaBDP could tailor the photo-electronic properties and increase solubility.

Additionally, azaBDPs derive from the well-studied BDPs, which are photoactive molecules with substantial absorption in the visible region of the electromagnetic spectrum. BDPs have been extensively combined with other potential chromophores such as ferrocene,[14] Rh-porphyrin[15] or pyrenes[16] performing electron-transfer systems for energy harvesting applications. In this context, azaBDP is an ideal candidate for building electron donor–acceptor systems absorbing and emitting in the near-IR region.[17] In fact, azaBDPs bearing an additional photoactive moiety have been examined as parts of hybrids with othe carbon-based nanomaterials such as fullerenes[18] and nanotubes.[19]

Firstly, we functionalized graphene with cyanines **1**, **2**, **3** and **4** yielding hybrid materials **8**, **9**, **10** and **11**, respectively. In addition, we synthesized azaBDP derivatives **14**, **15**, **19** and **20** and employed them in the functionalization of exfoliated graphene yielding hybrid materials **17**, **18**, **21** and **22**, respectively. Markedly, cyanines and azaBDP bear functional groups that enhance solubility of the developed hybrid materials such as the presence of an ethyleneglycol chain, allowing a proper spectroscopic study in liquid media. In addition, azaBDP **19** and **20** bear a second photoactive species of porphyrin in **19** and Zn-porphyrin in **20**, respectively, that enhances electronic interactions. Both dyes, cyanines and azaBDP, were found to have interesting electronic interactions with graphene in the ground and excited states. Additionally, the features of cyanines **1-4** and azaBDP **15, 19-20** and functionalized graphene **8**, **11**, **18**, **21** and **22** were studied by electrochemistry and features of azaBDP, **14, 15, 19** and **20** were detected by

EDX spectroscopy. Moreover, IR showed the presence of cyanines and azaBDPs in the hybrid materials, while SEM and TEM imaging offered detailed information about the morphology of the hybrid materials. Hybrids **8-11**, **18**, **21** and **22** proved to have interesting photophysical and redox properties, which in turn make them attractive materials in energy conversion applications.

3.2 RESULTS AND DISCUSSION

The preparation of graphene-based hybrid materials **8-11** incorporating cyanine dyes **1-4** is shown in Figure 1. Exfoliated graphene, obtained upon treatment with chlorosulfonic acid according to a previously reported procedure,[20] was initially functionalized through a diazotization reaction,[21] employing *N-tert*-butoxycarbonyl (BOC) protected derivatized aniline **5** and isoamyl nitrite to *in-situ* form the aryl diazonium salt able to covalently add to the graphene skeleton. Cleavage of the BOC protecting group by trifluoroacetic acid revealed plethora of amino functionalities onto the graphene sheets that were further condensed by the cyanine dyes **1** and **2** possessing free carboxylic species, yielding hybrids **8** and **9**, respectively. Notably, the first hint for the preparation of **8** and **9** arose by employing the Kaiser test. With the latter we were able to quantify the amount of free amine groups in **8** and **9**, ca. 15 μmol g^{-1}, which was found significantly lowered as compared with the one based in the precursor material **7**, ca. 140 μmol g^{-1}, hence proving the success for the condensation reaction between **7** and cyanines **1** and **2**. Analogously, by employing cyanine dyes **3** and **4**, carrying aniline moieties, in diazotization functionalization reaction with exfoliated graphene, hybrids **10** and **11** were prepared.

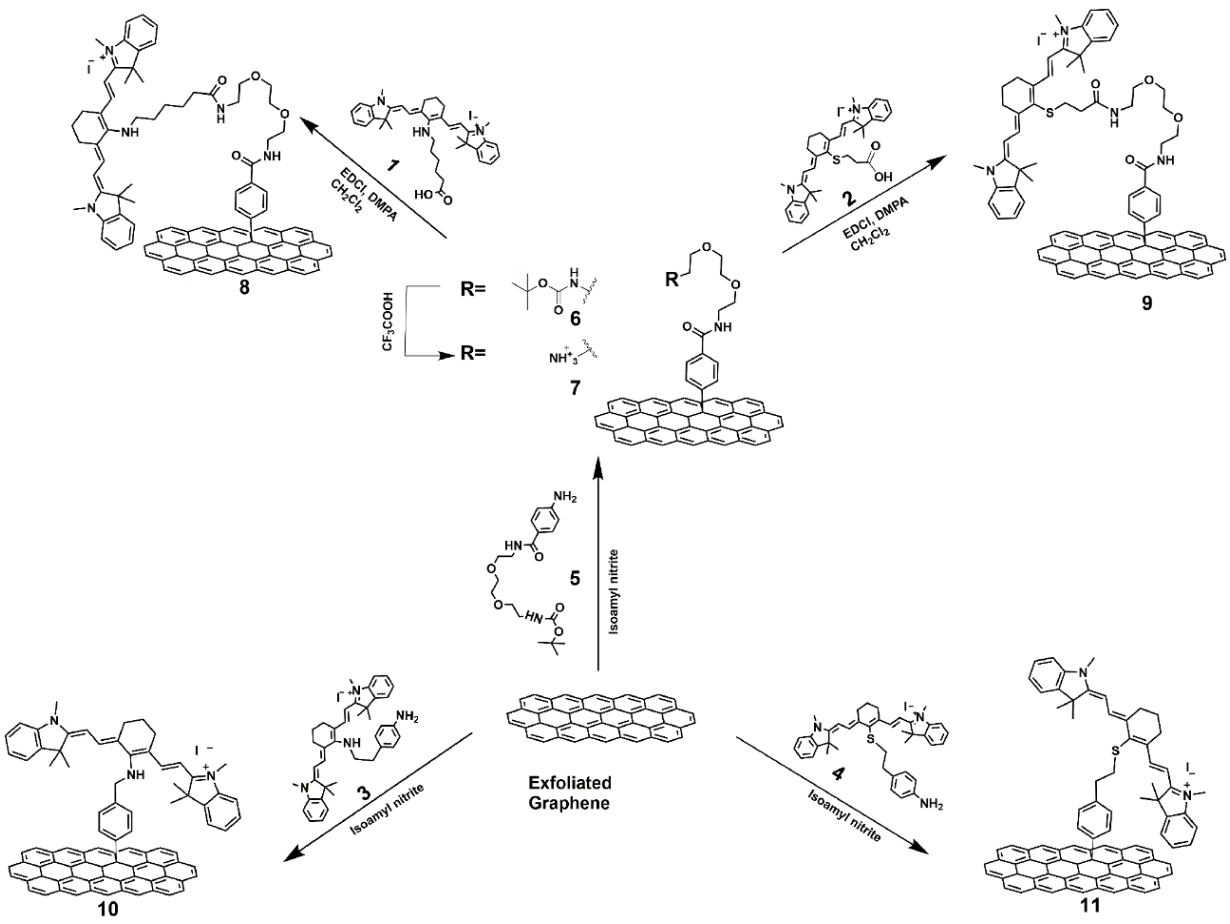

Figure 1. Functionalization of graphene-based hybrid materials **8-11** incorporating cyanine dyes **1-4**.

The characterization of hybrid materials **8-11** was accomplished by complementary spectroscopic, thermal and electron microscopy imaging means. In more detail, Raman spectroscopy was employed to prove the successful covalent modification of exfoliated graphene with the *in-situ* formed aryl diazonium salts, yielding **6**. In the Raman spectrum of **6**, three bands located at 1330, 1580 and 2670 cm^{-1} are discernable as shown in Figure 2. The G-band at 1580 cm^{-1} is attributed to vibrations due to sp^2 hybridized carbon atoms, while the D-band at 1330 cm^{-1} is ascribed to vibrations due to defect sites and sp^3 hybridized carbon atoms. The shape and frequency of the 2D band located at 2670 cm^{-1} is sensitive to the number of graphene sheets.[22] Evidently, an increased D/G ratio is found for **6** as compared with that owed to exfoliated graphene (I_D/I_G = 0.42 for **6**; I_D/I_G = 0.20 for exfoliated graphene). Furthermore, the D/G ratio for materials **8** and **9** was found unaltered (I_D/I_G = 0.42) as compared to that of **6**, in accordance with

the fact that the cleavage of the BOC unit followed by condensation with cyanine dyes **1** and **2**, respectively, do not further disrupt the skeleton of graphene, hence verifying the accomplishment of their preparation. In addition, the G-band for hybrids **8** and **9** was marginally shifted by ca. 3 cm^{-1}, as compared to the value registered for exfoliated graphene, implying the development of charge-transfer phenomena between the NIR dyes and the graphene sheets. As far as the Raman spectra for hybrids **10** and **11** concern, the D-band in both hybrids was enhanced as compared to that derived from exfoliated graphene (Figure 2), proving the successful covalent introduction of the cyanines dyes **3** and **4**, respectively, onto the graphene sheets.

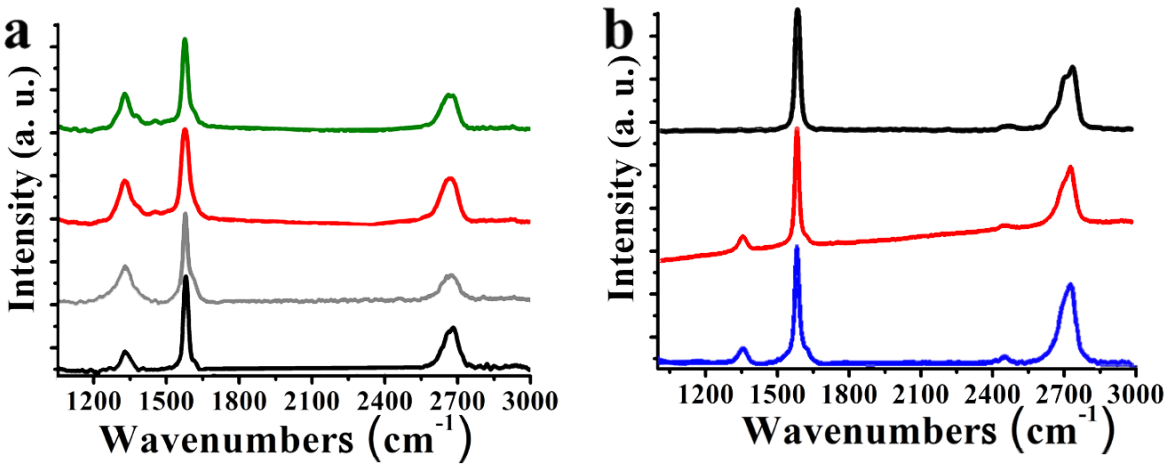

Figure 2. (a) Raman spectra for exfoliated graphene (black) and graphene-based materials **6** (grey), **8** (green), and **9** (red), normalized at the G-band and obtained upon 633 nm excitation. (b) Raman spectra for exfoliated graphene (black) and graphene-based materials **10** (red) **11** (blue), normalized at the G-band and obtained upon 514 nm excitation.

Next, attenuated-total-reflectance infrared (ATR-IR) studies further confirmed the effective coupling of aniline derivative **5** onto exfoliated graphene. In graphene-based material **6**, characteristic strong carbonyl vibrations at 1698 and 1630 cm^{-1} attributed to the presence of benzamide and BOC units, respectively, were evident. Markedly, in **7** the latter was disappeared, reflecting the effective cleavage of BOC that gives rise to the presence of free $–NH_2$ groups. In graphene-based hybrid material **8**, the carbonyl amide vibration was found enhanced as a result of the formation of new amide band at 1640 cm^{-1}, while also the vibration owed to the carboxylic acid moiety in the cyanine dye **1** at 1720 cm^{-1} was accordingly disappeared (Figure 3a). Similar

is the situation with the ATR-IR spectrum for hybrid **9** (Figure 3b). In the ATR-IR spectra of **10** and **11** only the C-H stretching vibration modes were discernable at 2800-2900 cm^{-1} (spectra not shown).

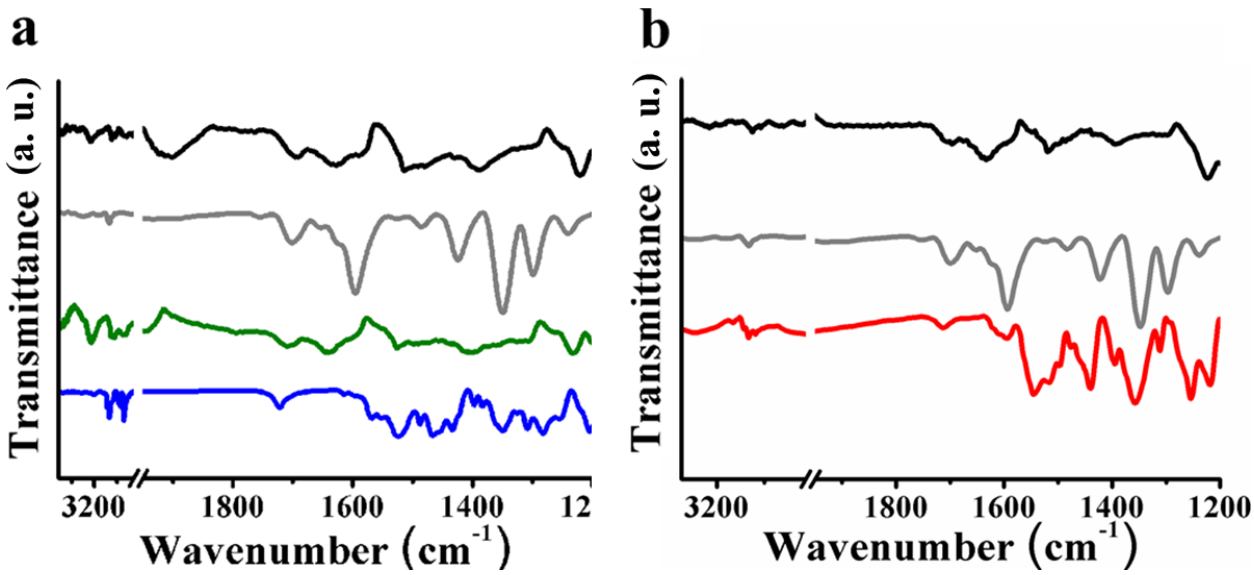

Figure 3. ATR-IR spectra for (a) graphene-based materials **6** (black), **7** (gray), and **8** (green) and cyanine dye **1** (blue) and (b) free cyanine dye **2** (red) as compared with functionalized graphene-based material **7** (grey) and hybrid **9** (black).

The functionalization degree for **8** and **9** was evaluated by thermogravimetric analysis (TGA). Exfoliated graphene is thermally stable under inert nitrogen atmosphere. For modified graphene-based material **7**, a mass loss of 12% was observed in the temperature range 200-560 °C, while for hybrids **8** and **9** the corresponding weight loss was 22 % and 17 %, respectively (Figure 4a). On this basis, the loading of cyanine dyes **1** and **2** onto graphene was calculated as 1 per every 270 and 360 carbon atoms for **8** and **9**, respectively. Analogously, from the thermal decomposition of **10** and **11** the mass loss observed, 2 and 8% respectively, (Figure 4b) the loading of **3** and **4** was calculated to be 1 unit per every 1560 and 900 carbon atoms for **10** and **11**, respectively. Although this represents a rather small amount of dyes incorporated onto the graphene sheets, it is consistent with the small perturbation of graphene lattice in **10** and **11** upon the covalent incorporation of **3** and **4**, as revealed with the small enhancement of the D-band in the corresponding Raman spectra (Figure 2b).

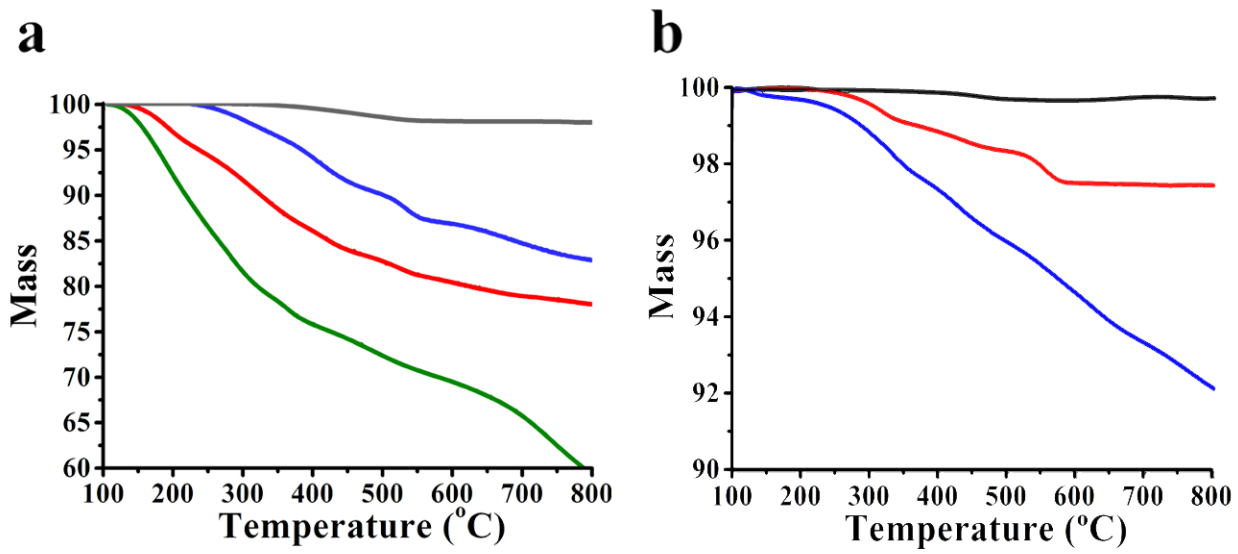

Figure 4. Thermographs for (a) exfoliated graphene (grey), graphene-based material **7** (blue), hybrids **8** (green) and **9** (red) and (b) exfoliated graphene (grey), hybrids **8** (green) and **9** (red) obtained under nitrogen atmosphere.

The morphology of graphene-based hybrid materials **8-11** was examined by FE-SEM imaging. Briefly, after dispersing the material by mild sonication in hexane, a drop was deposited onto the sample holder and examined. A representative image for **8** is shown in Figure 5a. It reveals the presence of overlapping oligolayered graphene sheets, of various sizes, with typical folding and ripple patterns. Although the exact number of layers cannot be accurately estimated, the absence of large graphitic particles is obvious, as it is also proved by Raman spectroscopy (cf. Figure 2). Similar were the morphological findings for hybrids **9**, **10** and **11** (Figure 5b-d).

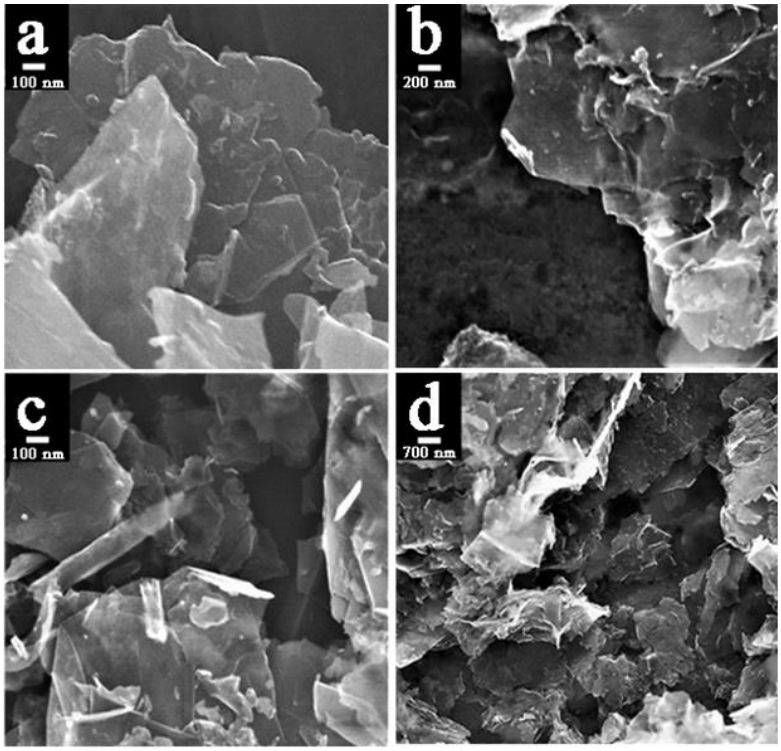

Figure 5. Representative FE-SEM image for graphene-based hybrids **8**, **9**, **10** and **11**.

The dispensability of hybrids **8-11** was enhanced in polar solvents such as *N*,*N*-dimethylformamide (DMF), allowing to perform spectroscopic studies in solution. Hence, examining possible ground-state interactions between cyanine dyes **1** and **2** with graphene within hybrid materials **8** and **9**, respectively, UV-Vis-NIR studies were performed. The electronic absorption spectrum for **8** obtained in DMF, showed the characteristic continuous absorption in the NIR region owed to graphene, followed by a broadened band centered at 660 nm (Figure 6a), corresponding to free cyanine dye **1** possibly possessing different conformational structures on graphene. This finding not only guarantees the successful integration of **1** onto graphene, by covalently forming hybrid **8**, but also indicates appreciable electronic interactions between the two species at the ground state. In case of hybrid **9**, the UV-Vis-NIR spectrum is a simple superposition of the absorption spectra owed to graphene and cyanine dye **2** (Figure 6b), suggesting the absence of appreciable interactions in the ground state. The low loading of **3** and **4** within hybrids **10** and **11** (Figure 6c and d) respectively, handicapped the electronic absorption measurements. In the latter, the characteristic absorption bands due to **3** and **4**, centered at 657 and 787 nm, respectively, were masked under the continuous and strong absorbance of graphene.

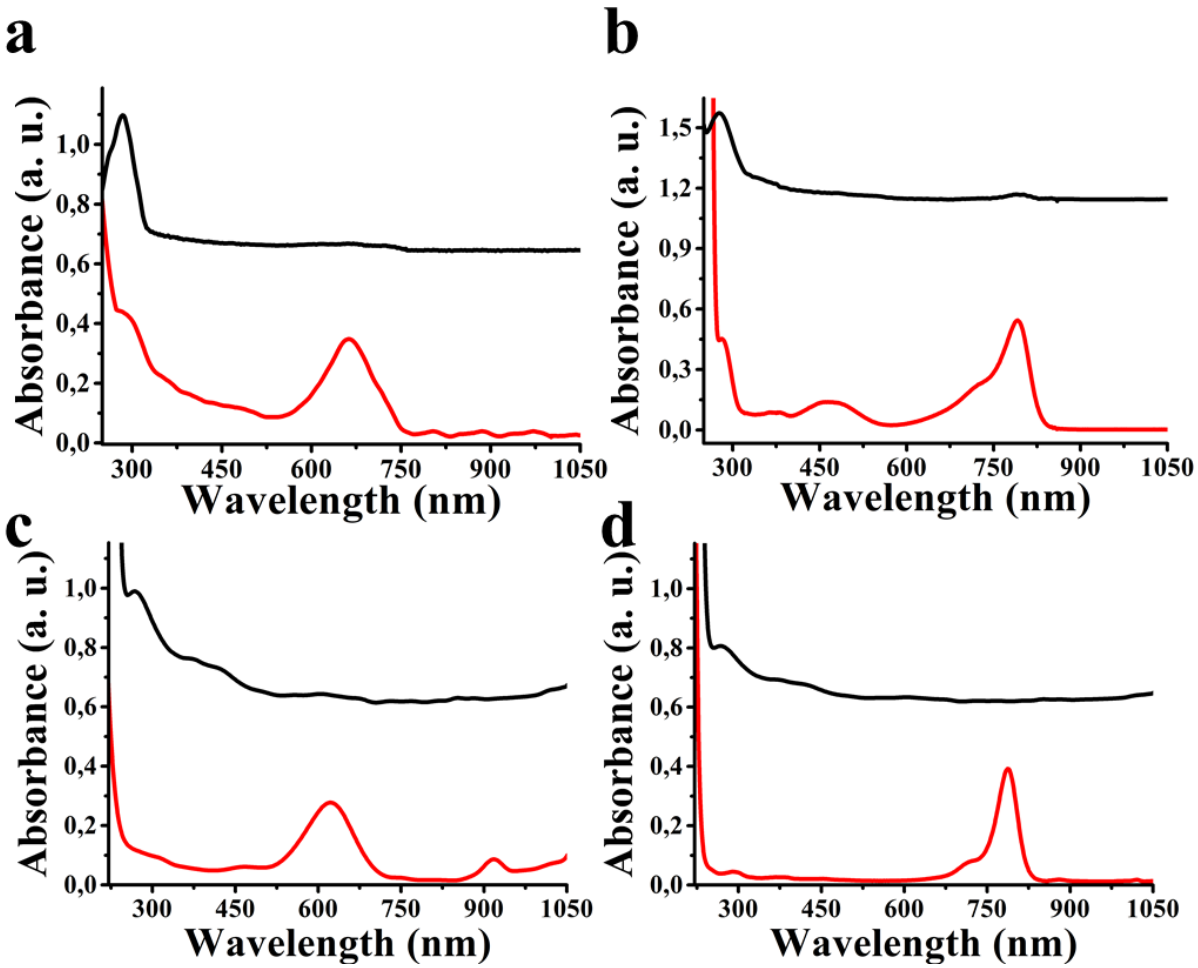

Figure 6. Absorption spectra of (a) free cyanine dye **1** (red) and graphene-based hybrid material **8** (black), (b) free cyanine dye **2** (red) and graphene-based hybrid material **9**, (c) free cyanine dye **3** (red) and graphene-based hybrid material **10** (black) and (d) free cyanine dye **4** (red) and graphene-based hybrid material **11** (black), obtained in DMF.

Next, focusing on excited state interactions, photoluminescence assays for hybrids **8** and **9** in comparison with the corresponding free cyanine dyes **1** and **2**, for samples displaying equal absorbance at the excitation wavelength, were performed. Upon 660 nm excitation, **1** revealed a broad emission band centred at 757 nm (Figure 7a). Markedly, in hybrid **8**, the latter emission was found significantly depressed, indicating strong electronic interactions between graphene and **1**, within **8** at the excited state, following electron and/or energy transfer as the decay mechanism of the singlet excited state of $^{1}\mathbf{1}^{*}$. Then, on the basis of the time-correlated-single-photon-counting method, the photoluminescence lifetime profiles for **1** were acquired. Analysis

of the time-profile of the decay at 757 nm upon excitation at 654 nm for the $^{1}\mathbf{1}^{*}$ was monoexponentially fitted with a lifetime of 0.84 ns. On the other hand, the decay component in hybrid **8** was found to be 500 ps. Analogously, the photoluminescence of hybrid **9**, at 810 nm was found quenched as compared to the one attributed to the free cyanine dye **2** (Figure 7b), while the corresponding lifetimes for **2** and **9** were evaluated as 0.81 ns and 250 ps, respectively. The photoluminescence spectra for hybrids **10** and **11**, as compared with those of the corresponding free cyanine dyes **3** and **4** are presented in Figure 7c and d. In addition, the emission time profiles for graphene-based hybrids **10** and **11** were characterized by quicker decays, as compared with those registered for the free cyanine dyes **3** and **4**, respectively, and in analogy with those belonging to hybrids **8** and **9**. Collectively, those findings are related with intrahybrid transduction of electron and/or energy from the electron donors **1-4** to graphene in hybrids **8-11**, respectively. The emission rate constants (k^{S}) and quantum yields (Φ^{S}) for free cyanine dyes **1-4** and graphene-based hybrid materials **8-11** were calculated based on equations (1) and (2), respectively, and presented in Table 1.

Equation 1: $k^{S} = (1/\tau_{f})_{\mathbf{hybrid}} - (1/\tau_{f})_{\mathbf{dye}}$,

where τ_{f} is the fluorescence lifetime of each specie.

Equation 2: $\Phi^{S} = k^{S}/(1/\tau_{f})_{\mathbf{hybrid}}$

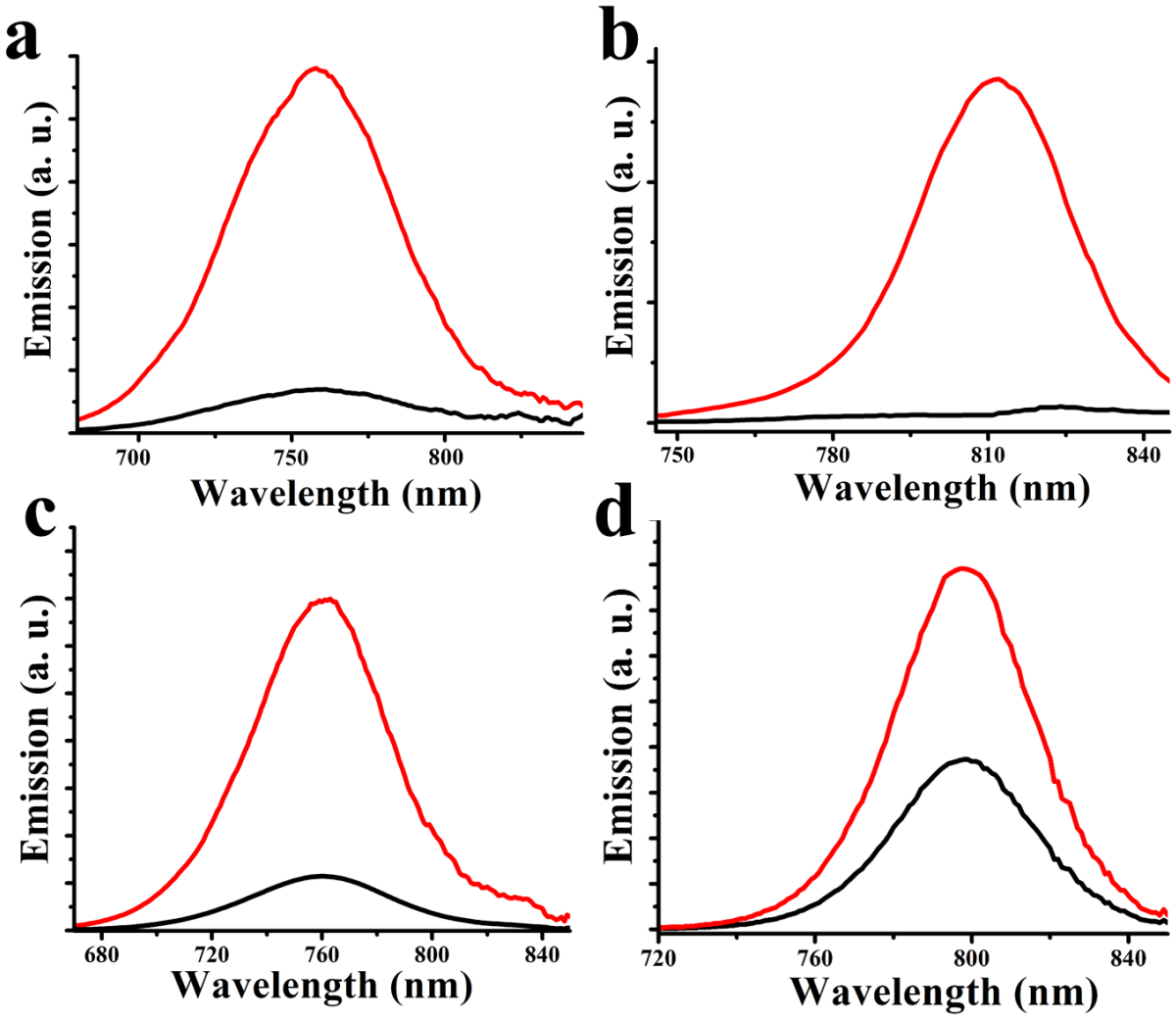

Figure 7. Photoluminescence spectra (excitation at 660 nm) for (a) free cyanine dye **1** (red) as compared with hybrid **8** (black), (b) free cyanine dye **2** (red) as compared with hybrid **9**, (c) free cyanine dye **3** (red) and graphene-based hybrid material **10** (black) and (d) free cyanine dye **4** (red) and graphene-based hybrid material **11** (black), obtained in DMF.

Next, shedding light on the redox properties of the hybrid materials, cyclic voltammetry (CV) measurements performed on acetonitrile employing Bu_4NPF_6 as electrolyte in a standard three-electrode cell with glassy carbon as working electrode and platinum wires as counter and pseudoreference electrodes were conducted. Hybrid materials **8** and **9** exhibit a reversible oxidation at 0.80 and 0.11 V versus Fc/Fc^+, cathodically shifted by approximately 10 and 4 mV, respectively, as compared with the oxidation processes registered for the corresponding free

cyanine dyes **1** and **2**. These shifts are attributed to intra-hybrid electronic interactions between the dyes and graphene sheets, rendering easier the oxidation of the latter within the graphene-based hybrid materials. Furthermore, a peak at -0.45 V associated with the reduction of graphene similarly with other reports,[23] as well as additional reversible reduction processes centered at -1.24 and -1.06 V, were identified in hybrids **8** and **9**. Disappointingly, due to the limited solubility of **10** and **11** we were not able to register suitable and reliable redox data. Collectively, the redox data are presented in Table 1.

Table 1. Summary of photophysical and electrochemical data for cyanine dyes **1-4** and graphene-based hybrids **8-11**.

Material	τ_f **(ps)**	k^S **(s^{-1})**	Φ^S	$E_{Ox.}$ **(V)**	$E_{Red.}^1$ **(V)**	$E_{Red.}^2$ **(V)**
Free cyanine dye **1**	840			0.90		-1.19
Hybrid **8**	500	8.10×10^8	0.40	0.80	-0.45	-1.24
Free cyanine dye **2**	810			0.15		-1.16
Hybrid **9**	250	2.77×10^9	0.69	0.11	-0.45	-1.06
Free cyanine dye **3**	1183			0.35		-1.34
Hybrid **10**	475	1.26×10^9	0.48			
Free cyanine dye **4**	1074			0.20		-1.35
Hybrid **11**	366	1.81×10^9	0.67			

The preparation of 4,4-difluoro-4-boron-3a,4a,8-triazo-s-indacene (azaborondipyrromethene – azaBDP) derivative was accomplished as follows. In the beginning 2-(2-methoxyethoxy)ethan-1-ol **A** reacts with tosyl chloride in dry dicloromethane (DCM) yielding ethylene-glycol derivative **B**. After purification, **B** reacts with 4-hydroxybenzaldehyde forming 2,4-diarylpyrrole derivative **C** and then this compound reacts with nitromethane yielding 5-nitroso derivative **D**. Compound **D** reacts with ammonium salts under microwave treatment conditions to give symmetric azadipyrromethene derivative **12**. AzaBDP **13** was obtained through boron complexation of **12** employing boron trifluoride diethyl etherate in presence of *N*,*N*-diisopropylethylamine (DIPEA). The synthesis of compounds **B**, **C**, **D**, **12** and **13** is shown in Figure 8a. The preparation of highly soluble azaBDP dyes bearing lauric acid (azaBDP **15)** and tetra-porphyrin (azaBDP **19**) was performed through coupling reactions as is showed in Figure 8b and c. Briefly, the acid group of

lauric acid, porphyrin or azidoazetic are activated by N-(3-dimethylaminopropyl)-N′-ethylcarbodiimide hydrochloride (EDCI) and 4-dimethylaminopyridine (DMAP) through coupling reaction with the aromatic alcohol moieties of azaBDP derivatives **12**, **13** or **14**. The structural characterization is presented in detail in the experimental section. Covalent functionalization with graphene yielding graphene-based hybrid materials **17**, **18**, **21** and **22** is shown in Figure 8b and c. Briefly, exfoliated graphene was initially functionalized through diazotization reaction, employing 4-((trimethylsilyl) ethynyl) aniline and isoamyl nitrite to *in-situ* form the aryl diazonium yielding **16**. Click chemistry between azide groups in **15** and **19** and alkyne group in **16**, yielded hybrids **17** and **21**, respectively. It is worth noting that copper was avoided due to the affinity of complexation of the azaBDP. A recent methodology was performed in which a base such as diisopropylamine (DIPA) abstract the acidic proton of arylynyl forming a reactive carbanion with affinity for azide group.[24] Further chemical reactions between hybrid **17** with boron trifluoride diethyl etherate in presence of DIPEA ensured the formation of material **18**. Finally, metal coordination between porphyrin in **21** with $Zn(OAc)_2$ in a mixture of 8/2 DCM/MeOH yielded graphene-based hybrid material **22**.

a

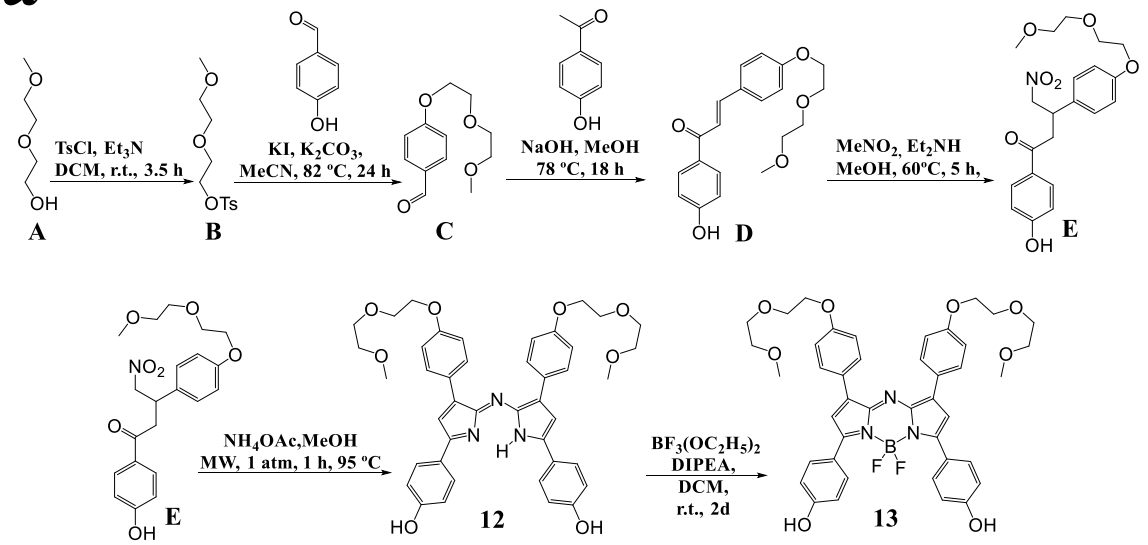

b

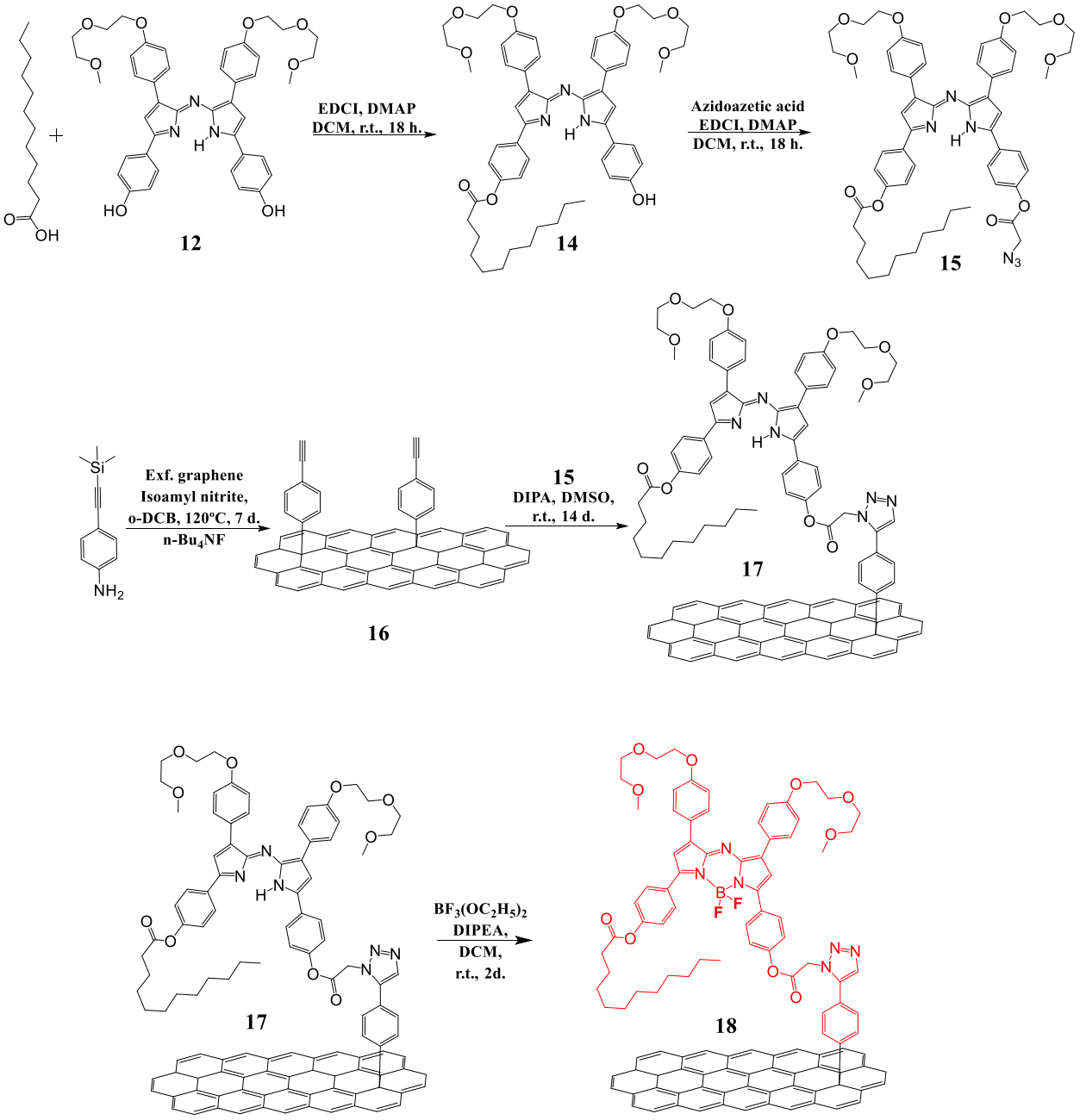
EDCI, DMAP
DCM, r.t., 18 h.
12
14
Azidoazetic acid
EDCI, DMAP
DCM, r.t., 18 h.
15
Exf. graphene
Isoamyl nitrite,
o-DCB, 120ºC, 7 d,
n-Bu4NF
16
15
DIPA, DMSO,
r.t., 14 d.
17
BF3(OC2H5)2
DIPEA,
DCM,
r.t., 2d.
17
18

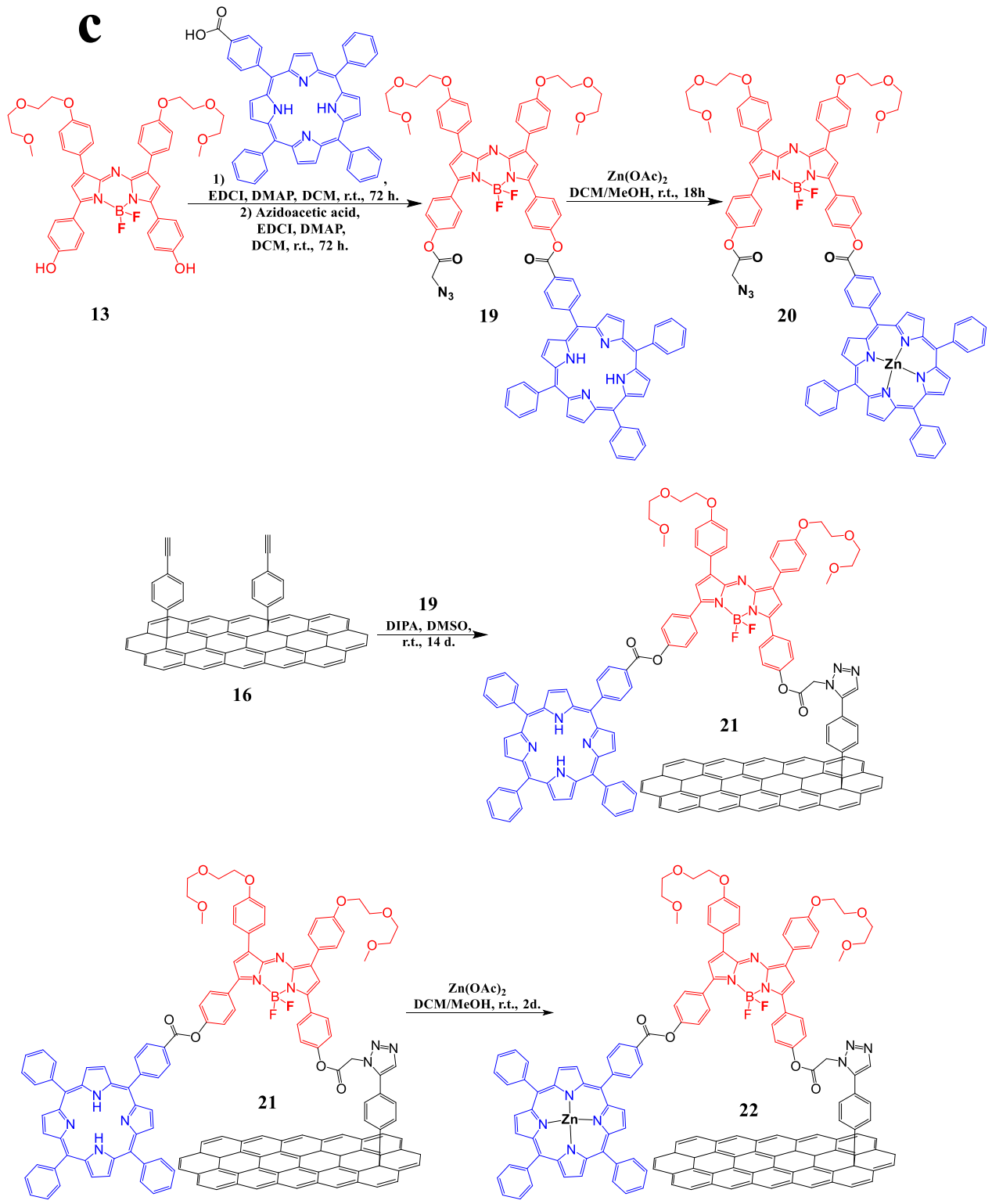

Figure 8. Synthesis of (a) azaBDP derivative **13**, (b) hybrid **17** and **18** and (c) hybrid **21** and **22**.

The characterization of hybrid materials **16-18**, **21** and **22** was accomplished by complementary spectroscopic, thermal and microscopy means. In detail, Raman spectroscopy was employed to prove the successful covalent modification **16** in which G, D and 2D bands, located at 1330, 1580 and 2659 cm^{-1} are discernable as shown in Figure 9. In hybrid **16,** the 2D band was red shifted by 15 cm^{-1} as compared with that of exfoliated graphene, meaning that functionalization reduces the number of layers. In addition, an increased D/G ratio is found for **16** as compared with that owed to exfoliated graphene (I_D/I_G = 0.40 for **16**; I_D/I_G = 0.08 for exfoliated graphene) associated with the success of covalent functionalization, by generating of sp^3 carbon atoms. Furthermore, the D/G ratio for materials **17** and **21** was found practically unaltered (I_D/I_G = 0.42 and 0.41, respectively) as compared to that of **16**, in accordance with the fact that click reaction with azaBDP dyes **15** and **19**, respectively, do not further disrupt the skeleton of graphene. Further, the D and 2D-band was blue-shifted by 18 and 38 cm^{-1} for hybrids **17** and by 3 and 5 cm^{-1} in **21**, respectively, probably due to electronic interactions at the ground states between the dyes and graphene. In fact, focusing in the 850-1600 cm^{-1} region of **15** and **19** Raman spectra show a series of signals principally associated with the C=C, C=N bonds of the macrocyclic structure. As far as the Raman spectra for hybrids **21** and **22** concern, the D-band intensity in both hybrids remain unaltered as compared to the precursors **17** and **21** respectively. On the other hand, the position of D, G and 2G bands was blue shifted by 4, 8 and 5 cm^{-1} in **18** with respect to **17**, but remained unaltered in **22** with respect to **21** as the graphene lattice remained unaltered. Finally, the Raman signals of the dye in **18** and **22** have a predominant blue shift, in some being as large as 14 cm^{-1} as compared with that of the free dye. The strong shift of some of the signals can be due to the covalent functionalization ensuring a close contact between graphene and azaBDP and moreover higher electronic communication.

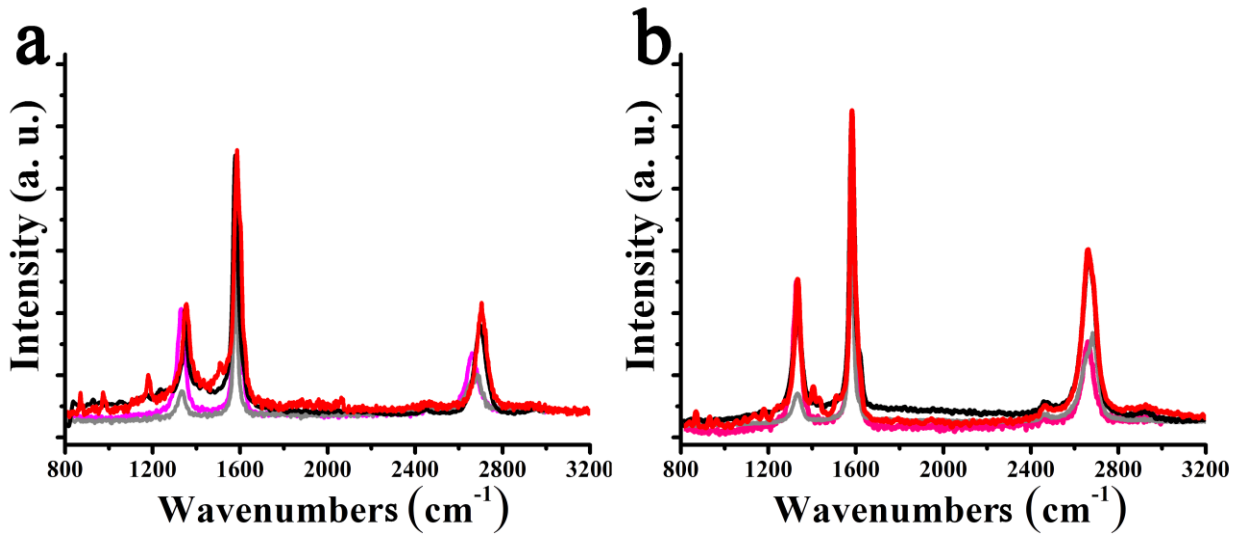

Figure 9. Raman spectra for (a) exfoliated graphene (gray) and graphene-based materials 1**6** (pink), **17** (black), and **18** (red) and (b) exfoliated graphene (gray) and graphene-based materials 1**6** (pink), **21** (black), and **22** (red) normalized at the G-band and obtained upon 633 nm excitation.

Next, ATR-IR studies further confirmed the effective "click" chemistry in **17** and **21** based in a loss of azide signal at 2111 and 2108 cm^{-1} from the azaBDP **15** and **19**. This not only confirms the covalent functionalization, but also strongly indicates the absence of any non-covalently interacting free azaBDP. In addition, characteristic strong carbonyl vibrations at 1753 and 1736 cm^{-1} in **15** and 1755 and 1731 cm^{-1} in **19**, and signals of C-H signatures at 3000-2770 cm^{-1}, aromatic features at 1700-1500 and ether signals at 1241, 1163 and 1139 cm^{-1} from in **15** and **19** also are present in **17** and **21** (Figure 10). Inclusion of boron in **17** yielding **18** was visible in IR through red-shift of the carbonyls at 1729 and 1712 cm^{-1}. Additionally, ATR-IR spectra of azaBDP **20** show distinguishable carbonyls at 1735 and 1728 cm^{-1} which are shifted in the hybrid **22**, appearing at 1720 and 1713 cm^{-1}, respectively.

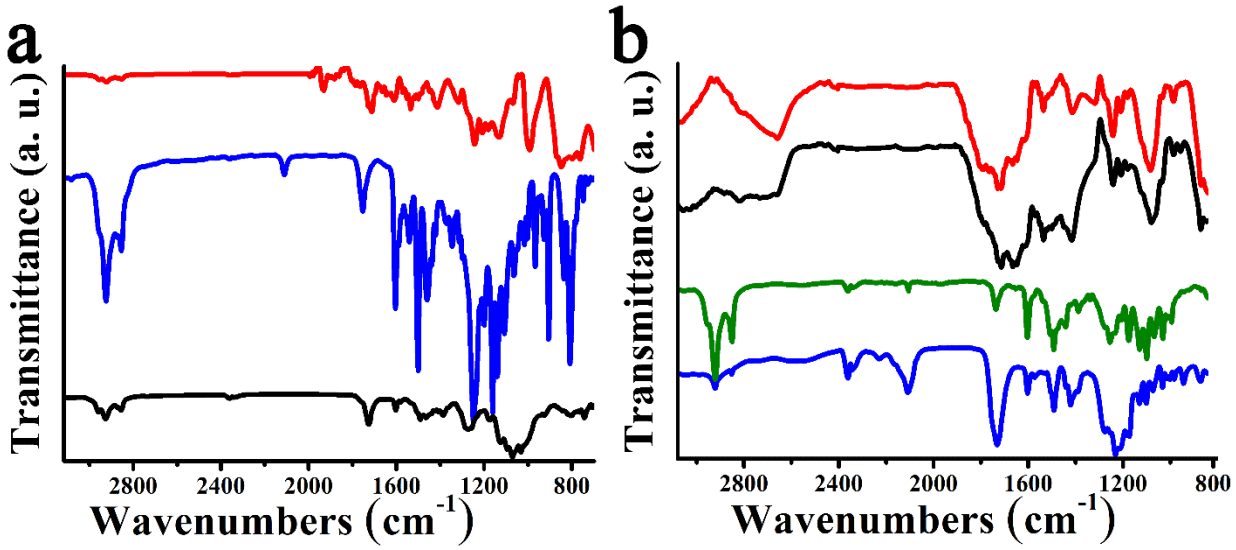

Figure 10. ATR-IR spectra for (a) azaBDP **15** (blue), and graphene-based materials **17** (black), and 1**8** (red) and (b) free azaBDP **19** (blue) and **20** (olive) and graphene-based materials **21** (black), and **22** (red).

The degree of functionalization for hybrids **16**, **17**, **18**, **21** and **22** was evaluated by TGA. For modified graphene-based material **16**, a mass loss of 5.0% was observed in the temperature range 200-600 °C, suggesting the presence of one functional group per every 230 C while for hybrids **17** and **21** the corresponding mass loss was 10.7 and 10.0 % (Figure 11) suggesting a load of azaBDP dyes **15** and **19** onto graphene of 1 per every 330 and 381 carbon atoms, respectively. Analogously, from the thermal decomposition of **18** and **22** the mass loss observed was 16.5% and 12.9%, which corresponds to 1 azaBDP unit per every 427 and 380 carbon atoms, respectively.

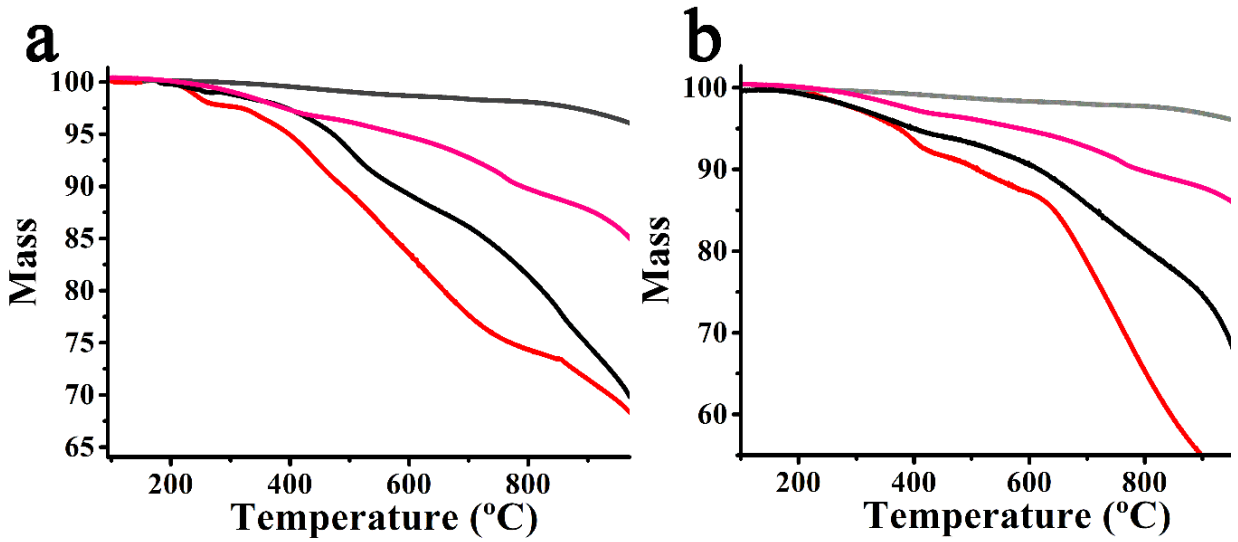

Figure 11. Thermographs for (a) exfoliated graphene (grey), graphene-based material **16** (pink), **17** (black) and **18** (red) and (b) exfoliated graphene (grey), graphene-based material **16** (pink), **21** (black) and **22** (red) obtained under nitrogen atmosphere.

The morphology of exfoliated graphene and hybrids **16**, **17**, **18**, **21** and **22** was examined by high-resolution transmission electron microscopy HR-TEM and supported by EDX imaging. Exfoliated graphene is a low defective material. The functionalization of graphene with the aryl diazonium salt resulted in more defects in the graphene network, being in in harmony with the information obtained in Raman. A representative image for **18** shows similar features without including additional damage on the basal plane (Figure 12a). In addition, EDX shows O and N as well as F and B signals in **18** revealing the addition of the dye azaBDP **15** and its BF_2 inclusion, in line with ATR-IR and TGA (Figure 12d). On the other hand, high magnification TEM images of materials **21** and **22** revealed an enhanced roughness, probably due to the addition of the azaBDP **19**, which is bulky moiety (Figure 12b and 12 c). In addition, the presence of **19** contributes to additional exfoliation, showing oligolayered material with size of several hundred nanometers. EDX data not only support the incorporation of azaBDP dyes **19** in **21** but also the metalation of the porphyrin in **22** due to the presence of the Zn signal (Figure 12e and f).

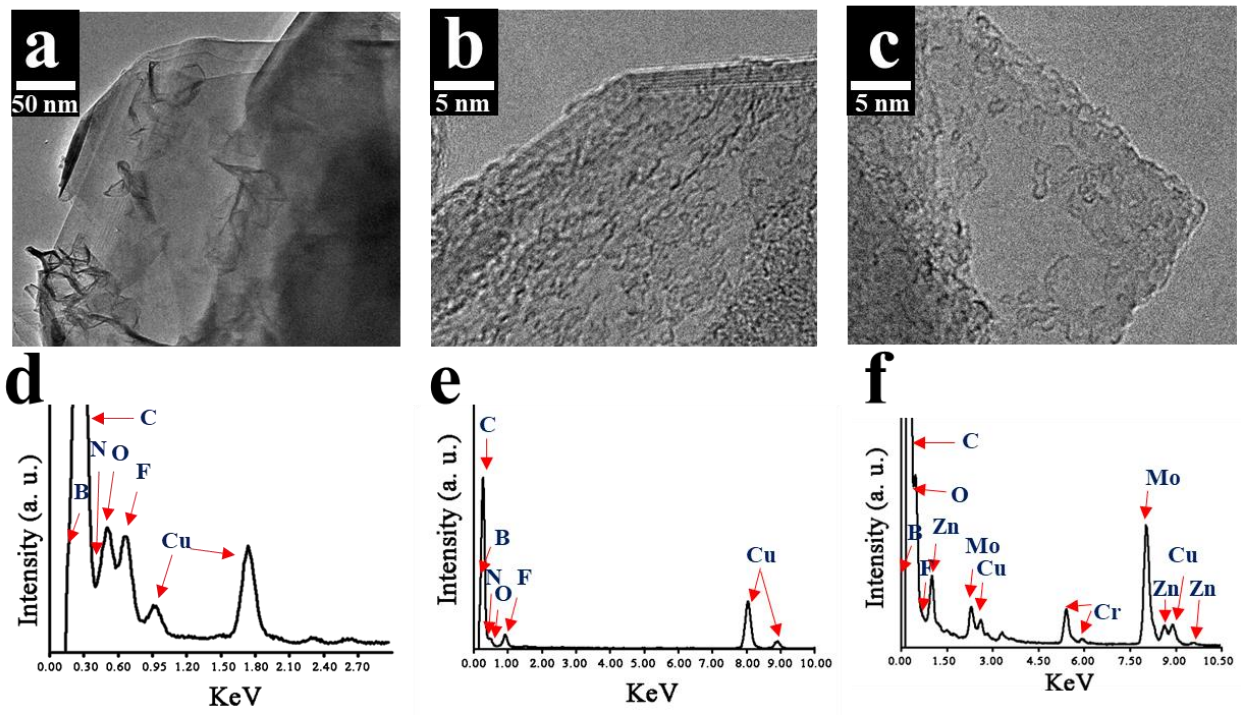

Figure 12. Representative TEM image for (a) **18** and (b) **21** and (c) **22** and EDX of graphene-based hybrid (d) **18**, (e) **21** and (f) **22** in which the presence of Cu, Mo and Cr is due to the substrate.

Material **16** has unstable dispersions in the majority of the solvents while it is marginally soluble in 1,2-dichlorobenzene (o-DCB). On the other hand, azaBDP **15** has two chains of ethyleneglycol and one alkyl chain responsible for the enhanced solubility observed. In fact, materials **17** and **18** show similar behavior producing stable dispersion in any of the solvents, for 1 hour. After 24 h, the materials have a solubility of 0.6, 0.2, 0.2 and 0.1 mg/ml in solvents like o-DCB, DCM, DMF and acetone. As far as the solubility for hybrids **21** and **22** concerns, azaBDP **19** and **20** bear two chains of ethyleneglycol, hence they exhibit good dispensability after 24 h in solvents as o-DCB, DMF, MeOH and acetone with solubility of 0.8, 0.9 0.2 and 0.2 mg/ml, respectively (Figure 13). The latter result is a clear advantage compared to the non-modified graphene, allowing us to perform photophysical studies in various solvents.

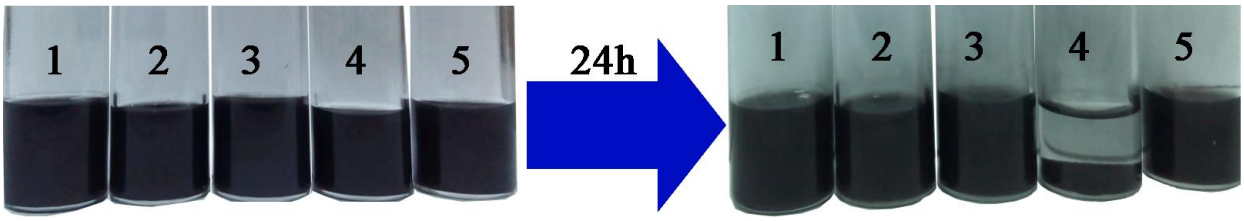

Figure 13. Representative solubility of **22** after (left) 1hour and (right) 24 hours in (1) o-DCB, (2) DMF, (3) MeOH, (4) H_2O and (5) acetone.

Next, UV-Vis-NIR studies were performed in order to shed light to the possible ground state interactions between azaBDP dyes **13**, **19** and **20** with graphene, within hybrid materials **18**, **21** and **22** respectively. AzaBDP **15** have two prominent bands at 313 nm (Soret) and 611 nm (Q band). The electronic absorption spectrum for **17** obtained in DCM is dominated by the characteristic continuous absorption in the NIR region of graphene, followed by a broadened band centered at 640 nm (Figure 14a) being red shifted by 29 nm compared with the free azaBDP **15**. This finding ensures the successful integration of **15** onto graphene, and also indicates appreciable electronic interactions between the two species at the ground state. In case of hybrid **18**, the UV-Vis-NIR spectrum shows higher azaBDP intensities at 696 and 748 nm corresponding to the inclusion of boron in **17**. Azide group of **15** is sensitive to the presence of boron, forcing us to use **13** as a representative azaBDP reference material. Markedly, azaBDP **13** and dye within hybrid **18** share the same sp^2 skeleton. Moreover, **18** possesses a different morphology as well as a strong red-shift by 21 nm compared with the free dye **13,** attributed to the strong electronic interactions between the two species at the ground state. The porphyrin bearing in azaBDP induces changes to the UV-Vis-NIR spectra of **19**, adding a sharp Soret band at 418 nm, small Q bands at 515, 550, and 590 nm and moving the azaBDP Q band at 673 nm. In fact, the shift of both, azaBDP and porphyrin suggest strong interactions between both species in the ground states. Hybrid **21** not only exhibits the Soret band of the porphyrin at 414 nm but also shows a blue shift of the Q bands at 515, 534 and 576 nm and a red shift of azaBDP at 685 nm, indicating more electronic interactions of dye **19** within hybrid **21**. Hybrid **22** possesses a Soret band at 423 nm and Q bands at 564 and 690 nm corresponding to the bands at 420, 549 and 673 nm of azaBDP **20**. Such appreciable shift suggests that porphyrin metalation changes the electronic interaction of **22** at ground states of dye **20** with graphene.

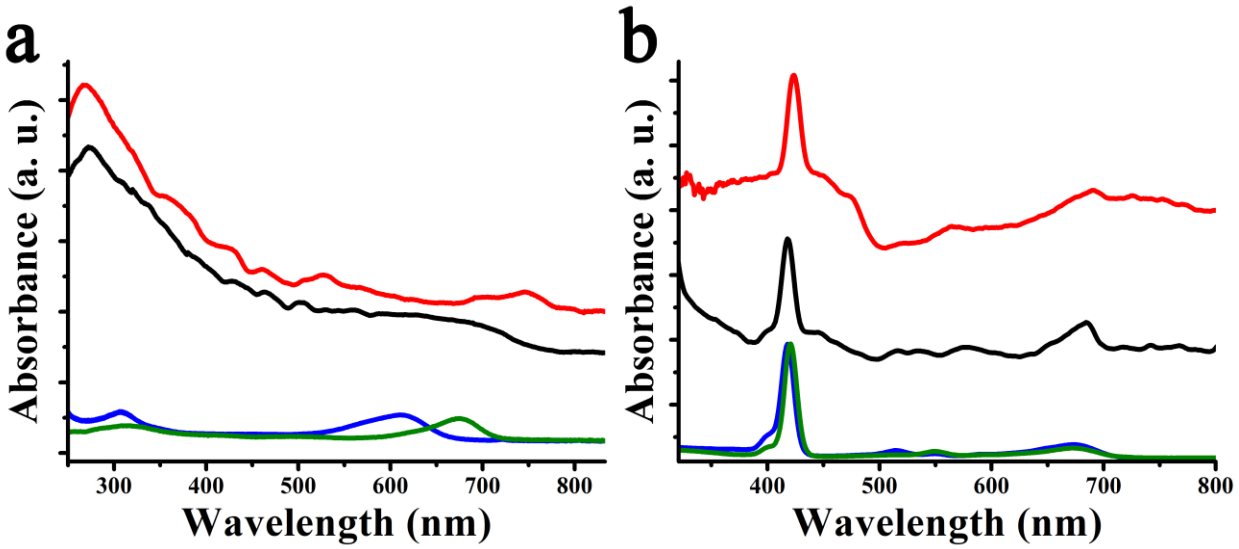

Figure 14. Absorption spectra of (a) free azaBDP **13** (olive) and **15** (blue) and graphene-based hybrid material **17** (black) and **18** (red), (b) free azaBDP **19** (blue) and **20** (olive) and graphene-based hybrid material **21** (black) and **22** (red), obtained in DCM.

Photoluminescence spectroscopy measurements were carried out to elucidate possible interactions between dyes **13**, **19** and **20** with graphene, within hybrids **18**, **21** and **22**, respectively, at the excited states. Firstly, we conclude that dye **15** and hybrid **17** have no emission, but after boron inclusion in **18**, the appearance of a band at 709 nm guarantees the successful integration of boron in the azaBDP skeleton (Figure 15a). A considerable depression of the emission of **18** compared with that of **13** is observed in samples possessing equal optical concentrations. On the other hand, dye **19** has two photoactive species, an azaBDP that emits at 705 nm under excitation at 680 nm and one porphyrin that emits at 650 nm when is excited at 420 nm. However, the emission of dye **19** is governed by the band of azaBDP although it is excited at porphyrin excitation region (Figure 15b). The latter result indicates strong electronic communication between the two photo-species, due, probably for electron-crossing-system or energy transfer from S^2 and/or S^1 excited porphyrin orbital to S^1 azaBDP and followed by emission relaxation. The attachment of **19** to graphene (material **21**) results in additional changes in the electronic behavior of dye **19** comprising an enhanced ratio of intensity emission porphyrin/azaBDP as well as strong quenching and red shift of both signals to 652 and 711 nm, suggesting an additional electronic pathway competing in this new system (Figure 15c). A plausible explanation is that part of the electrons on the excited states of porphyrin and azaBDP

are transferred to graphene, consequently graphene will reduce the electron transfer of porphyrin to azaBDP and enhance the ratio of intensity emission porphyrin/azaBDP. Inclusion of the metal in **19** yields **20** and produces strong changes in the morphology of the dye in comparison with starting material **19**. First, a new emission intensity related with the new ^{3}Zn*-porphyrin at 602 is acquired. Additionally, the bands of the porphyrin and azaBDP at 648 nm and 704 nm are blue-shifted due to the new overlapping with Zn. Additionally, the signals of dye **20** are moved to 606, 656 and 715 nm within graphene in hybrid **22**. This red shift accomplished with quenching as well as enhancement of the ratio of intensity emission porphyrin/azaBDP suggesting a electronic communication of the orbitals of azaBDP and graphene in **22**. In fact, graphene produces higher quenching in azaBDP than in zn-porphyin, probably because part of the energy/electrons of the excited states of the azaBDP is transferred to excited orbitals Zn-porphyrin and graphene and finally, ^{3}Zn*-porphyrin also transfer to graphene.

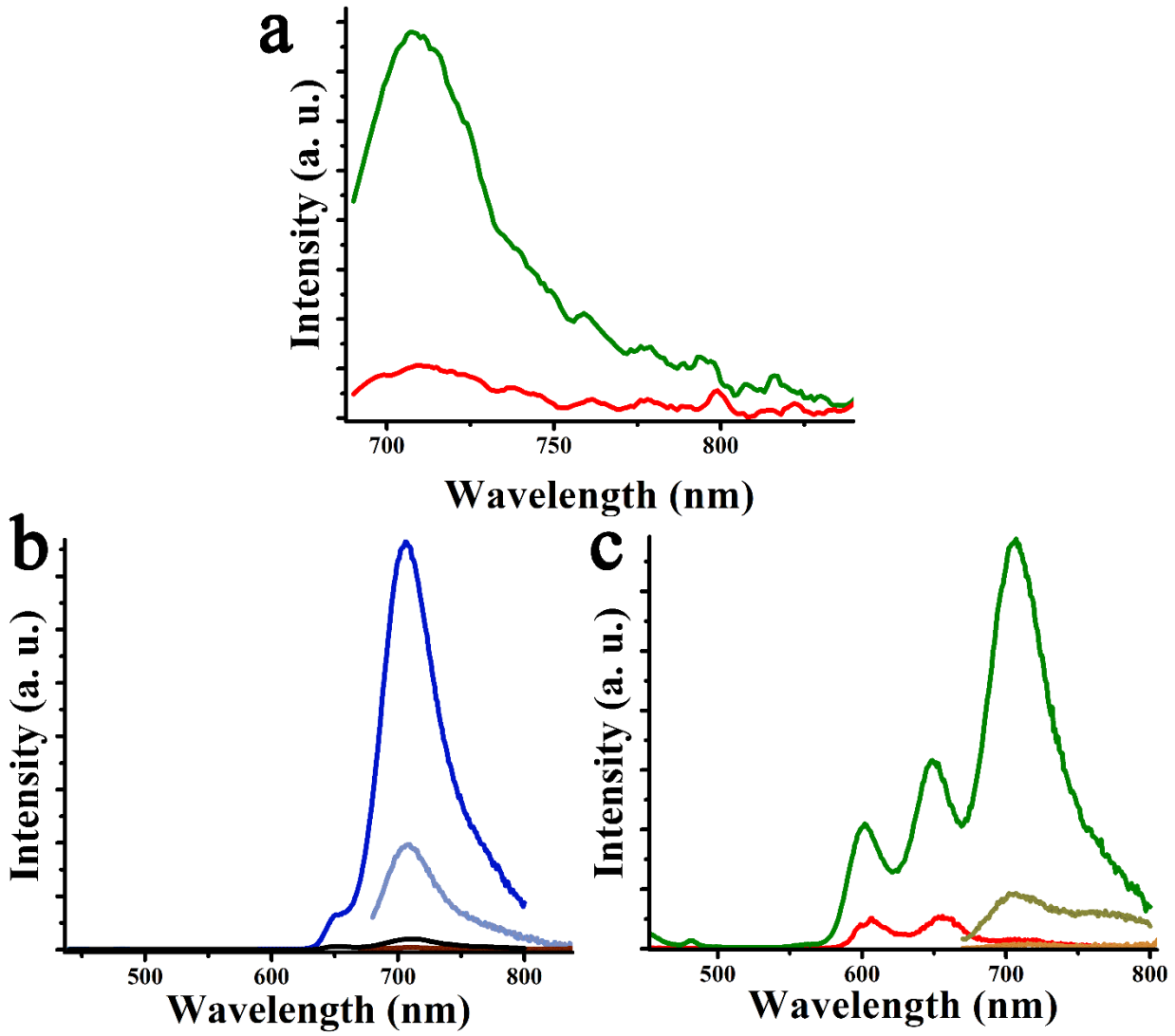

Figure 15. Photoluminescence spectra (a) at excitation at 660 nm for free azaBDP **13** (olive) and graphene-based hybrid **18** (red), (b) at excitation at 420 nm for free azaBDP **19** (blue) and graphene-based hybrid material **21** (black) and at excitation at 650 nm for free azaBDP **19** (purple) and graphene-based hybrid material **21** (brown) and (c) at excitation at 420 nm for free azaBDP **20** (olive) and graphene-based hybrid material **22** (red) and at excitation at 650 nm for free azaBDP **20** (dark yellow) and graphene-based hybrid material **22** (dark orange), obtained in dichloromethane.

Notably, time-resolved emission studies bring more light about the electronic interactions in the excited states between the different species. Analysis of the time-profile of the decay at 708 nm upon excitation at 654 nm for azaBDP **13** was mono-exponentially fitted with a lifetime of 1.40

ns. On the other hand, the decay component in hybrid **18** has an additional time of 0.9 ns, concluding in electron or energy transfer from azaBDP to graphene, according with emission spectra. Analogously, the photoluminescence of hybrid **21**, at 706 nm has a second decay parameter of 0.3 ns as compared to the mono-exponential free azaBDP dye **19** of 1.2 ns. More interesting is that this second decay of azaBDP in **21** remained at porphyrin excitation, evidencing electron or energy transfer from porphyrin to azaBDP and finally to graphene. However, material **22** has not reduced lifetimes, of the azaBDP in the dye **20** neither under excitation in azaBDP nor porphyrin region, but an additional 3 times faster decay was registered through porphyrin excitation and emission (exc. 441, em. 650) suggesting strong changes in the role of **19** and **20** dyes hybrids with graphene. In fact, a plausible explanation is that S^2 or S^1 porphyrin excitation produce electron or energy transfer to azaBDP, then azaBDP fast transfers to ^{3}Zn*-porphyrin which finally transfer to graphene. These findings are in line with photoluminescence assays, revealing electron or energy transfer cascade systems. The decays, emission rate constants (k^S) and quantum yields (Φ^S) for free azaBDP dyes **13**, **19** and **20** and graphene-based hybrid materials **18**, **21** and **22** were calculated based on equations (1) and (2), respectively, and presented in Table 2.

Table 2. Summary of photophysical and electrochemical data for BDP dyes **13, 19** and **20** and graphene-based hybrids **18**, **21** and **22** in DCM.

Parameters	**Material**	**τ_1 (ns)**	**τ_2 (ns)**	**k^S (s^{-1})**	**Φ^S**
	13	1.4			
	18	1.5	0.9	3.97×10^8	0.36
λ_{exc}= 654nm	19	1.2			
λ_{em}=707nm	21	1.3	0.31	2.48×10^9	0.76
λ_{exc}= 441nm	19	0.92			
λ_{em}=707nm	21	1.3	0.30	2.61×10^9	0.77
λ_{exc}= 441nm	20	2.64			
λ_{em}=650 nm	22	1.98	0.77	7.97×10^8	0.61

3.3 EXPERIMENTAL SECTION

3.3.1 Materials

Instrumentation. ^{1}H and ^{13}C NMR spectra were recorded in a 300 MHz Varian instrument operated by Vjnmr software, with TMS used as internal standard and D_2O as solvent. Steady-state UV-Vis electronic absorption spectra were recorded on a PerkinElmer (Lambda 19) UV-Vis-NIR spectrophotometer. Steady-state emission spectra were recorded on a Fluorolog-3 JobinYvon-Spex spectrofluorometer (model GL3-21). Pico-second time-resolved fluorescence spectra were measured by the time-correlated-single-photon-counting (TCSPC) method on a Nano-Log spectrofluorometer (Horiba JobinYvon), by using a laser diode as an excitation source (NanoLED, 375 nm) and a UV-Vis detector TBX-PMT series (250-850 nm) by Horiba JobinYvon. Lifetimes were evaluated with the DAS6 Fluorescence-Decay Analysis Software. Mid-infrared spectra in the region 500−4500 cm^{-1} were obtained on a Fourier transform IR spectrometer (Equinox 55 from Bruker Optics) equipped with a single reflection diamond ATR accessory (DuraSamp1IR II by SensIR Technologies). A drop of the solution was placed on the diamond surface, followed by evaporation of the solvent, in a stream of nitrogen, before recording the spectrum. Typically, 100 scans were acquired at 2 cm^{-1} resolution. Micro-Raman scattering measurements were performed at room temperature in the backscattering geometry using a RENISHAW inVia Raman microscope equipped with a CCD camera and a Leica microscope. A 2400 lines mm^{-1} grating was used for all measurements, providing a spectral resolution of ± 1 cm^{-1}. As an excitation source the Ar^+ laser (633 nm with less than 2.65 mW laser power) was used. Measurements were taken with 60 seconds of exposure times at varying numbers of accumulations. The laser spot was focused on the sample surface using a long working distance 50x objective. Raman spectra were collected on numerous spots on the sample and recorded with Peltier cooled CCD camera. The intensity ratio I_D/I_G was obtained by taking the peak intensities following any baseline corrections. The data were collected and analyzed with Renishaw Wire and Origin software. Thermogravimetric analysis was performed using a TGA Q500 V20.2 Build 27 instrument by TA in a nitrogen (purity >99.999%) inert atmosphere. X-ray photoelectron analysis (XPS) was performed with a Kratos AXIS Supra. The spectra were obtained using a monochromatized Al-Kα source at 1486.6 eV running at 15 kV and 10 mA. The survey spectrum was measured at 160 eV pass energy and for the individual peak regions,

spectra were recorded with pass energy of 20 eV. The energy resolution was < 0.48 eV. The analysis of peaks was performed with the Casa XPS software, using a weighted sum of Lorentzian and Gaussian components curves after Shirley background subtraction. The binding energies were referenced to the internal C1s standard at 284.6 eV. High-resolution tranmission electron microscopy (HRTEM) was performed on an aberration-corrected (image corrector) FEI Titan Cube microscope, working at 80 keV. STEM imaging and EELS studies have been conducted using an aberration-corrected FEI Titan Low-Base microscope operated at 80 kV. This microscope is equipped with a Cs probe corrector and a Gatan Tridiem ESR 865 EELS spectrometer. The energy resolution was ~1 eV. The convergence and collection angles were 25 and 50 mrad, respectively. To increase the signal/noise ratio, the datasets were then de-noised with the open-source program Hyperspy by using principal component analysis routines. TEM images were taken at room temperature using a JEOL JEM-2100F, operated at an acceleration voltage of 80 keV under a pressure of 10^{-5} Pa. The samples were sonicated in 3 mL hexane for 1 minute using an ultrasonic bath sonicator (Nanoruptor, NR-350, Cosmo Bio Co. Ltd), and 10 drops of the dispersion solution were deposited onto carbon-coated copper grids. TEM images were recorded on a Gatan MSC 794 1 k×1 k CCD camera with a typical exposure time of 0.3 s.

3.3.2 Synthesis

Preparation of graphene-based hybrid materials 8 and 9.

In a typical reaction, 15 mg of exfoliated graphene were dispersed by sonication in 10 mL of dry dichloromethane under nitrogen atmosphere. Then, the cyanine dye (15 mg for **1** and 10 mg for **2**) was added, followed by the quick addition of 4-dimethylaminopyridine (8.2 mg) and 1-ethyl-3-(3-dimethylaminopropyl) carbodiimide (5.5 mg), and stirred at reflux for 96 hours. After that period, the reaction mixture was cooled down to room temperature, filtered over a PTFE membrane filter (pore size 0.1 μm) and washed with a large amount of dichloromethane to remove completely any organic residual matter. The newly prepared graphene-based hybrid materials **8** and **9** were obtained as solids and stored under dark.

Preparation of graphene-based hybrid materials 10 and 11.

In a typical reaction, 10 mg of exfoliated graphene were dispersed by sonication in 10 mL of o-DCB, under a nitrogen atmosphere. Then, a solution of the NIR dye (30 mg for aniline derivative cyanine dye **3** and 35 mg for aniline derivative cyanine dye **4**) in 5 mL of acetonitrile was added, followed by the quick addition of isoamyl nitrite (10 mg) and the reaction mixture was stirred at 60 ^{o}C, under N_2, for 96 hours. After cooling down to room temperature, the reaction mixture was diluted with 30 mL of DMF, filtered over a PTFE membrane filter (pore size 0.1 μm) and washed with a large amount of DMF and DCM to remove completely any organic residuals. The newly prepared graphene-based hybrid materials **10** and **11** were obtained as solids and stored under dark.

Procedure for the synthesis of B: In a stirred solution of diethylene glycol momomethyl ether **A** (25 g, 0.208 mol) and tosyl chloride (33.75 g, 0.177 mol) in dry dichloromethane (250 mL) under N_2 at 0°C, freshly distilled triethylamine (24.18 g, 0.239 mol) was added dropwise over 1 h. The mixture was stirred for 3.5 h at r.t., filtered, and the filter cake washed with dichloromethane. The combined filtrates were washed with H_2O (2x100 mL) and brine (100 mL), dried (Na_2SO_4) and the solvent evaporated. The oily residue was filtered (through cotton wool in pipette), and the filtrate dried *in vacuo*, yielding 41.06 g (85%) of a clear yellow oil. ^{1}H-NMR (300 MHz, $CDCl_3$): δ (ppm) 7.82 – 7.76 (m, 2H), 7.35 – 7.31 (m, 2H), 4.14 – 4.18 (m, 2H), 3.70 – 3.66 (m, 2H), 3.59 – 3.55 (m, 2H), 3.49 – 3.45 (m, 2H), 3.34 (s, 3H), 2.44 (s, 3H); ^{13}C-NMR (75 MHz, $CDCl_3$): δ (ppm) 144.92, 133.12, 129.84, 128.06, 71.93, 70.80, 69.34, 68.83, 59.17, 21.61. (Figure17 shows ^{1}H and ^{13}C-NMR of **B**).

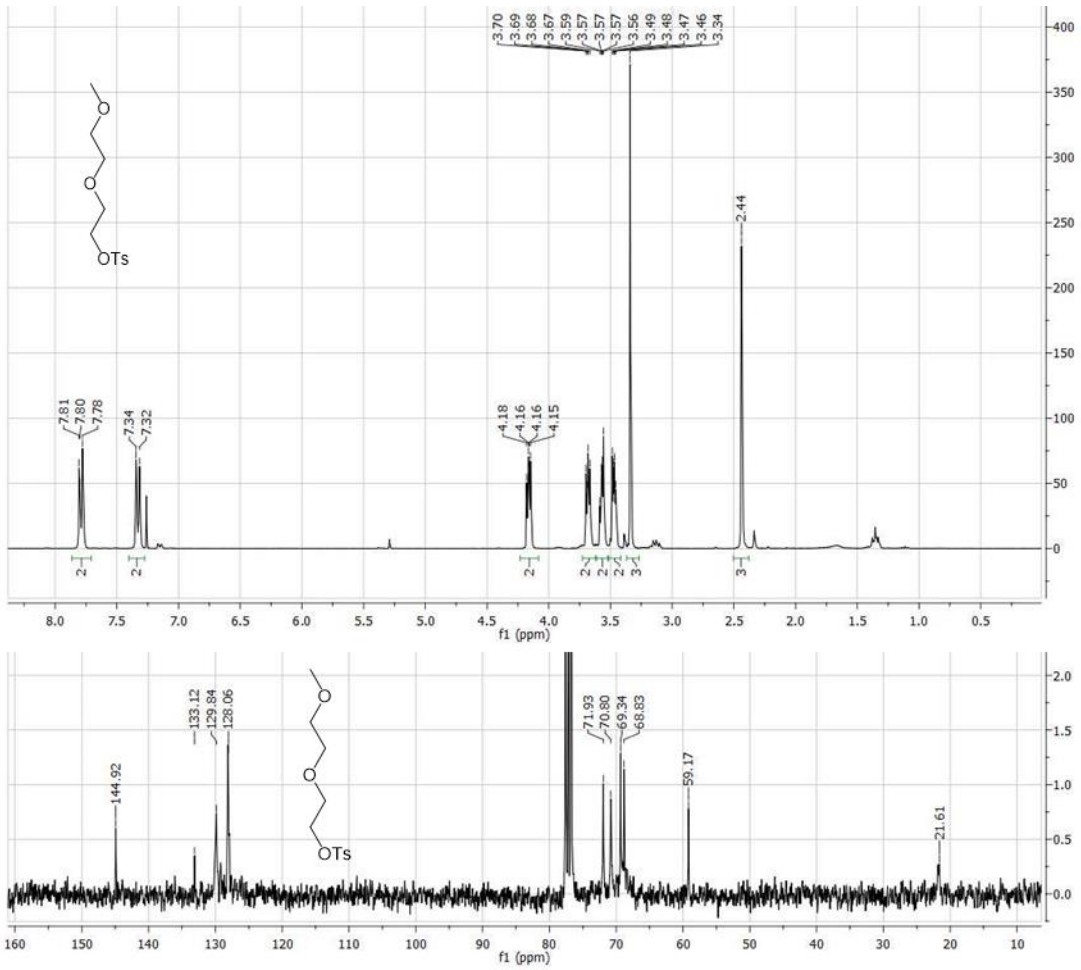

Figure 17. ^{1}H-NMR (top) and ^{13}C-NMR (bottom) of **B**.

Procedure for the synthesis of C: In a stirred solution of compound B (38 g, 0.139 mol) in dry acetonitrile (600 mL) under N_2, were added successively potassium iodide (60 mg, 0.36 mmol), 4-hydroxybenzaldehyde (25.4 g, 0.208 mmol) and potassium carbonate (28.75 g, 0.208 mmol) and the mixture was refluxed for 24 h. The white solid formed was filtered off and washed with acetonitrile. The combined filtrate and washings were concentrated, the oily residue was dissolved in ethyl acetate (300 mL), washed with 0.3N NaOH (3 x 200 mL) and brine, dried (Na_2SO_4) and the solvent evaporated, yielding **C** (23.47 g, 75%) as a yellow oil. ^{1}H-NMR (300 MHz, $CDCl_3$): δ (ppm) 9.87 (s, 1H), 7.84 – 7.89 (m, 2H), 7.03 – 6.99 (m, 2H), 4.23 – 4.20 (m, 2H), 3.89 – 3.86 (m, 2H), 3.73 – 3.70 (m, 2H), 3.58 – 3.55 (m, 2H), 3.38 (s, 3H); ^{13}C-NMR (75 MHz, $CDCl_3$): δ (ppm) 190.88, 163.94, 132.03, 130.17, 114.99, 72.04, 70.95, 69.60, 67.85,

59.19. ESI HRMS calcd for $C_{12}H_{16}O_4$: 224.25, found: m/z =224.30. (Figure 18 shows ^{1}H and ^{13}C-NMR of **C**).

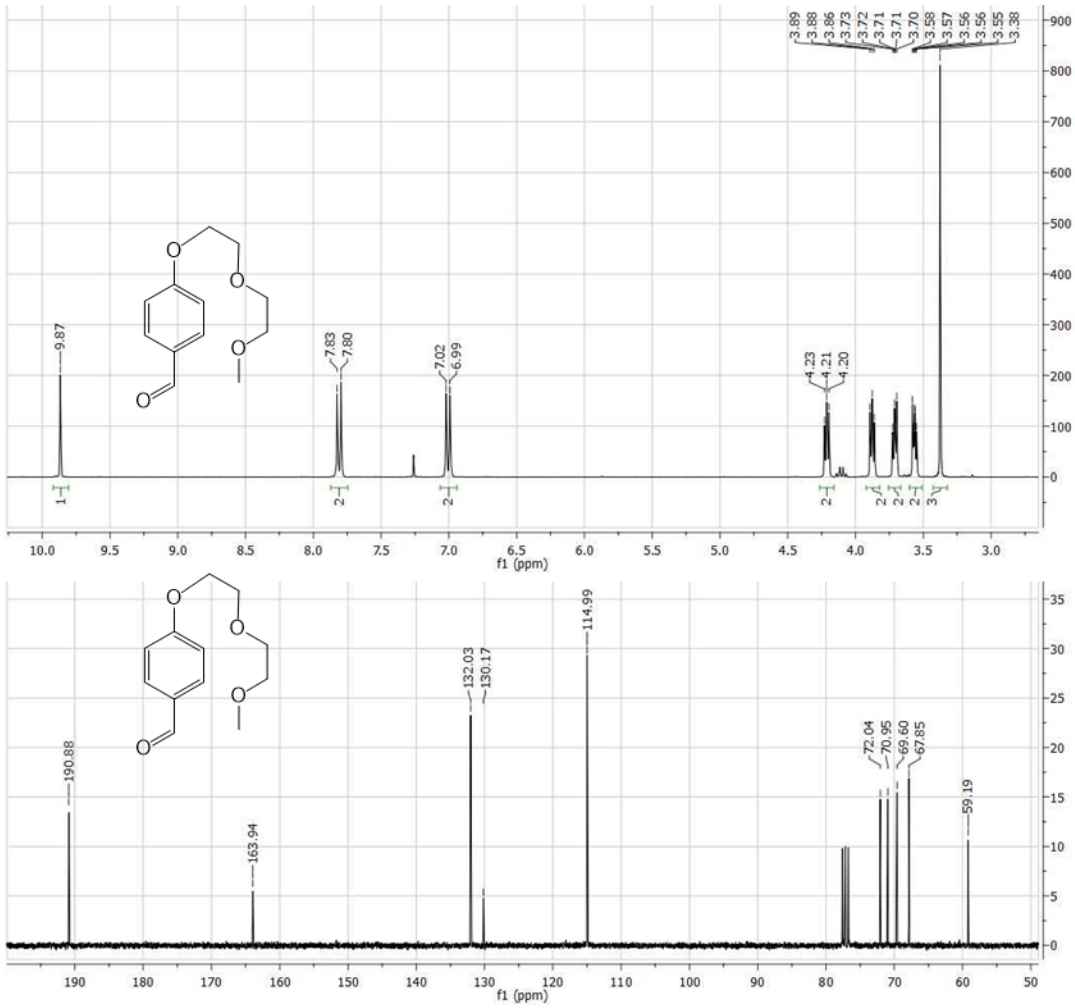

Figure 18. ^{1}H-NMR (300 MHz, $CDCl_3$), top, and ^{13}C-NMR (75 MHz, $CDCl_3$) bottom of **C**.

Procedure for the synthesis of D: In a stirred solution of compound **C** (11g, 0.049 mol) and 4'-hydroxyacetophenone (6.67 g, 0.049 mol) in ethanol (80 mL), 10% aq. NaOH (20 mL) was added and the resulting mixture was heated to reflux for 18 h. After cooling down, the solvent evaporated and water (300 mL) was added. Washing with DCM (pH = 12) removed mainly unreacted compound **C**. Aqueous layer Acidified with 10N HCl to pH = 10 and washed with CH_2Cl_2 (minor impurities removed). Further acidification to pH 9–7 and subsequently dicloromethane washings extracted product **D**. Further acidification extracted unreacted 4'-hydroxyacetophenone. The pH 9–7 washings were combined, dried (Na_2SO_4) and solvent evaporated. The residue was treated with cold methanol and filtered, affording compound **D** (4.64 g, 28 %) as yellow dust. ^{1}H-NMR (300 MHz, $CDCl_3$): δ (ppm) 8.47 (bs, 1H), 7.92 (d, J = 8.7 Hz, 2H), 7.72 (d, J = 15.6 Hz, 1H), 7.49 (d, J = 8.7 Hz, 2H), 7.35 (d, J = 15.6 Hz, 1H), 6.95 (d, J = 8.7 Hz, 2H), 6.83 (d, J = 8.7 Hz, 2H), 4.10 – 4.06 (m, 2H), 3.86 – 3.82 (m, 2H), 3.74 – 3.71 (m, 2H), 3.62 – 3.59 (m, 2H), 3.40 (s, 3H); ^{13}C-NMR (75 MHz, $CDCl_3$): δ (ppm) 189.55, 161.52, 160.77, 144.32, 131.21, 130.38, 130.22, 127.85, 119.43, 115.77, 114.97, 71.98, 70.68, 69.70, 67.43, 59.06. MALDI-MS calcd for $C_{20}H_{22}O_5$: 342.1457, found: m/z 342.1454 (Figure 19 shows ^{1}H and ^{13}C-NMR and MALDI-MS of **D**).

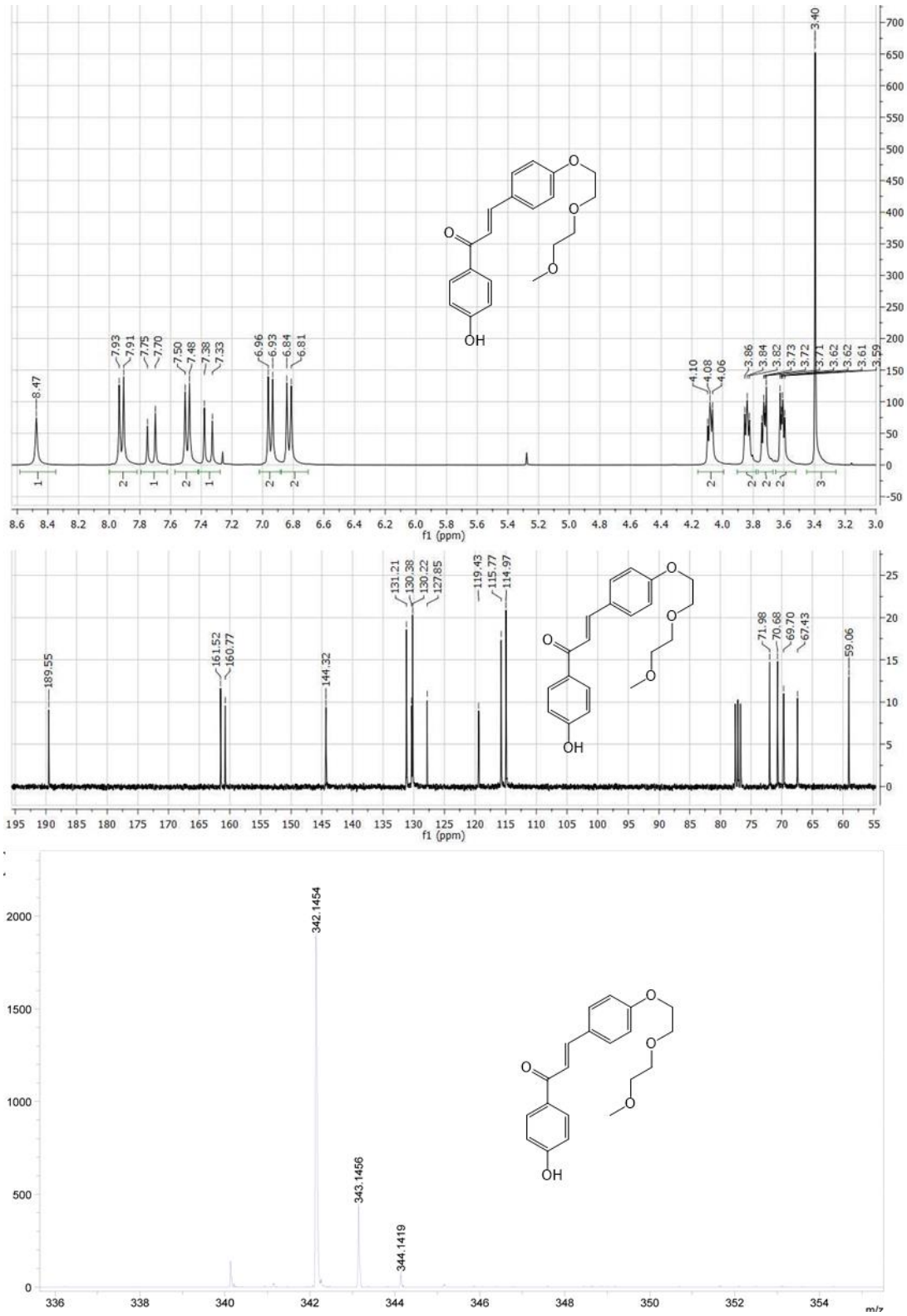

Figure 19 ^{1}H-NMR (top), ^{13}C-NMR (middle), and MALDI-MS of **D**.

Procedure for the synthesis of E: A stirred solution of compound **D** (6 g, 17.52 mmol), $MeNO_2$ (5.35 g, 87.62 mmol) and Et_2NH (6.41 g, 87.62 mmol) in MeOH (125 mL) was heated to reflux for 5 h. Another round of $MeNO_2/Et_2NH$ was added and heating continued for 18 h. Another round of $MeNO_2/Et_2NH$ was added and heating continued for 4 days. After cooling down, aq. sat. NH_4Cl (≈ 250 mL) was added, the mixture was extracted with CH_2Cl_2 (3x150 mL), combined organics washed with H_2O and dried (Na_2SO_4). Evaporation of the solvent left compound **E** (7.07 g, 100 %) as orange/red viscous oil. 1H-NMR (300 MHz, $CDCl_3$): δ (ppm) 7.78 (d, J = 8.4 Hz, 2H), 7.13 (d, J = 8.5 Hz, 2H), 6.82 – 6.79 (m, 4H), 5.49 (bs, 2H), 4.77 (dd, J = 12.3, 6.4 Hz, 1H), 4.61 (dd, J = 12.3, 8.3 Hz, 1H), 4.16 – 4.05 (m, 3H), 3.83 – 3.80 (m, 2H), 3.72 – 3.69 (m, 2H), 3.60 – 3.57 (m, 2H), 3.38 (s, 3H), 3.36 – 3.23 (m, 2H); 13C-NMR (75 MHz, $CDCl_3$): δ (ppm) 195.93, 161.92, 158.26, 131.48, 130.82, 128.94, 128.61, 115.80, 115.17, 80.00, 72.03, 70.71, 69.81, 67.46, 59.12, 41.36, 39.09. (Figure 20 shows ^{1}H and ^{13}C-NMR of **E**).

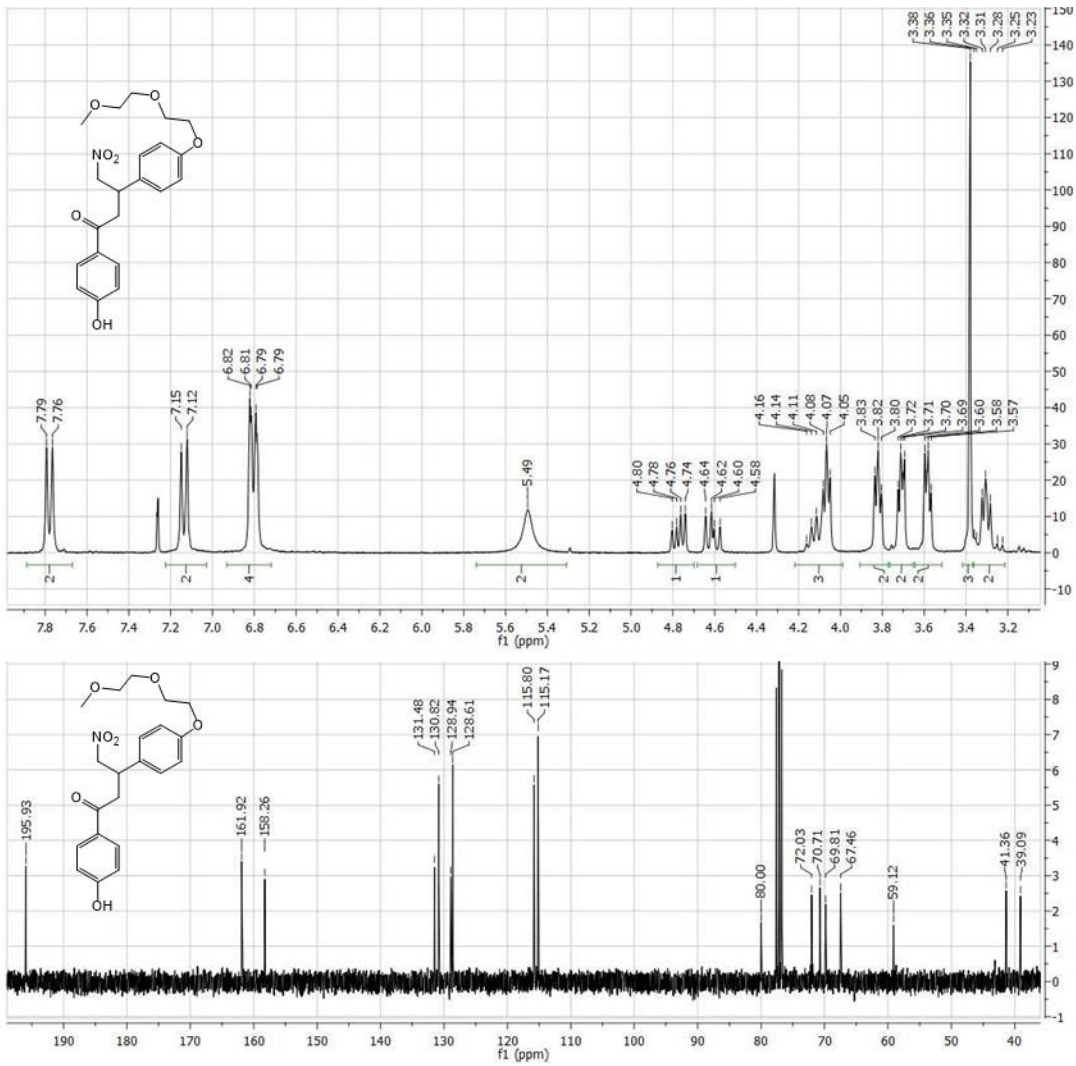

Figure 20 ^{1}H-NMR (top), and ^{13}C-NMR (bottom), of **E**.

Procedure for the synthesis of 12. Compound **E** (50 mg, 0.124 mmol), ammonium acetate (334 mg, 4.338 mmol), MeOH (1 mL) and a magnetic stirrer were placed in a 7 mL microwave vial, and the suspension was MW irradiated for 1h at 95°C (set: 100W, 95°C, 60 min; during the course: 5 W, 10 psi). A blue / purple solid was formed, methanol (5 mL) was added, the mixture was centrifuged and the residue was washed with methanol and petroleum ether leaving **12** (20 mg, 44%) as blue / iridescent violet solid. ^{1}H-NMR (300 MHz, DMSO-d$_6$): δ (ppm) 13 – 9.5 (br, 3H), 8.04 (d, J = 8.7 Hz, 4H), 7.89 (d, J = 8.6 Hz, 4H), 7.40 (s, 1H), 7.04 (d, J = 8.9 Hz, 4H), 7.00 (d, J = 8.7 Hz, 4H), 4.19 – 4.16 (m, 4H), 3.79 – 3.76 (m, 4H), 3.62 – 3.59 (m, 4H), 3.49 – 3.46 (m, 4H), 3.26 (s, 3H); ^{13}C-NMR (75 MHz, DMSO-d$_6$): δ (ppm) 159.87, 158.51, 154.05, 148.37, 140.57, 129.83, 128.36, 126.23, 122.64, 116.37, 114.36, 113.55, 71.31, 69.75, 68.94, 67.22, 58.08. MALDI-MS calcd for $C_{42}H_{43}N_3O_8$: 717.8061, found: m/z 718.3130 [M+H^{+}] (Figure 21 shows ^{1}H and ^{13}C-NMR and MALDI-MS of **12**).

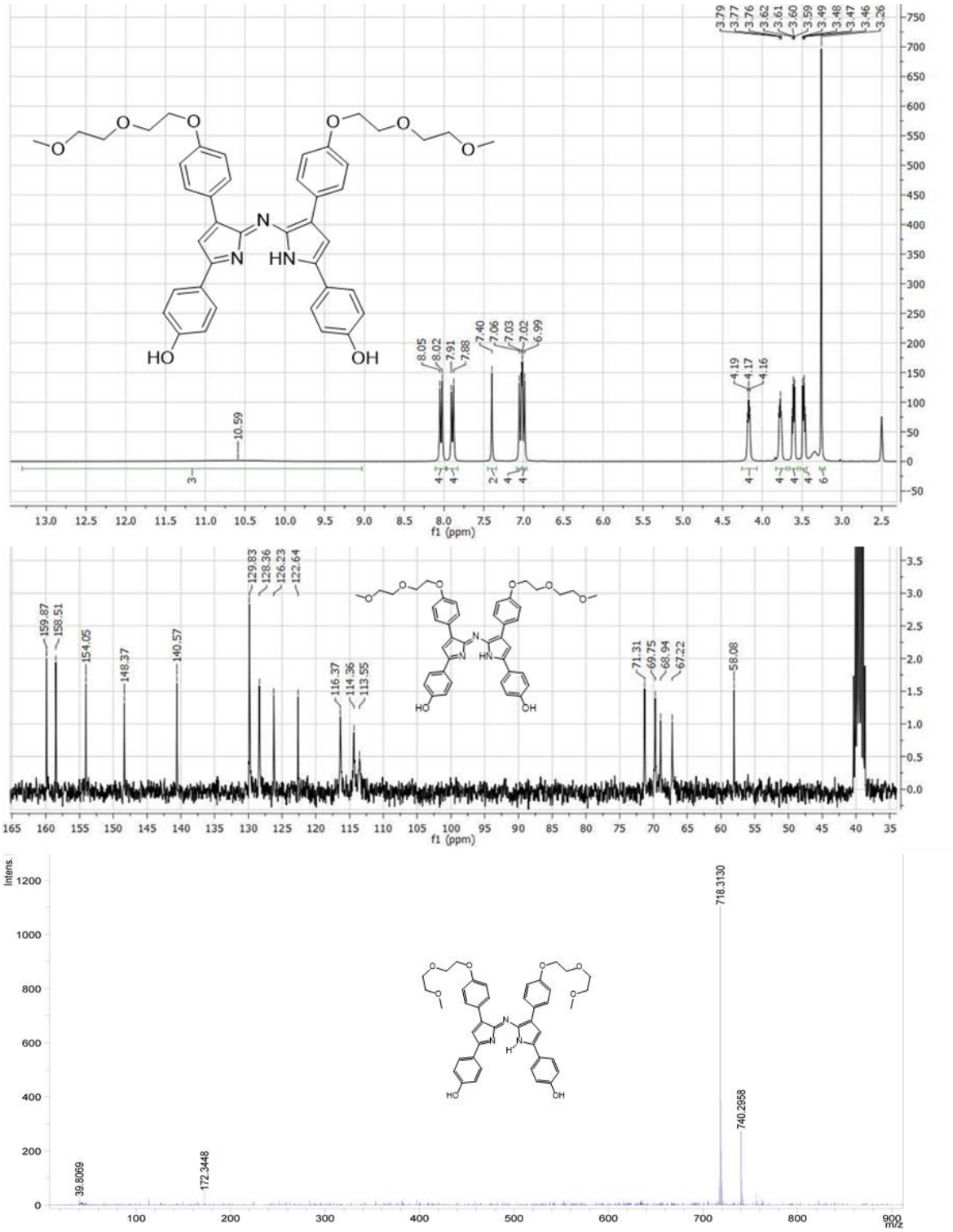

Figure 21. ^{1}H-NMR (top), ^{13}C-NMR (middle), and MALDI-MS (bottom) of **12**.

Procedure for the synthesis of 13: In a solution of dry DCM (30 mL) with **12** (200 mg, 0.279 mmol) was added diisopropylethylamine (361 mg, 2.79 mmol). The mixture was stirred for 0.5 h and then $BF_3 \cdot Et_2O$ was added (593 mg, 4.179 mmol). The reaction continued for 18 h. Then, sat. aq. NH_4Cl (3 mL) was added, and the mixture was stirred for 5 min. The solvent was evaporated under vacuo and 20 mL of water (20 mL) was added. Then, the suspension was filtered *in vacuo* and successively washed with water, 1:1 $MeOH/H_2O$, MeOH (2x3 mL), Et_2O (3 mL) and petroleum ether affording **13** (213 mg, 100%) as violet dust. Spectroscopic data for **13.** ^{1}H-NMR (300 MHz, DMSO-d_6): δ (ppm) 10.38 (bs, 2H), 8.14 (d, J = 8.6 Hz, 4H), 8.05 (d, J = 8.6 Hz, 4H), 7.41 (s, 2H), 7.12 (d, J = 8.6 Hz, 4H), 6.94 (d, J = 8.6 Hz, 4H), 4.22 – 4.17 (m, 4H), 3.80 – 3.75 (m, 4H), 3.64 – 3.58 (m, 4H), 3.50 – 3.45 (m, 4H), 3.26 (s, 6H); ^{13}C-NMR (75 MHz, DMSO-d_6): δ (ppm) 160.59, 159.77, 156.99, 144.08, 141.29, 131.84, 130.51, 124.69, 121.98, 117.75, 115.75, 114.84, 71.31, 69.75, 68.90, 67.37, 58.08. MALDI-MS calcd for $C_{42}H_{43}BF_2N_3O_8$: 765.3033, found: m/z 765.3021 [M] (Figure 22 shows ^{1}H and ^{13}C-NMR and MALDI-MS of **13**).

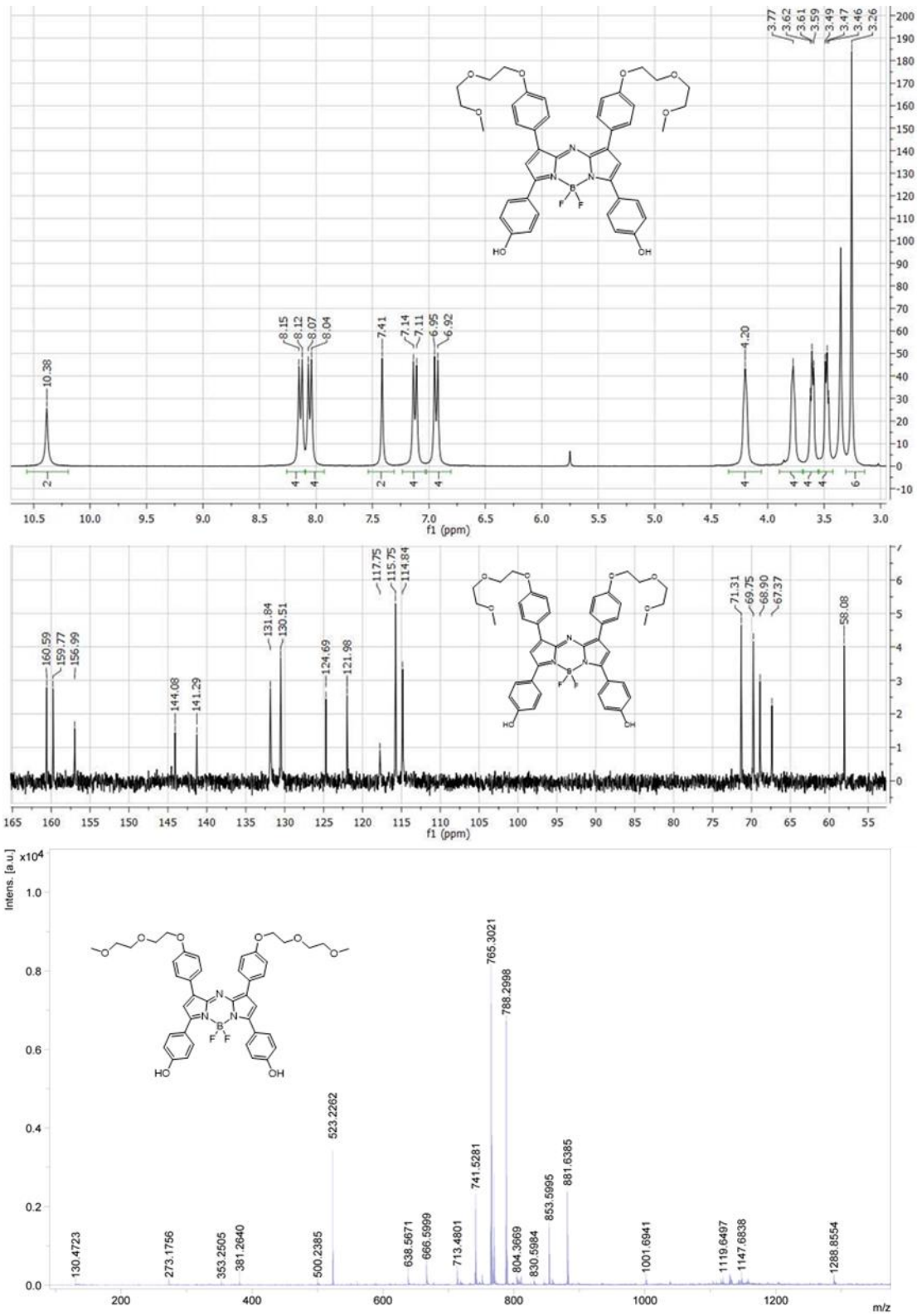

Figure 22. ^{1}H-NMR (top) ^{13}C-NMR (middle), and MALDI-MS (bottom) of **13**.

Procedure for the synthesis of 14: In a round bottom flask, lauric acid (88 mg, 1.05 equiv), azaBDP **12** (300 mg, 1 equiv.) for **1a**, EDCI (252 mg, 3 equiv.) and DMAP (205, 3 equiv.) were added in dry dicloromethane (50 mL). The reaction mixture was stirred under nitrogen at room temperature for 18 hours. Then, the organic phase was extracted with H_2O (5 x 100 mL), dried over $MgSO_4$ and purified by column chromatography (Hexane/DCM/acetone 50/90-80/10-20%) (F3, 100 mg, 25%) as dark blue solid. Spectroscopic data for **14.** ^{1}H NMR (300 MHz, $CDCl_3$) δ 8.06 – 7.79 (m, 5H), 7.63 (t, *J* = 7.8 Hz, 3H), 7.13 (d, *J* = 8.5 Hz, 2H), 7.04 (s, 1H), 6.96 (d, *J* = 8.8 Hz, 2H), 6.90 – 6.68 (m, 5H), 4.31 – 4.05 (m, 4H), 3.93 (m, 4H), 3.86 – 3.69 (m, 4H), 3.64 (m, 1H), 3.43 (m, 6H), 2.61 (m, 2H), 1.78 (m, 2H), 1.29 (s, 16H), 0.89 (t, *J* = 6.8, 5.5 Hz, 3H). ^{13}C NMR (75 MHz, $cdcl_3$) δ 172.13, 160.44, 158.93, 158.68, 158.45, 158.01, 153.66, 151.74, 150.68, 149.40, 145.98, 144.93, 143.68, 141.85, 137.32, 130.18, 129.80, 129.61, 128.85, 127.44, 127.28, 126.66, 126.47, 124.26, 122.11, 121.80, 115.90, 115.29, 114.18, 113.97, 113.72, 113.23, 110.11, 71.94, 70.67, 70.55, 69.90, 69.84, 69.78, 67.32, 67.10, 59.01, 58.97, 34.40, 31.88, 29.62, 29.60, 29.49, 29.31, 29.27, 29.17, 24.92, 22.65, 14.09. ESI HRMS calcd for $C_{54}H_{65}N_3O_9H^+$: 900,4794, found: m/z 900,4799 $[M+H]^+$ (Figure 23 shows ^{1}H and ^{13}C-NMR and Ms of **14**).

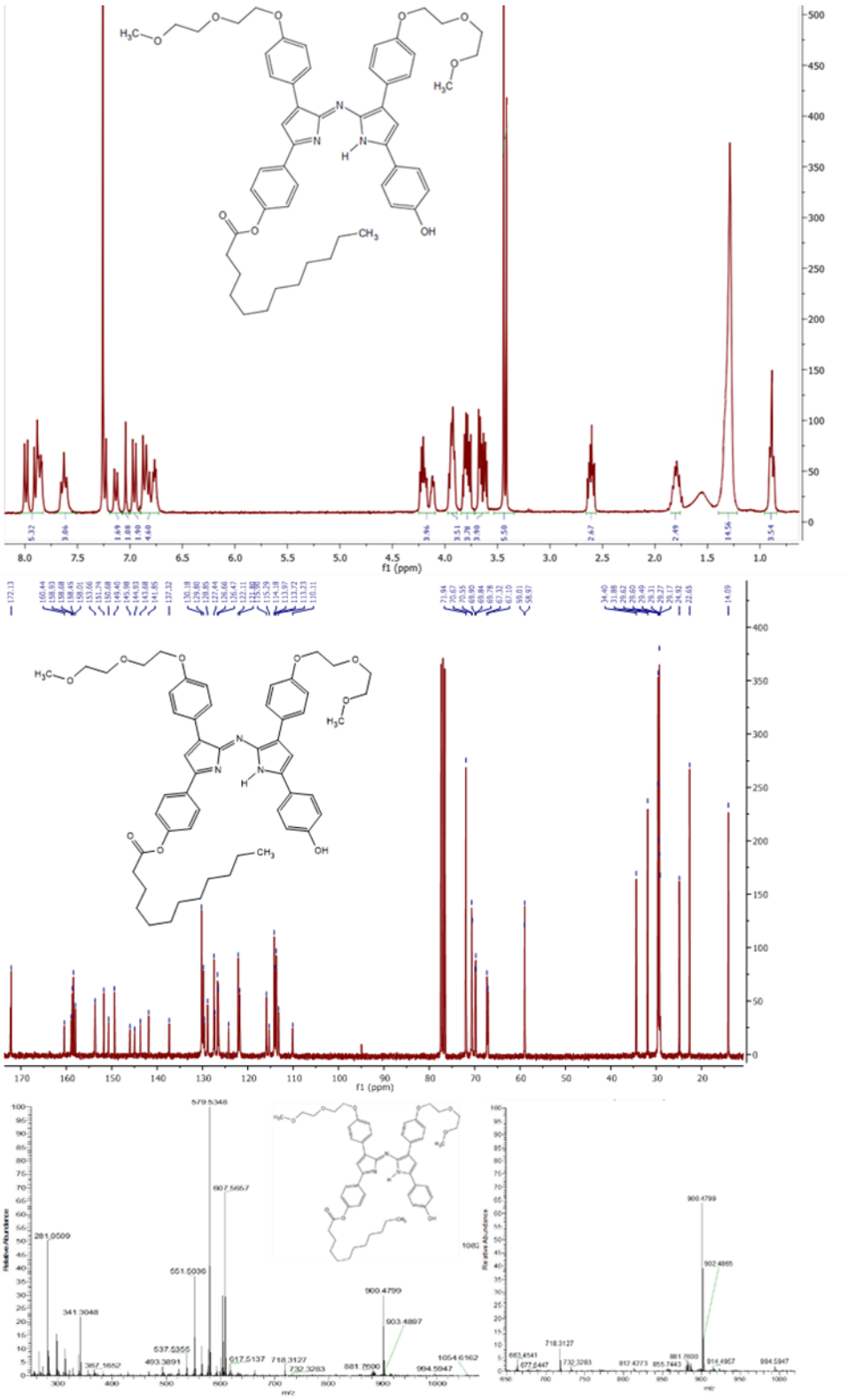

Figure 23. ^{1}H-NMR (top) ^{13}C-NMR (middle), and ESI-MS (bottom) of **14**.

Procedure for the synthesis of 15: In a round bottom flask, azaBDP **14** (100 mg, 1 equiv.), EDCI (252 mg, 3 equiv.) and DMAP (205, 3 equiv.) were added in dry dicloromethane (50 mL) and then was added 0.1 ml of Azoacetic acid. The reaction mixture was stirred under nitrogen at room temperature for 18 hours. Then, the sovent of the reaction was evaporated under vacuo without temperature. The solid was washed with water, redisolved in DCM, dried over $MgSO_4$ and purified by column chromatography (Hexane/DCM/acetone 50/40-30/10-20%) (F2, 20 mg, 17%) as dark blue solid. Noted that azide group is sensitive to the temperature. Spectroscopic data for **15.** ^{1}H NMR (300 MHz, $cdcl_3$) δ 8-007.63 (m, 4H), 7.68 – 7.46 (m, 4H), 7.11 (d, *J* = 8.1 Hz, 2H), 6.92-6.52 (m, 8H), 4.26 – 4.13 (m, 2H), 4.12 – 3.99 (m, 2H), 4.00 – 3.87 (m, 4H), 3.89 – 3.74 (m, 4H), 3.72-3.59 (m, 4H), 3.54 – 3.36 (m, 6H), 2.68 – 2.52 (m, 2H), 2.37 (s, 2H), 2.08 – 1.69 (m, 4H), 1.25 (s, 14H), 0.97 – 0.77 (m, 3H). ^{13}C NMR (75 MHz, $cdcl_3$) δ 169.37, 160.25, 158.86, 158.55, 158.08, 158.04, 153.48, 150.70, 143.66, 137.63, 130.18, 129.90, 129.77, 128.88, 127.92, 127.34, 126.62, 124.39, 121.84, 115.95, 115.23, 114.05, 113.80, 113.70, 110.33, 109.97, 71.96, 70.57, 69.93, 67.30, 67.17, 58.99, 58.94, 31.91, 30.91, 29.64, 29.50, 29.44, 29.12, 24.95, 22.67, 21.21, 14.10. ESI HRMS calcd for $C_{56}H_{66}N_5O_{10}$: 983,1760, found: m/z 984,5906 $[M+H]^+$ (Figure 24 shows ^{1}H and ^{13}C-NMR and ESI-MS of **15**).

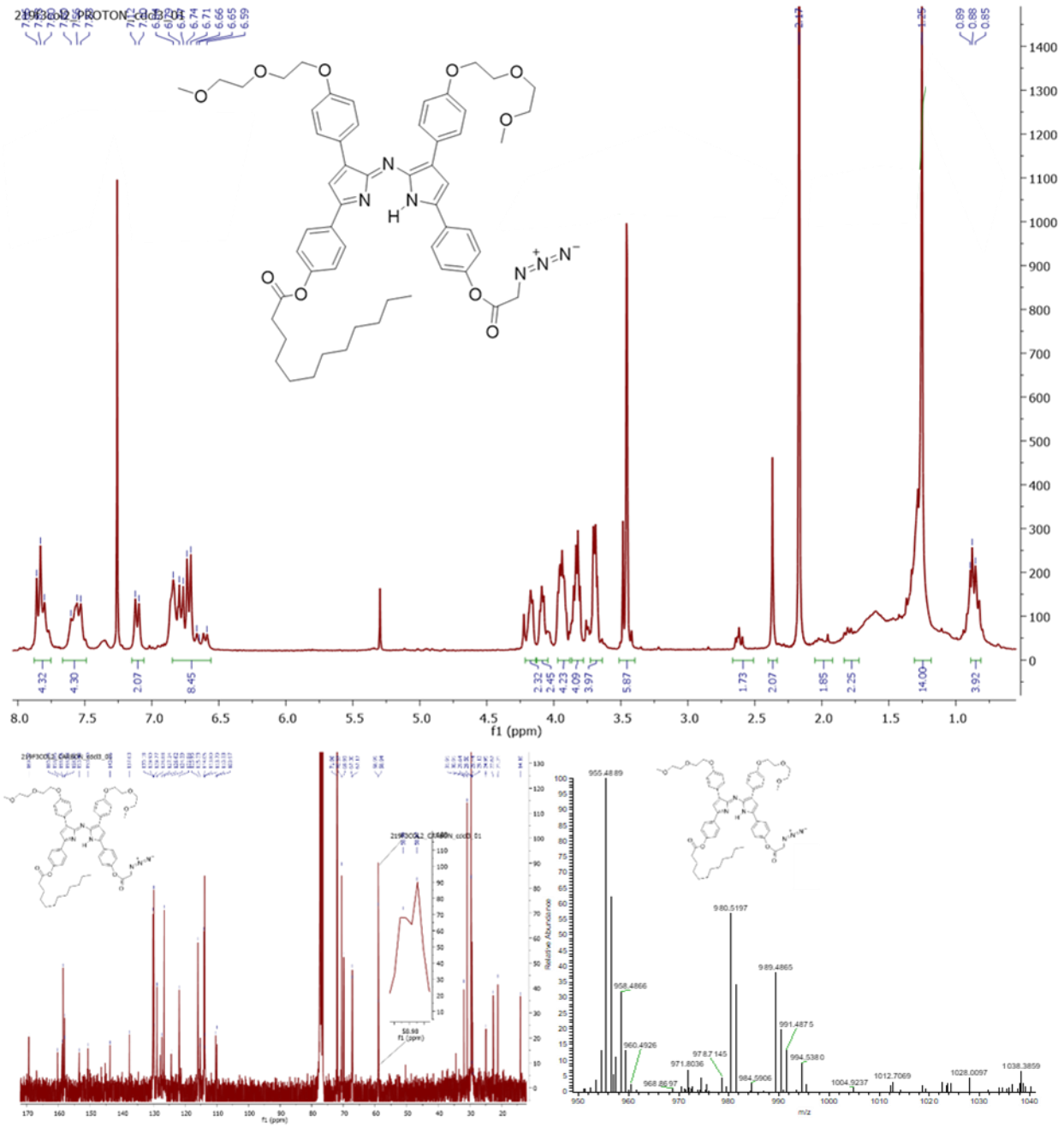

Figure 24. ^{1}H-NMR (top), ^{13}C-NMR (bottom left) and ESI-MS (bottom right) of **15**.

Procedure for the synthesis of 16: In a typical reaction, 80 mg of exfoliated graphene were dispersed by sonication in 15 mL of o-DCB, under a nitrogen atmosphere. Then, a solution of the 4-((trimethylsilyl)ethynyl)aniline (70 mg) in 5 mL of o-DCB was added, followed by the quick addition of isoamyl nitrite (1 ml). The reaction mixture was stirred at 120 ^{o}C, under N_2, for 7 days with occasional sonication. After cooling down to room temperature, the reaction mixture was diluted with 1 M of tetra-n-butylammonium fluoride trihydrate 30 mL in DMF and stirred overnight. Then filtered over a PTFE membrane filter (pore size 0.1 μm) and washed with a large amount of DMF and DCM to remove completely any organic residuals. The newly prepared graphene-based hybrid material **16** was obtained as solids and stored under dark.

Procedure for the synthesis of 17: Diisopropylamine (1.5 ml) was added to a solution of modified graphene **16** (60 mg) and compound **14** (16 mg) in DMSO (16.8 mL) at room temperature and stirred under a N_2 atmosphere. The reaction was stirred during 14 days with occasional sonication. Then, the reaction was filtered in a filter of 200 nm of porous and extensively washed with DMF, acetone and DCM. After that period, the reaction mixture was filtered over a PTFE membrane filter (pore size 0.1 μm) and washed with a large amount of dichloromethane to remove completely any organic residual matter. The newly prepared graphene-based hybrid material **17** were obtained as solids and stored under dark.

Procedure for the synthesis of 18: Boron trifluoride-diethyl ether complex (2ml) was added to a solution of modified graphene **17** (50 mg) in DCM (10 mL) and diisopropylethylamine (0.5 ml) at room temperature and stirred under a N_2 atmosphere. The reaction was stirred during 2 days with occasional sonication. After that period, the reaction mixture was filtered over a PTFE membrane filter (pore size 0.2 μm) and washed with a large amount of MeOH to remove completely any organic residual impurity. The newly prepared graphene-based hybrid material **22** were obtained as solids and stored under dark.

Procedure for the synthesis of 19. In a round bottom flask, TTP-COOH (21 mg, 0.9 equiv), azaBDP **15** (28 mg, 1 equiv.), EDCI (19 mg, 3 equiv.) and DMAP (12, 3 equiv.) were added in dry dicloromethane (50 mL) and the reaction was stirred under nitrogen at room temperature over weekend. Once free porphyrin was not detected by thin chromatography, 0.1 ml of Azoacetic acid and small spatula of EDCI was added to the reaction. The reaction mixture was

stirred under nitrogen at room temperature for three days. Then, the solvent of the reaction was evaporated under vacuo without temperature. The solid was washed with water, resolved in DCM, dried over $MgSO_4$ and purified by column chromatography (Hexane/DCM/acetone 50/40-30/10-20%) (20 mg, 15%) as dark blue solid. Spectroscopic data for **19.** ^{1}H NMR (300 MHz, $CDCl_3$) δ 8.98-8.78 (m,8 H), 8.62 (d, *J* = 7.9 Hz, 2H), 8.40 (d, *J* = 8.0 Hz, 2H), 8.30 – 8.15 (m, 9H), 8.15 – 7.95 (m, 6H), 7.75 (10H), 7.54 (m, 4H), 7.12 – 6.85 (m, 8H), 4.22 (m, 4H), 3.94 (m, 4H), 3.82 – 3.69 (m, 4 H), 3.63 (m, 4H), 3.46 – 3.35 (m, 6H), 2.17 (s, 2H).^{13}C NMR (75 MHz, $CDCl_3$) δ 165.00, 160.28, 152.96,147.98, 145.57, 143.87, 142.02, 142.01, 141.98, 134.81, 134.53, 132.07, 131.59, 131.20, 131.18, 131.16, 131.10, 130.93, 130.88, 130.78,130.75, 130.62, 130.61, 129.62, 128.70, 128.66, 128.59, 127.79, 127.77,126.70, 126.58, 126.54, 125.42, 122.06, 121.80, 121.36, 120.66, 120.64, 120.44, 120.42, 118.22, 118.20, 114.89, 114.70, 94.99, 71.98, 70.82, 69.69, 67.56, 59.11, 50.46. MALDI-HRMS calcd for $C_{89}H_{71}BF_3N_{10}O_{10}$: 1488.5416, found: m/z 1489.5518 $[M+H]^+$ (Figure 25 shows ^{1}H and ^{13}C-NMR and MALDI-HRMS of **19**).

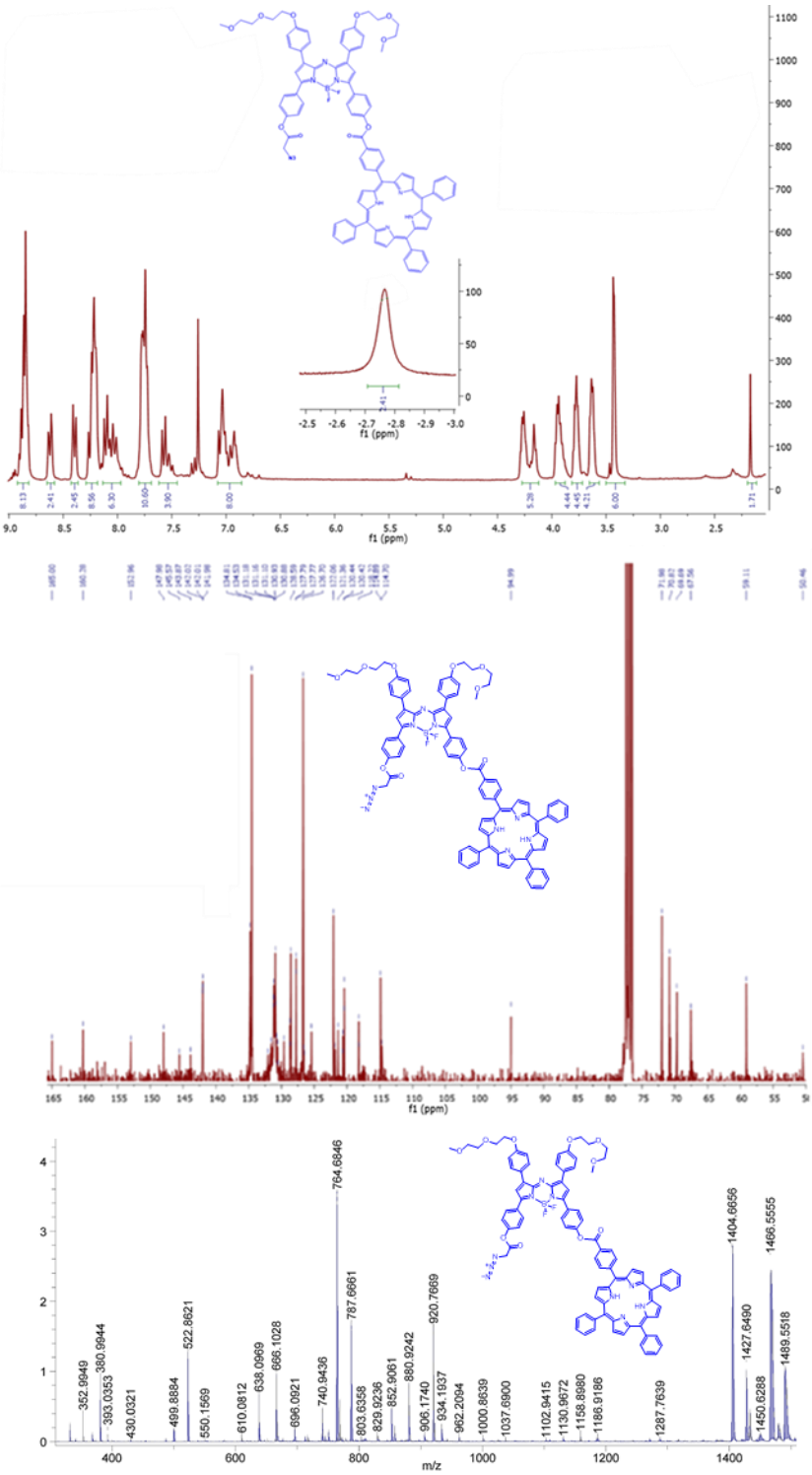

Figure 25. ^{1}H-NMR (top) ^{13}C-NMR (middle), and MALDI-MS (bottom right) of **19**.

Procedure for the synthesis of 20. Zinc acetate (20 mg) in 2 ml of MeOH was added to a solution of **19** (20 mg) in DCM (8 mL) at room temperature and stirred under N_2 atmosphere.

The reaction was stirred overnight. After that the solvent was evaporated under vacuum, the residue was dissolved in DCM (20 mL) and washed with H_2O (2 x 50 mL). Finally the solvent was dried over $MgSO_4$ and evaporated in vacuo. Yield 95%. The compound **20** is a dark blue/purple solid. Spectroscopic data for **20**. ^{1}H NMR (300 MHz, $CDCl_3$) δ 8.96 (s, 8H), 8.61 (d, *J* = 7.9 Hz, 2H), 8.40 (d, *J* = 6.8 Hz, 2H), 8.31 – 7.85 (m, 15H), 7.78 (s, 11H), 7.53 (m, 3H), 6.98 (m, 8H), 4.19 (s, 1H), 3.89 (s, 4H), 3.74 (s, 4H), 3.60 (s, 4H), 3.40 (s, 6H), 2.34 (s, 2H). ^{13}C NMR (75 MHz, $CDCl_3$) δ 165.12, 165.05, 164.62, 160.20, 159.72, 158.06, 152.98, 150.38, 150.27, 150.20, 149.48, 148.74, 143.80, 142.71, 134.70, 134.41, 132.38, 132.28, 132.16, 132.08, 132.01, 131.46, 131.15, 130.90, 130.88, 130.74, 129.55, 128.44, 127.53, 126.76, 126.55, 125.42, 122.04, 121.80, 121.55, 121.35, 119.24, 115.94, 114.86, 114.68, 110.00, 77.00, 71.82, 70.65, 70.59, 69.68, 69.61, 67.48, 62.97, 59.52, 58.99, 53.41, 50.41. (Figure 26 shows ^{1}H and ^{13}C-NMR of **20**).

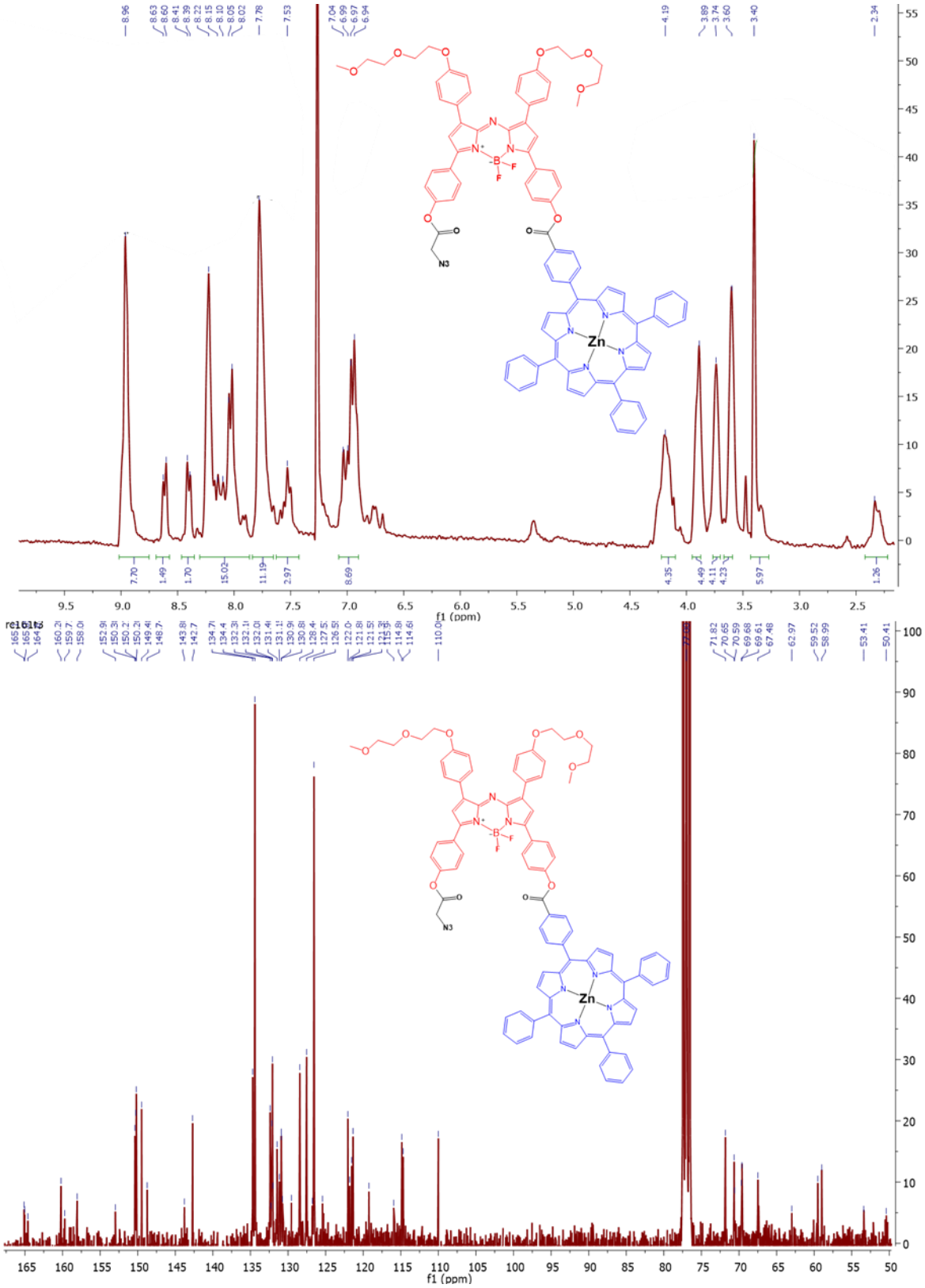

Figure 26. ^{1}H-NMR (top), and ^{13}C-NMR (bottom) of **20**.

Procedure for the synthesis of 21. Diisopropylamine (1.5 ml) was added to a solution of modified graphene **16** (60 mg) and compound **19** (16 mg) in DMSO (16.8 mL) at room temperature and stirred under a N_2 atmosphere. The reaction was stirred during 14 days with occasional sonication. After that period, the reaction mixture was filtered over a PTFE membrane filter (pore size 0.1 μm) and washed with a large amount of dichloromethane to remove completely any organic residual matter. The newly prepared graphene-based hybrid material **21** was obtained as solid and stored under dark.

Procedure for the synthesis of 22. Zinc acetate (10 mg) in 2 ml of MeOH was added to a solution of modified graphene **21** (21 mg) in DCM (8 mL) at room temperature and stirred under a N_2 atmosphere. The reaction was stirred during 2 days with occasional sonication. After that period, the reaction mixture was filtered over a PTFE membrane filter (pore size 0.2 μm) and washed with a large amount of MeOH to remove completely any organic residual impurity. The newly prepared graphene-based hybrid material **22** was obtained as solid and stored under dark.

3.4 CONCLUSION

In this chapter covalent grafting of NIR cyanine dyes **1-4** with exfoliated graphene through aryl diazonium salt reaction, was accomplished, yielding hybrids materials **8** – **11**. All hybrid materials were comprehensively characterized by complementary spectroscopic, thermal and microscopy imaging techniques, while the optical and redox properties were assessed by electronic absorption, fluorescence emission and electrochemistry. Overall, upon photoexcitation electron/energy transfer processes from the dyes to graphene acting as acceptor were observed. Due to these processes the newly prepared graphene-based hybrid materials are attractive in energy-related field.

In addition, NIR azaBDP dyes **13**, **19** and **21**, specifically designed to feature azide units, were synthesized following a multi-step synthetic approach and then reacted with the pre-modified graphene sheets via “click-chemistry” conditions forming hybrid materials **18**, **20** and **22**. The hybrid materials were fully characterized by complementary spectroscopic, thermal and electron microscopy imaging techniques. Furthermore, based on electronic absorption and steady-state and time-resolved photoluminescence spectroscopic assays, deactivation of photoexcited azaBDPs via energy/electron transfer to graphene takes place.

3.5 REFERENCES

1. K. S. Novoselov, A. K. Geim, S. V. Morozov, D. Jiang, Y. Zhang, S. V. Dubonos, I. V. Grigorieva and A. A. Firsov. Electric Field Effect in Atomically Thin Carbon Films. *Science*, **2004**, *306*, 666–669.
2. Y.-M. Lin, C. Dimitrakopoulos, K. A. Jenkins, D. B. Farmer, H.-Y. Chiu, A. Grill and P. Avouris. 100-GHz transistors from wafer-scale epitaxial graphene. *Science*, **2010**, *327*, 662-662.
3. Y. Cheng, H. Zhang, C. V. Varanasi and J. Liu. Improving the performance of cobalt–nickel hydroxide-based self-supporting electrodes for supercapacitors using accumulative approaches. *Energy Environ. Sci*. **2013**, *6*, 3314–3321.
4. M. Bernardi, J. Lohrman, P. V. Kumar, A. Kirkeminde, N. Ferralis, J. C. Grossman and S. Ren. Nanocarbon-Based Photovoltaics. *ACS Nano*. **2012**, *6*, 8896–8903.
5. P. Solís-Fernández, M. Bissett and H. Ago. Synthesis, structure and applications of graphene-based 2D heterostructures. *Chem Soc Rev.* **2017**, *46*, 4572-4613.
6. Y. Hernandez, V. Nicolosi, M. Lotya, F. M. Blighe, Z. Sun, S. De, I. T. McGovern, B. Holland, M. Byrne, Y. K. Gun'Ko, J. J. Boland, P. Niraj, G. Duesberg, S. Krishnamurthy, R. Goodhue, J. Hutchison, V. Scardaci, A. C. Ferrari and J. N. Coleman. High-yield production of graphene by liquid-phase exfoliation of graphite. *Nat. Nanotechnol*. **2008**, *3*, 563–568.
7. (a) A. Stergiou, G. Pagona and N. Tagmatarchis. Donor–acceptor graphene-based hybrid materials facilitating photo-induced electron-transfer reactions. *Beilstein J. Nanotechnol.* **2014**, *5*, 1580–1589; (b) V. Georgakilas, J. N. Tiwari, K. C. Kemp, J. A. Perman, A. B. Bourlinos, K. S. Kim and R. Zbori. Noncovalent Functionalization of Graphene and Graphene Oxide for Energy Materials, Biosensing, Catalytic, and Biomedical Applications. *Chem. Rev.* **2016**, *116*, 5464–5519; (c) K. Dirian, M. A. Herranz, G. Katsukis, J. Malig, L. RodriguezPerez, C. Romero-Nieto, V. Strauss, N. Martin and D. M. Guldi. Low dimensional nanocarbons–chemistry and energy/electron transfer reactions. *Chem. Sci.* **2013**, *4*, 4335–4353; (d) J. Malig, N. Jux and D. M. Guldi. Toward Multifunctional Wet Chemically Functionalized Graphene—Integration of Oligomeric, Molecular, and Particulate Building Blocks that Reveal Photoactivity and Redox Activity. *Acc. Chem. Res.* **2013**, *46*, 53–64.
8. R. J. Chen, Y. Zhang, D. Wang and H. Dai. Noncovalent Sidewall Functionalization of Single-Walled Carbon Nanotubes for Protein Immobilization. *J. Am. Chem. Soc.* **2001**, *123*, 3838−3839.

9. (a) A. Wang, J. Ye, M. G. Humphrey and C. Zhang. Graphene and Carbon-Nanotube Nanohybrids Covalently Functionalized by Porphyrins and Phthalocyanines for Optoelectronic Properties. *Adv Mater*. **2018**, *30*, 1705704-1705713; (b) G. Bottari, M. Á. Herranz, L. Wibmer, M. Volland, L. Rodríguez-Pérez, D. M. Guldi, A. Hirsch, N. Martín, F. D'Souza and T. Torres. Chemical functionalization and characterization of graphene-based materials. *Chem Soc Rev.* **2017**, 46, 4464-4500.

10. F. Iacono, C. Palencia, L. de la Cueva, M. Meyns, L. Terracciano, A. Vollmer, M. J. de la Mata, C. Klinke, J. M. Gallego, B. H. Juarez, R. Otero. Interfacing Quantum Dots and Graphitic Surfaces with Chlorine Atomic Ligands. *ACS Nano.* **2013**, *7*, 2559− 2565.

11. Y. Ge and D. F. O'Shea. Azadipyrromethenes: from traditional dye chemistry to leading edge applications. *Chem. Soc. Rev.* **2016**, *45*, 3846-3864; (b) M. E. El-Khouly, S. Fukuzumi, F. D'Souza. Photosynthetic Antenna–Reaction Center Mimicry by Using Boron Dipyrromethene Sensitizers. *ChemPhysChem.* **2014**, *15*, 30-47.

12. (a) J. Killoran and D. F. O'Shea. Impact of a conformationally restricted receptor on the BF_2 chelated azadipyrromethene fluorosensing platform. *Chem. Commun*. **2006**, *0*,1503-1505; (b) M. J. Hall, L. T. Allen and D. F. O'Shea. *Org. Biomol. Chem*. **2006**, 4, 776-780; (c) H. Li, P. Zhang, L. P. Smaga, R. A. Hoffman and J. Chan. Photoacoustic Probes for Ratiometric Imaging of Copper(II). *J. Am. Chem. Soc.* **2015**, *137*, 15628-15631; (d) A. Dvivedi, S. Kumar, M. Ravikanth, *Sens. Actuators B* **2016**, *224*, 364; (e) W.-J. Shi, R. Menting, E. A. Ermilov, P.-C. Lo, B. Roeder and D. K. P. Nog. Formation and photoinduced processes of the host–guest complexes of a β-cyclodextrin-conjugated aza-BODIPY and tetrasulfonated porphyrins. *Chem. Commun*. **2013**, *49*, 5277-5279.

13. G. FAN, L. YANG and Z. Chen. Front. Water-soluble BODIPY and aza-BODIPY dyes: synthetic progress and applications. *Chem. Sci. Eng.* **2014**, *8*, 405–417.

14. (a) C. J. Ziegler, K. Chanawanno, A. Hasheminsasab, Y. V. Zatsikha, E. Maligaspe and V. N. Nemykin. Synthesis, Redox Properties, and Electronic Coupling in the Diferrocene Aza-dipyrromethene and azaBODIPY Donor–Acceptor Dyad with Direct Ferrocene−α-Pyrrole Bond. *Inorg. Chem.* **2014**, *53*, 4751–4755; (b) A. N. Amin, M. E. El-Khouly, N. K. Subbaiyan, M. E. Zandler, M. Supur, S. Fukuzumi and F. D'Souza. Syntheses, Electrochemistry, and Photodynamics of Ferrocene–Azadipyrromethane Donor–Acceptor Dyads and Triads. *J. Phys. Chem. A* **2011**, *115*, 9810–9819.

15. J. Zhou, L. Gai, J. Mack, Z. Zhou, H. Qiu, K. S. Chan and Z. Shen. Synthesis and photophysical properties of orthogonal rhodium(III)–carbon bonded porphyrin–aza-BODIPY conjugates *J. Mater. Chem. C*, **2016**, *4*, 8422-8428.

16. X.-D. Jiang, D. Xi, C.-l. Sun, J. Guan, M. He and X. L.-Jiu. Synthesis of a pyrene-fused aza-BODIPY as a near-infrared dye having the absorption maximum at 746 nm. *Tetrahedron Letters*, *56*, **2015**, 4868-4870; (b) N. Balsukuri, N. Boruah, P. E. Kesavana and I. Gupta. Near infrared dyes based on pyrene aza-BODIPYs. *New J. Chem.* **2018**, *42*, 5875-5888.

17. V. Bandi, H. Babon, G. F. D'Souza. Ultrafast Photoinduced Electron Transfer and Charge Stabilization in Donor–Acceptor Dyads Capable of Harvesting Near-Infrared Lig. *Chem. Eur. J.* **2015**, *21*, 11483–11494.

18. (a) B. Grimm, J. Schornbaum, H. Jasch, O. Trukhina, F. Wessendorf, A. Hirsh, T. Torres and D.M. Guldi. *Proc. Natl. Acad. Sci. U.S.A.* **2012**, *109*, 15565-15571; (b) T. H. Ngo, D. Zieba, W. A. Webre, G. N. Lim, P.A. Karr, S. Kord, S. Jin, K. Ariga, M. Galli, S. Goldup, J. P. Hill and Francis D'Souza. Copper corrole, Zn-porphyrin fullerene photoinduced charge separation. Engaging Copper(III) Corrole as an Electron Acceptor: Photoinduced Charge Separation in Zinc Porphyrin–Copper Corrole Donor–Acceptor Conjugates. *Chem. Eur. J.* **2016**, *22*, 1301 – 1312.

19. S. K. Das, N. K. Subbaiyan, F. D'Souza, A.S.D. Sandanayake, T. Wakahara and O. Ito. Formation and photoinduced properties of zinc porphyrin-SWCNT and zinc phthalocyanine-SWCNT nanohybrids using diameter sorted nanotubes assembled via metal-ligand coordination and π–π stacking. *J. Porphyr. Phthalocyanines* **2011**, *15*, 1033–1043.

20. A. Stergiou, H. B. Gobeze, I. D. Petsalakis, S. Zhao, H. Shionhara, F. D'Souza and N. Tagmatarchis. Oligothiophene/graphene supramolecular ensembles managing light induced processes: preparation, characterization, and femtosecond transient absorption studies leading to charge-separation. *Nanoscale* **2015**, *7*, 15840- 15851.

21. E. Bekyarova, M. E. Itkis, P. Ramesh, C. Berger, M. Sprinkle, W. A. de Heer and R. C. Haddon. Chemical Modification of Epitaxial Graphene: Spontaneous Grafting of Aryl Groups. *J. Am. Chem. Soc.* **2009**, *131*, 1336-1337.

22. (a) A. C. Ferrari, J. C. Meyer, V. Scardaci, C. Casiraghi, M. Lazzeri, F. Mauri, S. Piscanec, D. Jiang, K. S. Novoselov, S. Roth and A. K. Geim. Raman Spectrum of Graphene and Graphene Layers. *Phys. Rev. Lett.* **2006**, *97*, 187401-187404; (b) A. Gupta, G. Chen, P. Joshi, S.

Tadigadapa and P. C. Eklund. Raman Scattering from High-Frequency Phonons in Supported n-Graphene Layer Films. *Nano Lett.* **2006**, *6*, 2667-26673.

23. A. Stergiou and N. Tagmatarchis. Fluorene–Perylene Diimide Arrays onto Graphene Sheets for Photocatalysis. *ACS Appl. Mater. Interf.* **2016**, *8*, 21576-21584; (b) N. Karousis, J. Ortiz, K. Ohkudo, T. Hasobe, S. Fukuzumi, A. Sastre-Santos, N. Tagmatarchis. Zinc Phthalocyanine–Graphene Hybrid Material for Energy Conversion: Synthesis, Characterization, Photophysics, and Photoelectrochemical Cell Preparation. *J. Phys. Chem. C* **2012**, *116*, 20564-20573.

24. Y. Liu, N. Song, Z. Lib, L. Chen and Z. Xie. Near-infrared nanoparticles based on aza-BDP for photodynamic and photothermal therapy. *Dyes Pigm.* **2019**, *160*, 71-78.

CHAPTER 4

Modification of transition metal dichalcogenides

ABSTRACT

The covalent functionalization of wet exfoliated semiconducting MoS_2 by 1,2-dithiolanes bearing an ethylene glycol alkyl chain terminated to a butoxycarbonyl-protected amine and a photoactive pyrene moiety was accomplished. The MoS_2-based nanohybrids were fully characterized by complementary spectroscopic, thermal and microscopy techniques. Markedly, density functional theoretical studies combined with XPS analysis demonstrated preferential edge functionalization, primarily via sulfur addition along partially sulfur saturated zig-zag MoS_2 molybdenum-edges, preserving intact the 2D basal structure as confirmed by high resolution transmission electron microscopy and electron energy loss spectroscopy. Based on steady-state and time-resolved photoluminescence spectroscopy assays, appreciable excited state electronic interactions between the photoactive pyrene and the semiconducting MoS_2, within the MoS_2-pyrene hybrid, were identified. Furthermore, a detailed study on the wet exfoliation of MoS_2 revealed that N-methyl-2-pyrrolidone, usually employed as solvent in the process, was susceptible to chemical degradation, giving rise to strong photoluminescence and interfering with the optical properties of MoS_2.

4.1 INTRODUCTION

Transition metal dichalcogenides (TMDs) are layered nanomaterials consisting of an atomic plane of a transition metal sandwiched by two atomic planes of chalcogens. Bulk TMDs are semiconductors with an intrinsic band-gap and exhibit noteworthy optical and electronic properties desirable for energy storage and conversion,[1-7] photodynamic/photothermal therapy[8,9] and sensing.[10-12] However, despite the close similarity of TMDs to graphene, they offer significant advantages related to their band-gap dependent electronic properties,[13, 14] which can be tuned by altering the transition metal and/or the chalcogen composition. In this context, it is imperative the functionalization of TMDs, permitting their better manipulation and processing in wet media by improving solubility in common organic solvents.

Diverse methodologies for exfoliating TMDs from the bulk exist, giving access predominantly to the metallic polytype lattice structure with octahedral coordination geometry.[15-21] Notably, NMP is the prototypical solvent for the dispersion of a wide range of carbon nanomaterials including graphene,[22] fullerenes,[23] and nanotubes[24]. This general applicability of NMP is attributed to the matching of surface tension and Hansen solubility parameters with those carbon-based nanomaterials,[25-27] resulting in low enthalpy of mixing, hence allowing individualization and/or debundling of nanotubes and exfoliation of graphene followed by their dispersion at high concentration. Consequently, there is renewed interest in employing NMP for 2D materials beyond graphene and liquid exfoliation of MoS_2 and WS_2. However, while clearly an effective solvent, NMP is also known to be very susceptible to sonochemical polymerization[28] and degradation[29] under the standard processing techniques for exfoliation of 2D materials. In addition, the yield and degree of exfoliation of TMDs are also sensitive to the concentration of dissolved oxygen and water present in the solvent.[29-31] The process involves chemical modification of NMP, generating degradation and polymerization products, which are difficult to characterize and maybe present as residual contaminants which influence the properties of the exfoliated 2D nanosheets. The influence of degradation during exfoliation may lead to considerable variation of the performance of NMP as a solvent for TMDs (as well as other nanomaterials) and potentially skewing of the measured optical properties and solubility

parameters of TMDs towards those of pristine NMP. Furthermore, it should be pointed out that the optical properties of NMP are also influenced by its degradation, with yellowing of the solvent usually attributed to increased scattering and of sonication products.[28] In addition, optical spectroscopy of NMP dispersions is further complicated, albeit rarely acknowledged in the literature on manomaterials, by weak photoluminescence of the solvent.[32,33]

Exfoliation with chlorosulfonic acid is an alternative methodology to obtain semiconducting MoS_2 or WS_2, in which the individual layers of the TMDs are protonated by the superacid, however, without being oxidized, and kept apart due to developed electrostatic repulsive interactions.[34] Nevertheless, despite the progress achieved so far with the exfoliation of MoS_2, its covalent functionalization is underdeveloped. In fact, the limited functionalization procedures reported to date mainly utilize exfoliated MoS_2 of the metallic polytype 1T, obtained by treatment with n-butyl lithium (n-BuLi), in which the negative charges on MoS_2 due to charge-transfer from n-BuLi, are quenched by diazonium salts[21] and alkyl halides.[35] Conversely, functionalization of semiconducting 2H-MoS_2 is achieved via conjugation of thiols at sulfur vacancies[20, 36-39] and metal carboxylate salts coordination to surface sulfur atoms.[40] Therefore, it is absolutely desirable and timely to develop new functionalization routes for semiconducting MoS_2 species and equally important to understand where and how functionalization occurs.

Herein, the degradation effect of different NMP samples employed for the sonochemical exfoliation of MoS_2 and its implication in the optoelectronic properties was examined. Additionally, the covalent functionalization of exfoliated semiconducting MoS_2 by 1,2-dithiolane derivatives was accomplished. Moreover, the location ("where") and the manner ("how") this functionalization occurs, based on density functional theoretical studies supported by X-ray photoelectron spectroscopy (XPS) and confirmed by high-resolution transmission electron microscopy (HRTEM) imaging and electron energy loss spectroscopy (EELS) was reported. Notably, the 1,2-dithiolane component possesses high binding affinity for Mo atoms, particularly those located at the edges of the corresponding TMDs, where sulfur vacancy sites were naturally introduced after chemical exfoliation from the bulk.[9] Such a facile approach for the chemical functionalization of MoS_2 offers the advantage of keeping intact the basal plane of MoS_2 and preserving to great extent their novel surface properties as well as their semiconducting character, while also allows the incorporation of a plethora of suitably modified organic

derivatives targeting diverse applications. Importantly, the presence of defects at the edges of MoS_2, as generated by either chemical exfoliation[20, 36-41] or ion irradiation,[42] guarantees the universal utility and versatility of the functionalization route. The newly derived MoS_2-based nanohybrids were fully characterized, while their optical properties were examined.

4.2 RESULTS AND DISCUSSION

Despite NMP being an excellent solvent for handling 2D nanomaterials, it suffers from degradation generating polymerized byproducts, which influence the properties of the examined nanosheets. These NMP degradation products emit in the same region where the excitonic bands of MoS_2 appear, handicapping correct assignment and bringing difficulties in proper spectroscopic characterization. In order to provide sufficient evidence to justify the undesired effect of NMP, we spectroscopically investigated its optical properties by screening samples of different ages and their behavior under sonication conditions. In more detail, Figure 1a shows UV-Vis absorption spectra for NMP samples stored in closed containers, in the dark and under ambient conditions for one, four and nine years. The samples were not externally treated in any way. Similar discoloration was also observed for sonicated NMP as well as produced from as-received NMP (HPLC grade, >99% purity). It is evident that such changes arise from increased optical absorption in the wavelength range below 450 nm. Given that NMP has been reported to be weakly photoluminescent,[32] the samples were illuminated with a 405 nm laser. Under this excitation, all samples were observed to exhibit strong blue-green photoluminescence with intensity clearly increasing with both ageing and sonication of the NMP, as shown in the inset photographs in Figure 1a.

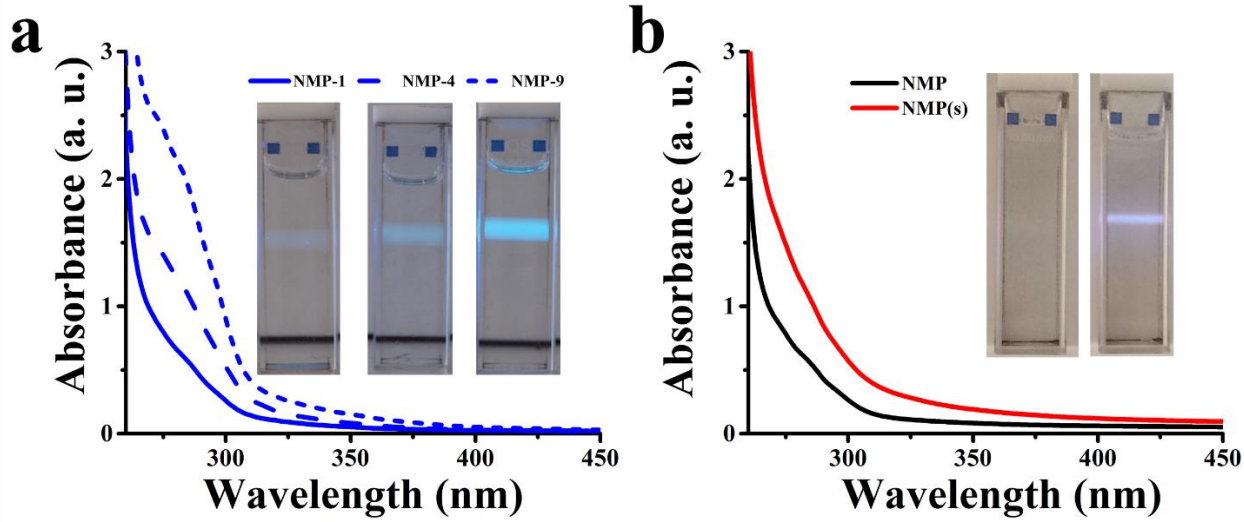

Figure 1. (a) UV-Vis absorption spectra of NMP showing absorbance below 450 nm increasing with the age of the NMP, from NMP-1 to NMP-9. Inset: Photographs of NMP-1, NMP-4 and NMP-9 exhibiting strong blue-green photoluminescence under illumination with 405 nm laser pointer. (b) UV-Vis absorption spectra for as-received NMP (black) and sonicated NMP (red).

In order to ascertain the extent of the emission from the new species, photoluminescence spectroscopy was performed to obtain photoluminescence excitation (PLE) maps containing all excitation and emission spectra (Figure 2a and b). These PLE maps indicated that NMP exhibits broad photoluminescence with peak emission around 400 nm under excitation at 325 nm. In addition, the spectroscopic changes after sonochemical degradation were illustrated by changes in the intensity of photoluminescence. For any given excitation wavelength, the peak intensity increased with the age of the NMP, resulting in the increasing brightness shown in the photographs in Figure 1. The as-received NMP exhibited only very weak photoluminescence, with Raman features observed as prominently as the photoluminescence peaks. For sonicated NMP, the photoluminescence intensity was increased by an order of magnitude with appreciable emission across the whole visible spectrum.

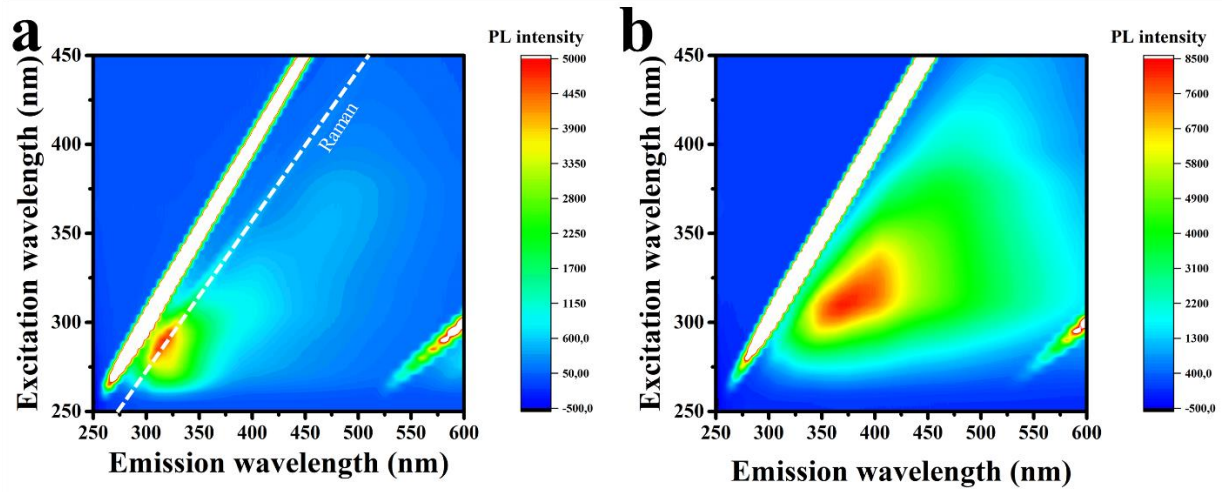

Figure 2. Photoluminescence excitation maps for (a) NMP and (b) sonicated NMP.

While the differences in absorbance between the samples were small, the differences in photoluminescence intensity were significant and therefore not simply due to the increasing absorbance. This suggests that the increasing photoluminescence was due to the emergence of new species whose concentration or photoluminescence efficiency increases with degradation. The photoluminescence spectra for peak emission (λ_{em} = 400 nm, λ_{exc} = 325 nm) of NMP and sonicated NMP are shown in Figure 3 and can be fitted as the sum of two components at approximately 380 nm and 440 nm. These two photoluminescence components correspond to two emission species in the samples. When excited at lower energy than one or both of the species, as is common for photoluminescence measurements of 2D materials, the breadth of the features resulted in a red-shifted contribution of that feature to the photoluminescence spectrum. This was illustrated by the significant photoluminescence intensity shown in the PLE maps for long wavelength excitation of sonicated NMP. The emission was dominated by the feature at 440 nm, which showed an apparent red-shift with increasing excitation wavelength and could result in secondary excitation of the dispersed nanomaterial.

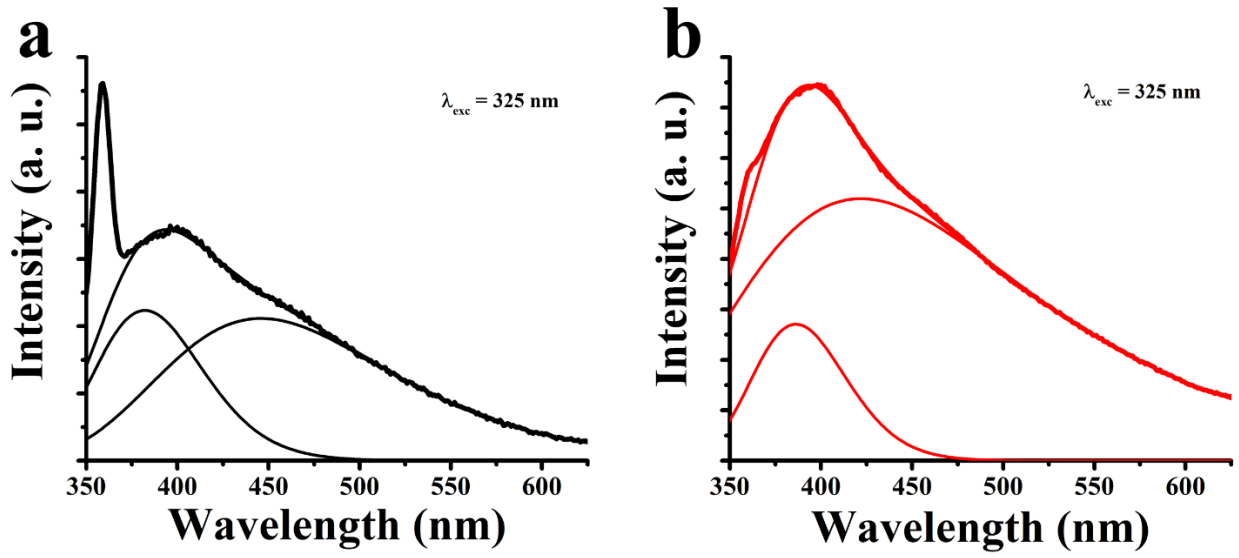

Figure 3. Photoluminescence spectra for peak emission with λ_{exc} = 325 nm for (a) NMP and (b) sonicated NMP, showing two component fitting with features at around 380 nm and 440 nm, the latter of which dominates photoluminescence emission in the sonicated NMP. Note the presence of broadened Raman feature at 358 nm (~2900 cm^{-1}), which has been excluded from the peak fitting.

The individual spectra of aged samples, showed a progressive enhance of the photoluminescence emission spectra with their antiquity at 405 nm excitation, suffering small changes when the spectra were recorded at 340 nm (Figure 4). Note the intensity increase at the same excitation wavelength as for the photographs under laser excitation in Figure 1 and the instrument-broadened Raman features at ~460 nm, which were neglected from the curve fitting. This fact clearly showed that the decomposition has strong relation with the age of the NMP even in under ambient conditions.

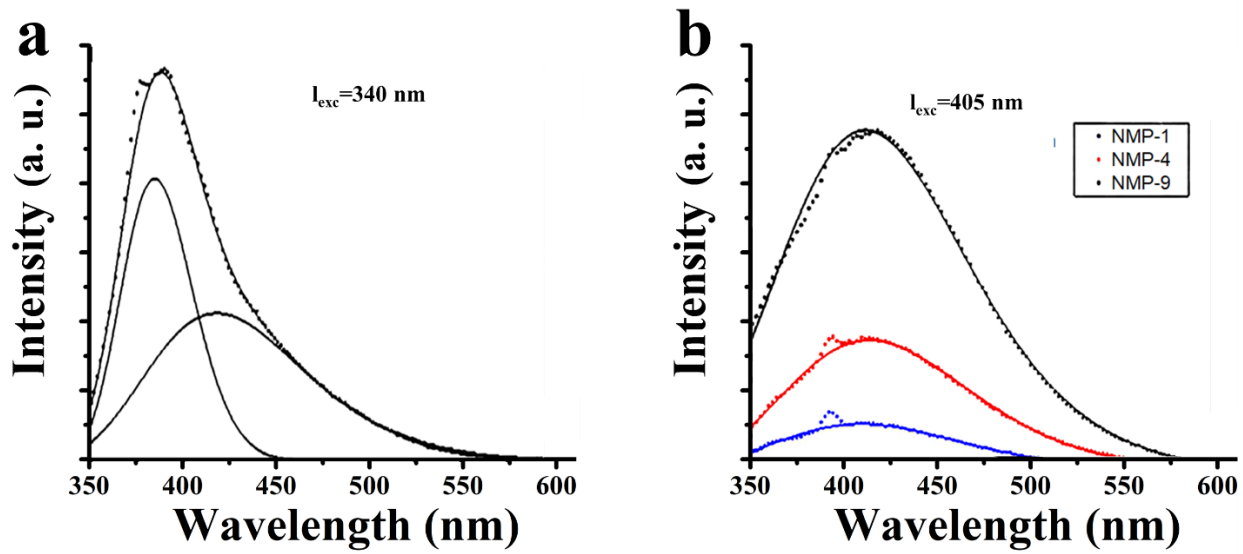

Figure 4. (a) Photoluminescence spectrum of NMP-1 for 340 nm excitation with two-component fitting confirming spectroscopically similar emission to that of NMP and sonicated NMP. (b) Photoluminescence spectrum of aged NMP for 405 nm excitation with single component fitting due to excitation of only the lower energy species in the samples.

Time-resolved photoluminescence spectroscopy was performed to provide characterization of the photoluminescence lifetimes of the species in the NMP samples. Figure 5 shows time-resolved photoluminescence measurements with excitation wavelength of 336 nm at an emission wavelength of 400 nm, chosen to be as comparable as possible with the steady-state spectra shown above. It is evident that the total photoluminescence lifetime was significantly increased for sonicated NMP compared with NMP. These time-correlated emission measurements can be fitted as the sum of exponential components, as shown in Figure 5, where both samples were found to have a short-lived species with lifetime around 1 ns and a longer-lived species with lifetime around 5 ns. In addition, sonicated NMP was found to have a third component with significantly greater lifetime of 19 ns. The relative abundances of the two shorter-lived species indicated that they likely correspond to the two components from the steady-state data, while the longer-lived species in sonicated NMP was a much smaller contribution, which was not identified in the steady-state fitting. In addition, the increase in the individual component lifetimes could suggest that the photoluminescence observed in as-received NMP was not due to the pristine NMP but due to the onset of ambient degradation. Greater delocalization of the

electron-hole pair in the excited state led to the observed increase in the excited state lifetime. As such, the overall increase in lifetime with degradation is consistent with the formation of a larger, possibly polymerized, species.

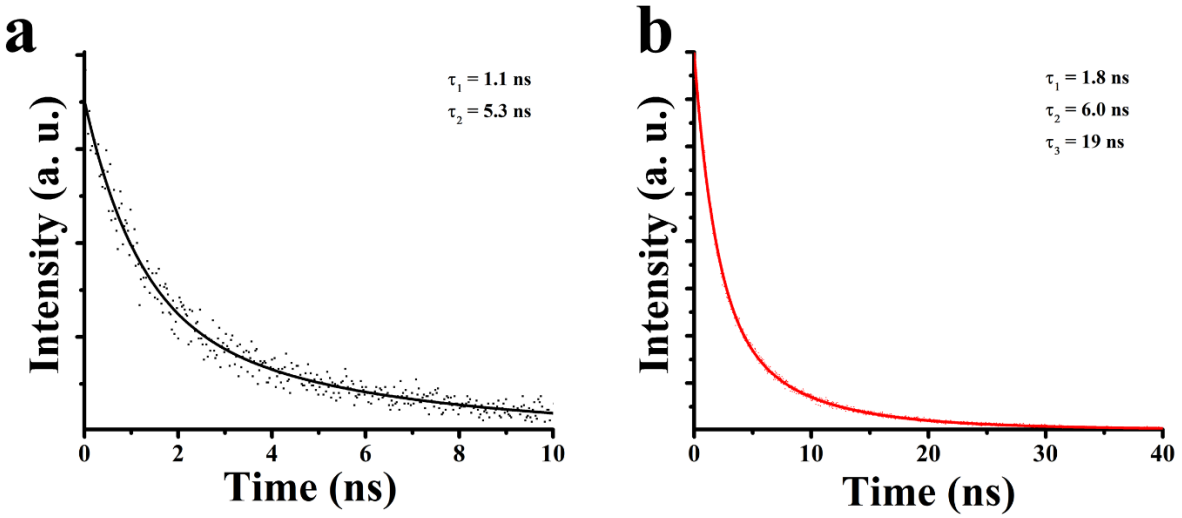

Figure 5. Time-resolved photoluminescence measurements of (a) NMP and (b) sonicated NMP for emission at 400 nm under excitation at 336 nm, fitted as the sum of exponential components, whose time constants are shown inset, with increased lifetimes and an additional component present in sonicated NMP.

Subsequently, ^{1}H NMR spectroscopy was performed to identify any covalently-modified species which were present at trace. In addition to the expected proton peaks for the NMP, the NMR spectra show a number of peaks present at around 0.1% by number. The peaks with chemical shifts of around 5 ppm in Figure 6 were attributed to alkenyl protons, suggesting the formation of R-C=CH_2 species, while the peaks around 0.9 ppm corresponded to protons in a methyl group. These characteristic features were also observed in a previous study of sonochemical degradation of NMP which proposed a mechanism for formation of an enamine species (-N-C=C-) which underwent polymerisation to form oligomeric nanoparticles.[28] The observation of similar features in the NMR spectra suggested that this mechanism could describe degradation due to both sonication and ageing. Furthermore, the presence of these features in the NMR spectra of all samples suggests that any degradation product was also present, at lower concentration, in the as-received NMP. Notably, the alkenyl and methyl protons associated with the previously-proposed

mechanism of enamine formation and polymerization, were present and show downfield shifts relative to the as-received NMP. This is consistent with the downfield shifting of peaks expected due to deshielding by a nearby π-system, which could be a conjugated species, giving rise to the absorption and photoluminescence in both aged and sonicated NMP.

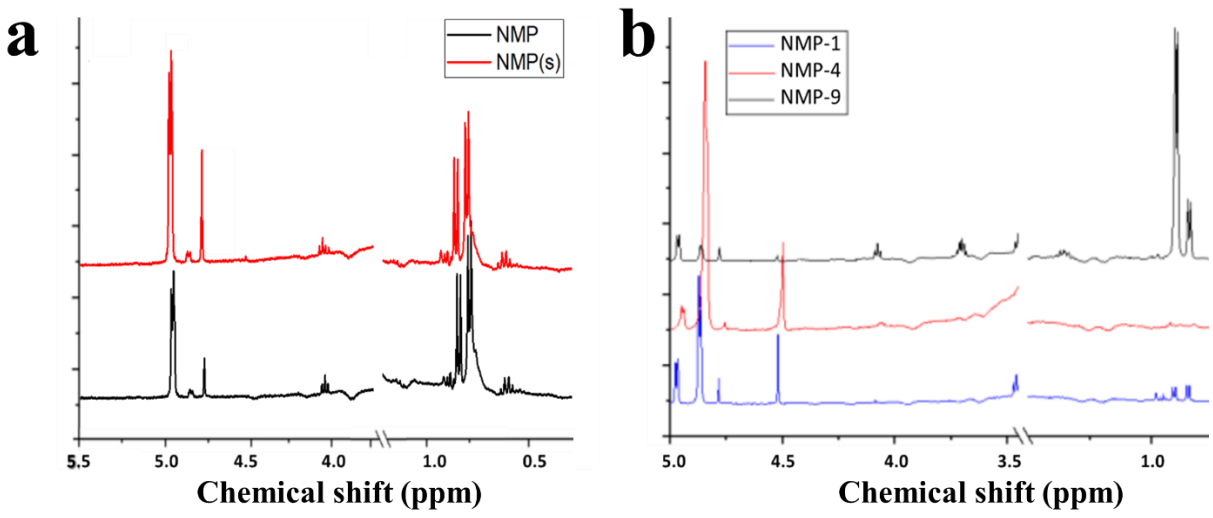

Figure 6. ^{1}H NMR spectra showing proton environments in NMP additional to those of the unmodified molecule with features corresponding to alkenyl species at a chemical shift of 5 ppm at around 0.1% (a) by number relative to the unmodified NMP molecules, (b) increasing intensity from the as-received to the sonicated NMP.

To illustrate the influence of NMP degradation, the photoluminescence spectrum for MoS_2 exfoliated into NMP for excitation at 450 nm is shown in Figure 7a. High quality of semiconducting MoS_2 dispersions typically show weak photoluminescence since emission is only from monolayer nanosheets and self-absorbance reduces the outgoing signal. As such, the photoluminescence spectrum shows features at low intensity corresponding to A and B exciton photoluminescence at ~680 nm and ~625 nm, respectively. The intense broad feature at ~530 nm is not due to the MoS_2 but is instead due to the NMP, observed at longer wavelength under excitation at 450 nm. To confirm this, the MoS_2 dispersion was centrifuged at high speed to sediment the nanosheets out of the dispersion. The NMP was then discarded and the material was redispersed into aqueous surfactant solution in a manner similar to liquid cascade centrifugation.[43] Figure 7b shows the photoluminescence spectrum for the dispersion of MoS_2 in

surfactant and water. The broad background due to the feature at ~530 nm is no longer present, confirming that it is indeed photoluminescence from the degraded NMP, and the spectrum shows only the photoluminescence from the MoS_2, albeit dominated by the B exciton due to self-absorbance by multilayers in the range of the A exciton. Together these spectra demonstrate the influence of NMP degradation on the photoluminescence spectra of liquid-exfoliated TMDs and present a potential route, through sedimentation and redispersion, to transfer nanomaterials into fresh or different solvents to minimize the influence of solvent degradation on spectroscopy of 2D materials.

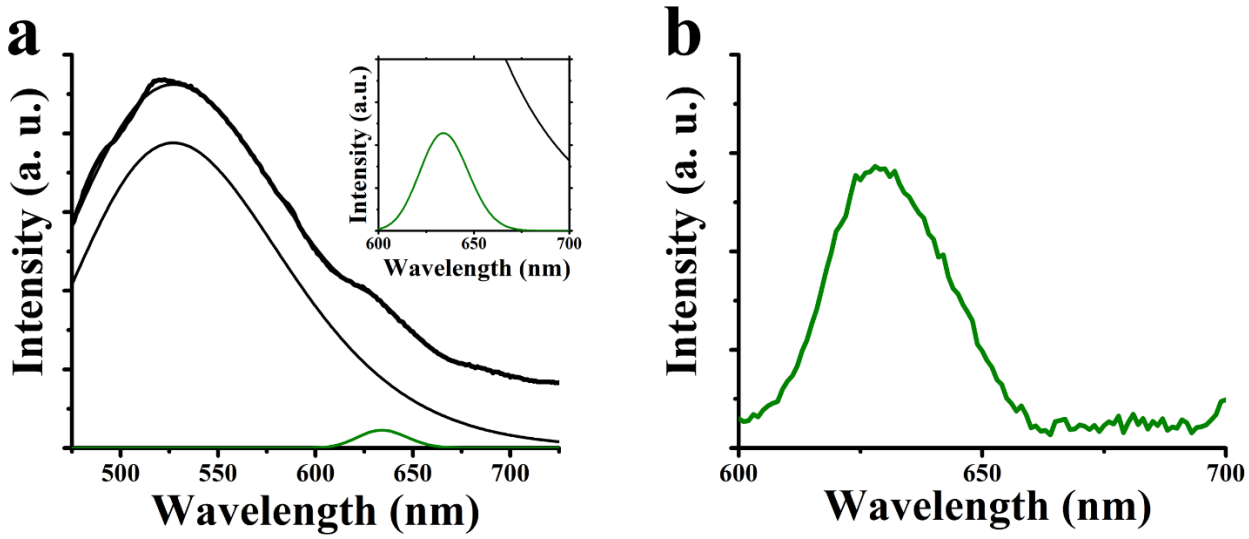

Figure 7. (a) Photoluminescence spectra for MoS_2 showing emission of NMP considerably more prominent than, and overlapping with, emission of MoS_2. Inset: expanded view of the same spectrum showing A and B exciton photoluminescence of MoS_2. (b) Photoluminescence spectrum of MoS_2 after centrifugation and redispersion into surfactant and water, showing the absence of the broad background NMP photoluminescence.

Having resolved the issue with NMP and associated problems, exfoliated semiconducting 2H-MoS_2 was prepared from the bulk upon chlorosulfonic acid treatment.[34] Next, the functionalization of exfoliated 2H-MoS_2 by 1,2-dithiolane derivatives bearing either an ethylene glycol alkyl chain terminated to a butoxycarbonyl (BOC)-protected amine **1a** or a pyrene **1b** as an electron donor was accomplished (Figure 8). The functionalized MoS_2-based nanohybrids **2** were found to be soluble in DMF, ca. 1.2 mg/mL, while their solubility in dichloromethane,

acetone and THF was limited. The so-derived MoS_2-based nanohybrids can be stored in DMF for months, without observing precipitation, hence justifying their stability in wet media. Treatment of **2a** with gaseous HCl results in cleaving the BOC-protecting group, yielding the cationic ammonium derivatized MoS_2-based material **2c**, soluble in protic solvents and aqueous media. The amino-loading of **2c** was calculated by performing the Kaiser test and found to be 103 μmol/g.

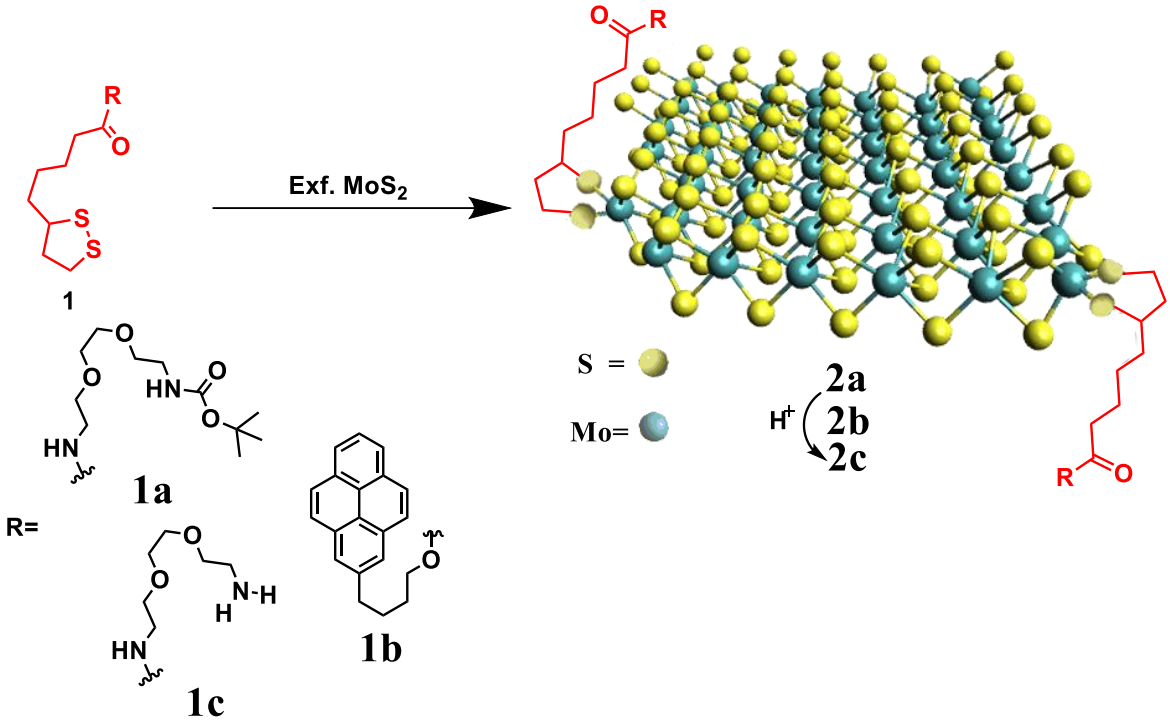

Figure 8. Reaction route for obtaining functionalized MoS_2-based nanohybrids **2** from exfoliated semiconducting MoS_2 flakes.

The MoS_2-based nanohybrids **2a-c** were fully characterized by complementary spectroscopic, thermal and electron microscopy techniques. Markedly, the functionalization appears to primarily occur via sulfur addition along partially sulfur-saturated zig-zag MoS_2 molybdenum-edges. Complementary density functional studies combined with XPS analysis demonstrated the preferential edge functionalization, preserving the 2D basal structure of the functionalized MoS_2-based nanohybrids as confirmed by HRTEM imaging and EELS. This is an extremely important finding, shedding ample light on the location and the manner the functionalization of exfoliated

2H-MoS_2 with 1,2-dithiolanes proceeds, hence allowing the design and development of a plethora of interesting hybrid materials for diverse applications - see Chapters 4 and 5.

In more detail, the developed functionalization largely deviates from recent studies based on thiol reactions, which were shown to oxidize to the corresponding disulfides which eventually only adsorb onto MoS_2.[44] With our experimental protocol, a mixture of exfoliated MoS_2 and 1,2-dithiolane derivatives **1a** or **1b** in DMF was stirred at 70 ^{o}C for 36 hours. Then, the reaction mixture was filtered over a PTFE membrane (0.1 μm pore size) and the solid residue collected onto the filter was extensively washed with dichloromethane to remove organic impurities, yielding MoS_2-based nanohybrids **2**. The strong binding of the organic addends on the MoS_2 was proved by examining their electronic absorption profile after extensive washing cycles to remove any loosely bound (physisorbed) organic compound. Evidently, after four consecutive washing cycles, the UV-Vis spectrum of functionalized MoS_2-based materials **2** remained unaffected, namely the characteristic absorptions due to pyrene as well as due to the MoS_2 retained their intensity, while also the filtrate failed to show characteristic absorptions due to the pyrene species.

Attenuated-total-reflectance IR assays gave spectroscopic proof for the success of the functionalization. Briefly, strong C-H stretching and bending modes are discernible in the 2840-2970 cm^{-1} range, while the ethylene glycol unit gives rise to vibrational modes in the region 1130-1190 cm^{-1} for functionalized materials **2**. Particularly for **2a**, two carbonyl moieties are identified at 1650 and 1710 cm^{-1} owed to the amide and BOC protecting units, respectively - the latter is absent in the IR spectrum of **2c**, in which free amine functionalities are present - while for **2b**, only the ester carbonyl is identified at 1730 cm^{-1} (Figure 9a and b).

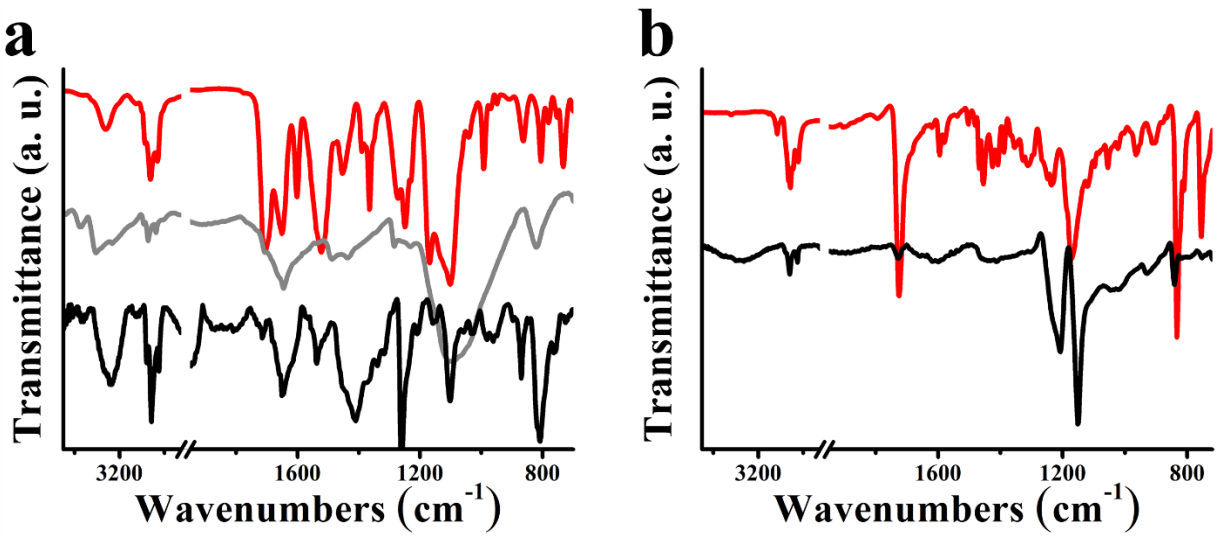

Figure 9. ATR-IR spectra for (a) 1,2-dithiolane derivative **1a** (red) and functionalized MoS_2-based hybrids **2a** (black) and **2c** (grey), and (b) 1,2-dithiolane derivative **1b** (red) and MoS_2-pyrene hybrid **2b** (black).

Next, Raman spectroscopy was employed as a valuable tool to obtain meaningful insight on the functionalization of MoS_2 with 1,2-dithiolanes. Upon in-resonance excitation at 633 nm, more rich spectra as compared with those when measurements conducted under off-resonance conditions at 514 nm were acquired. Upon comparison of the Raman spectra for functionalized MoS_2 with those owed to exfoliated MoS_2 flakes, the following points are deduced: (a) the intensity of the 2LA(M) mode at 447 cm^{-1} was decreased for the functionalized MoS_2 nanohybrids, for spectra normalized at the A_{1g} mode located at 404 cm^{-1}, in accordance with Raman studies performed on differently functionalized MoS_2 species,[21] and (b) phonon modes directly related to the metallic polytype of MoS_2 at 150, 225 and 325 cm^{-1},[45, 46] were totally absent, hence proving the semiconducting nature of MoS_2 in the functionalized nanohybrids **2**. The Raman spectrum for **2b** and **2c** are shown in Figure 10.

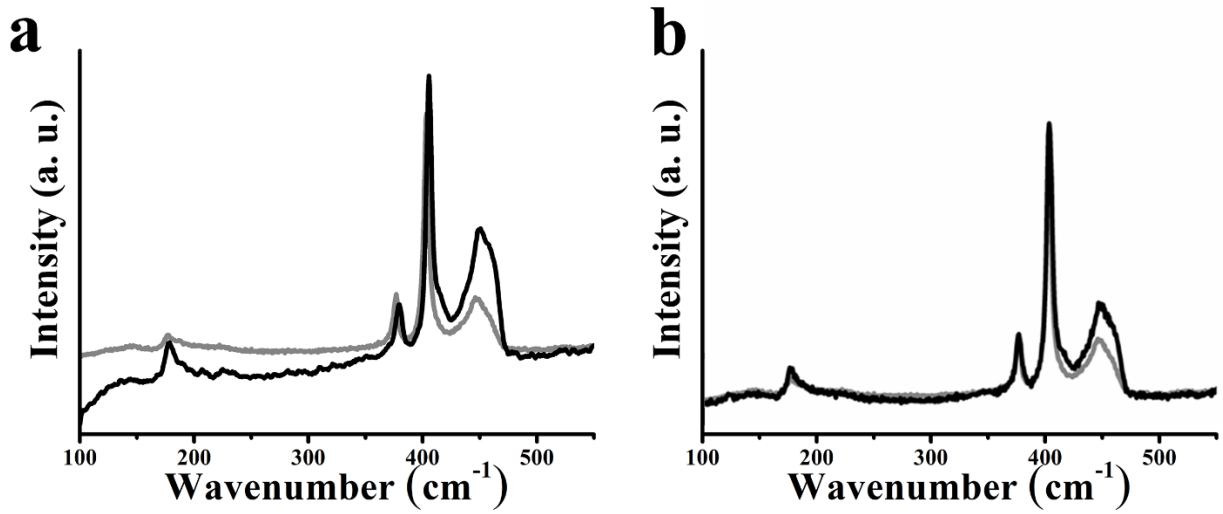

Figure 10. Raman spectra (633 nm) (a) exfoliated semiconducting 2H-MoS_2 (gray) as compared with functionalized MoS_2-pyrene **2b** (black), and (b) exfoliated semiconducting 2H-MoS_2 (gray) as compared with nanohybrid **2c** (black).

Additional proof for the success of the covalent functionalization of MoS_2 with 1,2-dithiolane derivatives **1a** and **1b** was delivered by thermogravimetric analysis (TGA). Exfoliated MoS_2 is thermally stable up to 250 °C under nitrogen atmosphere. However, in MoS_2-based nanohybrid **2b** an 8.1 % mass loss in the temperature range 250-550 °C was observed (Figure 11a). The latter is attributed to the thermal decomposition of the organic functionalities covalently bonded to Mo at the edges of MoS_2, i.e. at sulfur vacancies. Actually, the loading of one pyrene moiety onto MoS_2 was calculated to be one per every thirty-two MoS_2 units. Similarly, from the TGA for **2a** (Figure 11b), the loading of one organic addend per every twenty-four MoS_2 units was calculated. Markedly, the relatively low mass loss observed in the TGA for nanohybrids **2** clearly proves that the organic functionalities were covalently anchored onto MoS_2, contrasting the case where physisorption occurs, in which the coverage of MoS_2 is very high reaching a loading of one organic unit per every two Mo atoms.[44]

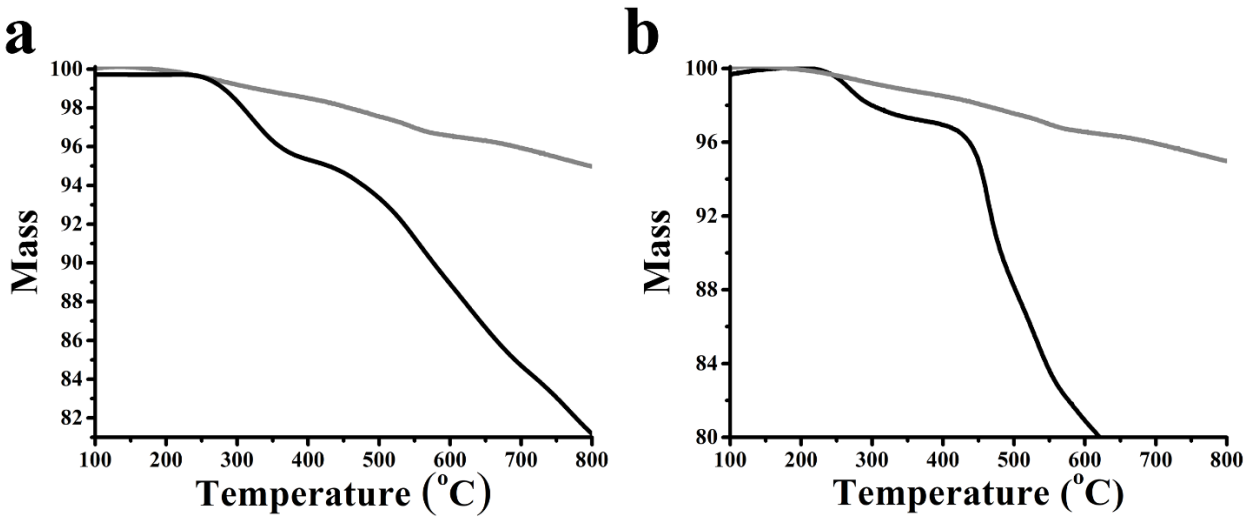

Figure 11. Thermographs for (a) exfoliated MoS_2 (gray) and functionalized MoS_2-pyrene **2b** (black), and (b) exfoliated MoS_2 (gray) and functionalized MoS_2-based nanohybrid **2c**, obtained under nitrogen atmosphere.

Examining the morphology of the functionalized materials, HR-TEM images revealed that the flakes of MoS_2-pyrene **2b** vary from single- to oligo-layer, with largely damage-free basal plane (Figure 12a and b). Although the edge structure was difficult to be determined conclusively, there is evidently strong preference for zig-zag edge orientation, consistent with theoretical predictions[47, 48] and experimentally observed structures,[48, 49] suggesting that 50% S and 100% S saturated zig-zag molybdenum-edges should be thermodynamically preferred.[49-51] The HR-TEM images also showed the presence of material at the edges, which may correspond to carbonaceous species. In order to investigate that point, spatially-resolved EELS studies were carried out. In more detail, Figure 12c displays the EEL spectrum recorded in a region close to the edge of a flake belonging to functionalized MoS_2-pyrene **2b** nanohybrid - see also high-angular annular dark field (HAADF) scanning TEM (STEM) image displayed as inset of Figure 12c. Apart from the expected Mo and S contributions, the C-K edge was visible. The fine structure of this C-K signal (shown in Figure 12d) includes a significant π* pre-peak, consistent with attribution to the organic addend incorporated in **2b** hybrid material and different to the one of amorphous carbon, further proving the success of functionalization of semiconducting MoS_2 with pyrene species.[52-54]

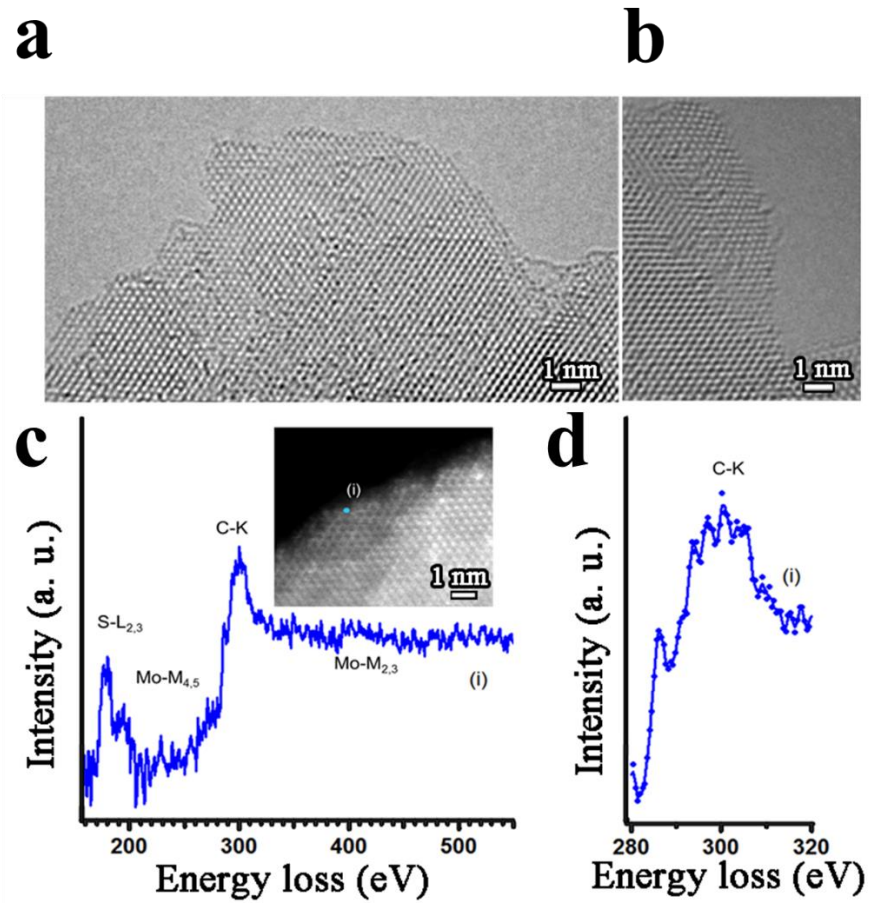

Figure 12. (a, b) HR-TEM micrographs of functionalized MoS_2-pyrene **2b**. Edges are primarily zig-zag type, with evidence of protruding chain-like carbonaceous material, terraced layers with extensive exposed edges. (c) EEL spectrum acquired in a flake of functionalized MoS_2-pyrene **2b** shown in the inset. The S-$L_{2,3}$, Mo-$M_{4,5}$, C-K and Mo-$M_{2,3}$ edges are highlighted in this spectrum. (d) C-K edge fine structures (ELNES), extracted from the spectrum shown in Figure 5c. The scale bar of all images is 1 nm.

Next, density functional theory modeling was employed to better understand the functionalization mechanism. In order to gain insight into the covalent binding behavior, the interaction of 3-methyl-1,2-dithiolane with the MoS_2 edge and basal plane was firstly modeled. The former molecule represents the covalent linking segment of **1a-c** with the carbon chain attached to neighboring S atoms of MoS_2 either in the basal plane or at zig-zag 100% S

molybdenum-edge (Figure 13a-d). Preferential binding for the edge compared to the basal plane was found to be 2.54 eV per molecule for the most stable configuration. At the edge, 3-methyl-1,2-dithiolane was most stable with its carbon chain approximately perpendicular to the edge (Figure 13b) breaking apart a single S_2 pair. The other less stable edge configurations resulted in two broken S_2 pairs, which then reconstruct horizontally (Figure 13c, d). Neighboring bonds in MoS_2 around the covalent anchoring site were also distorted, notably in Figures 6c and d, the distance between Mo atoms connected to the S atoms bound to the carbon chain of 3-methyl-1,2-dithiolane was reduced from 3.13 Å for the bulk to around 2.96 Å.

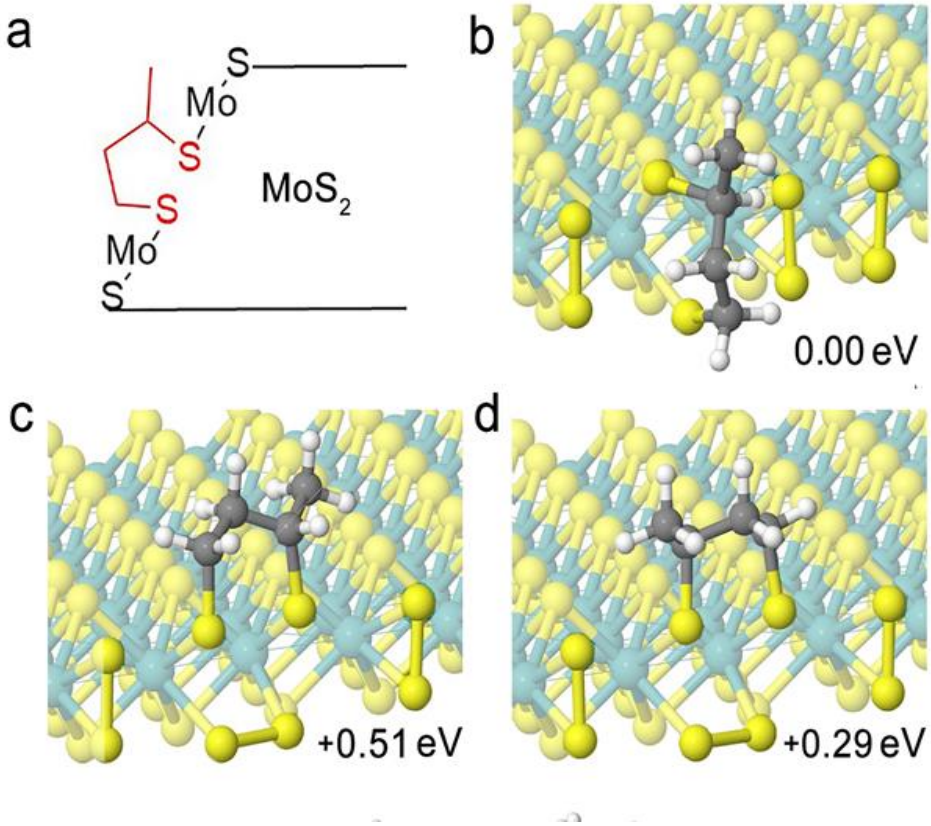

Figure 13. (a-d) 3-methyl-1,2-dithiolane binding to MoS_2 edge: (a) Schematic representation, (b) most stable binding configuration found for the edge functionalization, with the aliphatic chain connected to S atoms from the same reconstructed edge S_2 pair, (c, d) less stable configurations with the aliphatic chain connected to S atoms from neighboring S_2 pairs. Enthalpy differences (eV) are relative to structure in Figure 6b. Atom color code: green-blue = Mo, yellow = S, grey = C, white = H, red = O.

Starting with the most stable 50 % S zig-zag edges, 1,2-dithiolanes can directly bind to the exposed Mo at this edge, saturating and resulting in 100 % S coverage with covalently attached species, preferentially in a binding configuration perpendicular to the edge (*cf*. Figure 13b). This converts the sulfur bonding at the extensive edge sites to a configuration much closer to the bulk, and can also be viewed as filling 'vacant sulfur' edge sites. The model is supported by XPS studies of the semiconducting MoS_2 samples before and after functionalization with **1b** (i.e. MoS_2-pyrene **2b** hybrid material) as depicted in Figure 14. Before functionalization, the S 2p signal shows a superposition of the conventional semiconducting MoS_2 signal, the split peak pair at 163.4 and 162.2 eV, with a second pair of peaks at 163.1 and 161.9 eV, typically associated with "vacancy" or damaged material,[55] which it was asocciated here with the unsaturated sulfur edges. After functionalization, these additional peaks were removed as the edges all become fully sulfur saturated. At the same time, there was very little change in the Mo 3d signal. Notably, the XPS signal showed no secondary peaks corresponding to oxidized S and Mo proving the high purity of functionalized MoS_2-pyrene **2b** hybrid material. The same was also confirmed by the EELS measurements (*cf*. Figure 12c).

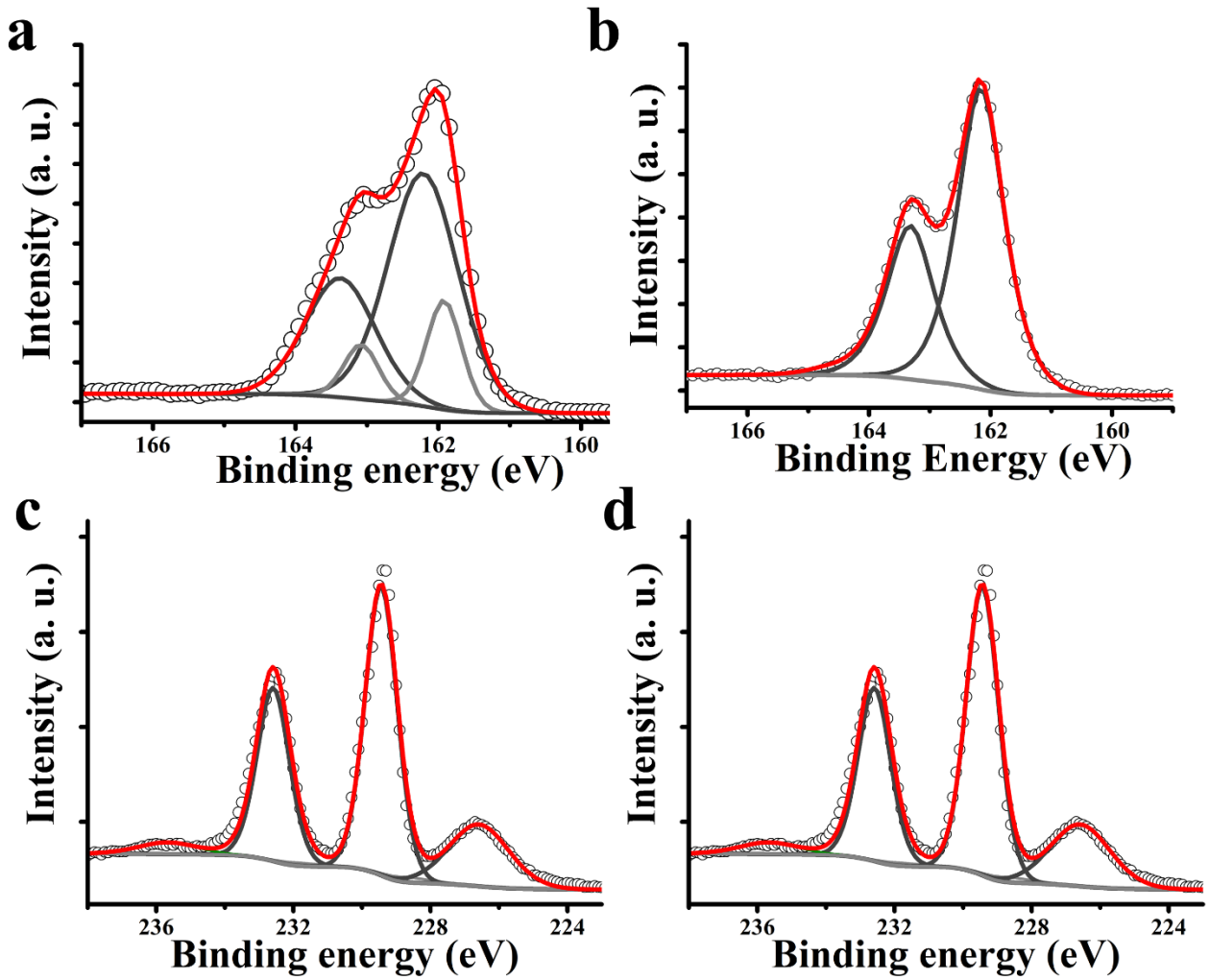

Figure 14. XPS (a, b) S 2p and (c, d) Mo 3d signal from (a, c) exfoliated semiconducting MoS_2 and (b, d) functionalized MoS_2-pyrene **2b** hybrid material. Components in maroon show the presence of MoS_2, while in grey are due to vacancies or damaged material.

The UV-Vis spectrum for **2a** in DMF exhibits the characteristic features due to the semiconducting polytype of MoS_2. Discernible are the excitonic transitions at 400, 500, 630 and 690 nm (Figure 15a), justifying the semiconducting nature of the functionalized MoS_2-based species.[56] For the pyrene modified MoS_2-based nanohybrid **2b**, additional bands directly derived from the optical absorption of the pyrene are identified at 315, 330 and 345 nm (Figure 15b), hence, directly implying the success of the functionalization reaction. Overall, the UV-Vis spectrum of MoS_2-pyrene nanohybrid **2b** is a simple superimposition of the spectra owed to the

semiconducting polytype of MoS_2 and to the pyrene derivative **1b**, implying the absence of appreciable electronic interactions between the two species in the ground state.

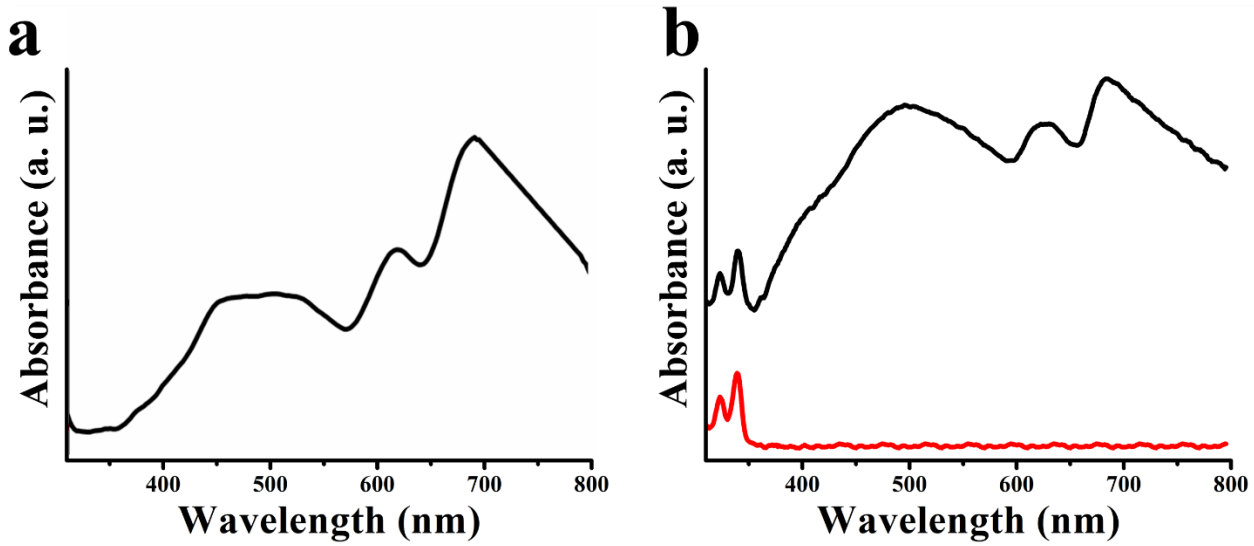

Figure 15. UV-Vis absorption spectra of (A) exfoliated MoS_2 and (B) MoS_2-pyrene hybrid **2** (black) as compared with pyrene **1b**.

On the other hand, at the excited states, strong electronic communication between MoS_2 and pyrene within **2b** was identified. More precisely, based on steady-state photoluminescence assays, the characteristic emission bands of pyrene in **1b**, located at 376, 396 and 418 nm upon photoexcitation at 340 nm, were quenched in **2b** (Figure 16a), for samples possessing equal absorptions at the excitation wavelength. Notably, a blank sample prepared by mixing exfoliated MoS_2 with pyrene derivative **1b** failed to show photoluminescence quenching of the pyrene emission (Figure 16b). Hence, intrahybrid transduction of electron and/or energy from the pyrene singlet excited state to MoS_2 for **2b** occurs, implying that MoS_2 acts as electron/energy acceptor. Moving further, based on the time-correlated-single-photon-counting method, the fluorescence lifetime profiles for **1b** were obtained and analyzed. The evaluation of the time profile of the fluorescence decay at 396 nm for the singlet-excited state of free pyrene in **1b** was monoexponentially fitted with a lifetime of 3.79 ns. Conversely, two decay components in MoS_2-based nanohybrid **2b** were identified. Biexponential fitting for the fluorescence decay gives rise to a slower component with 5.01 ns, attributed to non-interacting pyrene and a faster one with

280 ps, corresponding to the fluorescence quenching of the emission intensity of the singlet excited state of pyrene in MoS_2-pyrene **2b**. Then, based on equation (1) the quenching rate constant k^S_q for the singlet excited state of pyrene in MoS_2-pyrene **2b** was evaluated as 3.3×10^9 s^{-1}. Furthermore, by employing the equation (2), the quantum yield Φ^S_q for **2b** was determined to be 0.85.

(1) $$k^S_q = (1/\tau_f)-(1/\tau_o)$$

(2) $$\Phi^S_q = [(1/\tau_f)-(1/\tau_o)]/(1/\tau_f)$$

where τ_f refers to the lifetime of the fast-decaying component in **2b**, and τ_o refers to the lifetime of free pyrene in **1b**.

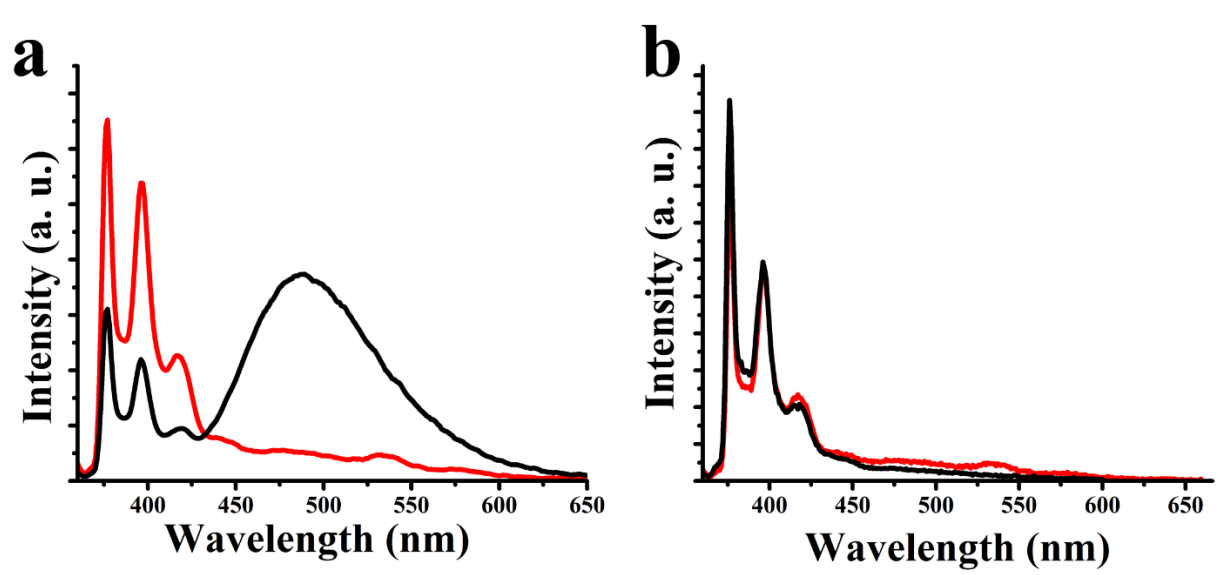

Figure 16. Photoluminescence spectra (excitation at 340 nm) for (a) 1,2-dithiolane-based pyrene derivative **1b** (red) as compared with functionalized MoS_2-pyrene **2b** hybrid material (black) and (a) dithiolane-based pyrene derivative **1b** (red) as compared with blank samples prepared upon mixing with functionalized MoS_2-pyrene nanohybrid **2b** (black), obtained in DMF.

4.3 EXPERIMENTAL SECTION

4.3.1 Materials

Instrumentation. ^{1}H and ^{13}C NMR spectra were recorded in a 300 MHz Varian instrument operated by Vjnmr software, with TMS used as internal standard and D_2O as solvent. Steady-state UV-Vis electronic absorption spectra were recorded on a PerkinElmer (Lambda 19) UV-Vis-NIR spectrophotometer. Steady-state emission spectra were recorded on a Fluorolog-3 JobinYvon-Spex spectrofluorometer (model GL3-21). Pico-second time-resolved fluorescence spectra were measured by the time-correlated-single-photon-counting (TCSPC) method on a Nano-Log spectrofluorometer (Horiba JobinYvon), by using a laser diode as an excitation source (NanoLED, 375 nm) and a UV-Vis detector TBX-PMT series (250-850 nm) by Horiba JobinYvon. Lifetimes were evaluated with the DAS6 Fluorescence-Decay Analysis Software. Mid-infrared spectra in the region 500−4500 cm^{-1} were obtained on a Fourier transform IR spectrometer (Equinox 55 from Bruker Optics) equipped with a single reflection diamond ATR accessory (DuraSamp1IR II by SensIR Technologies). A drop of the solution was placed on the diamond surface, followed by evaporation of the solvent, in a stream of nitrogen, before recording the spectrum. Typically, 100 scans were acquired at 2 cm^{-1} resolution. Micro-Raman scattering measurements were performed at room temperature in the backscattering geometry using a RENISHAW inVia Raman microscope equipped with a CCD camera and a Leica microscope. A 2400 lines mm^{-1} grating was used for all measurements, providing a spectral resolution of ± 1 cm^{-1}. As an excitation source the Ar^{+} laser (633 nm with less than 2.65 mW laser power) was used. Measurements were taken with 60 seconds of exposure times at varying numbers of accumulations. The laser spot was focused on the sample surface using a long working distance 50x objective. Raman spectra were collected on numerous spots on the sample and recorded with Peltier cooled CCD camera. The intensity ratio ID/IG was obtained by taking the peak intensities following any baseline corrections. The data were collected and analyzed with Renishaw Wire and Origin software. Thermogravimetric analysis was performed using a TGA Q500 V20.2 Build 27 instrument by TA in a nitrogen (purity >99.999%) inert atmosphere. X-ray photoelectron analysis (XPS) was performed with a Kratos AXIS Supra. The spectra were obtained using a monochromatized Al-Kα source at 1486.6 eV running at 15 kV and 10 mA. The survey spectrum was measured at 160 eV pass energy and for the individual peak regions,

spectra were recorded with pass energy of 20 eV. The energy resolution was < 0.48 eV. The analysis of peaks was performed with the Casa XPS software, using a weighted sum of Lorentzian and Gaussian components curves after Shirley background subtraction. The binding energies were referenced to the internal C1s standard at 284.6 eV. High-resolution tranmission electron microscopy (HRTEM) was performed on an aberration-corrected (image corrector) FEI Titan Cube microscope, working at 80 keV. STEM imaging and EELS studies have been conducted using an aberration-corrected FEI Titan Low-Base microscope operated at 80 kV. This microscope is equipped with a Cs probe corrector and a Gatan Tridiem ESR 865 EELS spectrometer. The energy resolution was ~1 eV. The convergence and collection angles were 25 and 50 mrad, respectively. To increase the signal/noise ratio, the datasets were then de-noised with the open-source program Hyperspy by using principal component analysis routines.

4.3.2 Synthesis

General procedure for the synthesis of 1,2-dithiolanes 1a and 1b. In a round bottom flask, α-lipoic acid (1.6 mmol), tert-butyl-(2-(2-(2-aminoethoxy)ethoxy)ethyl)carbamate (2.00 mmol, 1.25 equiv.) for **1a** or 1-pyrenebutanol (1.6 mmol, 1 equiv.) for **1b**, EDCI (4.8 mmol, 3 equiv.) and DMAP (4.8 mmol, 3 equiv.) were added in dry dicloromethane (100 mL). The reaction mixture was stirred under nitrogen at room temperature for 18 hours. Then, the organic phase was extracted with H_2O (5 x 100 mL), dried over $MgSO_4$ and purified by column chromatography (petroleum ether/ethyl acetate 50%). Yield ~ 80%. Spectroscopic data for **1a**: ^{1}H NMR (300 MHz, $CDCl_3$) δ: 6.07 (s, 1H), 5.01 (s, 1H), 3.58 (m, 8H), 3.44 (d, *J* = 4.6 Hz, 2H), 3.30 (s, 2H), 3.11 (m, 2H), 2.44 (m, 1H), 2.18 (t, *J* = 7.3 Hz, 3H), 1.89 (m, 1H), 1.66 (s, 4H), 1.43 (s, 9H); ^{13}C NMR (75 MHz, $CDCl_3$) δ: 172.80 (1C), 155.97 (1C), 79.31 (1C), 70.24 (1C), 70.15 (1C), 56.40 (1C), 40.32 (1C), 40.19 (1C), 39.14 (2C), 38.42 (1C), 36.20 (1C), 34.61 (2C), 28.86 (1C), 28.39 (3C), 25.37 (1C) (Figure 17 a, c). Spectroscopic data for **1b**: ^{1}H NMR (300 MHz, $CDCl_3$) δ: 8.17 (d, J = 9.3 Hz, 1H), 7.97 (m, 7H), 7.77 (d, J = 7.8 Hz, 1H), 4.06 (t, J = 6.4 Hz, 2H), 3.39 (m, 1H), 3.28 (t, J = 7.5 Hz, 2H), 2.98 (m, 2H), 2.23 (m, 3H), 1.77 (m, 5H), 1.51 (m, 4H), 1.32 (m, 2H). ^{13}C NMR (75 MHz, $CDCl_3$) δ: 173.54, 136.31, 131.42, 130.87, 129.86, 128.59, 127.49, 127.27, 127.22, 126.64, 125.83, 125.09, 125.01, 124.90, 124.81, 124.72, 123.27, 64.18, 56.30, 40.15, 38.44, 34.54, 34.10, 33.04, 28.73, 28.66, 28.13, 24.71 (Figure 17 b, d).

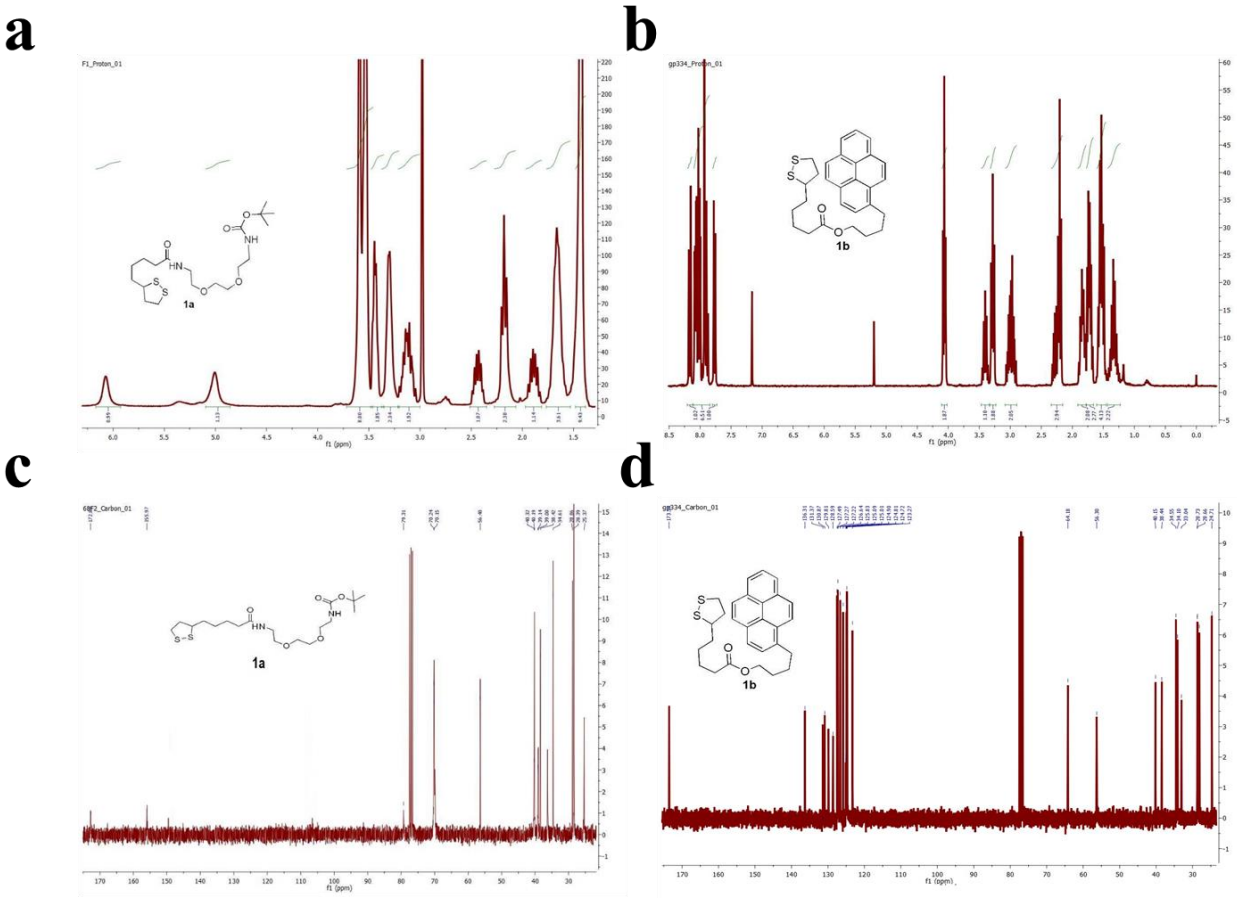

Figure 17. ^{1}H (a, b) and ^{13}C (c, d) NMR spectra.

General procedure for the preparation of functionalized MoS_2-based nanohybrids. In a round bottom flask, exfoliated MoS_2 (20 mg) and 1,2-dithiolane derivative (**1a** or **1b**; 10 mg) in DMF (10 mL) were stirred at 70 °C for 36 hours. After that period, the reaction mixture was filtered through a PTFE membrane (0.1 mm pore size), the solid residue was extensively washed with DMF and dichloromethane and then collected as a dispersion in dichloromethane. In order to deprotect the BOC group, 5 mg of the material **2a** were redisperse in dichloromethane and treated with gaseous HCl. The reaction mixture was left under stirring for 12 hours and then filtered through a PTFE membrane (0.2 μm pore size) to yield **2c.**

Sonochemical degradation of NMP. Experiments were performed with a Sonics Vibra-Cell VCX130 ultrasonic probe employing 20 mL of NMP, which was sonicated for 1 hour at 75% amplitude (~30 W power output), to produce the sample designated as sonicated NMP. For the

liquid-exfoliated MoS_2 samples, bulk MoS_2 powder was added to 20 mL of NMP at an initial concentration of 25 mg/mL. The supernatant was then discarded and the sediment was redispersed into another 20 mL of NMP. This was then sonicated for 1 hour at 50% amplitude with a pulse of 6 s on and 2 s off. The sample was then centrifuged for 1 hour at 2000 g, the sediment was discarded and the supernatant was collected. After the final centrifugation, all samples were left to stand overnight before characterisation. For the non-degraded samples, as-received NMP was used throughout the process. For the degraded samples, sonicated NMP was used throughout the process.

4.4 CONCLUSION

In this chapter we showed that covalent functionalization of exfoliated MoS_2 with 1,2-dithiolanes occurs preferentially at the sheet edges, with functionalization likely progressing via physisorption to the basal plane followed by migration and chemisorption to the edge. The presence of the 1,2-dithiolane end-group in our attaching species facilitates incorporation at the available edge sites. This is mediated through easy variation in sulfur saturation (50-100%) along the edge sites. Preferential edge reactivity is highly reminiscent of the chemistry of non-exfoliated MoS_2, known for its strong catalytic capability, and suggests that other bulk MoS_2 functionalization and treatment strategies may be transferable to the 2D system. Furthermore, the photophysical properties of the hybrid material **2b** featuring charge-transfer interactions were scrutinized revealing potentiality for managing energy conversion schemes.

In addition, we demonstrated that NMP can not be used as solvent in any spectroscopic study of TMDs because it is susceptible to degradation under sonochemical treatment or with ageing under ambient conditions. Both, ambient and sonochemical degradation result in chemically similar products, which give rise to strong visible photoluminescence of the NMP, masking any photochemical assays.

4.5 REFERENCES

1. D. Voiry, H. Yamaguchi, J. Li, R. Silva, D. C. B. Alves, T. Fujita, M. Chen, T. Asefa, V. B. Shenoy, G. Eda and M. Chhowalla. Enhanced catalytic activity in strained chemically exfoliated WS_2 nanosheets for hydrogen evolution. *Nat. Mater*. **2013**, *12*, 850-855.
2. K. Wang, J. Wang, J. Fan, M. Lotya, A. O'Neill, D. Fox, Y. Feng, X. Zhang, B. Jiang, Q. Zhao, H. Zhang, J. N. Coleman, L. Zhang and W. J. Blau. Ultrafast saturable absorption of two-dimensional MoS_2 nanosheets. *ACS Nano* **2013**, *7*, 9260-9267.
3. X. Huang, Z, Zenga and H. Zhang. Metal dichalcogenide nanosheets: preparation, properties and applications. *Chem. Soc. Rev*. **2013**, *42*, 1934-1946.
4. A, Pospischil, M. M. Furchi and T. Mueller. Solar-energy conversion and light emission in an atomic monolayer p-n diode. *Nat. Nanotechnol*. **2014**, *9*, 257-261.
5. J. S. Ross, P. Klement, A. M. Jones, N. J. Ghimire, J. Yan, D. G. Mandrus, T. Taniguchi, K. Watanabe, K. Kitamura, W. Yao, D. H. Cobden and X. Xu. Electrically tunable excitonic light-emitting diodes based on monolayer WSe_2 p-n junctions. *Nat. Nanotechnol*. **2014**, *9*, 268-272.
6. M. Pumera, Z. Soferb and A. Ambrosi. Layered transition metal dichalcogenides for electrochemical energy generation and storage. *J. Mater. Chem. A* **2014**, *2*, 8981-8987.
7. T. Stephenson, Z. Li, B. Olsen and D. Mitlin. Lithium ion battery applications of molybdenum disulfide (MoS_2) nanocomposites. *Energy Environ. Sci*. **2014**, 17, 209-231.
8. W. Yin, L. Yan, J. Yu, G. Tian, L. Zhou, X. Zheng, X. Zhang, Y. Yong, J. Li, Z. Gu and Y. Zhao. High-throughput synthesis of single-layer MoS_2 nanosheets as a near-infrared photothermal-triggered drug delivery for effective cancer therapy. *ACS Nano* **2014**, *8*, 6922-6933.
9. T. Liu, C. Wang, X. Gu, H. Gong, L. Cheng, X. Shi, L. Feng and S. Z. Liu. Drug delivery with PEGylated MoS_2 nanosheets for combined photothermal and chemotherapy of cancer. *Adv. Mater*. **2014**, *26*, 3433-3440.
10. B. Radisavljevic, A. Radenovic, J. Brivio, V. Giacometti and A. Kis. Single-layer MoS_2 transistors. *Nat. Nanotechnol*. **2011**, *6*, 147-150.
11. H. S. Lee, S.-W. Min, Y.-G. Chang, M. K. Park, T. Nam, H. Kim, J. H. Kim, S. Ryu and S. Im. MoS_2 Nanosheet phototransistors with thickness-modulated optical energy gap. *NanoLett*. **2012,** *12*, 3695-3700.

12. J. Z. Ou, A. F. Chrimes, Y. Wang, S.-y. Tang, M. S. Strano, and K. Kalantar-zadeh. Ion-driven photoluminescence modulation of quasi-two-dimensional MoS_2 nanoflakes for applications in biological systems. *NanoLett.* **2014**, *14*, 857-863.
13. H. S. S. R, Matte, A. Gomathi, A. K. Manna, D. J. Late, R. Datta, S. K. Pati and C. N. R. Rao. MoS_2 and WS_2 analogues of graphene. *Angew. Chem. Int. Ed*. **2010**, *49*, 4059-4062.
14. K. F. Mak, C. Lee, J. Hone, J. Shan and T. F. Heinz. Atomically thin MoS_2: A New direct-gap semiconductor. *Phys. Rev. Lett*. **2010**, *105*, 136805.
15. Z. Zeng, T. Sun, J. Zhu, X. Huang, Z. Yin, G. Lu. Z. Fan, Q. Yan, H. H. Huang and H. Zhang. An effective method for the fabrication of few-layer-thick inorganic nanosheets. *Angew. Chem. Int. Ed*. **2012**, *51*, 9052-9056.
16. H. J. Conle, B. Wang, J. I. Ziegler, R.F. Haglund Jr., S. T. Pantelides and K. I. Bolotin. Bandgap engineering of strained monolayer and bilayer MoS_2. *NanoLett*. **2013**, *13*, 3626-3630.
17. A. Castellanos-Gomez, R. Roldán, E. Cappelluti, M. Buscema, F. Guinea, H. S. J. van der Zant and G. A. Steele. Local strain engineering in atomically thin MoS_2. *NanoLett*. **2013**, 13, 5361-5366.
18. J. Coleman, M. Lotya, A. O'Neill, S. D. Bergin, P. J. King, U. Khan, K. Young, A Gaucher, S. De, R. J. Smith, I.V. Shvets, S. K. Arora, G. Stanton, H. Y. Kim, K. Lee, G. T. Kim, G. S. Duesberg, T. Hallam, J. J. Boland, J. J. Wang, J. F. Donegan, J. C. Grunlan, G. Moriarty, A. Shmeliov, R. J. Nicholls, J. M. Perkins, E. M. Grieveson, K. Theuwissen, D. W. McComb, P. D. Nellist and V. Nicolosi. Two-dimensional nanosheets produced by liquid exfoliation of layered materials. *Science* **2011**, *331*, 568-571.
19. Z. Tang, Q. Weia and B. Guo. A generic solvent exchange method to disperse MoS_2 in organic solvents to ease the solution process. *Chem. Commun*. **2014**, *50*, 3934-3937.
20. S. S. Chou, M. De, J. Kim, S. Byun, C. Dykstra, J. Yu, J. Huang and V. P. Dravid. Ligand conjugation of chemically exfoliated MoS_2. *J. Am. Chem. Soc*. **2013,** *135*, 4584.
21. K. C. Knirsch, N. C. Berner, H. C. Nerl, C. S. Cucinotta, Z. Gholamvand, N. McEvoy, Z. Wang, I. Abramovi, P. Vecera, M. Halik, S. Sanvito, G. S. Duesberg, V. Nicolosi, F. Hauke, A. Hirsch, J. N. Coleman and C. Backes. Basal-plane functionalization of chemically exfoliated molybdenum disulfide by diazonium salts. *ACS Nano* **2015**, *9*, 6018-6030.

22. Y. Hernandez, V. Nicolosi, M. Lotya, F. M. Blighe, Z. Sun, S. De, I. T. McGovern, B. Holland, M. Byrne, Y. K. Gun'Ko, J. J. Boland, P. Niraj, G. Duesberg, S. Krishnamurthy, R. Goodhue, J. Hutchison, V. Scardaci, A. C. Ferrari and J. N. Coleman. High-yield production of graphene by liquid-phase exfoliation of graphite. *Nat. Nanotechnol*. **2008**, *3*, 563-568.
23. R. G. Alargova, S. Deguchi and K. Tsujii. Stable colloidal dispersions of fullerenes in polar organic solvents. *J. Am. Chem. Soc*. **2001**, *123*, 10460-10467.
24. Y. Hernandez, V. Nicolosi, M. Lotya, F. M. Blighe, Z. Sun, S. De, I. T. McGovern, B. Holland, M. Byrne, Y. K. Gun'Ko, J. J. Boland, P. Niraj, G.Duesberg, S. Krishnamurthy, R.Goodhue, J. Hutchison, V. Scardaci, A. C. Ferrari and J. N. Coleman. Dispersions of single-walled carbon nanotubes: Toward solutions of pristine nanotubes. *J. Phys. Chem. B* **2000**, *104*, 8911-8915.
25. C. M. Hansen and A. L. Smith. Using Hansen solubility parameters to correlate solubility of C_{60} fullerene in organic solvents and in polymers. *Carbon* **2004**, *42*, 1591-1597.
26. S. D. Bergin, Z. Sun, D. Rickard, P. V. Streich, J. P. Hamilton and J. N. Coleman. Multicomponent solubility parameters for single-walled carbon nanotube-solvent mixtures. *ACS Nano* **2009**, *3*, 2340-2350.
27. Y. Hernandez, M. Lotya, D. Rickard S. D. Bergin and J. N. Coleman. Measurement of multicomponent solubility parameters for graphene facilitates solvent discovery. *Langmuir* **2010**, *26*, 3208-3213.
28. H. C. Yau, M. K. Bayazit, J. H. G. Steinke and M. S. P. Shaffer. Sonochemical degradation of N-methylpyrrolidone and its influence on single walled carbon nanotube dispersion. *Chem. Commun*. **2015**, *51*, 16621-16624.
29. A. Jawaid, D. Nepal, K. Park, M. Jespersen, A. Qualley, P. Mirau, L. F. Drummy and R. A. Vaia. Mechanism for liquid phase exfoliation of MoS_2. *Chem. Mater*. **2016**, *28*, 337-348.
30. A. Gupta, V. Arunachalam and S. Vasudevan. Liquid-phase exfoliation of MoS_2 nanosheets: The critical role of trace water. *J. Phys. Chem. Lett*. **2016**, *7*, 4884-4890.
31. K. Manna, C.-Y. Hsieh, S.-C. Lo, Y.-S. Li, H.-N. Huang and W.-H.-Chiang. Graphene and graphene-analogue nanosheets produced by efficient water-assisted liquid exfoliation of layered materials. *Carbon* **2016**, *105*, 551-555.

32. G. Song, Y. Lin, Z. Zhu, H. Zheng, J. Qiao and C. He, and H. Wang. Strong fluorescence of poly(N-vinylpyrrolidone) and its oxidized hydrolyzate. *Macromol. Rapid Commun*. **2015**, *36*, 278-285.
33. A Naumenko, M. Biliy, V. Gubanov and A. Navozenko. Spectroscopic studies of fullerene clusters in N-methyl-2-pyrrolidone. *J. Mol. Liq*. **2017**, 235, 115-118.
34. G. Pagona, C. Bittencourt, R. Arenal and N. Tagmatarchis. Exfoliated semiconducting pure 2H-MoS_2 and 2H-WS_2 assisted by chlorosulfonic acid. *Chem. Commun*. **2015,** *15*, 12950-12953.
35. D. Voiry, A. Goswami, R. Kappera, C. C. C. Silva, D. Kaplan, T. Fujita, M. Chen, T. Asefa and M. Chhowalla. Covalent functionalization of monolayered transition metal dichalcogenides by phase engineering. *Nat. Chem*. **2015**, *7*, 45-49.
36. W. Liu, X. Yang, Y. Zhang and M. X. H. Chen. Ultra-stable two-dimensional MoS_2 solution for highly efficient organic solar cells. *RSC Adv*. **2014**, *4*, 32744-32748.
37. T. Liu, C. Wang, W. Cui, H. Gong, C. Liang, X. Shi, Z. Li, B. Suna and Z. Liu. Combined photothermal and photodynamic therapy delivered by PEGylated MoS_2 nanosheets. *Nanoscale* **2014**, *6*, 11219-11225.
38. E. P. Nguyen, B. J. Carey, J. Z. Ou, J. van Embden, E. D. Gaspera, A. F. Chrimes, M. J. Spencer, S. Zhuiykov, K. Kalantar-Zadeh and T. Daeneke. Electronic tuning of 2D MoS_2 through surface functionalization. *Adv. Mater*. **2015**, *17*, 6225-6229.
39. J.-S. Kim, H.-W. Yoo, H. O. Choi and H.-T. Jung. Tunable volatile organic compounds sensor by using thiolated ligand conjugation on MoS_2. *NanoLett*. **2014**, *14*, 5941-5947.
40. C. Backes, N. C. Berner, X. Chen, P. Lafargue, P. LaPlace, M. Freeley, G.S. Duesberg, J. N. Coleman and A. R. McDonald. Functionalization of liquid-exfoliated two-dimensional 2H-MoS_2. *Angew. Chem. Int. Ed*. **2015**, *54*, 2638-2642.
41. H. Li, Q. Zhang, C. C. R. Yap, B.K. Tay, T. H. T. Edwin, A. Oliver and D. Baillargeat. From bulk to monolayer MoS_2: Evolution of Raman scattering *Adv. Funct. Mater*. **2012**, *22*, 1385-1390.
42. M. Makarova, Y. Okawa and M. Aono. Selective adsorption of thiol molecules at sulfur vacancies on MoS_2 (0001), followed by vacancy repair via S-C dissociation. *J. Phys. Chem. C* **2012**, *116*, 22411-22416.

43. C. Backes, B. M. Szydłowska, A. Harvey, S. Yuan, V. Vega-Mayoral, B. R. Davies, P.-l. Zhao, D. Hanlon, E. J. G. Santos, M. I. Katsnelson, W.J. Blau, C. Gadermaier and J. N. Coleman. Production of highly monolayer enriched dispersions of liquid-exfoliated nanosheets by liquid cascade centrifugation. *ACS Nano* **2016**, 10, 1589-1601.
44. X. Chen, N. C. Berner, C. Backes, G. S. Duesberg and A. R. McDonald. Functionalization of two-dimensional MoS_2: On the reaction between MoS_2 and organic thiols. *Angew. Chem. Int. Ed*. **2016**, *55*, 5803-5808.
45. S. J. Jimenez-Sandoval, D. Yang, R. F. Frindt and J. C. Irwin. Raman study and lattice dynamics of single molecular layers of MoS_2. *Phys. Rev. B* **1991**, *44*, 3955-3962.
46. A. P. Nayak, T. Pandey, D. Voiry, J. Liu, S. T. Moran, A. Sharma, C. Tan, C.-H. Chen, L.-J. Li, M. Chhowalla, J.-F. Lin, A. K. Singh and D. Akinwande. Pressure-dependent optical and vibrational properties of monolayer molybdenum disulfide. *NanoLett*. **2015**, *15*, 346-353.
47. Y. Li, Z. Zhou, S. Zhang and Z. Chen. MoS_2 Nanoribbons: High stability and unusual electronic and magnetic properties. *J. Am. Chem. Soc*. **2008**, *130*, 16739-16744.
48. Z. Wang, H. Li, Z. Liu, Z. Shi, J. Lu, K. Suenaga, S.-K. Joung, T. Okazaki, Z. Gu, J. Zhou, Z. Gao, G. Li, S. Sanvito, E. Wang and S. Iijima. Mixed low-dimensional nanomaterial: 2D Ultra narrow MoS_2 inorganic nanoribbons encapsulated in quasi-1D carbon nanotubes. *J. Am. Chem. Soc*. **2010**, *132*, 13840-13847.
49. J. V. Lauritsen, M. V. Bollinger, E. Lægsgaard, K. W. Jacobsen, J. K. Nørskov, B. S. Clausen, H. Topsøe and F. Besenbacher. Atomic-scale insight into structure and morphology changes of MoS_2 nanoclusters in hydrotreating catalysts. *J. Catal*. **2004**, *221*, 510-522.
50. H. Schweiger, P. Raybaud G. Kresse, and H. Toulhoat. Shape and edge sites modifications of MoS_2 catalytic nanoparticles induced by working conditions: A theoretical study. *J. Catal*. **2002**, *207*, 76-87.
51. M. V. Bollinger, K. W. Jacobsen and J. K. Nørskov. Atomic and electronic structure of MoS_2 nanoparticles. *Phys. Rev. B* **2003**, *67*, 085410.
52. R. Arenal and O. Stephan, in *Advanced Transmission Electron Microscopy: Applications to Nanomaterials* (eds. L. Francis, A. Mayoral, R. Arenal, Chapter 5, Springer, Basel, **2015**).
53. R. Czerw, M. Terrones, J.-C. Charlier, X. Blase, B. Foley, R. Kamalakaran, N. Grobert, H. Terrones, D. Tekleab, P. M. Ajayan, W. Blau, M. Rühle and D. L. Carroll. Identification of electron donor states in N-doped carbon nanotubes. *NanoLett*. **2014**, *14*, 5509-5516.

54. K. Suenaga and M. Koshino. Atom-by-atom spectroscopy at graphene edge. *Nature* **2012,** *468*, 1088-1090.
55. G. Deokar, D. Vignaud, R. Arenal, P. Louette and J.-F. Colomer. Synthesis and characterization of MoS_2 nanosheets. *Nanotechnology* **2016**, *27*, 075604.
56. The metallic polytype of MoS_2 shows two electronic transitions at higher energies located at 255 nm and 307 nm. G. Eda, H. Yamaguchi, D. Voiry, T. Fujita, M. Chen and M. Chhowalla. Photoluminescence from chemically exfoliated MoS_2. *NanoLett*. **2011**, *11*, 5111-5116.

CHAPTER 5

Covalently incorporated photoactive units onto transition metal dichalcogenides

ABSTRACT

Exfoliated semiconducting MoS_2 and WS_2 were covalently functionalized with 1,2-dithiolane-modified carbon nanodots (CNDs). The newly synthesized CND-MoS_2 and CND-WS_2 hybrids were characterized by spectroscopic, thermal and electron microscopy imaging methods. Based on electronic absorption and fluorescence emission spectroscopy, modulation of the optoelectronic properties of TMDs by interfacing with CNDs was accomplished. Electrochemical studies revealed facile oxidation of MoS_2 over WS_2 in the examined hybrids, suggesting it to be better electron donor. Excited state events, investigated by femtosecond transient absorption spectroscopic studies, revealed ultrafast energy transfer from photoexcited CNDs to both MoS_2 and WS_2. Interestingly, upon MoS_2 photoexcitation charge transfer from an exciton dissociation path of MoS_2 to CNDs, within CND-MoS_2, was observed. However, such process in CND-WS_2 was found to be absent due to energetic reasons. The present study highlights the importance of TMD-derived donor-acceptor hybrids in light energy harvesting and optoelectronic applications. Furthermore, the fundamental information obtained from the current results will benefit design strategies and impact the development of additional TMD-based hybrid materials to efficiently manage and perform in electron-transfer processes.

Furthermore, covalently modified MoS_2 and WS_2 with porphyrin moieties were prepared and fully characterized. Efficient photoluminescent quenching of the porphyrin's emission by MoS_2 and WS_2 was identified, implying the existence of effective deactivation of the singlet excited state of porphyrin via charge/energy transfer to MoS_2 and WS_2 in the corresponding hybrids.

Finally, zinc phthalocyanine (ZnPc) carrying an 1,2-dithiolane oxide linker was employed to functionalize MoS_2 at defected sites located at the edges. The structure of ZnPc-MoS_2 was fully assessed by complementary spectroscopic, thermal and microscopy imaging techniques. Markedly, evidence of charge or energy transfer in the hybrid was demonstrated using time-resolved photoluminescence spectroscopic assays.

5.1 INTRODUCTION

Transition metal dichalcogenides (TMDs) consist of an atomic thick layer of transition metals sandwiched by two atomic layers of chalcogens. The atoms within discrete layers of TMDs are covalently connected, whereas adjoining layers interact each other via multiple van der Waals forces.[1] Although the crystal structure of TMDs can greatly vary, depending on the number of the d-electrons of the transition metal, the most commonly observed polytypes are those with trigonal prismatic D_{3h} symmetry possessing semiconducting properties and with octahedral O_h coordination which conversely show metallic behavior.[2] Furthermore, the presence of tunable band gap in TMDs and their layered-dependent optoelectronic properties give them high prospect for technological applications.[3] Nonetheless, managing and controlling the electronic properties of semiconducting TMDs, which are governed by excitonic transitions, is mandatory for their realization as prototype devices in energy-related applications such as solar cells, photodetectors and photo-catalysis. To this end, among other sophisticated and complicated processes employed in nano-sized semiconducting materials, a facile yet straightforward approach to gain precise control over the optoelectronic properties is by decorating the surface of TMDs with photo- and/or electro-active species[4] and tuning the charge-carrier density.[5]

Covalent functionalization unlocks the potentiality of TMDs by opening new opportunities and broadening the spectrum of applications.[6] The starting point, prior of applying chemical means to modify the structure of TMDs, is to efficiently exfoliate oligo-layered nano-sheets, leading to the formation of stable colloidal dispersions. The most widely employed exfoliation strategies for TMDs are based on treatment of the bulk material with butyl lithium under inert conditions, giving access to the metastable metallic polytype, which can be converted to the semiconducting one by annealing,[7] and chlorosulfonic acid, yielding TMDs with semiconducting properties.[8] Based on such exfoliated TMDs, routes for the covalent bonding and/or coordination of organic species have been explored targeting either the basal plane or the edges of TMDs. Despite that the basal plane of TMDs is highly inert, because chalcogen atoms are saturated, while metal atoms are not easily accessible for functionalization, since they are embedded beneath the chalcogen layer, organic addends were anchored via reactions with organoiodides and aryl diazonium salts.[9] In addition, organometallic complexes with TMDs[10] were also formed. Conversely, exploiting sulfur vacant/defect sites existing at the edges and the high binding affinity of molybdenum for 1,2-dithiolanes, the functionalization of exfoliated semiconducting

MoS_2 with 1,2-dithiolane derivatives was accomplished.[11] However, interfacing TMDs with photoactive species via robust covalent bonding toward the development of advanced hybrid materials has yet to be fully matured. Veritably, the development of such hybrids deserves investigation, especially in the context of their ability to function as donor-acceptor systems upon photo-illumination.

Carbon nano-dots (CNDs) are recognized as promising materials for energy conversion schemes.[12] In general, CNDs are photo-chemically stable,[13] and possess size in the order of 1-10 nm.[14] The CNDs are abundantly prepared by economic, facile and environmental benign routes, mainly involving poly-condensation reactions of small organic molecules at medium or elevated temperatures under hydrothermal or microwave irradiation conditions.[15] Notably, depending on the precursors employed for the synthesis, the periphery of the surface of CNDs can be decorated with diverse functional units, which can serve as anchors to conjugate other species en route the preparation of functional hybrid nanomaterials. For example, CNDs have already been covalently conjugated with carbon nanotubes,[16] porphyrins[17] and extended tetrathiafulvalene (exTTF)[18] and found to participate in photo-induced charge-transfer processes. Among the marked characteristics of CNDs are the broad and tunable absorption in the visible region and the intrinsic photoluminescence,[19] while interestingly, CNDs can act as either electron donors or acceptors, owed to their bivalent redox character.[20] This is to say that upon photo-irradiation, CNDs donate electrons when assembled with carbon nanotubes or perylenediimides,[16, 21] and accept electrons upon interaction with porphyrins and exTTF.[17, 18, 22]

Next, porphyrins have an 18π-electron aromatic structure, absorb efficiently light in the visible region with high molar absorbance coefficients and relatively high quantum yield. Such compounds are also photo-chemically stable and possess redox potentials and photo-physical properties that can be easily tuned by altering the metal center of the macrocycle or through modification of the peripheral substituents.[23] Therefore, porphyrins are quite attractive materials for participating in charge-transfer processing as electron donors. Without surprise, a plethora of supramolecularly and covalently associated porphyrins with graphene, the direct all-carbon two-dimensional analogue of TMDs, have been reported.[24] Similar to porphyrins, phthalocyanines also are electron donor structures which have been employed as active components in variety of nano-carbon materials such as graphene,[25, 26] and fullerenes[27]. The major characteristic feature of

phthalocyanines is the intense absorption in the near-IR region, which is beneficial when donor-acceptor hybrids for managing charge-transfer processes are considered.[28]

Functionalization of TMDs with CNDs, porphyrins and phthalocyanines is of high interest en route the development of novel hybrid nanomaterials for energy conversion. Specifically, herein we present the conjugation of modified CNDs, porphyrin and Zn-phthalocyanine species, featuring 1,2-dithiolane moieties, at the edges of exfoliated semiconducting MoS_2 and WS_2. Moreover, the comprehensive characterization together with the assessment of the photo-physical and electrochemical properties of the aforementioned TMD-based hybrid materials is presented.

Starting with CNDs, the modulation and engineering of the optoelectronic properties of photoexcited TMDs was accomplished. The newly prepared CND-MoS_2 and CND-WS_2 hybrid materials were fully characterized by complementary spectroscopic, thermal and electron microscopy imaging means, undoubtfully verifying the structures derived by the functionalization process. The optical and redox properties of CND-MoS_2 and CND-WS_2 were probed by electronic absorption, fluorescence emission spectroscopy and electrochemistry, respectively, revealing the existence of excited state intra-hybrid electronic interactions between the two species, while also showing that MoS_2 was a better electron donor compared to WS_2. Furthermore, with the aid of femtosecond transient spectroscopy, by exciting the TMD part within the hybrid materials, strong electronic interactions between the two species leading to photo-induced charge-separation only within CND-MoS_2 but not for CND-WS_2 were identified. In addition, upon excitation of CNDs in CND-TMDs ultrafast energy transfer from excited CNDs to both MoS_2 and WS_2 was identified.

Similarly, the porphyrin-MoS_2, porphyrin-WS_2 and Zn-phthalocyanine-MoS_2 materials were comprehensively characterized by spectroscopic, thermal and microscopy means. Moreover, electronic interactions between porphyrin and Zn-phthalocyanine with MoS_2 and WS_2, upon photoexcitation, were identified. The fundamental information obtained from the current study will impact the development of additional TMD-based hybrid materials to efficiently manage and perform in electron-transfer processes aiming to photovoltaic and solar energy related applications.

5.2 RESULTS AND DISCUSSION

Firstly, the properties and structure of CNDs were studied. CNDs **1** were prepared at room temperature, exploiting carbodiimide chemistry. The coupling agent *N,N'*-diisopropylcarbodiimide was employed to selectively catalyze the condensation of citric acid (CA) and ethylenediamine (EDA) (1:1 molar ratio) at room temperature (see experimental section) affording **1** as product of the reaction.

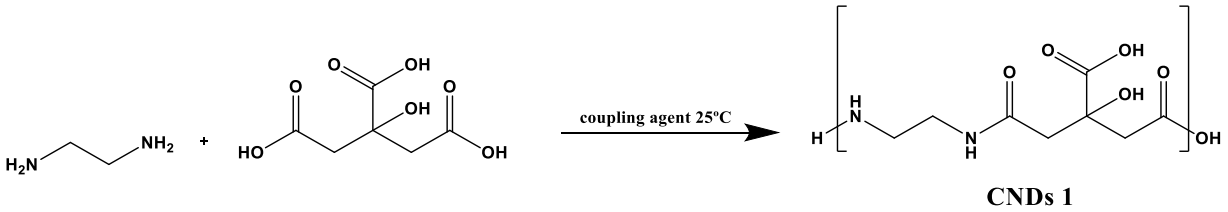

Figure 1. (a) Reaction of CA with EDA to produce CNDs **1**.

The optical properties of CNDs **1** were studied by UV-Vis spectroscopy (Figure 2a), steady state photoluminescence spectroscopy (Figure 2b) and time-resolved photoluminescence spectroscopy. An absorption band at 350 nm appears in the UV-Vis spectrum of **1**, which is directly related to the photoluminescence emission at 445 nm. The optical properties of CNDs **1** are very similar to those obtained from different amine and carboxylic acid precursors, as reported in the literature.[12c, 14a, 16, 17, 29]

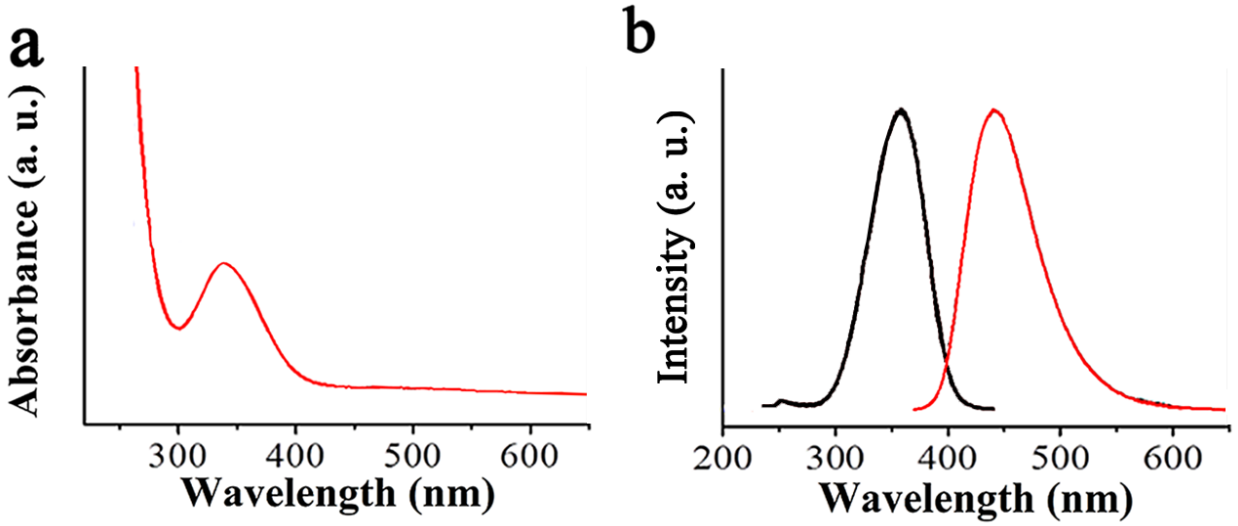

Figure 2. (a) UV-Vis, and (b) excitation (black) and emission (red) spectra of CNDs **1**.

In the IR spectrum of CNDs **1** (Figure 3a) the typical C=O stretching mode of the carboxylic group splits in two bands. The band at 1710 cm^{-1} reflects the carboxylic acid involved in H-bond, while the band at 1780 cm^{-1} is the free form. The former exhibits a significantly higher intensity than the latter one. This indicates that almost all of the carboxylic groups are involved in H-bonds. The amide vibrational modes I and II are found at 1653 and 1560 cm^{-1}, respectively. Their shifted position is comparable to the peptide bond vibrational modes and reflects the amide participation in H-bonds that increases the rigidity of the polymer.[30] More features, such as O-H and N-H stretching, are observed at 3500-2900 cm^{-1} and C-O and C-N stretching at 1438, 1402, 1341 cm^{-1}. Therefore, IR spectroscopy reveals that the structure of CNDs **1** encompasses a high involvement of H-bonds and ionic supramolecular interactions that contribute to enhance the rigidity of the system.

^{1}H NMR assays of the CNDs in D_2O allowed gathering significant information about the chemical structure and connectivity of the material (Figure 3b). Based on these NMR results, the chemical structure of CNDs **1** is unambiguously identified as a non-conjugated polymer consisting of the condensation product between CA and EDA. Furthermore, NMR spectroscopy provided valuable information regarding the conformation of the polymeric carbon dots. In the ^{1}H NMR spectra, the sharp line-shape of the peaks (singlets and triplets) strongly suggests a compact and static structure, in fast motion with respect to the time of response of the technique. The high density of sharp signals is related to the variety of static chemical environments that surrounds these protons and can be explained with the presence of various chain isomers of the repetitive unit that coexist in the polymer, as well as with the existence of different ionized forms. These data highlight the branched and rigid conformation of the polymeric CNDs. Conclusively CNDs possess a polyamide structure and their optical properties are due to their rigidity, while there was not identified any conjugated π-π system within CNDs **1**.

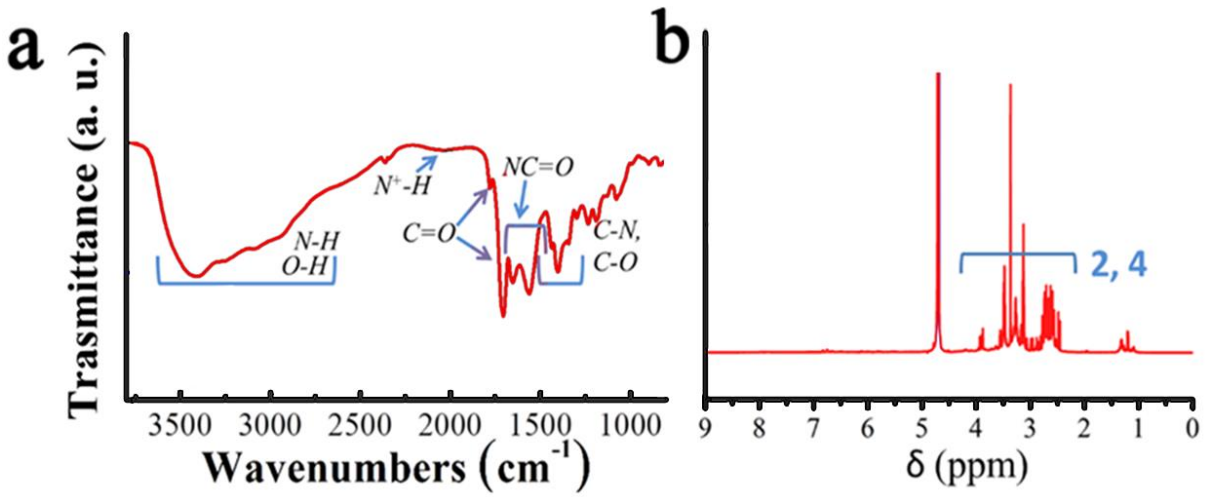

Figure 3. (a) IR, and (b) ^{1}H NMR spectra of CNDs **1**.

Condensation reaction of CNDs **1** with butylamine enhances the lipophilicity of the material, by introducing plethora of butyl units. Next, lipoic acid, activated by (3-dimethylaminopropyl)-N′-ethylcarbodiimide, was condensed with **1** yielding modified CNDs **2**. Spectroscopic characterization of **2** by ^{1}H NMR shows the methylene protons of citric acid and ethylenediamine structural components (4.0-2.3 ppm) and butyl units (1.6-0.7 ppm), while new signals between 2.6-1.5 ppm, corresponding to the incorporation of the 1,2-dithiolane moiety in **2** (Figure 4a) were identified. In addition, in the IR spectrum of **2**, the intensity of the band due to the stretching of the amide unit (C=O) at 1685 cm^{-1} was enhanced as compared to the corresponding band present in **1** (Figure 4b). Further proof for the successful modification of CNDs was delivered by the Kaiser test, where the amount of free amines on CNDs **2** was found significantly decreased as compared to the corresponding value calculated in CNDs **1**, from 1810 µmol/g for the latter to 72 µmol/g for the former.

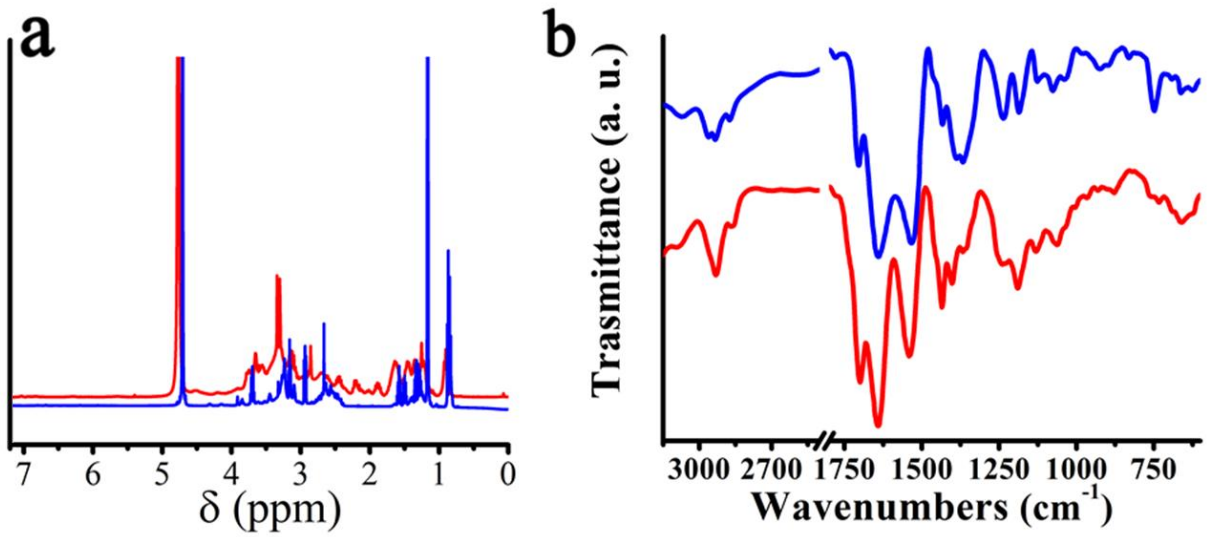

Figure 4. (a) ^{1}H NMR spectrum, and b) ATR-IR spectra for as-produced CNDs **1**, butylamine modified (blue), and lipoic acid modified CNDs **2** (red).

In parallel, bulk MoS_2 and WS_2 were wet exfoliated by chlorosulfonic acid,[8] and following the functionalization methodology for TMDs with 1,2-dithiolanes,[11] the conjugation of modified CNDs **2** was accomplished, furnishing CND-MoS_2 **3** and CND-WS_2 **4** according to Figure 5.

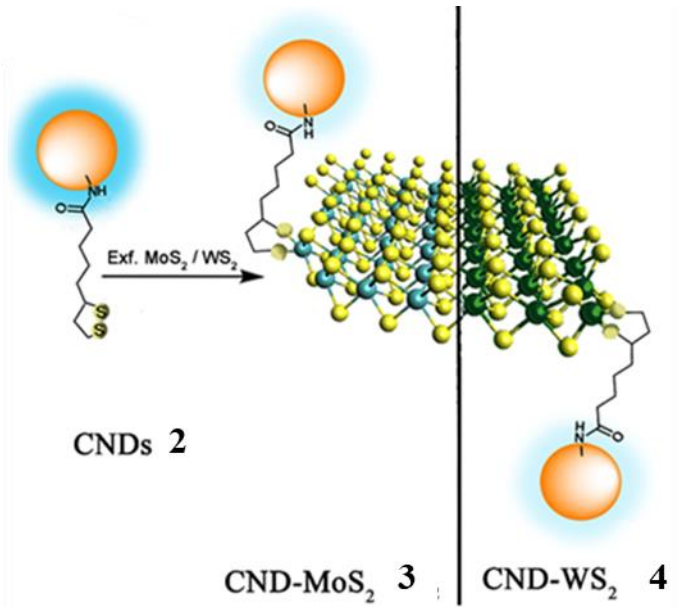

Figure 5. Illustrative preparation of CND-MoS_2 **3** and CND-WS_2 **4** upon covalent 1,2-dithiolane functionalization of exfoliated semiconducting MoS_2 and WS_2 nanosheets.

The newly derived hybrid materials were found to be soluble in polar solvents such as dimethylformamide (DMF), o-dichlorobenzene, and methanol, while they remained insoluble in less polar and apolar solvents such as dichloromethane, toluene, and hexane. In fact, **3** and **4** showed the highest solubility in DMF, with the corresponding registered values being 0.48 and 0.44 mg/mL, respectively. Notably, the stability of **3** and **4** in DMF was high, evidenced by the absence of precipitated material even after a period of a few months.

Next, complementary characterization of CND-MoS_2 **3** and CND-WS_2 **4** by IR and Raman spectroscopy, thermogravimetric analysis (TGA) and transmission electron microscopy (TEM) imaging was performed. The presence of characteristic bands at 1640 and 1550 cm^{-1}, related with stretching and bending modes of carbonyl amide vibrations were evident in the ATR-IR spectra of **3** and **4** (Figure 6). In addition, C-H stretching vibrations at 2960 and 2915 cm^{-1} due to the alkyl chain of 1,2-dithiolane were present.

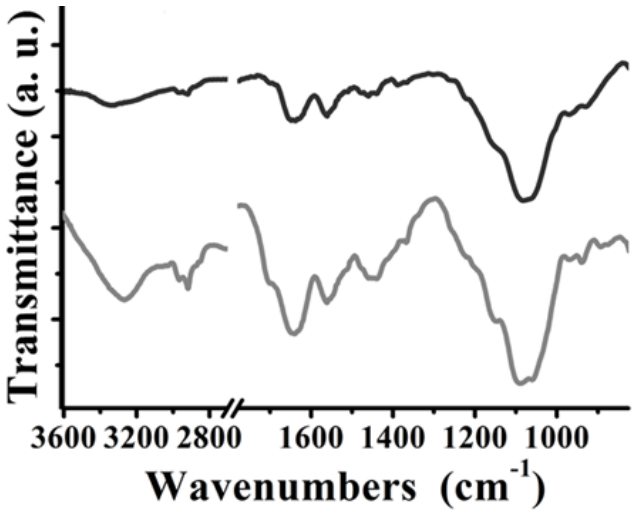

Figure 6. ATR-IR spectra of **3** (black) and **4** (grey).

Comparing Raman spectra of exfoliated MoS_2 and **3**, obtained upon excitation under on-resonance conditions at 633 nm and normalized at the A_{1g} mode at 404 cm^{-1}, it was found that the intensity of the 2LA(M) band associated to disorder and defects[31] and located at 447 cm^{-1} was found decreased in **4** as compared to that owed to exfoliated MoS_2 (Figure 7a).[32] The latter comes as a result of the reduced number of S defects due to edge functionalization of MoS_2.[33] Moreover, the absence of the characteristic phonon modes of metallic polytype MoS_2 so-called J_1, J_2 and J_3 at 150, 225 and 325 cm^{-1}, respectively,[34] ascertained the semiconducting behavior of

MoS_2 in the hybrid material **3**. Regarding hybrid material **4**, bands due to 2LA(M), E^1_{2g}, and A_{1g}, upon on-resonance excitation at 514 nm, were evident at 350, 354 and 419 cm^{-1}, with the intensity of the 2LA(M) mode decreased by 20% as compared to that due to exfoliated WS_2 (Figure 7b). Furthermore, for both **3** and **4**, the A_{1g} and E^1_{2g} modes found red-shifted by 1-2 cm^{-1} as compared to the values registered for exfoliated MoS_2 and WS_2 respectively. The latter is attributed to intra-hybrid charge-transfer phenomena developed between CNDs **2** and the TMDs, in accordance with literature reports.[35] Since **2** is highly fluorescent, weak and broad Raman bands attributed to –NC=O, C=O and C-H units were observed for both **3** and **4** only upon excitation at 1064 nm (Figure 7c-d).

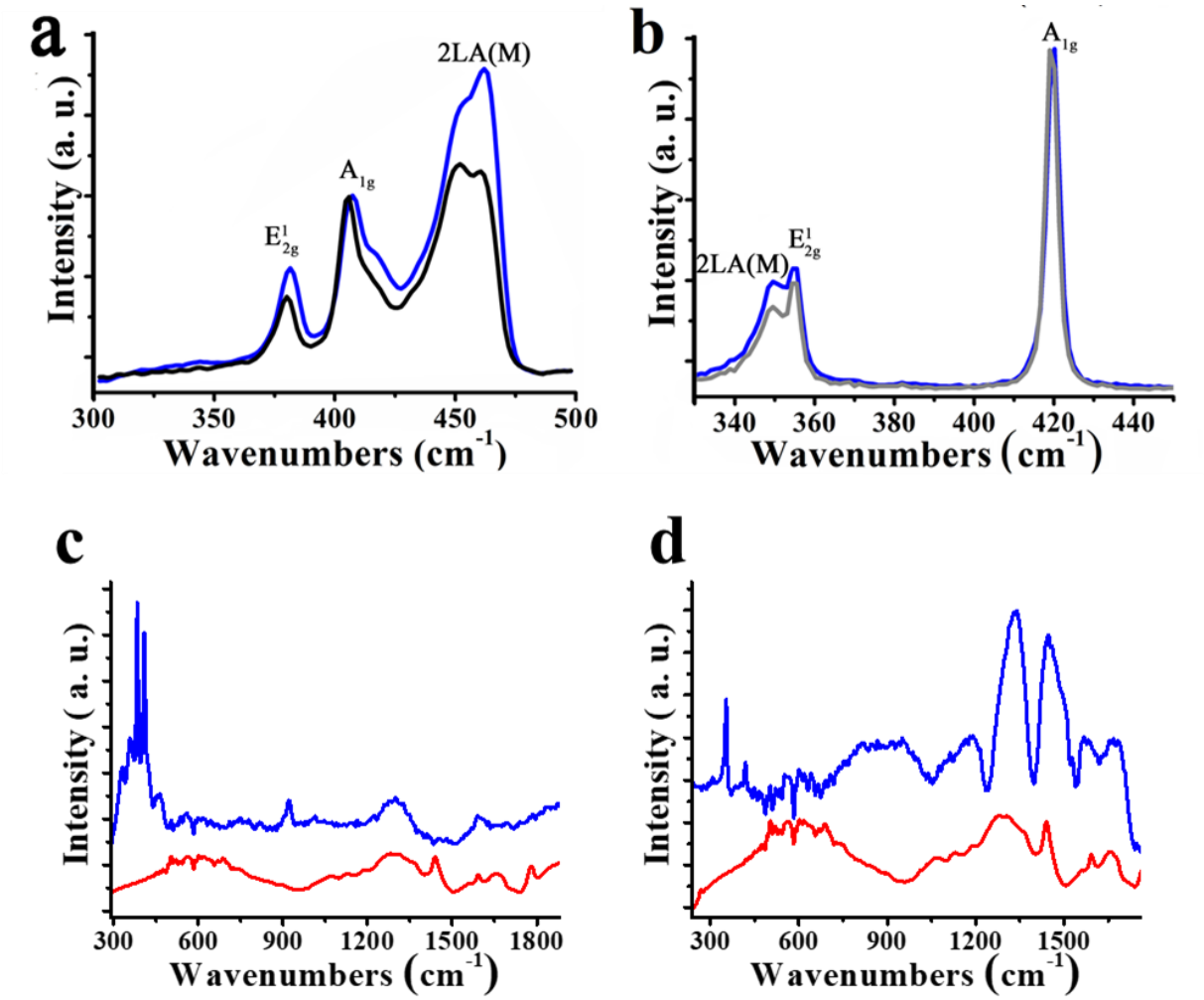

Figure 7. Raman spectra normalized at A_{1g} mode for (a) exfoliated MoS_2 (blue) and **3** (black) at λ_{exc} 633 nm, and (b) exfoliated WS_2 (blue) and **4** (grey) at λ_{exc} 514 nm. (c, d) Raman spectra at λ_{exc} 1064 nm for CNDs **2** (red) and **3** (blue), and CNDs **2** (red) and **4** (grey), respectively.

The loading of CNDs onto MoS_2 and WS_2 in hybrid materials **3** and **4**, respectively, was evaluated by TGA (Figure 8). The modified CNDs **2** bearing 1,2-dithiolane units were thermally stable up to 200 ºC under nitrogen atmosphere, while a 65% of mass loss was identified at the temperature range 200-500 ºC. Since MoS_2 and WS_2 are thermally stable in that temperature range, the observed mass loss for **3** and **4**, 7.5% and 3.0% respectively, is related to the decomposition of modified CNDs present in the two hybrids. Although this is a relatively small mass loss, it is consistent with the edge functionalization of the limited S vacant sites of MoS_2 and WS_2.

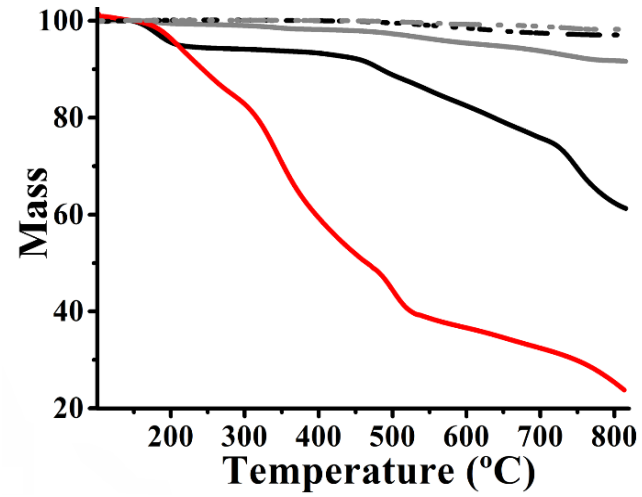

Figure 8. Thermographs for **2** (red), exfoliated MoS_2 (dotted black), exfoliated WS_2 (dotted gray), **3** (black), and **4** (grey), obtained under inert atmosphere.

The hybrids **3** and **4** were morphologically imaged by HR-TEM. A few drops of a dispersion of the materials in hexane were deposited on the TEM grid and imaged after the solvent was evaporated. Extensive imaging of several different areas and flakes of **3** and **4** revealed that the size of MoS_2 and WS_2 is in the order of few hundred nanometers, e.g. around 200-400 nm. Although mostly oligolayered flakes were observed, most likely due to restacking of the TMDs during the drying process of the sample after depositing it on the TEM grid, the presence of some monolayered ones were also identified. In order to get better insight on **3** and **4**, TEM studies complemented with spatially-resolved electron energy loss spectroscopy (EELS) were performed. Figures 9a and 9f show high angle annular dark field (HAADF) scanning TEM (STEM) micrographs for **3** and **4**, respectively. Based on the following spectroscopic/chemical TEM analyses, the bright small objects, observed in these images, were assigned to CNDs

covalently anchored on TMDs flakes. This is confirmed by energy dispersive X-ray spectroscopy (EDS) analyses (Figures 9b, g) and EELS (Figures 9c-e and 9h-j, respectively). Figure 9c displays an ADF micrograph of **3** and an EELS spectrum-image (SPIM) recorded in the red marked rectangular area. Three EEL spectra were extracted in the highlighted square regions (Figure 9e(i)-(iii)). The S-$L_{2,3}$ and Mo-M edges are visible in the three spectra and correspond to MoS_2.[36] It is worth mentioning that no MoO_x was observed highlighting the high quality and purity of the materials. In addition, C was detected in specific areas, see the presence of the C-K edge (Figure 9e(ii)-(iii)). This C-K edge, which is superposed to the Mo-Mo[37] edge, is associated with the presence of **2** within the hybrid **3**. The chemical C map obtained from the analysis of C-K edge (Figure 9d) clearly supports this finding.[36] Indeed, **2** is observed not only in the ADF-STEM micrograph (Figure 9c) but also in this C-map (Figure 9d). Similar assays were performed for **4** and from TEM analyses (Figures 9f-j) the presence of **2** attached on WS_2 was confirmed.

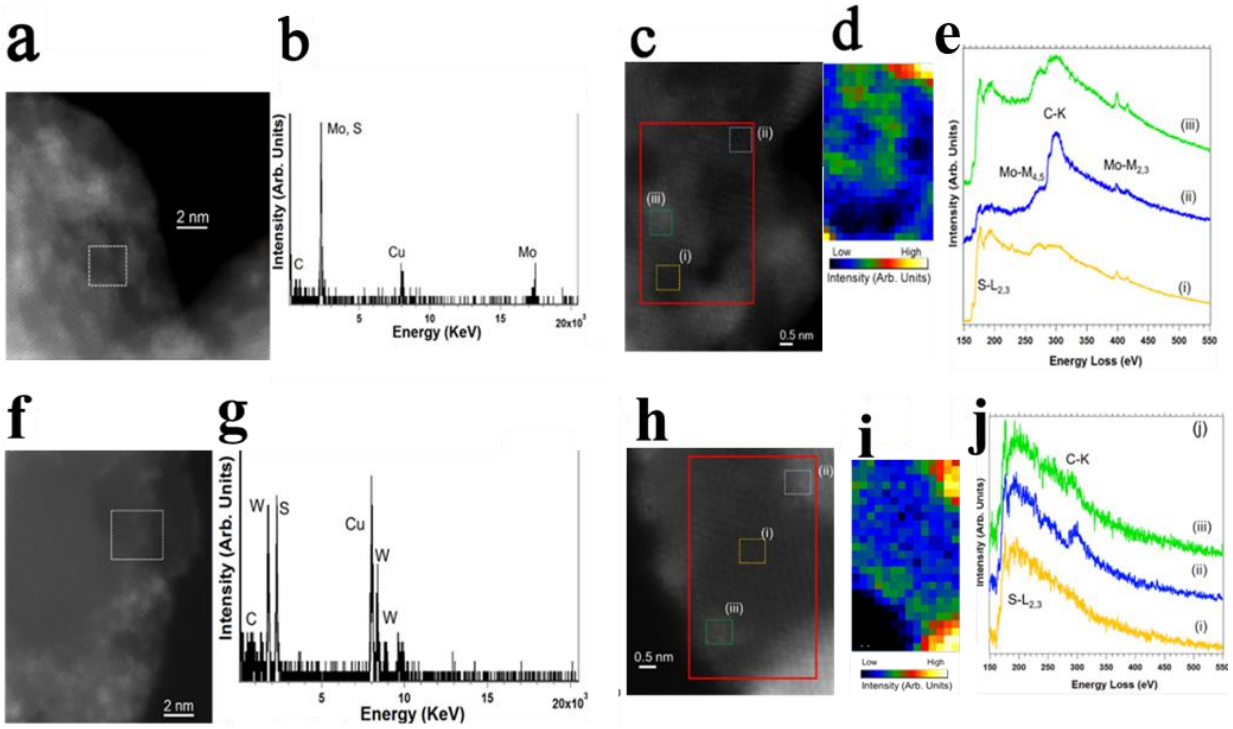

Figure 9. Representative HRSTEM-ADF images for (a, d) **3**, and (f, h) **4**. (b, g) EDS on the squared white areas in (a, f), respectively. In the red regions of (c, h) spectrum-images SR-EELS were recorded. (d, i) Carbon elemental maps extracted from the integrated intensity of the C-K edge of the two EELS spectra-image recorded in the red areas in (c, h). (e) Three spectra from the sum of 9 (3x3) EELS extracted from the marked areas of the EELS SPIM of (c). The C-K

edge (~284 eV) is observed in (ii) and (iii) superposed with the Mo-M edge. The S-$L_{2,3}$ and Mo-M edge of MoS_2 are visible in the 3 spectra ((i)-(iii)). (j) Similar analysis for **3** as in (e). Three spectra from the sum of 16 (4x4) EELS extracted from the EELS SPIM of (h), showing the S-$L_{2,3}$ and C-K (in this case only in (ii) and (iii)) edges.

Focusing on the optical properties of **3** and **4**, electronic absorption and fluorescence assays were conducted. In more detail, characteristic bands centered at 680, 620, 485, 400 nm, and 645, 535, 475, 420 nm, corresponding to semiconducting MoS_2 and WS_2, respectively (Figure 10a) were identified for hybrids **3** and **4**, respectively. Unfortunately, the strong absorption features of **2** masked the broad band of modified **2**, appearing at 370 nm, hence hampering to defer conclusive statements regarding possible intra-hybrid electronic communication between the two species in the ground state. Nevertheless, the situation is rather clear at the excited state, wherein the strong emission of modified **2**, centered at 470 nm upon excitation at 370 nm, was found blue-shifted by 30 nm, at 440 nm, and quantitatively quenched in both **3** and **4** (Figure 10b). The later postulates the occurrence of an additional deactivation path for the singlet-excited state of **2**, through an energy or charge-transfer process. Next, analysis of the fluorescence emission decay profiles at 450 nm for the singlet excited state of CNDs upon excitation at 376 nm, gave a monoexponentially fitted lifetime of 6.3 ns. However, the corresponding analysis for **3** and **4** resulted in a biexponential decay, with the identification of major faster components with 1.2 and 1.1 ns lifetime, corresponding to the quenching of singlet excited state of CNDs **2** in **3** and **4**, respectively.

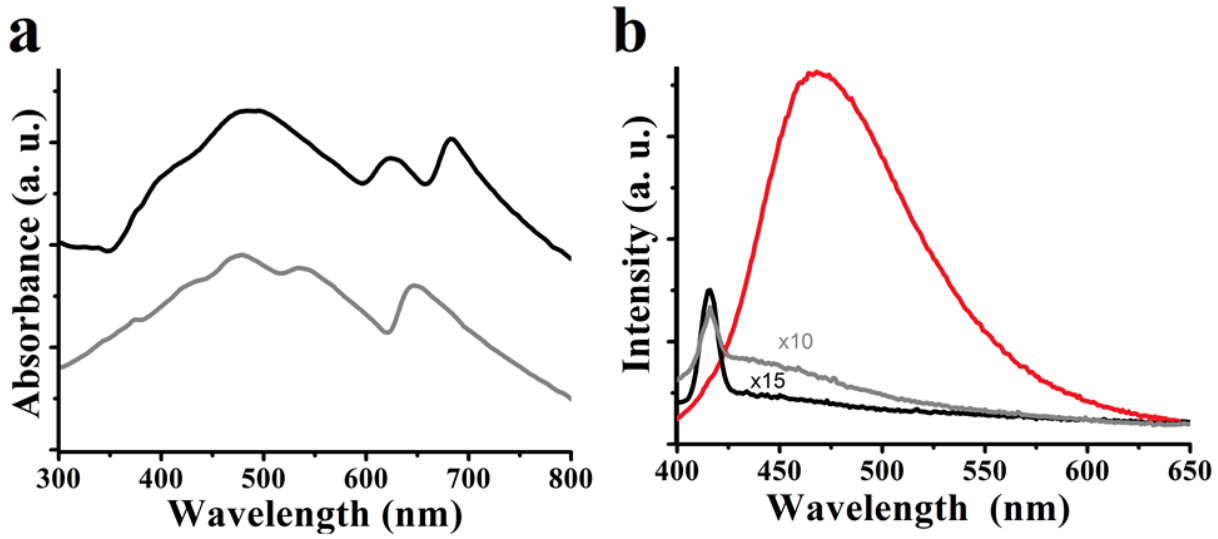

Figure 10. (a) Absorption and (b) emission spectra (λ_{exc} 370 nm) of **3** (black), **4** (grey) and **2** (red), in DMF.

The electrochemical behavior of **3** and **4** was successively investigated in DMF (Figure 11). The cyclic voltammogram (CV) of exfoliated MoS_2 revealed irreversible oxidations at Epa = -0.08 and 0.48 V and reductions at Epc = -1.20 and -1.69 V vs Fc/Fc^+. In **3**, the first oxidation wave was too broad to pick the peak potential, while the second one was better defined with an Epa = 0.54 V. The two reductions were located at Epc = -1.48 and -2.20 V as a consequence of the covalent functionalization. The CV of exfoliated WS_2 revealed irreversible oxidations at Epa = 0.23 and 0.44 V and reductions at Epc = -1.40 and -1.98 V. Upon covalent attachment of **2**, the oxidation waves broadened, making it difficult to identify the peak potential, while the reduction was anodically shifted to Epc = -1.37 and -1.63 V. Importantly, both MoS_2 and WS_2 were found to be electroactive and such property persisted upon chemical functionalization with **2**. The facile oxidation of MoS_2 over WS_2 suggests it to be better electron donor. The CV of **2** revealed no measurable electrochemical activity within the potential window.

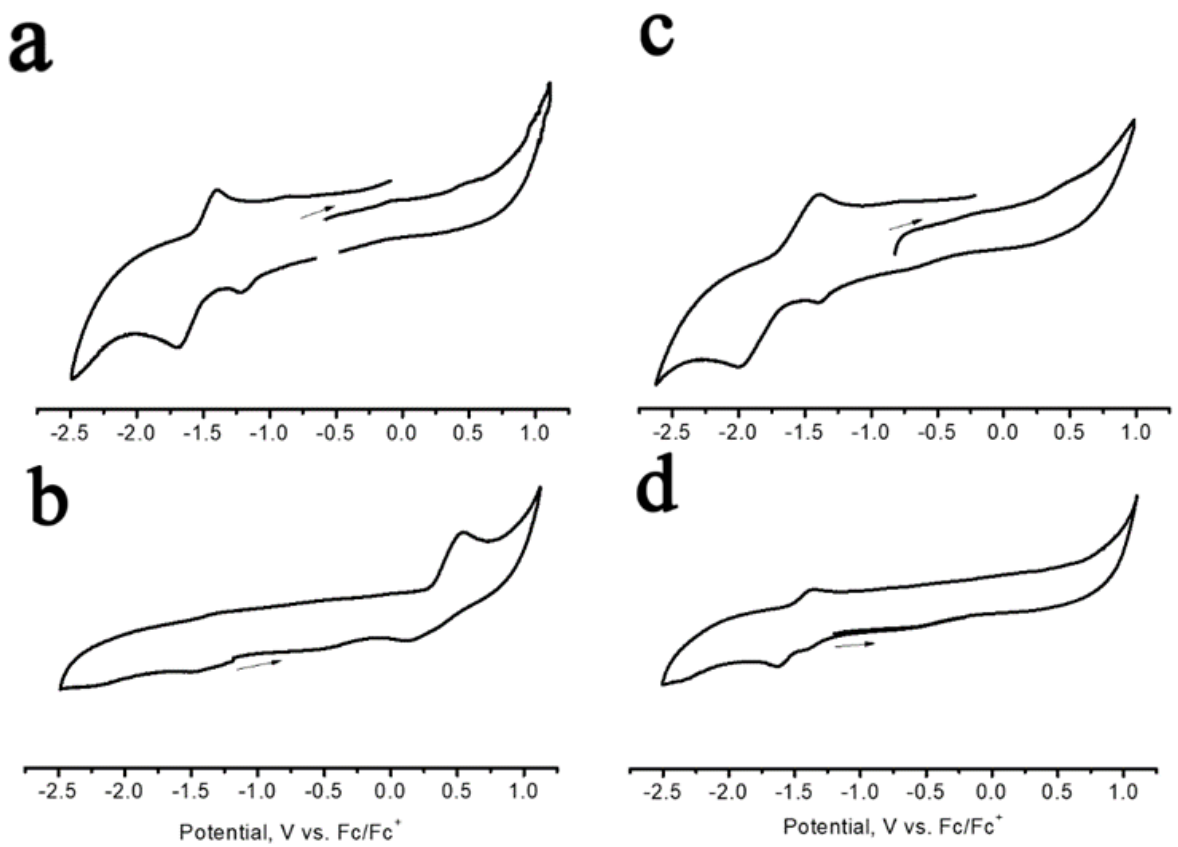

Figure 11. Cyclic voltammograms of (a) exfoliated MoS_2, (b) exfoliated WS_2, (c) **3**, and (d) **4** in DMF containing 0.1 M of n-Bu_4NClO_4 as electrolyte. Scan rate = 100 mV/s.

The excited state events were probed by femtosecond pump-probe transient absorption spectroscopy in DMF, where dispersion of the hybrids was appreciable. The samples were excited at 370 nm, corresponding mainly to the excitation of **2** and at 425 nm corresponding mainly to the excitation of TMDs. In agreement with literature reports,[38] immediately after 425 nm excitation of exfoliated MoS_2, three minima at 503, 637 and 696 nm due to excitonic transitions as seen in the absorption spectrum, and two maxima at 595 and 663 nm corresponding to induced absorption of B and A excitons, were observed (Figure 12a). During the first 10 ps, all peaks experienced blue shift ascribed to cooling of hot excitons and/or inter-excitonic interactions. In the case of exfoliated WS_2, two minima at 545, and 652 nm (B and A excitons, by comparison with the absorption spectrum) and two maxima at 516 and 617 nm were observed (Figure 12b). The peak positions also experienced a small blue-shift of 2 nm within the first 10 ps.

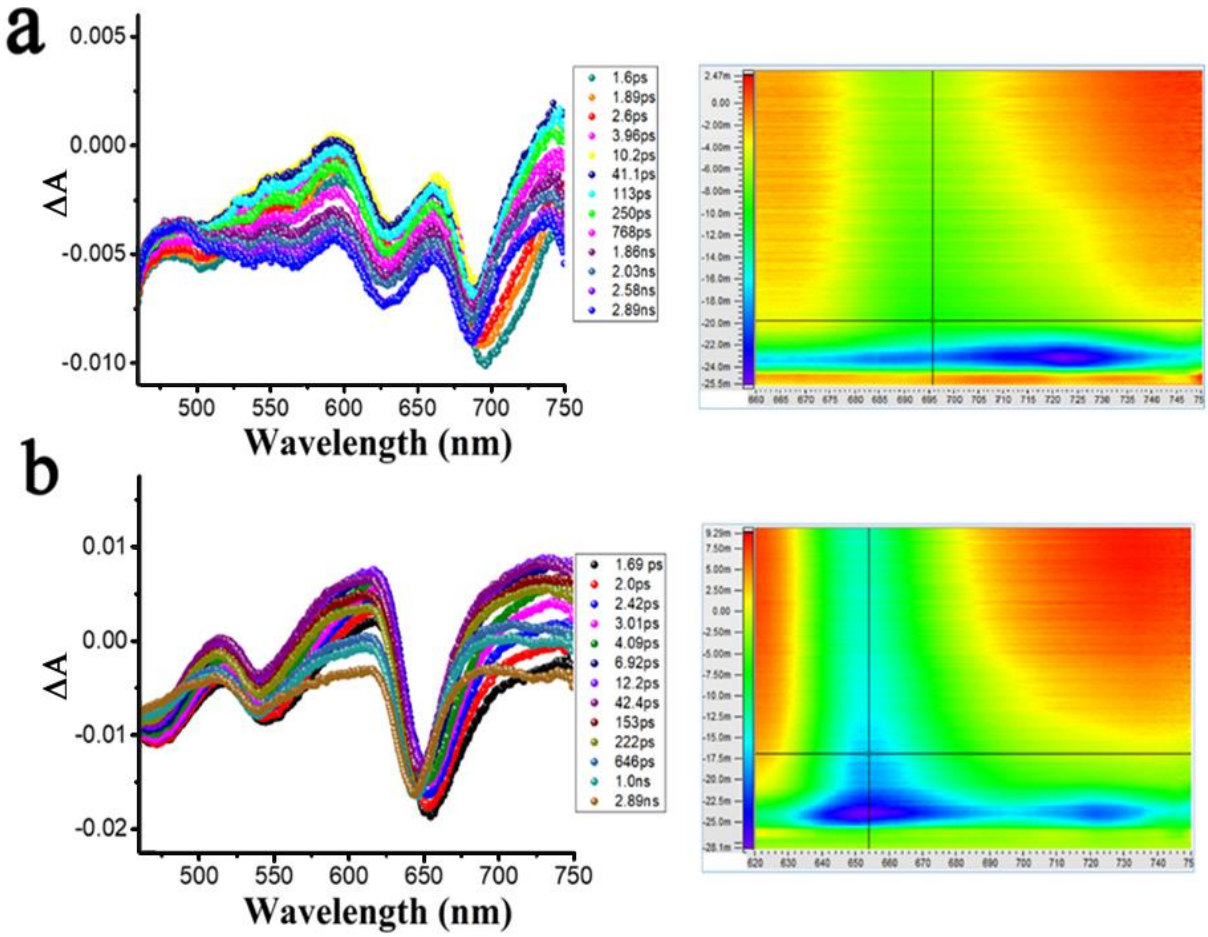

Figure 12. Femtosecond transient absorption spectra at the indicated delay times of exfoliated (a) MoS_2 and (b) WS_2, in DMF at the excitation wavelength of 425 nm. The right-hand panel shows intensity-wavelength maps.

Figure 13 shows the transient absorption spectra and intensity-wavelength maps of CNDs **2**, CND-MoS_2 **3** and CND-WS_2 **4** dispersions in DMF at λ_{exc} 370 nm mainly exciting the **2**. The transient spectra of CNDs (λ_{exc} 370 nm) revealed positive peaks at 460 and 590 nm (Figure 13a) originating from transitions involving excited **2**. The decay of these peaks was rather slow, consistent with the longer fluorescence lifetime of **2** (6.3 ns). When exfoliated MoS_2 and WS_2 were excited at 370 nm (Figure 13b, c), the spectra revealed features corresponding to these materials, however, with much diminished peak intensities compared to that shown in Figure 12 at λ_{exc} 425 nm. These observations suggest that at λ_{exc} 370 nm, in addition to CNDs, both MoS_2 and WS_2 also get excited to some extent. Interestingly, when **3** and **4** were excited at 370 nm, the peaks corresponding to the excited **2** revealed rapid deactivation with simultaneous development

of strong excitonic peaks of MoS_2 and WS_2, more so for **3** than that for **4** (Figure 13d-e). These results indicate occurrence of energy transfer from singlet excited **2** to MoS_2 and WS_2 in the hybrids. In both hybrids the excitation transfer was complete within 4-5 ps, indicating an efficient process.

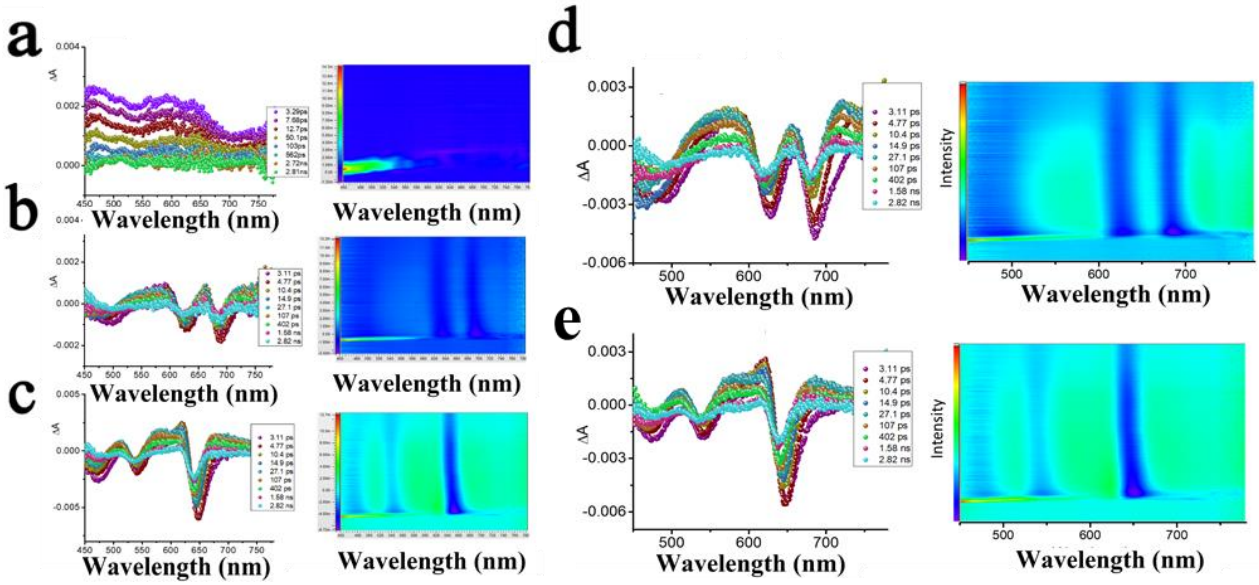

Figure 13. Femtosecond transient absorption spectra at the indicated delay times of (a) **2**, (b) MoS_2 and (c) WS_2 (d) **3**, and (e) **4** in DMF (λ_{exc} 370 nm). The right-hand panel shows intensity-wavelength maps.

Next, the hybrids were excited at 425 nm, wherein majority of MoS_2 and WS_2 have absorbance. The transient spectral features of **3** (Figure 14a) were distinctly different from that of exfoliated MoS_2 (Figure 12a), especially with respect to the peak time profiles (see intensity-wavelength maps). Figure 14a(iii) shows the time profile of the 688 nm peak of exfoliated MoS_2 and **3** corresponding to the excitonic peak at 688 nm. The recovery of the exciton peak was slow for **3** suggesting occurrence of excited state events from the excited MoS_2 to the covalently linked **2.** Earlier, a facile oxidation was observed for MoS_2 (Epa = -0.08 V) suggesting that it could act as an electron donor generating charge separated state.[38] In such an event, charge transfer from a dissociated excitonic state would be promoted to **2** conduction band, generating a charge separated state. The hole in MoS_2 layer would recover slowly due to a charge recombination process. On the other hand, transient spectra recorded for **4** (Figure 14b) were close to that of unmodified WS_2 (Figure 12b). The time profiles of the 652 nm peak (Figure 14b(iii)) were superimposable suggesting lack of major excited state events such as charge transfer from

excited WS_2 to **2**. This could be rationalized to the harder oxidation of WS_2 (Epa = 0.23) that would dampen any charge transfer events due to energy considerations. Hence, no further analysis was performed on this hybrid material **4**.

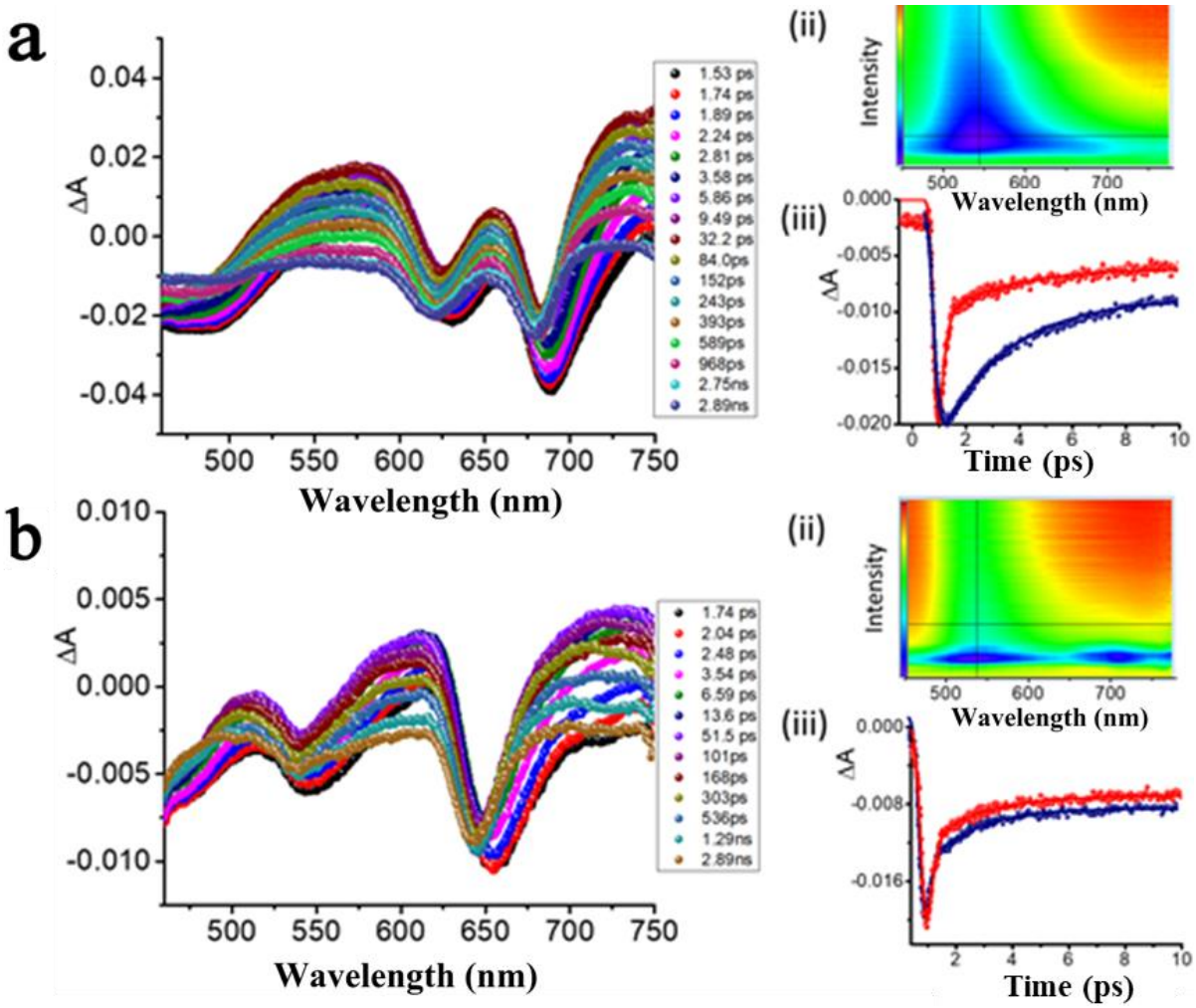

Figure 14. Femtosecond transient spectra of (a) **3**, and (b) **4**, in DMF (λ_{exc} 425 nm). The right-hand panels show (ii) intensity-wavelength map and (iii) an overlap time profile of the 688 nm of **3** (blue) and exfoliated MoS_2 (red) and 652 nm of **4** (blue) and exfoliated WS_2 (red).

Further, the transient data of exfoliated MoS_2 and hybrid material **3** were subjected to global analysis for kinetic evaluations (Figure 15). Decay associated spectra of exfoliated MoS_2 revealed three major components; the spectrum at 2.3 ps consists of positive peaks at the spectral range, where excitonic peaks are expected. The spectrum at 1.1 ns had decay of positive transients. The final component with over 3 ns related to only the excitonic signals with positive shift relative to A exciton. Earlier, for the ultimate decay of the excitons, a lifetime of around 30

ns was established.[38] Interestingly, for **3**, at least 5 components were needed for satisfactory fit. The component at 1 ps was too fast to be assigned to any excited state process as several ultrafast processes such as vibrational cooling, solvent relaxation, etc. occur. The 4.2 and 1.3 ps components had features of excitons in the growth and decay, respectively. The 246 ps component had features in the 450-550 nm range, ascribed to trionic state that revealed faster decay. The long-lived decay component had only the excitonic features similar to that observed for unmodified MoS_2. These results suggest that the charge separation occurs with a time constant of about 250 ps in the hybrid **3**.

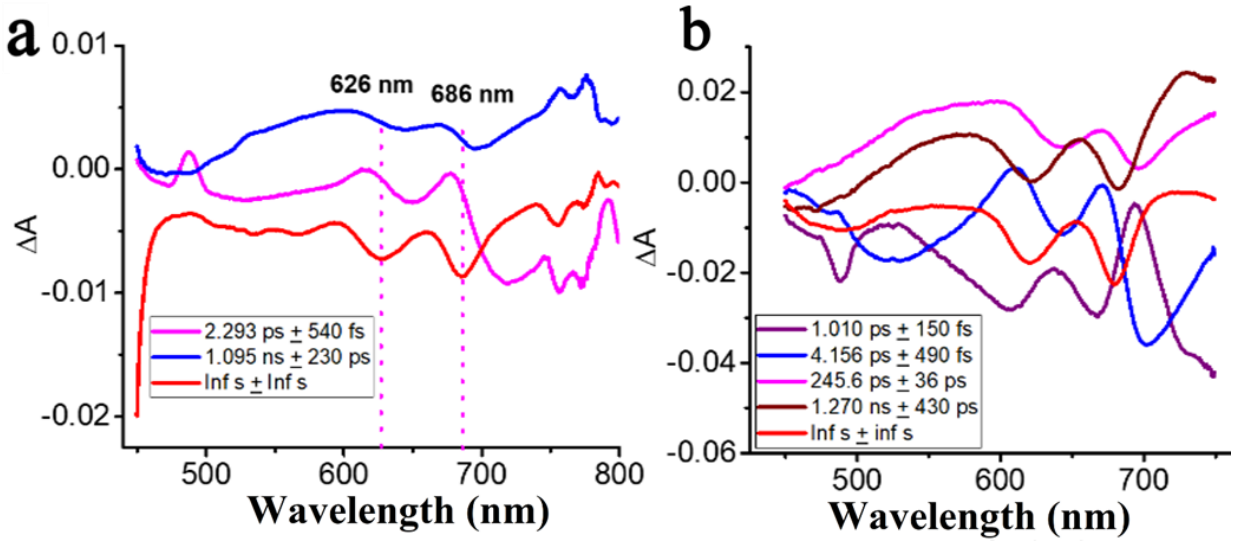

Figure 15. Decay associated spectra of (a) exfoliated MoS_2, and (b) **3** for the transient data shown in Figure 14 and Figure 12.

Moving on the development of TMD-based hybrids with porphyrin and Zn-phthalocyanine, the 1,2-dithiolane-based porphyrin (H_2P) **5** was initially synthesized by a condensation reaction between α-lipoic acid and 5-(4-aminophenyl)-10,15,20-(triphenyl)porphyrin, and the product was confirmed by NMR spectroscopy and mass spectrometry (see experimental section). Next, based on the general functionalization protocol of exfoliated transition metal dichalcogenides with 1,2-dithiolanes,[8] reaction of exfoliated MoS_2 and WS_2 with **5** yielded H_2P-MoS_2 hybrid material **6**, and H_2P -WS_2 hybrid material **7**, respectively, according to Figure 16. Filtration of the reaction mixture over a PTFE membrane (0.2 μm pore size) followed by extensive washing with dichloromethane, assured the removal of any non-covalently physisrobed porphyrin **5** species from the MoS_2 and WS_2 nano-sheets. The purified hybrid materials **6** and **7** showed better

solubility in DMF, benzonitrile and isopropanol, while they were completely and completely insoluble in dichloromethane and water.

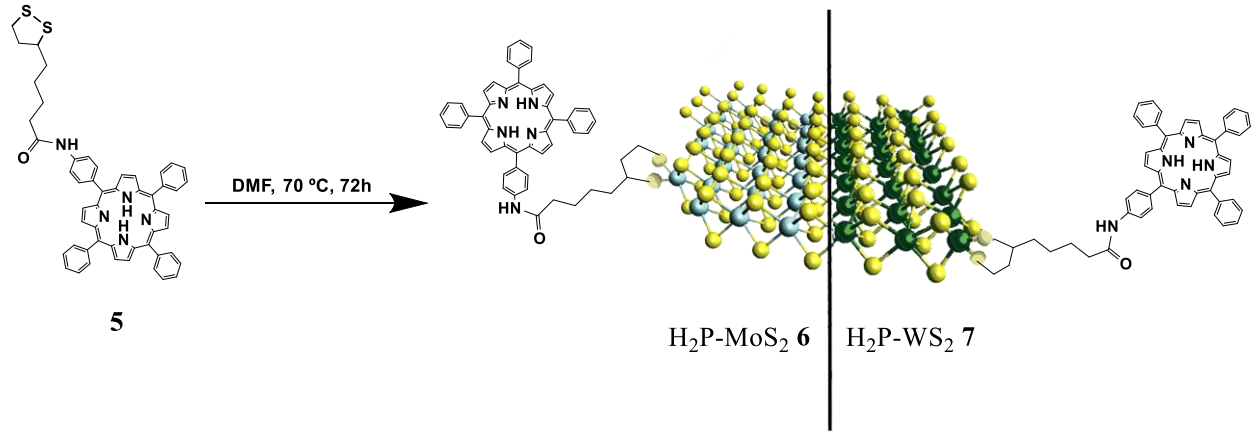

Figure 16. Reaction route for obtaining H_2P-MoS_2 and H_2P -WS_2 hybrid materials **6**, and **7** respectively.

The successful covalent incorporation of **5** on MoS_2 and WS_2 was initially probed by vibrational spectroscopic means. Attenuated total reflectance infra-red ATR-IR spectroscopy revealed for hybrid materials **6** and **7** (Figure 17) the presence of (a) C-H stretching vibration modes due to the alkyl chain that connects the porphyrin unit with the transition metal dichalcogenides at 2950 and 2848 cm^{-1}, (b) amide carbonyl vibration at 1660-1652 cm^{-1}, and (c) the aromatic C=C bending modes at 1590 cm^{-1}.

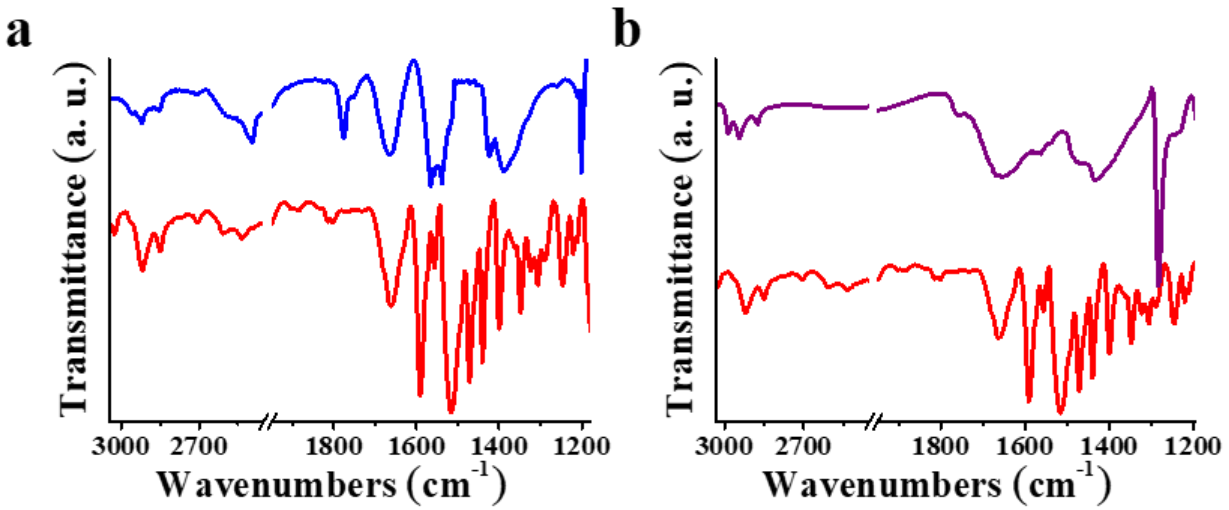

Figure 17. ATR-IR spectra for **5** (red) and (a) H_2P-MoS_2 hybrid material **6** (blue), and (b) H_2P-WS_2 hybrid material **7** (purple).

Similar to CND-MoS_2 **3**, Raman spectrum of H_2P-MoS_2 **6** obtained by excitation at 633 nm under on-resonance conditions for MoS_2, revealed characteristic modes for MoS_2 in the region 150-500 cm^{-1}. In more detail, Raman bands centered at 451, 403 and 379 cm^{-1} (Figure 18a) associated to the 2LA(M) due to disorder and defects, the out-of-plane vibrations of S atoms A_{1g} and the in-plane vibrations of S and Mo atoms E^1_{2g} modes, respectively. The location of E^1_{2g} and A_{1g}, precisely their frequency difference calculated to be 24 cm^{-1} which is directly related with the thickness and number of layers of MoS_2,[31] showcasing the presence of few MoS_2 layers in the hybrid material **6**. Markedly, the intensity ratio of the modes 2LA(M)/A_{1g} for **6** decreases by around 60%, as compared to the corresponding one for exfoliated MoS_2, proving that the amount of sulfur vacancies was reduced. The latter is well understood by considering the MoS_2 functionalization, as occurred by the grafting of 1,2-dithiolane moiety of **5**, at the edges possessing Mo atoms with S vacant sites. Along similar lines is the situation with the Raman spectrum for the exfoliated WS_2 and the corresponding hybrid material **7**. In brief, the Raman spectrum of exfoliated WS_2 shows three bands, namely the 2LA(M) at 348 cm^{-1}, the E^1_{2g} at 353 cm^{-1} and the A_{1g} at 419 cm^{-1} (Figure 18b). In H_2P-WS_2 hybrid material **7**, a 10% of reduction in the intensity ratio of 2LA(M)/A_{1g} was observed (2.0 for **7** vs 1.8 for WS_2), associated with the functionalization of WS_2 with the 1,2-dithiolane-based porphyrin **5.**

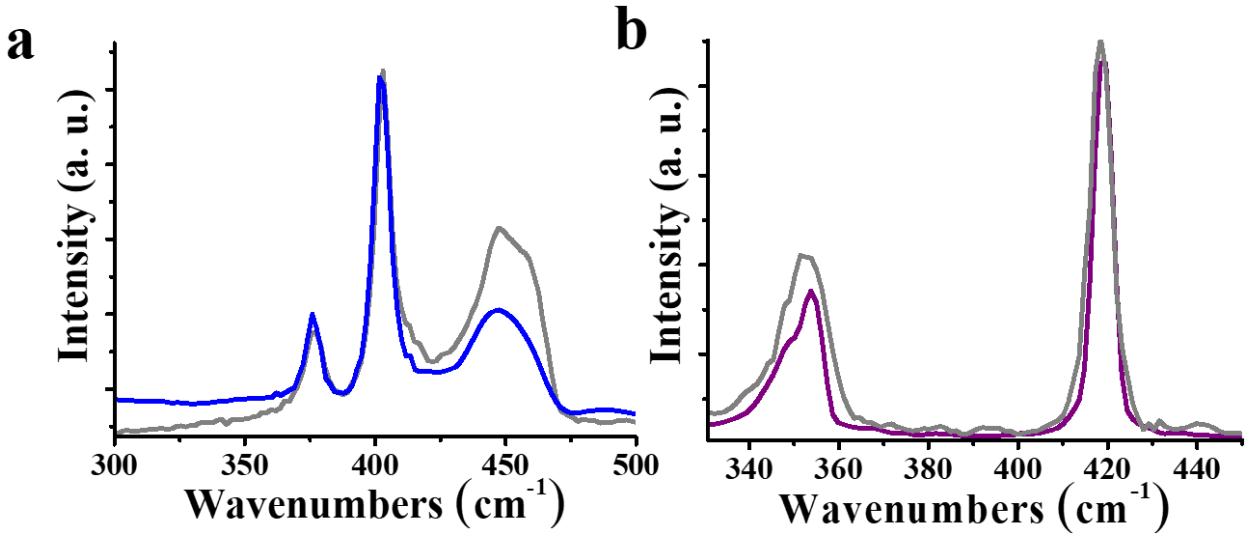

Figure 18. (a) Raman spectra for exfoliated MoS_2 (gray) and H_2P-MoS_2 hybrid material **6** (blue) at 633. Inset: Raman spectra for H_2P-MoS_2 hybrid material **6** (blue) and exfoliated MoS_2 (gray) at 514 nm. (d) Raman spectra at 514 for exfoliated WS_2 (gray) and H_2P-WS_2 hybrid material **7** (purple).

Thermogravimetric analysis (TGA) delivered information related with the degree of functionalization in **6** and **7**. Since exfoliated MoS_2 and WS_2 were found to be thermally stable under nitrogen atmosphere in the temperature region 100-800 ºC, the mass loss observed in the modified nano-sheets is directly related to the thermal decomposition of the organic addends. Hence, the mass loss of 9% for **6** and 17 % for **7** (Figure 19a) occurred up to 520 ºC is ascribed to the porphyrin addend. Based on those mass losses, the loading of one porphyrin moiety per 54 and 20 units of MoS_2 and WS_2, respectively, was calculated.

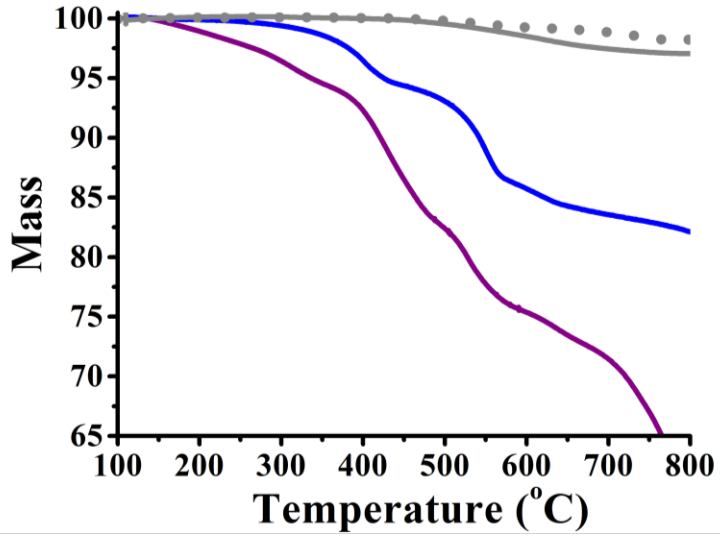

Figure 19. Thermographs for exfoliated MoS_2 (gray), exfoliated WS_2 (dot gray), H_2P-MoS_2 hybrid material **6** (blue) and H_2P-WS_2 hybrid material **7** (purple).

The morphology of modified MoS_2 and WS_2 with porphyrin addends was imaged with the aid of FE-SEM. Aggregations were observed in all materials (Figure 20a and b) most likely due to sample preparation for imaging. Even though dispersions of **6** and **7** in dichloromethane were drop-casted onto the sample-holder and imaged after the solvent evaporated, restacking of the nano-sheets during the evaporation of solvent took place. Nevertheless, the size of the flakes can be estimated to be few hundreds of nm, while the lattice of MoS_2 and WS_2 within **6** and **7** was observed undamaged and free of visible defects.

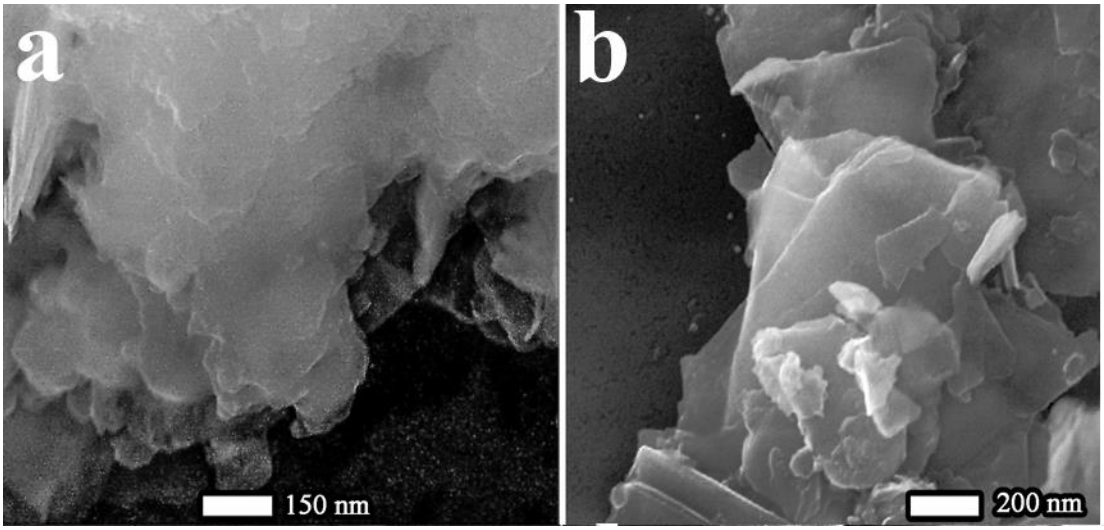

Figure 20. Representative FE-SEM images for (a) H_2P-MoS_2 hybrid material **6,** (b) H_2P-WS_2 hybrid material **7**.

Next, focusing on the optical properties of the H_2P-MoS_2 **6** and H_2P-WS_2 **7**, the electronic absorption spectra were registered and compared with those derived from the free porphyrin **5**. In more detail, the UV-Vis absorption spectrum of **5** showed a sharp absorption at 418 nm owed to the Soret or B band ($\pi \rightarrow \pi^*$), accompanied by small Q ($n \rightarrow \pi^*$) bands at 516, 550, 596 nm and 648 nm (Figure 21). The UV-Vis spectra for hybrid materials **6** and **7** represented basically a superimposition of the spectra belonging to the individual components. The spectra **6** and **7** are dominated by the characteristic Soret band at 418 nm, while also some bands due to MoS_2 (418, 625 and 686 nm) in **6** and due to WS_2 (474, and 642 nm) in **7** were discernable.

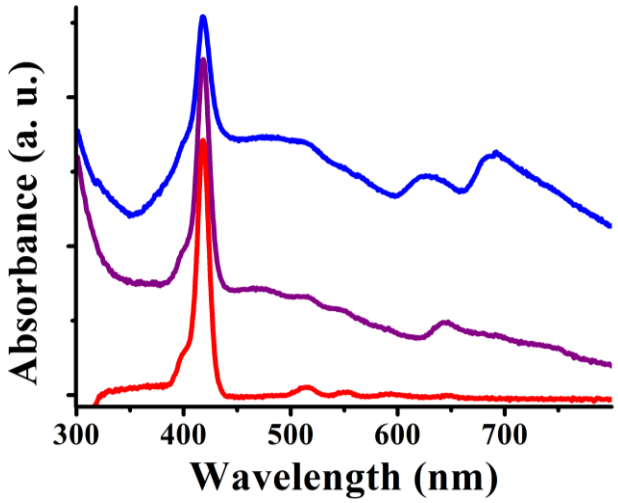

Figure 21. Absorption spectra of (a) free porphyrin derivative **5** (red), H_2P-MoS_2 hybrid material **6** (blue) and H_2P-WS_2 hybrid material **7**, in DMF.

Next, electronic interactions at the excited state between porphyrin and MoS_2 or WS_2 within hybrid materials **6** and **7** were probed by fluorescence emission spectroscopy. Specifically, upon excitation at the Soret band (i.e. 420 nm) of **5**, strong fluorescence emission centered at 650 and 720 nm was observed. Photoexcitation of hybrids **6** and **7** at 420 nm resulted on significant depression of the porphyrin's photoluminescence as compared with that registered for **5**, for samples possessing equal absorption at the excitation wavelength (Figure 22). These findings imply the existence of effective deactivation of the singlet-excited state of **5** via charge/energy transfer to MoS_2 and WS_2 in hybrids **6** and **7**, respectively. Exactly the same result, namely quenching of photoluminescence, was obtained when the Q-bands of the porphyrin were excited at 516, 550, 596 or 648 nm (Figure 22b-d). In addition, time-resolved photoluminescence assays based on the time-correlated-single-photon-counting method were conducted to get further insight on the electronic communication between the porphyrin and MoS_2 and WS_2 within hybrids **6** and **7**, respectively. The fluorescence decay profile for porphyrin **5** was monoexponenetially fitted, showing a lifetime of 10.1 ns. Instead, hybrids **6** and **7** better fitted with a biexponential equation, giving rise to both a faster lifetime of 2.2 and 1.8 ns, accompanied for a slow of 9.7 and 8.6 ns, for **6** and **7**, respectively. The fast processes are related with transduction of charge/energy from the photoexcited porphyrin to MoS_2 and WS_2, while the slower ones are attributed to free porphyrin. The quenching rate constant and quantum yield of the singlet excited state were calculated to be 1.41×10^{-8} and 1.43×10^{-8} s^{-1} and 0.56 and 0.57, for **6** and **7**, respectively. Further, both techniques are in agreement with the results, probing strong electronic interactions between the two components, porphyrin and TMDs, at the excited states.

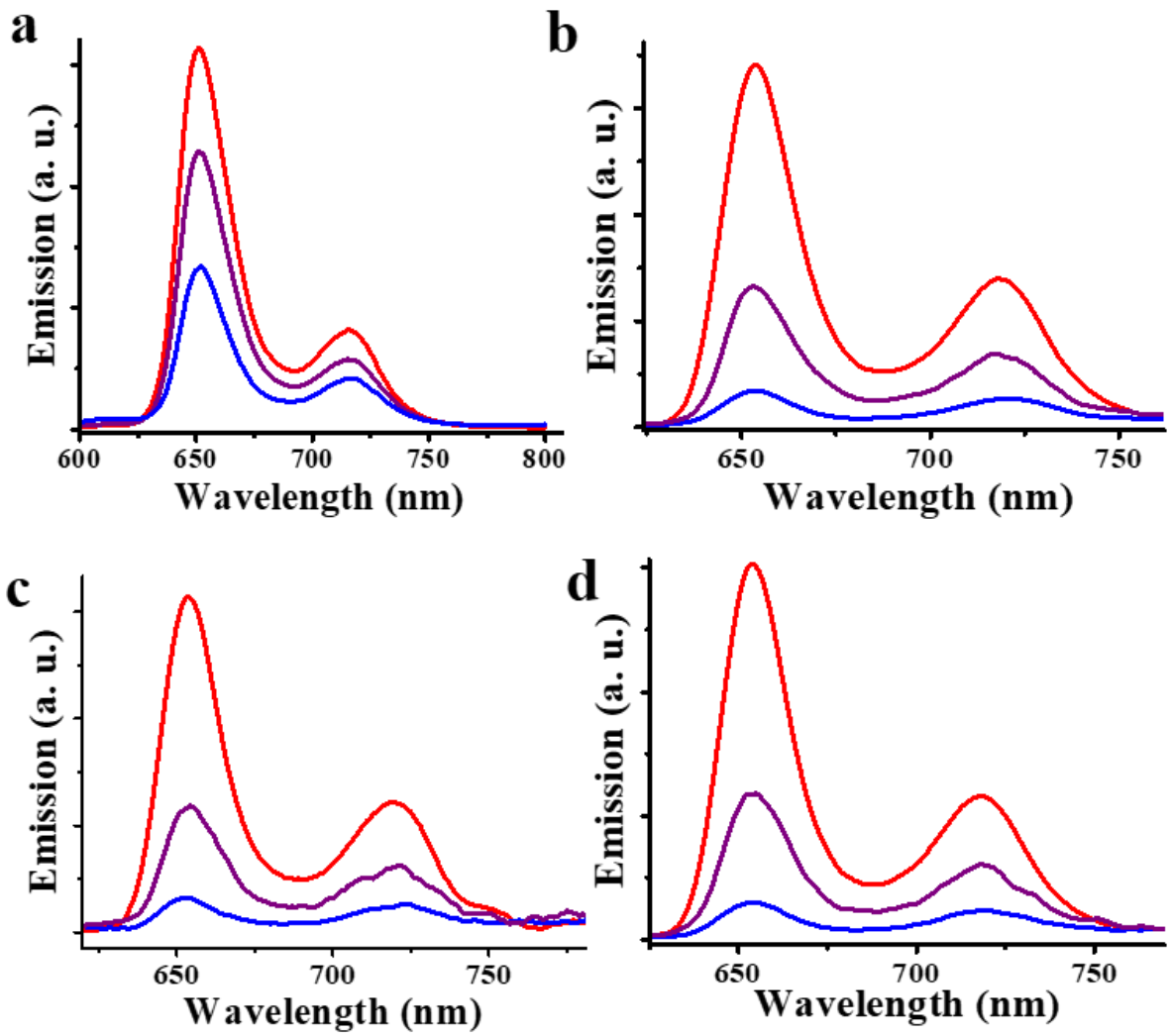

Figure 22. Emission spectra of free porphyrin derivative **5** (red), H_2P-MoS_2 hybrid material **6** (blue) and H_2P-WS_2 hybrid material **7**, at (a) λ_{exc} 420 nm, and (b) λ_{exc} 516 nm, (c) λ_{exc} 550 nm, (d) λ_{exc} 595, obtained in DMF.

In the last part of the study, the functionalization of MoS_2 with Zn-phthalocyanine was accomplished. Briefly, the synthetic route started with the condensation of zinc-metallated 4-((4,17,24-tri-tert-butylphthalocyanine-9-yl)oxy)ethan-3-amine with α-lipoic acid, yielding zinc phthalocyanine **8**. The chemical structure of **8** was confirmed by NMR spectroscopy and mass spectrometry (see experimental section). Reaction with MoS_2 in DMF at 70 ºC for 96 hours afforded ZnPc-MoS_2 hybrid material **9** (Figure 23). The hybrid material **9** was isolated in the solid-state via filtration on a PTFE membrane filter (0.2 μm pore size), followed by extensive

washing with dichloromethane. The latter allowed to completely remove unreacted **8** as well as soluble organic byproducts formed, confirmed by the absence of any UV-Vis bands in the electronic absorption spectrum of the filtrate.

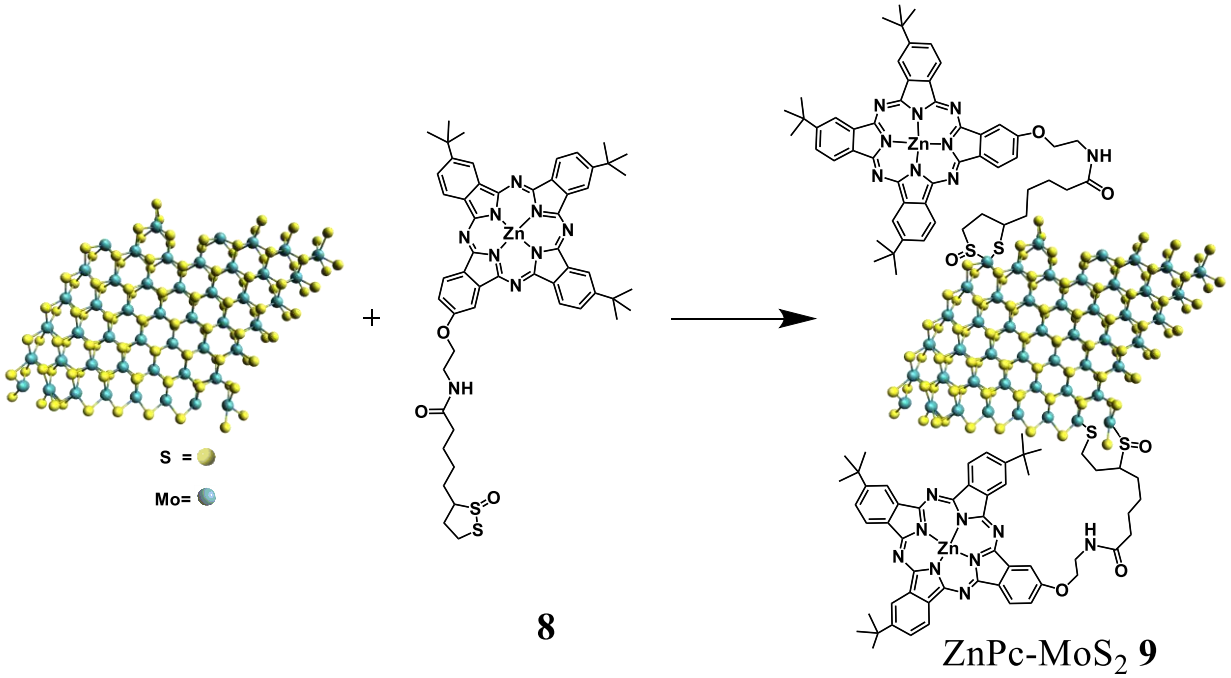

Figure 23. Functionalization of exfoliated semiconducting MoS_2 with ZnPc derivative **8** yielding ZnPc-MoS_2 hybrid material **9**.

The first indirect proof for the success of functionalization and production of **9** was given by the solubility enhancement achieved and the stability attained in wet media. Although exfoliated MoS_2 is marginally soluble in DMF (*ca*. 0.4 mg/mL) and practically insoluble in other solvents, the ZnPc-MoS_2 hybrid material **9** showed superior solubility in DMF (*ca*. 3.4 mg/mL), while also dissolved in MeOH (*ca*. 0.7 mg/mL) and benzonitrile (*ca*. 0.8 mg/mL). In fact, those solubility values refer to samples that remained stable even after a period of few weeks, without observing any precipitation, contrasting the case of exfoliated MoS_2 which after a couple of days in DMF significant precipitation was observed (Figure 24). The presence of *tert*-butyl units as side groups in ZnPc is judged beneficial for improving solubility since they lay perpendicular to the phthalocyanine core, keeping apart adjacent MoS_2 layers via steric repulsive forces.

Figure 24. Digital images of soluble ZnPc-MoS_2 hybrid material **2** in DMF (*ca*. 1.4 mg/mL) as compared with those of exfoliated MoS_2 in DMF. The presence of significant precipitation in the latter is evidenced after 7 days.

The Raman spectrum of ZnPc-MoS_2 hybrid material **9**, obtained by excitation at 633 nm under on-resonance conditions for MoS_2, revealed not only characteristic modes for MoS_2 in the region 150-500 cm^{-1} but also bands attributed to ZnPc derivative **8** at 1150-1600 cm^{-1}. In more detail, Raman bands centered at 451, 403 and 379 cm^{-1} (Figure 25) associated to the 2LA(M) due to disorder and defects,[39] the out-of-plane vibrations of S atoms A_{1g} and the in-plane vibrations of S and Mo atoms E^1_{2g} modes, respectively. The location of E^1_{2g} and A_{1g}, precisely their frequency difference calculated to be 24 cm^{-1} is directly related with the thickness and number of layers of MoS_2,[31] showcasing the presence of few MoS_2 layers in the hybrid material **9**. Markedly, the intensity ratio of the modes 2LA(M)/A_{1g} for **9** was found to be 0.5, decreased by around 60% as compared to the corresponding one for exfoliated MoS_2, proving that the amount of sulfur vacancies was reduced. The latter is well understood by considering the MoS_2 functionalization, as occurred by the grafting of 1,2-dithiolane moiety of ZnPc derivative **8**, at the edges possessing Mo atoms with S vacant sites. In addition, the A_{1g} and E^1_{2g} bands for ZnPc-MoS_2 hybrid material **9** appeared red-shifted by 4 cm^{-1} as compared with the ones due to exfoliated MoS_2 (*ca*. 402 and 377 cm^{-1}, respectively), attributed to intrahybrid charge-transfer phenomena between ZnPc and MoS_2.[34] Specifically, the latter red-shift of these phonon modes is directly associated with n-doping of MoS_2, as induced by electron donation from ZnPc within hybrid material **9**. In addition to the 2LA(M), A_{1g} and E^1_{2g} modes, a lower frequency band at 178 cm^{-1} is observed, which is assigned as A_{1g}-LA(M). It is also worth noticing the absence of the metallic MoS_2 polytype so-called J_1, J_2 and J_3 bands at 150, 225 and 325 cm^{-1}, respectively,[34] therefore assuring that

semiconducting is the predominant phase of MoS_2 the hybrid material **9**. Then, focusing in the 1150-1600 cm^{-1} region of the Raman spectrum of **9**, ZnPc showed signals at 1214 and 1279 cm^{-1} related with the isoindole bending vibration, 1326 cm^{-1} associated with the C-C stretching vibration of the pyrrole groups, 1424 cm^{-1} correlated with the C–N–C bridging mode and the most intense peak at 1505 cm^{-1} that correspond to the stretching vibration of the C-C band in the pyrrole[40] were evident. In fact, the 1214 and 1326 cm^{-1} bands of ZnPc in hybrid material **9** were found blue-shifted as compared with those due to intact ZnPc derivative **8** (i.e. 4 and 4 cm^{-1}, respectively).

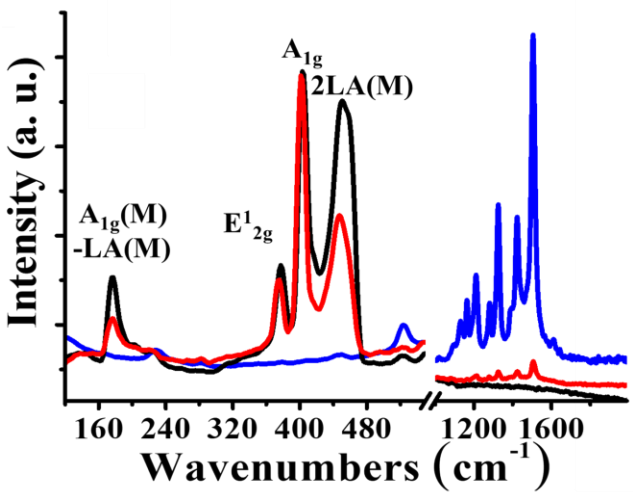

Figure 25. a) Raman spectra (λ_{exc} 633 nm) normalized at the A_{1g} mode, and b) ATR-IR spectra for exfoliated MoS_2 (black), ZnPc derivative **8** (blue) and ZnPc-MoS_2 hybrid material **9** (red).

Complementary to Raman spectroscopy characterization of **9**, ATR-IR, thermogravimetric analysis (TGA) and transmission electron microscopy (TEM) imaging was subsequently performed. In the ATR-IR spectrum of ZnPc-MoS_2 hybrid material **9** is mainly governed by the presence of aliphatic C-H stretching vibration bands at 2957, 2916 and 2866 cm^{-1}, stretching and bending of the carbonyl amide at 1652 cm^{-1} and the C-N at 1486 cm^{-1} (Figure 26). All of those bands are similarly present in the IR spectrum of ZnPc derivative **8**, corroborating the loading of MoS_2 sheets with ZnPc units.

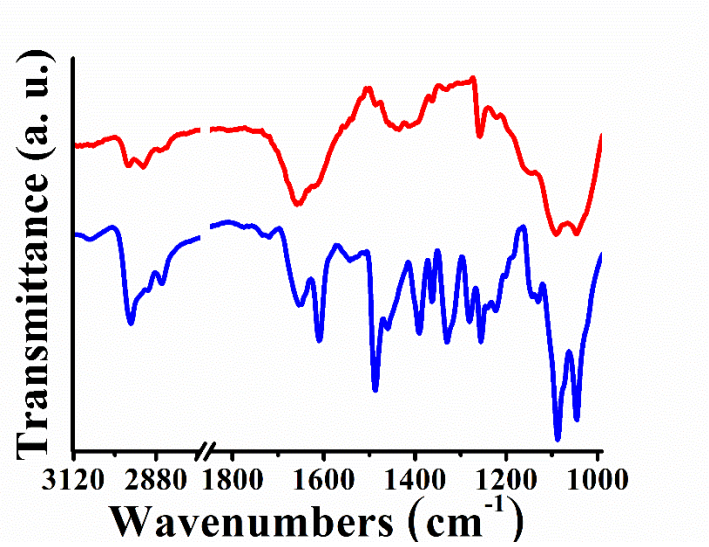

Figure 26. ATR-IR spectra for exfoliated MoS_2 (black), ZnPc derivative **8** (blue) and ZnPc-MoS_2 hybrid material **9** (red).

Information related with the degree of functionalization and the loading of ZnPc onto MoS_2 in the hybrid material **9** was delivered by TGA. The thermal stability of ZnPC-MoS_2 hybrid material **9** in the temperature range 100-800 ^{o}C under inert atmosphere was assessed and compared with the corresponding individual species, exfoliated MoS_2 and ZnPc derivative **8**. While exfoliated MoS_2 is practically thermally stable up to around 500 ^{o}C, above which starts to decompose due to the presence of defects, losing 4.9 % up to 800 ^{o}C, ZnPc derivative **8** decomposes in the temperature range 200-530 ^{o}C, leaving behind 50 % due to Zn atom as well as amorphous carbon residue. For the hybrid material **9**, the 4.3% mass loss observed at 200-550 ^{o}C (Figure 27) is related with the presence of ZnPc covalently anchored on MoS_2 and represents one ZnPc per every 103 units of MoS_2. Considering the covalent attachment of 3,4-dithiolanes at sulfur defected sites located at the edges of MoS_2, the relatively low-loading of ZnPc was expected.

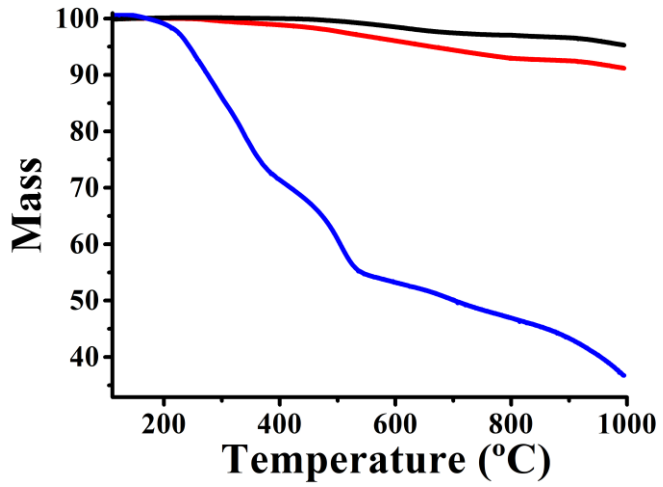

Figure 27. TGA of ZnPc derivative **8** (blue), exfoliated MoS_2 (black) and ZnPc-MoS_2 **9** (red).

A typical HR-TEM image for **2** is shown in Figure 2d. After imaging numerous flakes, the lateral diameter of MoS_2 in exfoliated MoS_2 and hybrid material **2** is found to be around 100 nm on average. TEM imaging shows that dark dots, highlighted for clarity by yellow arrows, are localized at edges of MoS_2, while the surface remains intact. In contrast to its surface, the edge of MoS_2, at which S vacant sites are concentrated, are more reactive in the functionalization with the 1,2-dithiolane oxide moiety present in **1**. According to the aforementioned reactivity, the dark dots are attributed to Zn atoms of Pc.

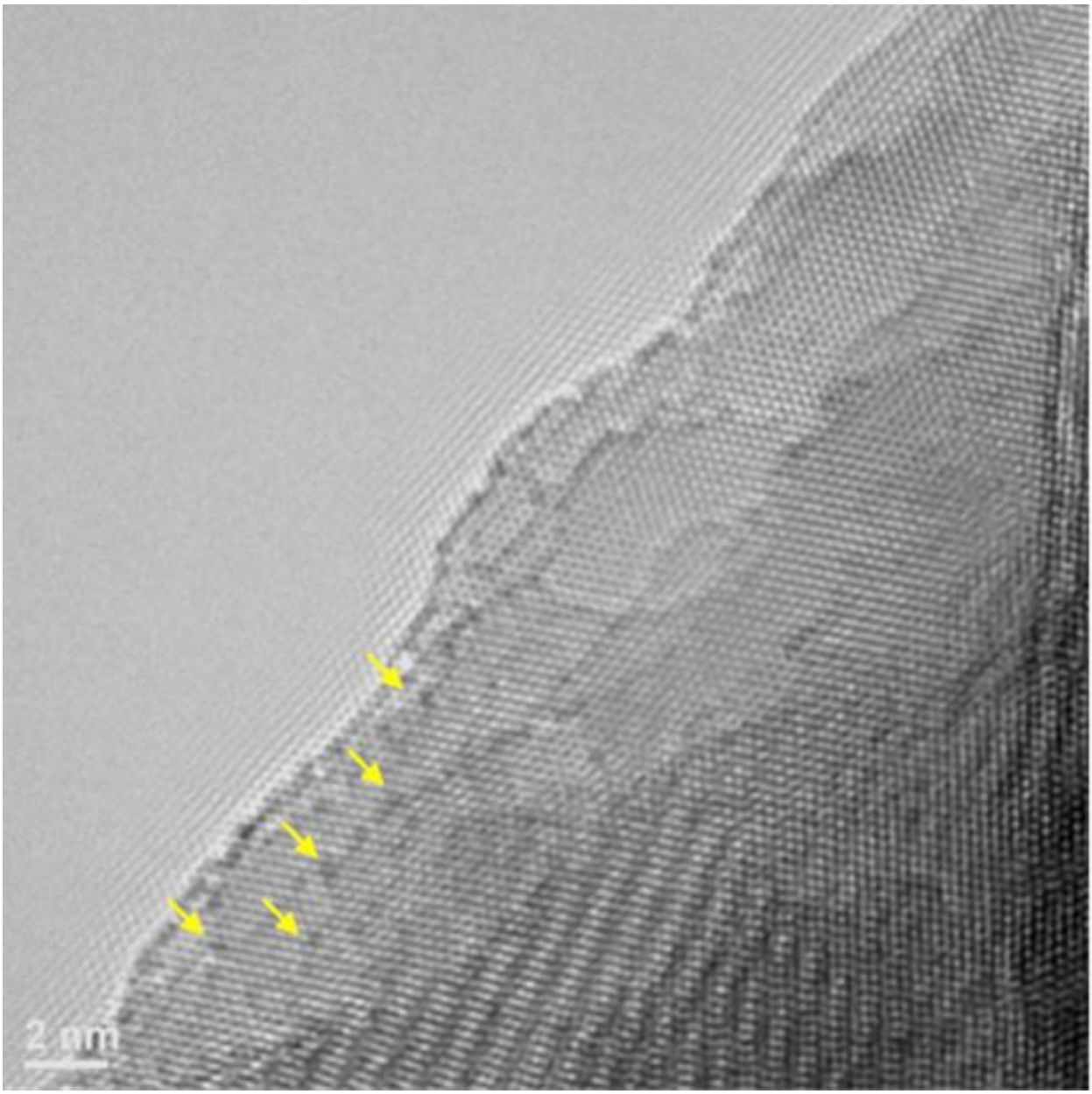

Figure 28. Representative TEM image of ZnPc-MoS_2 hybrid **9**

The solubility achieved in ZnPc-MoS_2 hybrid **9** allows performing solution spectroscopic assays and examine possible electronic interactions between the two species forming the hybrid material. Initiating with UV-Vis absorption measurements, ZnPc derivative **8** possesses characteristic absorption features, the Soret or B band ($\pi \rightarrow \pi^*$) at 351 nm and three Q bands ($n \rightarrow \pi^*$) at 609 assigned to the stretching vibration of the macrocycle, 650 due to the dimers and the strongest band at 675 nm related with the monomer, while for exfoliated MoS_2 the A and B

excitonic transitions at 683 and 626 nm, respectively, followed by direct transitions from the valence to the conduction band at 492 and 393 nm exist. Focusing in ZnPc-MoS_2 hybrid material **9**, the major absorption due to ZnPc at around 680 nm masks the A excitonic band of MoS_2, while in reverse the B excitonic band of MoS_2 overshadows the ZnPc absorption centered at 609 nm (Figure 29). Although such overlapping effects do not allow to deliver robust and conclusive statements about possible electronic interactions between ZnPc and MoS_2 within hybrid material **9** at the ground sate, amelioration of the absorption of MoS_2 in the NIR region.

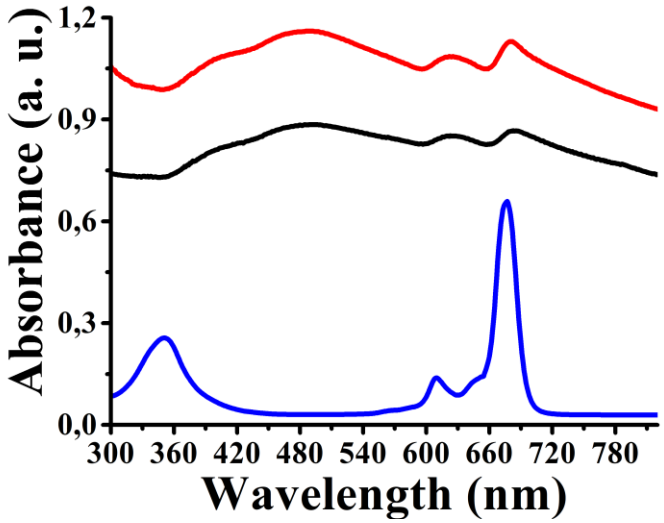

Figure 29. UV-Vis spectra of exfoliated MoS_2 (black), ZnPc derivative **8** (blue) and ZnPc-MoS_2 hybrid material **9** (red), obtained in DMF.

Evaluating the electronic interactions at the excited states, upon excitation of **8** and **9** at 609 nm, for samples possessing same optical concentration, an appreciable quenching of ZnPc emission at 692 nm in **9** is observed (Figure 30a). The latter is in agreement with the corresponding fluorescence lifetime profiles (Figure 30b). While **8** exhibited typical monoexponential decay of 2.7 ns associated with the S1 state, an additional three times faster lifetime decay was registered for **9**.

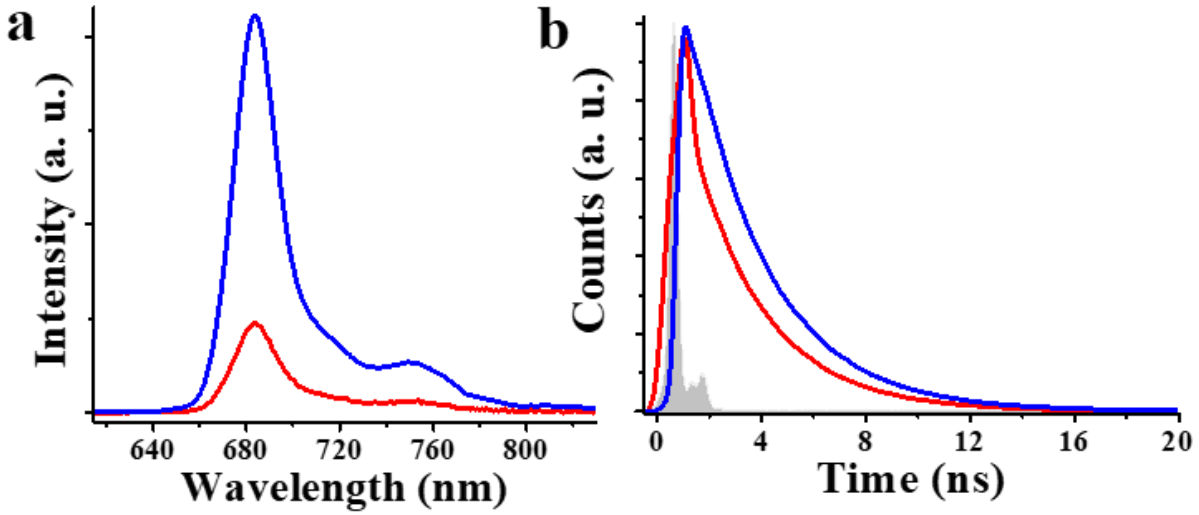

Figure 30. a) Emission spectra (λ_{exc} 609 nm), and b) fluorescence decay lifetime (λ_{exc} 654 nm) for ZnPc derivative **8** (blue) and ZnPc-MoS_2 hybrid material **9** (red), obtained in DMF.

5.3 EXPERIMENTAL SECTION

5.3.1 Materials

Citric acid anhydrous (≥99.5%), tricarballylic acid (99%), ethylendiamine (99+%), N,N'-diisopropylcarbodiimide (99%), nickel (II) nitrate hexahydrate (98.5%), iron (III) chloride (97%), cobalt (II) nitrate hexahydrate (98%), zinc (II) chloride (≥97%), magnesium (II) nitrate hexahydrate (99%), calcium (II) chloride dihydrate (99%), copper (II) nitrate hemi(pentahydrate) (98%), lead (II) nitrate (≥99%), mercurium (II) nitrate hydrate (98%), were used without further purifications. Dialysis tubes with molecular weight cut-off (MWCO) 0.5-1 KDa were bought from Spectrum Labs. The microwave-assisted reaction was performed in a CEM Discover SP reactor employed in open-batch modality. Samples were prepared on silica substrates by drop casting of diluite water solutions. Particle height distribution analysis was carried out by using the Gwyddion software. Size exclusion chromatography was performed on a system composed by: pump (Izasa Scientific), automatic injector (Izasa Scientific), PL aquagel column OH-mixed-H (Agilent) and refractive index detector T-REX (Wyatt Technology). The mobile phase (0.1 M sodium acetate) was flowed at 1ml/min at 35°C. For the calibration, PEO/PEG polymers were used in the range of 1970-44400 g/mol. The samples were dissolved in the mobile phase at concentration around 1mg/ml. The DLS measurements were recorded on a Malvern Nano Zetasizer HT, on a 10 mm path-length plastic cuvette. Elemental analyses were performed in a Thermo Flash EA 1112 instrument with ~3 mg of powder samples. Infrared absorption

measurements were performed on powder samples pressed with KBr into pellets with a Bruker Vertex 70 spectrometer. ^{1}H and ^{13}C NMR spectra were recorded in D_2O solutions at 25 ºC on a Bruker AV500 spectrometer (δ in ppm and J in Hz) at a ^{1}H NMR operating frequency of 500.13 MHz. ^{1}H and ^{13}C NMR spectra were referenced using the solvent signal as an internal standard. The assignment of the ^{1}H NMR signals and the corresponding ^{13}C NMR peaks was carried out using standard ^{1}H-^{13}C edited-HSQC and ^{1}H-^{13}C HMBC (J_{HC} = 8 Hz) 2D-experiments. The determination of the diffusion coefficients D (m^2/s) was performed at controlled temperature (300 K) in spinning solutions of the corresponding compounds in D_2O (concentrations about 2 mM). The values of delta (δ) and delta (Δ) were optimized for each sample. In the case of δ the values found were in the range 1.7-2.0 ms, while for Δ the optimized values ranged from 0.17-0.20 s. X-ray photoelectron spectroscopy (XPS) measurements were taken with an ESCAPlus spectrometer using a Mg anode (1253.5 eV) and a power of 225 W. XPS data analysis was performed with casaXPS software. UV/Vis absorption spectra were recorded on a Shimadzu UV-2401 PC spectrophotometer. Photoluminescence excitation and emission spectra were recorded on a Horiba Jobin Yvon Fluoromax-P, slits of excitation and emission at 1 mm. All the spectra were recorded at room temperature using 10 mm path-length quartz cuvette. Pico-second time-resolved fluorescence spectra were measured by the time-correlated-single-photon-counting (TCSPC) method on a Nano-Log spectrofluorometer (Horiba JobinYvon), by using a laser diode as an excitation source (NanoLED, 375 nm) and a UV-Vis detector TBX-PMT series (250-850 nm) by Horiba JobinYvon. Lifetimes were evaluated with the DAS6 Fluorescence-Decay Analysis Software. Mid-infrared spectra in the region 500-4500 cm^{-1} were obtained on a Fourier transform IR spectrometer (Equinox 55 from Bruker Optics) equipped with a single reflection diamond ATR accessory (DuraSamp1IR II by SensIR Technologies). A drop of the solution was placed on the diamond surface, followed by evaporation of the solvent, in a stream of nitrogen, before recording the spectrum. Typically, 100 scans were acquired at 2 cm^{-1} resolution. Micro-Raman scattering measurements were performed at room temperature in the backscattering geometry using a RENISHAW in Raman microscope equipped with a CCD camera and a Leica microscope. A 2400 lines/mm grating was used for all measurements, providing a spectral resolution of ± 1 cm^{-1}. As an excitation source the Ar+ laser (633 nm with less than 2.65 mW laser power and 514 nm with less than 0.91 mW laser power) was used. Measurements were taken with 15 seconds of exposure times at varying numbers of accumulations. The laser spot

was focused on the sample surface using a long working distance 50x objective. Raman spectra were collected on numerous spots on the sample and recorded with Peltier cooled CCD camera. The data were collected and analyzed with Renishaw Wire and Origin software. Thermogravimetric analysis was performed using a TGA Q500 V20.2 Build 27 instrument by TA in a nitrogen (purity >99.999%) inert atmosphere.

Electron microscopy imaging. STEM imaging and EELS studies were conducted using an aberration-corrected FEI Titan Low-Base microscope operated at 80 kV. This microscope was equipped with a Cs probe corrector and a Gatan Tridiem ESR 865 electron energy loss spectroscopy (EELS) spectrometer. The energy resolution was ~1 eV. The convergence and collection angles were 25 and 50 mrad, respectively. The EELS studies were conducted in STEM mode, using the spectrum-line scan mode. To increase the signal/noise ratio of the EEL spectra, the datasets were then de-noised with the open-source program Hyperspy by using principal component analysis routines.

Femtosecond transient absorption spectroscopy. Ex-periments were performed using an Ultrafast Femtosecond Laser Source (Libra series) by Coherent Inc. (Santa Clara, CA) incorporating diode-pumped, mode locked Ti:Sapphire laser (Vitesse) and diode-pumped intra cavity doubled Nd:YLF laser (Evolution) to generate a com-pressed laser output of 1.45 W. For optical detection, a Helios transient absorption spectrometer from Ultrafast Systems (Sarasota, FL) was used. The source for the pump and probe pulses were derived from the fundamental out-put of Libra (Compressed output 1.45 W, pulse width 100 fs) at a repetition rate of 1 kHz. About 95% of the funda-mental output of the laser was introduced into a TOPAS-Prime-OPA system with 290-2600 nm tuning range from Altos Photonics Inc., (Bozeman, MT), while the rest of the output was used for generation of white light continuum. Kinetic traces at appropriate wavelengths were assembled from the time-resolved spectral data. Data analysis was performed using Surface Xplorer software supplied by Ul-trafast Systems. All measurements were conducted in de-gassed solutions at room temperature.

5.3.2 Synthesis

Synthesis of CNDs 1. 1.0 g of anhydrous citric acid (5.2 mmol, 1 equiv.) was dissolved in 5.0 mL of DMF. The solution was cooled in an ice bath and 2.6 mL of diisopropyl carbodiimide

(DIC, 3 equiv.) were added. Subsequently, 0.35 mL of EDA (1 eq.) in 5 mL of water were slowly added and the reaction was stirred for 30 minutes at room temperature, during which the mixture turns its color from slightly yellow to red. The filtered reaction was stopped by adding slowly during a time of 3 hours a NaOH solution at pH=10, until no formation of DIC-urea precipitate was observed. The crude was diluted in ultrapure water, filtered and washed with ethyl acetate. During these operations the coupling agent urea byproduct, in the form of a white precipitate, was removed. The water phase was dialyzed against ultrapure water (MW_{CO} = 0.5-1.0 KDa, 3 days, twice a day). The dry product was obtained by freeze-drying, with a yield in mass of 29 wt. %. It appears as a brownish powder.

Synthesis of CNDs 2. The addition of 0.21 g of butylamine to 0.5g of CNDs **1** allowed the *in-situ* introduction of butyl groups on the CNDs surface, enhancing lipophilicity and at the same time consuming all remaining carboxylic groups, in presnce of diisopropyl carbodiimide (DIC, 3 equiv.) and 0.35 mL of EDA (1 eq.). Then, the solution was filtered to remove the DIC urea byproduct, the filtrate was washed three times with diethylether and the excess of butylamine was removed under vacuum evaporation. Finally, the water phase was purified by dialysis in ultrapure water (molecular weight cut-off = 0.5-1 kDa, 3 days). The dry product of CNDs-NH_2 (0.7 g) was obtained as a yellow powder by freeze-drying. In the next step, CNDs-NH_2 (200 mg) were dissolved in a mixture of methanol (5 mL) and dichloromethane (25 mL) and cooled to 0 °C. In another flask, lipoic acid (300 mg) was dissolved in dichloromethane (5 mL), cooled at 0 °C and 336 mg of (3-dimethylaminopropyl)-N'-ethylcarbodiimide (EDC) were added. After 20 minutes, the lipoic acid solution was poured into that of CNDs-NH_2. The reaction mixture was left under stirring for 24 hours and after that period additional lipoic acid (100 mg) and EDC (56 mg) were added. After 3 hours the reaction mixture was extracted with distilled water, aqueous NaOH (pH=11) and with brine. The organic phase was dried over $MgSO_4$, the dichloromethane was partially evaporated by vacuum and diluted with ethyl acetate, resulting on the precipitation of the particles (centrifugation at 3200 rpm, 5 minutes). The redispersion-precipitation process was repeated until the lipoic acid spot in TLC disappeared. The precipitate was dissolved again in methanol/dichloromethane 1:1 v/v and dried over $MgSO_4$ to obtain CNDs carrying 1,2-dithiolane chains as a brown solid, after vacuum evaporation of the solvent.

Exfoliation of semiconducting MoS_2. Bulk MoS_2 (150 mg) were dispersed in chlorosulfonic acid (15 mL), sonicated for 2 hours and left under stirring at room temperature for 700 hours. Afterwards, cold water was added drop by drop with extreme care – please notice that the reaction is exothermic and releases gaseous hydrochloric acid. Next, the mixture was filtrated over a PTFE filter (0.2 μm pore size) and washed with a good amount of methanol and acetone. The solid material was added to 150 mg of N-methyl pyrrolidone and sonicated for 1 hour (tip sonication at 30-35% of amplitude (100% of 200W)). After 3 days the supernatant was taken, filtrated on PTFE filter (0.2 μm pore-size) and washed with a large amount of methanol, acetone and dichloromethane.

Preparation of hybrid materials CND-MoS_2 3 and CND-WS_2 4. The 1,2-dithiolane modified CNDs **2** (50 mg) were dissolved in methanol (1 mL). In an-other flask, exfoliated TMDs (20 mg) were dispersed in DMF (10 mL) by sonication (10 min) and dropped in the CNDs solution. The flask was covered with aluminum foil and the reaction mixture was stirred at 70 °C for 4 days. After that period, it was cooled and filtered through a PTFE membrane (0.2 nm pore size). The solid residue was extensively washed with methanol and dichloromethane to obtain the CND-TMDs.

Preparation of porphyrin 5. In a round bottom flask, α- lipoic acid (1.6 mmol), tert-butyl (2-(2-(2-aminoethoxy)ethoxy)ethyl)carbamate (4.8 mmol, 3 equiv.), 4-Dimethylaminopyridine (4.8 mmol, 3 equiv.) and 4-(10,15,20-triphenylporphyrin-5-yl)aniline (1.6 mmol) were added in dry dicloromethane (100 mL). The reaction mixture was stirred under nitrogen atmosphere at room temperature for 18 hours. Then, the organic phase was extracted with H_2O (5 x 100 mL), dried over $MgSO_4$ and purified by column chromatography (petroleum ether/ethyl acetate 50%). Yield ~ 80%. ^{1}H NMR (300 MHz, $CDCl_3$) δ 8.84 (m, 8H), 8.20 (m, 8H), 7.93 – 7.81 (m, 2H), 7.77 (s, 9H), 7.48 (s, 1H), 4.27 (s, 1H), 3.53 (ddd, *J* = 22.3, 12.4, 5.4 Hz, 2H), 2.75 – 2.63 (m, 1H), 2.54 (t, *J* = 7.2 Hz, 2H), 2.36 (s, 1H), 2.05 – 1.45 (m, 6H). ^{13}C NMR (300 MHz, $CDCl_3$) δ 171.38 (C, Aril Amide), 142.19, 8x (C) 138.04, 2x (C) 137.66, 3x (C) 135.12, 2x (CH) 134.60, 4x (CH) 131.21 8x (CH), 127.79 3x(CH), 126.76, 6x (CH), 120.26, 2x(CH) 118.04, 4x(CH), 56.49(CH), 40.34(CH_2), 38.56(CH_2), 34.76(CH_2), 29.77(CH_2), 28.97(CH_2), 25.35(CH_2). ESI-HRMS calc. for $C_{52}H_{43}ON_5S_2$: 817,2909, found: m/z 840.28006 $[M+Na]^+$.

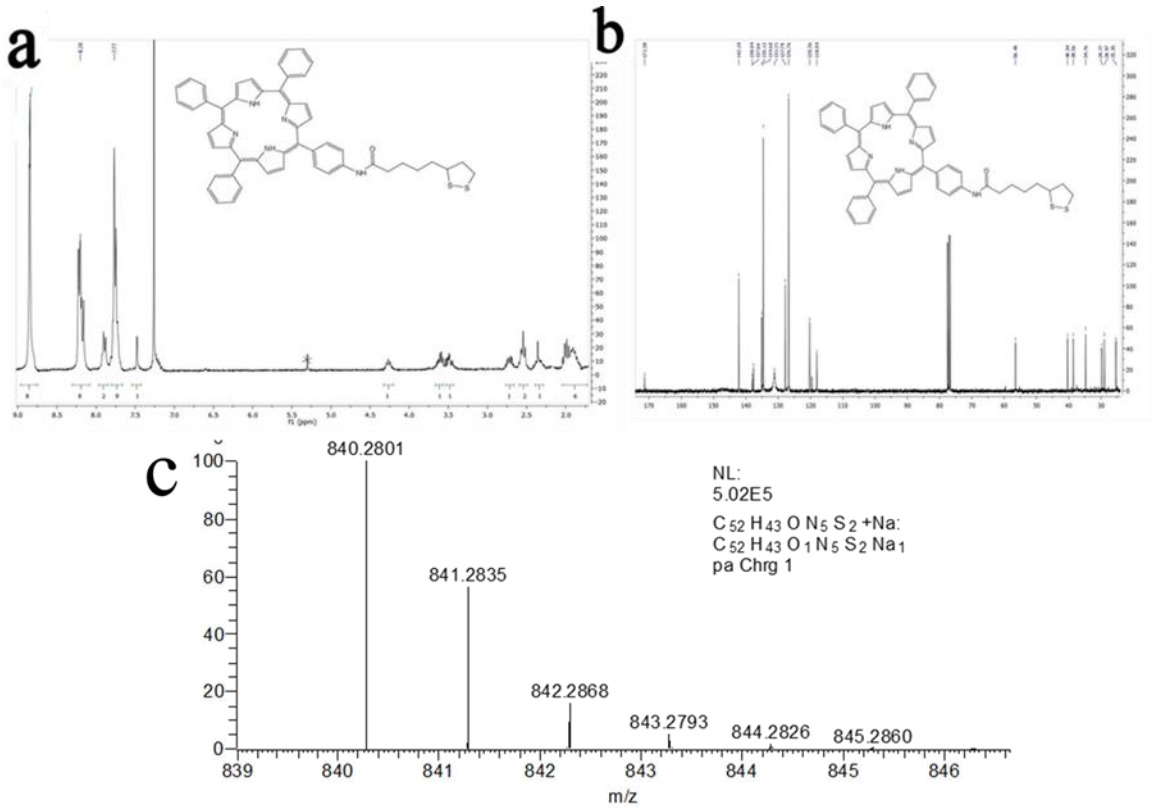

Figure 31. (a) ^{1}H NMR, (b) ^{13}C NMR obtained in $CDCl_3$ and (c) ESI-HRMS of **5**.

Preparation of hybrid materials H_2P-MoS_2 6 and H_2P-WS_2 7. In a round bottom flask, exfoliated MoS_2 or WS_2 (15 mg) and **5** (10 mg) in DMF (10 mL) were stirred at 75 °C for 72 hours. After that period, the reaction mixture was filtered through a PTFE membrane (0.2 µm pore size), the solid residue was washed with DMF and dichloromethane to obtain material **6** or **7** as black powder.

Synthesis of ZnPc 8. In a round bottom flask, α-lipoic acid (31 mg, 0.15 mmol), *N*,*N′*-dicyclohexylcarbodiimide (30 mg, 0.24 mmol) and 4-(dimethylamine)pyridine (5.1 mg, 0.09 mmol) were dissolved in dichloromethane (6 mL) and stirred under argon atmosphere at 0 °C. After 30 minutes, (2-(2′-aminoethoxy)-tri-*tert*-butylphthalocyaninato zinc (II) (100 mg, 0.12 mmol) was added and the reaction mixture was stirred for 12 hours at room temperature. After that period, the reaction mixture was diluted with dichloromethane and extracted with aqueous 2 M HCl, $NaHCO_3$ and brine. The organic layer was dried with $MgSO_4$, concentrated in vacuum and purified by column chromatography (dichloromethane:tetrahydrofuran/95:5) to afford 74 mg of ZnPc **8** (58 %). ^{1}H-NMR (DMSO-d_8) δ 1.40-1.78 (m, 37H, 3x[(CH_3)C](CH_2)), 2.26 (t, *J*= 7,

2H, S-$(CH)_2$-$(CH)_2$), 2.73 (q, *J*= 7, 1H, (CH)-$(CH_2)_2$), 3.76, (br s, 2H, CH_2NH), 4.61 (br s, 2H, CH_2O), 7.79 (br s, 1H, HPc), 8.23-8.36 (m, 4H, HPc), 8.89 (m, 1H, HPc), 9.25-9.46 (m, 6H, HPc). HRMS (MALDI-TOF, Dithranol): *m/z*: $[M]^-$ calc. for $C_{54}H_{58}N_9O_3S_2Zn$ 1007.331; found 1007.399. See Figure 32

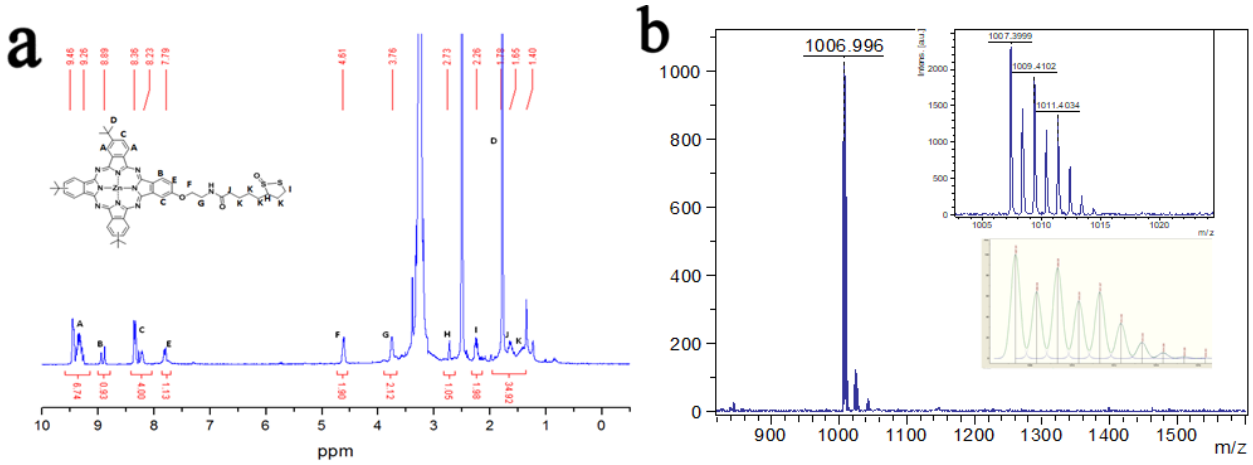

Figure 32. (a)^{1}H NMR spectrum of ZnPc derivative **8** obtained in DMSO-d_8 and (b) HR MALDI-TOF-MS of ZnPc derivative **8** obtained with dithranol matrix.

Preparation of ZnPc-MoS_2 hybrid material 9. Exfoliated MoS_2 (50 mg) and ZnPc **8** (5 mg) in DMF (10 mL) were stirred at 70 °C for 4 days. After that period, the reaction mixture was filtered through a PTFE membrane (0.2 µm pore size), the solid residue was washed (5 x 5 mL) with dichloromethane and then collected as a black solid.

5.4 CONCLUSION

In summary, the synthesis of CNDs **1** and **2** and CND-MoS_2 **3** and CND-WS_2 **4** hybrid materials was accomplished. The hybrid materials were fully characterized by complementary spectroscopic, thermal and electron microscopy imaging techniques. Furthermore, electrochemical assays revealed that MoS_2 was a better electron donor compared to WS_2. Photochemical events upon preferential photoexcitation of **2** and TMDs were probed. Excitation of **3** and **4** at 370 nm revealed ultrafast energy transfer from excited **2** to MoS_2 and WS_2, while exciting the TMDs within the hybrid materials at 425 nm, charge transfer in **3** but not in **4** was seen. The observed excited state electron transfer processes bring us one-step closer to utilize the covalently modified TMDs in donor-acceptor type hybrids for energy harvesting applications.

In addition, covalent grafting of poryphyrin **5** onto exfoliated MoS_2 and WS_2 was accomplished, forming hybrid materials **6** and **7**, which were fully characterized. Furthermore, based on electronic absorption and steady-state and time-resolved photoluminescence spectroscopic assays, deactivation of photoexcited porphyrin via energy/electron transfer to MoS_2 and WS_2 takes place.

Finally, covalent grafting of ZnPc **8** carrying an 1,2-dithiolane oxide linker on semiconducting MoS_2 was proven to be a versatile method of building ZnPc-MoS_2 **9** donor-acceptor systems. By systematic optical absorption and fluorescence spectroscopy and fluorescence lifetimes, deactivation of photoexcited phthalocyanine via energy/electron transfer to MoS_2 takes place. Such hybrid materials may be useful for energy concersion applications.

5.5 REFERENCES

1. (a) D. L. Duong, S. J. Yun and Y. H. Lee. van der Waals Layered Materials: Opportunities and Challenges. *ACS Nano* **2017**, *11*, 11803-11830. (b) P. Miro, M. Audiffred and T. Heine. An atlas of two-dimensional materials. *Chem. Soc. Rev*. **2014**, *43*, 6537-6545.
2. M. Chhowalla, H. S. Shin, G. Eda, L. J. Li, K. P. Loh and H. Zhang. The chemistry of two-dimensional layered transition metal dichalcogenide nanosheets. *Nat. Chem*. **2013**, *5*, 263-275.
3. D. Jariwala, V. K. Sangwan, L. J. Lauhon, T. J. Marks and M. C. Hersam. Emerging Device Applications for Semiconducting Two-Dimensional Transition Metal Dichalcogenides. *ACS Nano* **2014**, *8*, 1102-1120.
4. C. R. Ryder, J. D. Wood, S. A. Wells and M. C. Hersam. Chemically Tailoring Semiconducting Two-Dimensional Transition Metal Dichalcogenides and Black Phosphorus. *ACS Nano* **2016**, *10*, 3900-3917.
5. Q. Fang, Y. Dong, Y. Chen, C.-H. Lu, Y. Chi, H.-H. Yang and T. Yu. Luminescence origin of carbon based dots obtained from citric acid and amino group-containing molecules. *Carbon* **2017**, *118*, 319-326.
6. (a) F. Ehrat, S. Bhattacharyya, J. Schneider, A. Löf, R. Wyrwich, A. L. Rogach, J. K. Stolarczyk, A. S. Urban and J. Feldmann. Tracking the Source of Carbon Dot Photoluminescence: Aromatic Domains versus Molecular Fluorophores. *Nano Lett.* **2017**, *17*, 7710-7716. (b) E. Zhao, Lam, J. W. Y. Lam. Meng, Y. Hong, H. Deng, G. Bai, X. Huang, J.

Hao and B. Z. Tang. Poly[(maleic anhydride)-alt-(vinyl acetate)]: A Pure Oxygenic Nonconjugated Macromolecule with Strong Light Emission and Solvatochromic Effect. *Macromolecules* **2015**, *48*, 64-71. (c) Z. A. Qiao, Q. Huo, M. Chi, G. M. Veith, A. J. Binder and S. Dai. A "ship-in-a-bottle" approach to synthesis of polymer dots@silica or polymer dots@carbon core-shell nanospheres. *Adv. Mater*. **2012**, *24*, 6017-6021. (d) S. Tao, Y. Song, S. Zhu, J. Shao and B. Yang. A new type of polymer carbon dots with high quantum yield: From synthesis to investigation on fluorescence mechanism. *Polymer* **2018**, *116*, 472-478. (e) S. Tao, S. Lu, Y. Geng, S. Zhu, S. A. T. Redfern, Y. Song, T. Feng, W. Xu and B. Yang. Design of Metal-Free Polymer Carbon Dots: A New Class of Room-Temperature Phosphorescent Materials. *Angew. Chem. Int. Ed.* **2018,** *57*, 2393-2398.

7. (a) E. D. Grayfer, M. N. Kozlova and V. E. Fedorov. Colloidal 2D nanosheets of MoS_2 and other transition metal dichalcogenides through liquid-phase exfoliation. *Adv. Colloid Interface Sci*. **2017**, *245*, 40-61. (b) H. Tao, Y. Zhang, Y. Gao, Z. Sun, C. Yan and J. Texter. Scalable exfoliation and dispersion of two-dimensional materials - an update- *Phys. Chem. Chem. Phys*. **2017**, *19*, 921-960. (c) L. Niu, J. N. Coleman, H. Zhang, H. Shin, M. Chhowalla and Z. Zheng. Production of Two-Dimensional Nanomaterials via Liquid-Based Direct Exfoliation. *Small* **2016**, *12*, 272-293. (d) X. Zhang, Z. Lai, C. Tan and H. Zhang. Solution-Processed Two-Dimensional MoS_2 Nanosheets: Preparation, Hybridization, and Applications. *Angew. Chem. Int. Ed*. **2016**, *55*, 8816-8838. (e) X. Fan, P. Xu, Y. C. Li, D. Zhou, Y. Sun, M. A. T. Nguyen, M. Terrones and T. E. Mallouk. Controlled Exfoliation of MoS_2 Crystals into Trilayer Nanosheets. *J. Am. Chem. Soc*. **2016**, *138*, 5143-5149.
8. G. Pagona, C. Bittencourt, R. Arenal and N. Tagmatarchis. Exfoliated semiconducting pure 2H-MoS_2 and 2H-WS_2 assisted by chlorosulfonic acid. *Chem. Commun*. **2015**, *51*, 12950-12953.
9. (a) D. Voiry, A. Goswami, R. Kappera, C. d. C. Silva, D. Kaplan, T. Fujita, M. Chen, T. Asefa and M. Chhowalla. Covalent functionalization of monolayered transition metal dichalcogenides by phase engineering. *Nat. Chem*. **2015**, *7*, 45-49. (b) E. E. Benson, H. Zhang, S. A. Schuman, S. U. Nanayakkara, N. D. Bronstein, S. Ferrere, J. L. Blackburn and E. M. Miller. Balancing the Hydrogen Evolution Reaction, Surface Energetics, and Stability of Metallic MoS_2 Nanosheets via Covalent Functionalization. *J. Am. Chem. Soc.* **2018**, *140*, 441-450.

10. (a) C. Backes, N. C. Berner, X. Chen, P. Lafargue, P. LaPlace, M. Freeley, G. S. Duesberg, J. N. Coleman and A. R. McDonald. Functionalization of liquid-exfoliated two-dimensional 2H-MoS_2. *Angew. Chem. Int., Ed*. **2015**, *54*, 2638-2642. (b) G. S. McAdams, E. A. Lewis, J. R. Brent, S. J. Haigh, A. G. Thomas, P. O'Brien, F. Tuna and D. J. Lewis. Dual Functionalization of Liquid-Exfoliated Semiconducting 2H-MoS_2 with Lanthanide Complexes Bearing Magnetic and Luminescence Properties. *Adv. Funct. Mater.* **2017**, *27*, 1703646.

11. R. Canton-Vitoria, Y. Sayed-Ahmad-Baraza, M. Pelaez-Fernandez, R. Arenal, C. Bittencourt, C. P. Ewels and N. Tagmatarchis. Functionalization of MoS_2 with 1,2-dithiolanes: toward donor-acceptor nanohybrids for energy conversion. *NPJ 2D Mater. App.*, **2017**, *1*, 1-9.

12. (a) Q. Liu, N. Zhang, H. Shi, W. Ji, X. Guo, W. Yuan and Q. Hu. One-step microwave synthesis of carbon dots for highly sensitive and selective detection of copper ions in aqueous solution. *New J. Chem.* **2018**, *42*, 3097-3101. (b) Y. Jiang, Q. Han, C. Jin, J. Zhang and B. Wang. A fluorescence turn-off chemosensor based on N-doped carbon quantum dots for detection of Fe^{3+} in aqueous solution. *Mater. Lett*. **2015,** *141*, 366-368. (c) J. He, H. Zhang, J. Zou, Y. Liu, J. Zhuang, Y. Xiao and B. Lei, Carbon dots-based fluorescent probe for "off-on" sensing of Hg(II) and I^-. *Biosens. Bioelectron*. **2016,** *79*, 531-535.

13. X. Kong, Y. Gong and Z. Fan. The Sensitive Turn-On Fluorescence Detection of Ascorbic Acid Based on Iron(III)-Modulated Nitrogen-Doped Graphene Quantum Dots. *J. Fluoresc.* **2016**, *26*, 1755-1762.

14. (a) M. Yang, B. Li, K. Zhong and Y. Lu. Photoluminescence properties of N-doped carbon dots prepared in different solvents and applications in pH sensing. *J. Mater. Sci.* **2018**, *53*, 2424-2433. (b) A. H. Loo, Z. Sofer, D. Bouša, P. Ulbrich, A. Bonanni and M. Pumera. Carboxylic Carbon Quantum Dots as a Fluorescent Sensing Platform for DNA Detection. *ACS Appl. Mater. Interfaces* **2016,** *8*, 1951-1957.

15. (a) T. Sarkar, H. B. Bohidar and P. R. Solanki. Carbon dots-modified chitosan based electrochemical biosensing platform for detection of vitamin D. *Int. J. Biol. Macromol.* **2018,** *109*, 687-697. (c) R. Guo, B. Chen, F. Li, S. Weng, Z. Zheng, M. Chen, W. Wu, X. Lin and C. Yang. Positive carbon dots with dual roles of nanoquencher and reference signal for the ratiometric fluorescence sensing of DNA. *Actuator B-Chem.* **2018**, *264*, 193-201.

16. J. Wang, Q. Li, J. Zhou, Y. Wang, L. Yu, H. Peng and J. Zhu. Chirality and Chiroptical Effects in Metal Nanostructures: Fundamentals and Current Trends. *Opt. Mater*. **2017**, *72*, 15-19.

17. Q. Xiao, Y. Liang, F. Zhu, S. Lu and S. Huang. Colorimetric glutathione assay based on the peroxidase-like activity of a nanocomposite consisting of platinum nanoparticles and graphene oxide. *Microchim. Acta* **2017**, *184*, 2429-2438.

18. K. Sun, Y. Tang, Q. Li, S. Yin, W. Qin, J. Yu, D. T. Chiu, Y. Liu, Z. Yuan, X. Zhang and C. Wu. In Vivo Dynamic Monitoring of Small Molecules with Implantable Polymer-Dot Transducer. *ACS Nano* **2016**, *10*, 6769-6781.

19. A. Kundu, J. Lee, B. Park, C. Ray, K. V. Sankar, W. S. Kim, S. H. Lee, I.-J. Cho and S. C. Jun. Facile approach to synthesize highly fluorescent multicolor emissive carbon dots via surface functionalization for cellular imaging. *J. Colloid Interface Sci*. **2018**, *513*, 505-514.

20. F. Khodadadei, S. Safarian and N. Ghanbari. Methotrexate-loaded nitrogen-doped graphene quantum dots nanocarriers as an efficient anticancer drug delivery system. *Mater. Sci. Eng. C* **2017**, *79*, 280-285.

21. (a) Y. Sun, W. Cao, S. Li, S. Jin, K. Hu, L. Hu, Y. Huang, X. Gao, Y. Wu and X.-J. Liang. Ultrabright and multicolorful fluorescence of amphiphilic polyethyleneimine polymer dots for efficiently combined imaging and therapy. *Sci. Rep*. **2013**, *3*, 3036-3042. (b) G. Zuo, A. Xie, X. Pan, T. Su, J. Li and W. Dong. Fluorine-Doped Cationic Carbon Dots for Efficient Gene Delivery *ACS Appl. Nano Mater*. **2018**, *1*, 2376-2385.

22. (a) Z. Min, L. Shi, L. Jing, Q. Dan, Z. Haifeng, G. Xingang, H. Xiuli, X. Zhigang, J. Xiabin and S. Zaicheng. Integrating oxaliplatin with highly luminescent carbon dots: an unprecedented theranostic agent for personalized medicine. *Adv. Mater*. **2014**, *26*, 3554-3560.

23. (a) G. D. Torre, G. Bottari, M. Sekita, A. Hausmann, D. M. Guldi and T. A Torres. Voyage into the Synthesis and Photophysics of Homo- and Heterobinuclear Ensembles of Phthalocyanines and Porphyrins. *Chem. Soc. Rev*. **2013**, *42*, 8049-8105. (b) F. D. Souza and K. M. Kadish. *Handbook of Carbon Nano Materials*: *Synthesis and supramolecular systems*; World Scientific: Singapore, **2011**.

24. (a) G. Bottari, M. A. Herranz, L.Wibmer, M. Volland, L. Rodrıguez-Perez, D. M. Guldi, A. Hirsch, N. Martın, F. D. Souza and T. Torres. Chemical Functionalization and Characterization of Graphene-Based Materials. *Chem. Soc. Rev*. **2017**, *46*, 4464-4500. (b) G.

Bottari, O. Trukhina, M. Ince and T. Torres. Towards Artificial Photosynthesis: Supramolecular, Donor-Acceptor, Porphyrin- and Phthalocyanine/Carbon Nanostructure Ensembles. *Coord. Chem. Rev*. **2012**, *256*, 2453-2477.

25. N. Karousis, J. Ortiz, K. Ohkudo, T. Hasobe, S. Fukuzumi, A. Sastre-Santos and N. Tagmatarchis. Integrating oxaliplatin with highly luminescent carbon dots: an unprecedented theranostic agent for personalized medicine. *J Phys Chem C* **2012**, *116*, 20564-20573.

26. X. Zhao, X.-Q. Yan, Q. Ma, Y. Yao, X-L. Zhang, Z-B. Liu and J-G. Tian. Nonlinear optical and optical limiting properties of graphene hybrids covalently functionalized by phthalocyanine. *Chem Phys Lett*. **2013**, *577*, 62-67.

27. S. K. Das, K. Ohkubo, Y. Yamada, S. Fukuzumi and F. D'Souza. Decorating single layer graphene oxide with electron donor and acceptor molecules for the study of photoinduced electron transfer. *Chem Commun.* **2013**, *49*, 2013-2015.

28. M.-E. Ragoussi, G. Katsukis, A. Roth, J. Malig, G. de la Torre, D. M. Guldi and T. Torres. Electron-Donating Behavior of Few-Layer Graphene in Covalent Ensembles with Electron-Accepting Phthalocyanines. *J. Am Chem Soc*. **2014**, *136*, 4593-4598.

29. (a) Z. Bagheri, H. Ehtesabi, M. Rahmandoust, M. M. Ahadian, Z. Hallaji, F. Eskandari and E. Jokar. New Insight into the Concept of Carbonization Degree in Synthesis of Carbon Dots to Achieve Facile Smartphone Based Sensing Platform. *Sci. Rep*. **2017**, *7*, 11013-11024. (b) J. Schneider, C. J. Reckmeier, Y. Xiong, M. von Seckendorff, A. S. Susha, P. Kasák and A. L. Rogach. Molecular Fluorescence in Citric Acid-Based Carbon Dots. *J. Phys. Chem. C* **2017**, *121*, 2014-2022. (c) F. Gao, S. Ma, J. Li, K. Dai, X. Xiao, D. Zhao and W. Gong. Rational design of high quality citric acid-derived carbon dots by selecting efficient chemical structure motifs. *Carbon* **2017**, *112*, 131-141. (d) Y. Zhang, Y. Wang, X. Feng, F. Zhang, Y. Yang and X. Liu. Effect of reaction temperature on structure and fluorescence properties of nitrogen-doped carbon dots. *Appl. Surf. Sci.* **2016**, *387*, 1236-1246. (e) Z.-Q. Xu, J.-Y. Lan, J.-C. Jin, P. Dong, F.-L. Jiang and Y. Liu. Highly Photoluminescent Nitrogen-Doped Carbon Nanodots and Their Protective Effects against Oxidative Stress on Cells. *ACS Appl. Mater. Interfaces* **2015**, *7*, 28346-28352. (f) T. Ogi, K. Aishima, F. A. Permatasari, F. Iskandar, E. Tanabe and K. Okuyama. Kinetics of nitrogen-doped carbon dot formation via hydrothermal synthesis. *New J. Chem*. **2016**, *40*, 5555-5561. (g) M. Rong, Y. Feng, Y. Wang and X. Chen. One-pot solid phase pyrolysis synthesis of nitrogen-doped carbon dots for Fe^{3+} sensing and

bioimaging. *Actuators B-Chem.* **2017**, *245*, 868-874. (h) S. Bhattacharyya, F. Ehrat, P. Urban, R. Teves, R. Wyrwich, M. Döblinger, J. Feldmann, A. S. Urban and J. K. Stolarczyk. Effect of nitrogen atom positioning on the trade-off between emissive and photocatalytic properties of carbon dots. *Nat. Comm.* **2017**, *8*, 1401-1410. (i) G. Tong, J. Wang, R. Wang, X. Guo, L. He, F. Qiu, G. Wang, B. Zhu, X. Zhu and T. Liu. Amorphous carbon dots with high two-photon fluorescence for cellular imaging passivated by hyperbranched poly(amino amine). *J. Mater. Chem. B* **2015**, *3*, 700-706. (j) W. Zhang, L. Shi, Y. Liu, X. Meng, H. Xu, Y. Xu, B. Liu, X. Fang, H.-B. Li and T. Ding. Supramolecular interactions via hydrogen bonding contributing to citric-acid derived carbon dots with high quantum yield and sensitive photoluminescence. *RSC Adv.* **2017**, *7*, 20345-20353. (k) Y. Hu, J. Yang, J. Tian and J.-S. Yu. How do nitrogen-doped carbon dots generate from molecular precursors? An investigation of the formation mechanism and a solution-based large-scale synthesis. *J. Mater. Chem. B* **2015**, *3*, 5608-5614. (l) J. Wang, P. Zhang, C. Huang, G. Liu, K. C.-F. Leung and J. Y. X. Wáng. High Performance Photoluminescent Carbon Dots for In Vitro and In Vivo Bioimaging: Effect of Nitrogen Doping Ratios. *Langmuir* **2015**, *31*, 8063-8073. (m) A. Sharma, T. Gadly, S. Neogy, S. K. Ghosh and M. Kumbhakar. Molecular Origin and Self-Assembly of Fluorescent Carbon Nanodots in Polar Solvents. *Journal Phys. Chem. Lett.* **2017**, *8*, 1044-1052. (n) Y. Zhang, X. Liu, Y. Fan, X. Guo, L. Zhou, Y. Lv and J. Lin. One-step microwave synthesis of N-doped hydroxyl-functionalized carbon dots with ultra-high fluorescence quantum yields. *Nanoscale* **2016**, *8*, 15281-15287.

30. (a) N. S. Myshakina, Z. Ahmed and S. A. Asher. *J. Phys. Chem. B* **2008**, *112*, 11873-11877. (b) A. Barth. Infrared spectroscopy of proteins. *Biochim. Biophys. Acta Bioenerg.* **2007**, *9*, 1073-1101.

31. H. Li, Q. Zhang, R. Y. C. Chong, K. T. Beng, T. E. T. Hang, A. Olivier and D. Baillargeat. From bulk to monolayer MoS_2: Evolution of Raman scattering. *Adv. Funct. Mater*. **2012**, *22*, 1385-1390.

32. (a) K. C. Knirsch, N. C. Berner, H. C. Nerl, C. S. Cucinotta, Z. Gholamvand, N. McEvoy, Z. Wang, I. Abramovic, P. Vecera, M. Halik, S. Sanvito, G. S. Duesberg, V. Nicolosi, F. Hauke, A. Hirsch, J. N. Coleman and C. Backes. Basal-plane functionalization of chemically exfoliated molybdenum disulfide by diazonium salts. *ACS Nano* **2015**, *9*, 6018-6030.

33. (a) A. P. Nayak, T. Pandey, D. Voiry, J. Liu, S. T. Moran, A. Sharma, C. Tan, C.-H. Chen, L.-J. Li, M. Chhowalla, J.-F. Lin, A. K. Singh and D. Akinwande. Pressure-dependent optical and vibrational properties of monolayer molybdenum disulfide. *Nano Lett*. **2015**, *15*, 346-353. (b) S. S. Jimenez, D. Sandoval, R. F. Yang, J. C. Frindt and J. C. Irwin. Raman study and lattice dynamics of single molecular layers of MoS_2. *Phys. Rev. B* **1991**, *44*, 3955-3962.

34. (a) B. Chakraborty, A. Bera, D. V. S. Muthu, S. Bhowmick, U. V. Waghmare and A. K. Sood. Symmetry-dependent phonon renormalization in monolayer MoS_2. *Phys. Rev. B: Condens. Matter*. **2012**, *85*, 161403. (b) Y. Shi, J.-K. Huang, L. Jin, Y.-T. Hsu, S. F. Yu, L.-J Li and H. Y. Yang. Selective decoration of Au nanoparticles on monolayer MoS_2 single crystals. *Sci. Rep*. **2013**, *3*, 1839-1846.

35. (a) K. K. R. Data, G. Qi, R. Zboril and E. P. Giannelis. Yellow emitting carbon dots with superior colloidal, thermal, and photochemical stabilities. *J. Mater. Chem. C* **2016**, *4*, 9798-9803. (b) J. Gu, D. Hu, J. Huang, Q. Zhang, X. Jia and K. Xi. One-pot synthesis and control of aqueous soluble and organic soluble carbon dots from a designable waterborne polyurethane emulsion. *Nanoscale* **2016**, *8*, 3973-3981.

36. (a) R. Arenal, L. De Matteis, L. Custardoy, A. Mayoral, M. Tence, V. Grazu, J. M. de la Fuente, C. Marquina and M. R. Ibarra. Spatially-resolved EELS analysis of antibody distribution on biofunctionalzied magnetic nanoparticles. *ACS Nano* **2013**, *7*, 4006-4013. (b) R. Arenal, K. March, C. P. Ewels, X. Rocquefelte, M. Kociak, A. Loiseau and O. Stephan, Atomic configuration of nitrogen-doped single-walled carbon nanotubes. *Nano Lett*. **2014**, *14*, 5509-5516.

37. (a) L. Wibmer, S. Lages, T. Unruh and D. M. Guldi. Excitons and trions in one-photon- and two-photon-excited MoS_2: A study in dispersions. *Adv. Mater.* **2018**, *30*, 1706702. (b) R. K. Chowdhury, S. Nandy, S. Bhattacharya, M. Karmakar, B. N. S. Bhaktha, P. K. Datta, A. Taraphder and S. K. Ray. Broadband. pump-probe study of biexcitons in chemically exfoliated layered WS_2. *Cond. Mater*. **2018**, 1-8.

38. (a) T. Jiang, R. Chen, X. Zheng, Z. Xu and Y. Tang. Photo-induced excitonic structure renormalization and broadband absorption in monolayer tungsten disulphide. *Optics Expr*. **2018**, *26*, 859-869. (b) S. B. Homan, V. K. Sangwan, I. Balla, H. Bergeron, E. A. Weiss and M. C. Hersam. Ultrafast exciton dissociation and long-lived charge separation in a

photovoltaic pentacence-MoS_2 van der Waals heterojunction. *Nano Lett*. **2017**, *17*, 164-169. (c) T. R. Kafle, S. Kattel, S. D. Lane, T. Wang, H. Zhao and W.-L. Chan. Charge-transfer exciton and spin flipping at organic-transition-metal dichalcogenide interfaces. *ACS Nano* **2017**, *11*, 10184-10192. (d) E. P. Nguyen, B. J. Carey, C. J. Harrison, P. Atkin, K. J. Berean, E. D. Gaspera, J. Z. Ou, R. B. Kaner, K. Kalantar-zadeh and T. Daeneke. Excitation dependent bidirectional electron transfer in phthalocyanine MoS_2 nanosheets. *Nanoscale* **2016**, *8*, 16276-16283.

39. S. Bae, N. Sugiyama, T. Matsuo, H. Raebiger, K.-i. Shudo and K. Ohno. Defect-Induced Vibration Modes of Ar+ -Irradiated MoS_2. *Phys. Rev. Appl.* **2017,** *7*, 024001.

40. C. Jennings, R. Aroca, A.-M. Hor and R.O. Loutfy. Raman spectra of solid films $^{3-}$Mg, Cu and Zn phthalocyanine complexes. *J. Raman Spectrosc.* **1984**, 15, 34-37.

CHAPTER 6

Non-covalent functionalization of transition metal dichalcogenides with photoactive units

ABSTRACT

Ammonium-modified MoS_2 and WS_2 were prepared and characterized by complementary spectroscopic, thermal, and microscopy imaging means. The positive charges on functionalized MoS_2 and WS_2, due to the presence of ammonium units, were exploited to electrostatically bring in contact anionic species of a porphyrin, carbon dots (CDs), and poly (3-thiophene sodium acetate). Efficient fluorescence quenching of porphyrin, CDs and poly (3-thiophene sodium acetate) by MoS_2 and WS_2 was observed and attributed to photoinduced electron/energy transfer. Furthermore, the electro-catalytic performance of CDs/MoS_2 was assessed towards the hydrogen evolution reaction and found superior as compared to that owed to the individual CDs species.

In addition, basal plane functionalization of MoS_2 and WS_2 with pyrene via multiple S-π interactions furnished MoS_2/pyrene and WS_2/pyrene nanoensembles. Energy transduction from the photoexcited pyrene to the transition metal dichalcogenides was identified. Moreover, the non-covalently immobilized pyrene was found to protect MoS_2 and WS_2 by inhibiting oxidation.

6.1 INTRODUCTION

Two-dimensional nanomaterials, in particular, layered transition-metal dichalcogenides (TMDs), have triggered increasing scientific interest and stay at the forefront of recent research investigations.[1-4] This is not only due to their unique structure in which a metal cation is bonded to four chalcogenide anions in a honeycomb lattice, but also to their exciting physicochemical properties,[5, 6] and great potentiality in nano-electronics, energy storage, sensing, and catalysis.[7-10] Molybdenum and tungsten disulfide, MoS_2 and WS_2, as typical examples of TMDs, form different polytypes, semiconducting or metallic, depending on the exfoliation process employed.[11-17]

A major drawback of TMDs materials is associated with poor solubility, since multiple van der Waals forces between the layers keep them tightly together. Those forces, preventing the separation and individualization of sheets within the TMDs, can be overcome by chemical functionalization and the incorporation of species that due to steric and/or electronic reasons may keep apart, by avoiding re-stacking, the sheets of TMDs. Hence, functionalization of TMDs is imperative for fully harnessing their capabilities, and broaden their application in a variety of fields. However, TMDs tend to be rather inert; chalcogen atoms in the basal plane are saturated and not highly reactive, while the metal atoms are embedded beneath the chalcogen layer, thus not susceptible to functionalization. Nevertheless, reactions of metallic MoS_2 with organoiodides or diazonium salts yielded MoS_2-based materials carrying organic addends at the basal plane.[18] Moreover, ligand conjugation of thiols to Mo atoms of metallic MoS_2,[19] as a rather debatable route of functionalization, since thiols can convert to the corresponding disulfides in a catalytic reaction activated by the presence of MoS_2, which eventually physisorb onto the basal plane of MoS_2,[20] was also reported. However, a more straightforward route for obtaining functionalized MoS_2 and WS_2 involves reaction with 1,2-dithiolanes, which possess high binding affinity for Mo and W atoms with S vacant sites located at the edges.[21] In fact, with the latter approach, innovative hybrid materials with interesting photophysical properties, with the advantage of preserving intact the basal plane since the functionalization reaction occurs only at edges, where the majority of S defects are concentrated.[21] Nevertheless, considering that the covalent bonding between the addends and the TMDs may affect the intrinsic electronic properties of the latter,

alternative approaches were considered. Hence, phthalocyanines,[22] tetrathiafulvalene[23] as well as perylene and porphyrin dyes[24] were physisorbed in a non-destructive manner onto TMDs.

Porphyrins, widely tested in artificial photosynthetic systems, possess an 18π-electron aromatic structure, absorb efficiently light in the visible region with high molar absorbance coefficients, are photochemically stable and have redox potentials and photophysical properties that can be easily tuned by altering the metal center of the macrocycle or through modification of the peripheral substituents.[25] All these features, make porphyrins quite attractive materials for participating in charge-transfer processing as electron donors. As a result, a plethora of supramolecularly and covalently associated porphyrins with graphene, the direct all-carbon two-dimensional analogue of TMDs, have been reported.[26]

Next, carbon dots (CDs), since their serendipitously discovery in 2004,[27] proved to be a valuable new entry in the horizon of carbon-based nanomaterials. In general, CDs are nano-sized particles, with diameter in the order of 10 nm or less, showing solubility in aqueous and organic media,[28] biocompatibility[29] and photochemical stability.[30] Among the novel physicochemical properties of CDs is their intrinsic photoluminescence,[31] which can be exploited in energy conversion schemes.[32] In particular, photoinduced energy and/or electron transfer processes in CDs have been identified, for example, when combined with carbon nanotubes,[33] graphene oxide,[34] perylene diimides,[35] and porphyrins.[36] Moreover, the high stability and good electrical conductivity of CDs enable them to be considered as interesting contenders for electrocatalysis.[37]

On the other hand, polythiophenes, exhibit environmentally stable behaviour and can find useful applications in organic electronics such as for example in field effect transistors, organic solar cells and organic light emitting devices.[38] For instance, a water soluble polythiophene derivative was combined with graphene quantum dots to yield hybrid nanostructures, which upon fabrication in an organic photovoltaic device exhibited a power-conversion efficiency of 1.76%.[39] Conversely, incorporating C_{60} as electron acceptor species within water-soluble polythiophene micelles, resulted in quenching of the emission of polythiophene, indicating the development of photoinduced excited state interactions.[40]

Although unique the structure of TMDs, it is handicapped by the direct exposure of all atoms to the environment, which in turn can induce significant structural modifications, thus, affecting the

novel electronic, optical and mechanical properties.[41] Edges and defected sites of TMDs are susceptible to oxidation, when exposed under atmospheric conditions and/or moisture to light illumination, forming oxides, which significantly disturb the properties of the material and subsequently the performance in energy and tribology related applications.[42] In fact, even defect-free TMDs can be oxidized at the basal plane when exposed to atomic oxygen found in low earth orbit environment,[43] which can severely impact their use as lubricants for space machines. In addition, the presence of oxygen on the surface of TMDs can become a critical issue in most opto-electronic applications, where high electrical conductivity and carrier mobility is required.

Based on the aforementioned considerations, the electrostatic association of a porphyrin, CDs and poly(3-thiophene sodium acetate) possessing negative charges to modified TMDs bearing opposite charges, was accomplished. Furthermore, intra-ensemble electronic interactions between the two species within the so-formed electron donor-acceptor porphyrin/TMDs, CDs/MoS_2 and poly(3-thiophene sodium acetate)/TMDs ensembles, were scrutinized. Also, the electrocatalytic performance of CDs/MoS_2 towards the hydrogen evolution reaction (HER) was assessed. In addition, the non-covalent immobilization of pyrene onto the surface of MoS_2 and WS_2 via S-π forces, yielding MoS_2/pyrene and WS_2/pyrene ensembles was performed. Interestingly, on top of the electronic communication identified, protection from photo-degradation of MoS_2 and WS_2 by light from the physisorbed pyrene was found.

6.2 RESULTS AND DISCUSSION

Initially, bulk MoS_2 and WS_2 were exfoliated to semiconducting nanosheets upon treatment with chlorosulfonic acid, according to our previously reported protocol.[12] Next, exfoliated MoS_2 and WS_2 were functionalized with 1,2-dithiolane *tert*-butyl carbamate (BOC) derivative **1** yielding materials **2a** and **2b**, respectively (Figure 1a). The BOC protecting group in **2a** and **2b** can be efficiently removed by acidic treatment of their solutions with gaseous HCl, to furnish **3a** and **3b**, respectively, in which positively charged ammonium terminating units decorate the edges of modified TMDs. The work up procedure followed, namely, filtration of the reaction mixture through a PTFE membrane with 0.2 μm pore size followed by extensive washing of the solid residue obtained on top of the membrane filter with dichloromethane, assured that all TMDs-based functionalized materials were free from non-covalently interacting organic species. Zeta-

potential measurements revealed high difference in the values obtained between exfoliated MoS_2 (-28 mV) and WS_2 (-24 mV) as compared with those owed to ammonium modified materials **3a** (+2.6 mV) and **3b** (+0.5 mV), respectively. Hence, noting that zeta-potential measures the overall surface charge of the system and not that due to individual species, the presence of positive charges in the ammonium modified TMDs **3a** and **3b** is unambiguously proven. Additionally, the amount of ammonium units existing onto modified MoS_2 and WS_2 was calculated by performing the Kaiser test and found to be 49 and 47 μmol/g for **3a** and **3b,** respectively. Then, having in hand functionalized MoS_2 and WS_2 carrying positive charges in the form of ammonium units in **3a** and **3b**, respectively, Coulombic interactions were employed to bring them in contact with negatively charged porphyrin **4**, CDs **5**, and poly(3-thiophene sodium acetate) **6**, forming porphyrin/MoS_2 **7a** and porphyrin/MoS_2 **7b**, CDs/MoS_2 **8**, poly(3-thiophene sodium acetate)/MoS_2 **9a** and poly(3-thiophene sodium acetate)/WS_2 **9b**, nanoensembles, according to Figure 1.

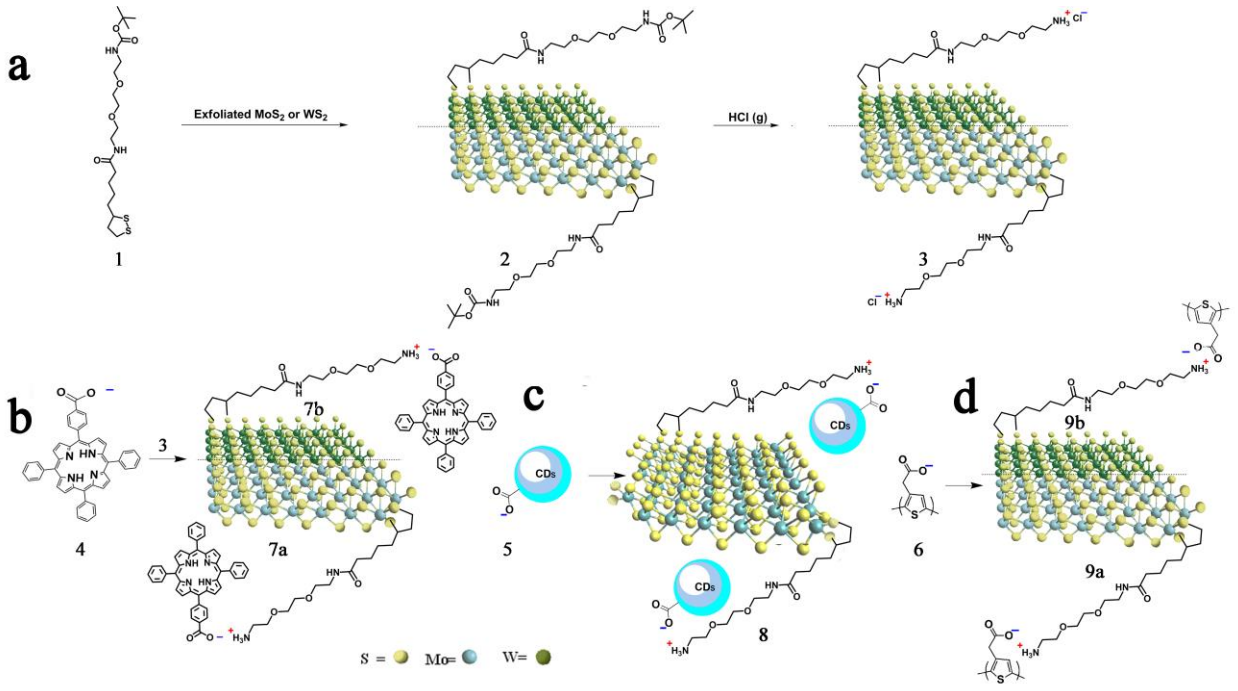

Figure 1. (a) Functionalization of MoS_2 leading to ammonium modified MoS_2-based material **3**. Formation of (b) porphyrin/MoS_2 **7a** and porphyrin/WS_2 **7b**, (c) CDs/MoS_2 **8**, and (d) poly (3-thiophene sodium acetate)/MoS_2 **9a** and poly(3-thiophene sodium acetate)/WS_2 **9b** ensembles based on electrostatic interactions.

Spectroscopic evidence for the successful functionalization of exfoliated MoS_2 and WS_2 with 1,2-dithiolane derivative **1** and the cleavage of the BOC protecting units was delivered by ATR-IR and Raman assays. In particular, the presence of the carbonyl amide and BOC protecting units in **1** gave rise to stretching vibrations identified at 1650 and 1710 cm^{-1}, respectively. The same functional units can be found in **2a**, however, after BOC deprotection only the amide carbonyl is identified at 1650 cm^{-1} in ammonium modified material **3a** (Figure 2a). In addition, characteristic stretching vibrations due to aliphatic C-H units were present in both **2a** and **3a** materials at around 2900-2980 cm^{-1}. Analogously, BOC-protected and ammonium modified WS_2-based materials **2b** and **3b** gave rise to similar IR bands (Figure 2b).

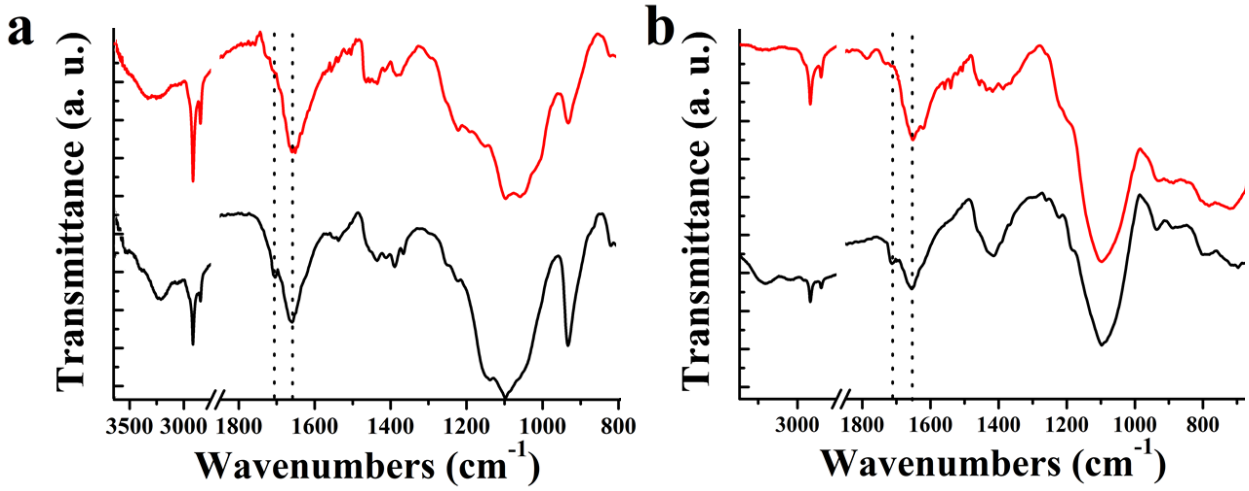

Figure 2. ATR-IR spectra for (a) BOC modified MoS_2-based material **2a** (black) and ammonium modified MoS_2-based material **3a** (red) and (b) BOC modified WS_2-based material **2b** (black) and ammonium modified WS_2-based material **3b** (red).

Next, Raman spectroscopy upon on-resonance excitation conditions, 633 nm for MoS_2 and 514 nm for WS_2, revealed richer spectra as compared to those acquired under off-resonance scattering conditions, due to strong electron-phonon coupling interactions.[44] For exfoliated MoS_2, three characteristic bands were evident, the in-plane E^1_{2g} at 376 cm^{-1}, the out-of-plane A_{1g} at 404 cm^{-1} and the 2LA(M) at 448 cm^{-1} vibration modes (Figure 3a). The intensity ratio of 2LA(M) over A_{1g} bands was found 0.52 for **2a**, almost double as compared to the value of 0.27 measured for exfoliated MoS_2. Since the 2LA(M) is associated with disorder and defects on MoS_2, also providing valuable information on the electronic states of MoS_2, the corresponding

intensity changes may well be attributed to the incorporation of the organic addends in **2a**, which simultaneously facilitates further exfoliation of the modified MoS_2 sheets in wet media. Although detailed analysis is beyond the scope of this work, the overall Raman spectrum characteristics for the ammonium modified MoS_2-based material **3a** were almost identical with that owed to **2a**, revealing that the BOC deprotection did not influence the electronic structure of MoS_2. Similar behavior was found in the Raman of WS_2-based materials. For exfoliated WS_2, the 2LA(M), E^1_{2g} and A_{1g} modes were evident at 350, 355 and 419 cm^{-1}, respectively (Figure 3b). Also, other first- and second-order bands with smaller intensity were evident (e.g. 176, 230, 297, 312 and 324 cm^{-1}), however, their analysis is not relevant with the current study. The intensity of the ratio $I_{2LA(M)}/I_{A1g}$ was also increased from 0.39 for exfoliated WS_2, by almost 50%, to 0.58 for **2b** and **3b**, which can be associated with the modification of WS_2 by the 1,2-dithiolane *tert*-butyl carbamate and the improvement of the level of exfoliation,[45] due to solubilization enhancement achieved.

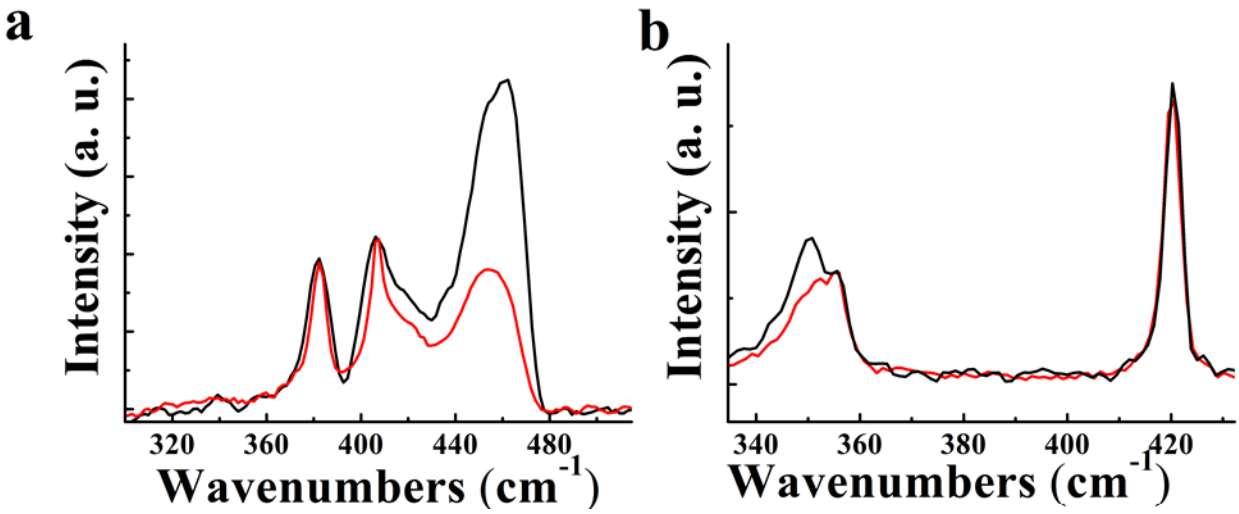

Figure 3. Raman spectra for (a) BOC modified MoS_2-based material **2a** (black), ammonium modified MoS_2-based material 3**a** (red) and (b) BOC modified WS_2-based material **2b** (black), ammonium modified WS_2-based material **3b** (red).

Continuing the characterization of ammonium modified **3a** and **3b** in the solid-state, thermogravimetric analysis (TGA) gave information about the stability of the materials and allowed to estimate the amount of ammonium units decorating the modified TMDs. Under nitrogen atmosphere, **3a** and **3b** are thermally stable up to 200 ^oC and then starts the thermal

decomposition of the organic addends that continues up to 550 ºC. Beyond that temperature, decomposition of the lattice at sulfur defected sites takes place. As it is shown in Figure 4, a mass loss of 2.6% for 3a and 2.3 % for **3b** was observed, corresponding to the loading of one organic unit per every 48 MoS_2 units and 35 WS_2 units, respectively. The relatively low loading can be safely rationalized by considering that the 1,2-dithiolane modification of MoS_2 and WS_2 network took place at the edges, where S vacancy sites were naturally introduced during the chemical exfoliation from the bulk.[21]

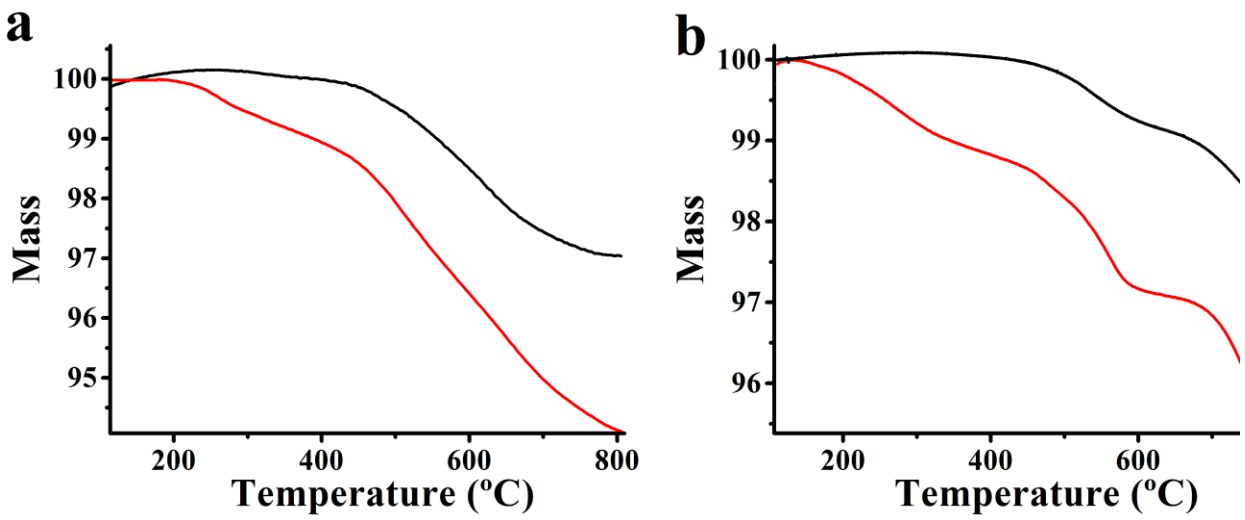

Figure 4. Thermographs for (a) BOC modified MoS_2-based material **2a** (black), ammonium modified MoS_2-based material **3a** (red) and (b) BOC modified WS_2-based material **2b** (black), ammonium modified WS_2-based material **3b** (red).

Morphological insight on the modified MoS_2 and WS_2 materials comes from FE-SEM imaging. Briefly, **3a** and **3b** were dispersed in MeOH and a drop was deposited onto the sample holder and thoroughly examined. Representative images for **3a** and **3b** obtained at lower and higher magnification as shown in Figure 5, reveal the presence of rectangular overlapping oligolayered MoS_2 and WS_2 sheets of varied size. The observation of semi-transparent sheets can be safely associated with the presence of few (or even mono) layers of TMDs, with lattice free of any visible defects and absence of large bulk particles, suggesting that the functionalization methodology applied as well as the acidic treatment for the removal of the BOC protecting group did not affect the original structure of the material.

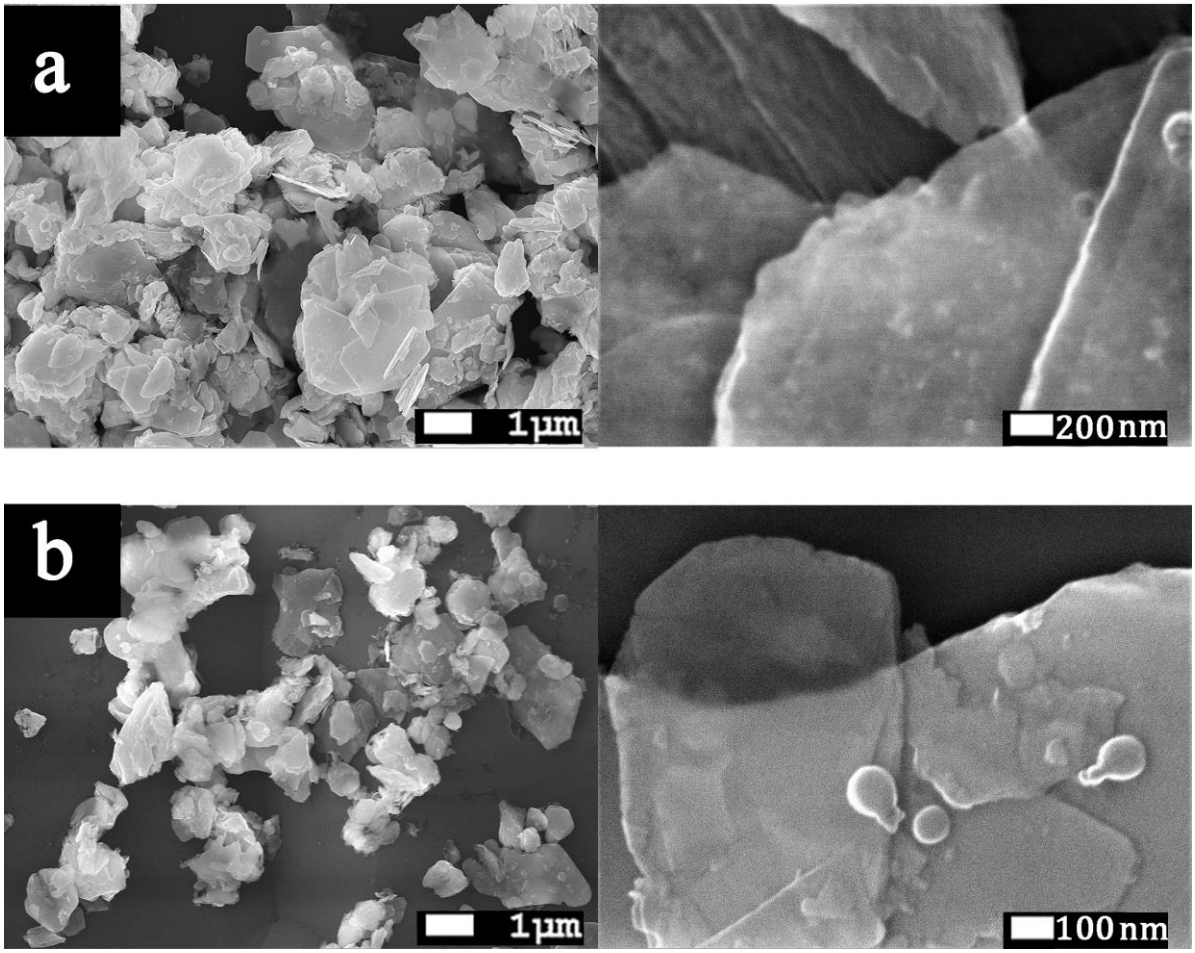

Figure 5. Representative FE-SEM images obtained at lower (left panel) and higher (right panel) magnification for (a) MoS_2-based material **3a**, and (b) WS_2-based material **3b**, respectively.

Next, having in hand ammonium modified MoS_2 and WS_2 with positive charges in material **3**, and negatively charged porphyrin **4**, CDs **5** and poly (3-thiophene sodium acetate) **6**, electrostatic attractive interactions between the species bearing opposite charges were exploited en route the realization of porphyrin/MoS_2 **7a**, porphyrin/WS_2 **7b**, CDs/MoS_2 **8b**, poly (3-thiophene sodium acetate)/MoS_2 **9a** and poly(3-thiophene sodium acetate)/WS_2 **9b** ensembles.

The realization of porphyrin/MoS_2 **7a** and porphyrin/WS_2 **7b** ensembles was monitored by absorption and emission spectroscopy techniques, based on titration assays. The titration of anionic porphyrin **4** with positively charged ammonium modified materials **3a** and **3b** was performed in benzonitrile, while the concentration of the porphyrin remained invariant during the titration measurements. More precisely, a benzonitrile solution of porphyrin (10^{-6} M) was titrated

by adding increasing volumes (0 to 450 μL) of MoS_2-based material **3a** or WS_2-based material **3b** and the corresponding absorption spectra were recorded. The main features present in the UV-Vis spectrum of porphyrin **4** were at 421 nm (Soret band) and 516, 552, 592 and 650 nm (Q bands), while, any absorption spectral changes in the presence of increasing amounts of **3a** and **3b** in benzonitrile were negligible. As seen from the representative UV-Vis spectra (Figure 6a), the decrease in the intensity of the Soret band by the presence of **3a** or **3b** is not dramatic, suggesting weak electronic interactions between the two species, porphyrin and MoS_2 or WS_2, in the ground state. It should be noted that subtraction of the absorption background owed to MoS_2 and WS_2 occurred in order to allow a well-defined observation of the titration results. UV-Vis titration spectra without subtraction of the MoS_2 and WS_2 bands are in Figure 6b-c, where the characteristic absorptions for the semiconducting phase of MoS_2 appear at 630 and 680 nm, while for WS_2 appear at 645 nm. It is worth to mention that first addion 10 μl of **3b** in figure c doesn't not affect to the optical properties due to the low amount of positively charged ammonium WS_2 material, detecting appreciable changes ones extra 40 μl are added.

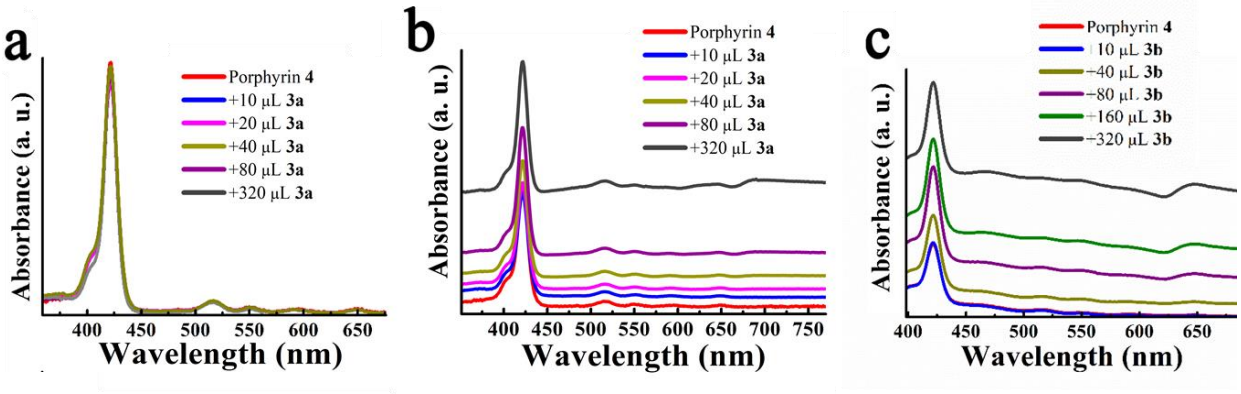

Figure 6. Absorption spectra of anionic porphyrin **4** upon incremental additions of positively charged MoS_2-based material **3a** (a) without and (b) with subtraction of MoS_2 signals and (c) absorption spectra of anionic porphyrin **4** upon incremental additions of positively charged WS_2-based material **3b**, in benzonitrile.

In stark contrast, turning to steady-state fluorescence measurements, quite strong interactions in the excited state were observed. Figure **7a** shows fluorescence spectral changes of the porphyrin's emission during increased additions of positively charged ammonium modified MoS_2 **3a** in benzonitrile, when excited at 420 nm. Particularly, the intensity of the porphyrin-

centered fluorescence, with maxima at 655 and 720 nm, was found to depend on the concentration of **3a** and progressively quenched, specifying the formation of **7a** ensembles. In an analogous fashion, quenching of the porphyrin's photoluminescence upon incremental additions of positively charged ammonium modified WS_2 **3b** (Figure 6b), leading to the realization of **7b** was observed. Notably, in blank titration assays of the negatively charged porphyrin **4** employing neutral **2a** and **2b** instead of the positively charged **3a** and **3b**, (Figures 7c and 7d, respectively), a significantly lower quenching rate for the emission of porphyrin was observed, proving the beneficial role of the electrostatic interactions between the two components for achieving effective electronic communication. Overall, these results justify the efficient deactivation of the singlet-excited state of porphyrin to MoS_2 or WS_2 either via energy or electron-transfer as the effective decay mechanism.

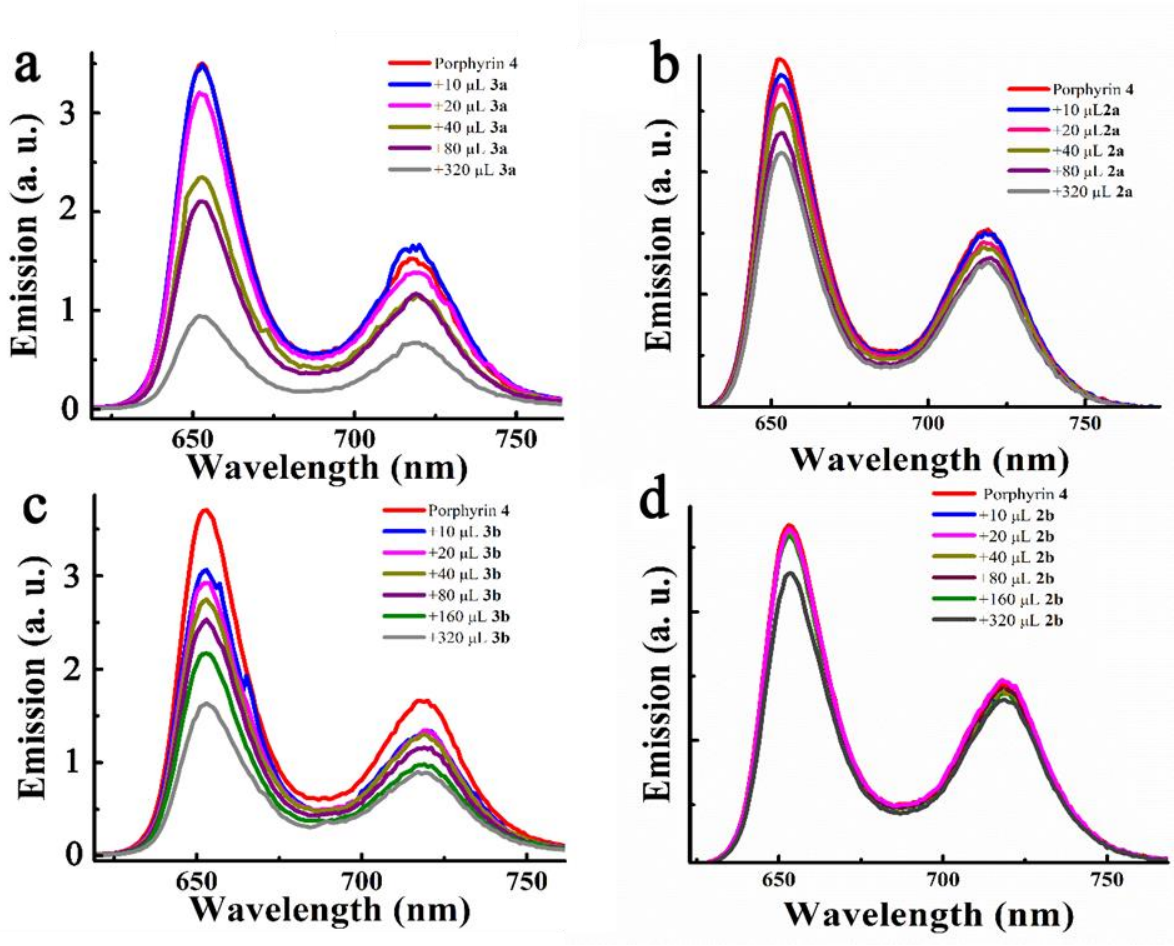

Figure 7. (a) Emission titration assays of anionic porphyrin **4** upon incremental additions of (a) positively charged MoS_2-based material **3a**, (b) WS_2-based material **3b**, (c) neutral MoS_2-based

material **2a** and (c) neutral WS_2-based material **2b** respectively. Measurements were conducted in benzonitrile upon excitation at 420 nm.

Next, to further support the results obtained and get additional insight on the electronic interplay between porphyrin and MoS_2 in **7a** and WS_2 in **7b**, time-resolved photoluminescence studies based on the time-correlated-single-photon-counting method were performed. The fluorescence decay at 655 nm corresponding to anionic porphyrin **4** was monoexponentially fitted with a lifetime of 9.21 ns. However, by the same fitting of the fluorescence decay of **7a** and **7b**, the corresponding lifetimes were evaluated to be faster, 4.23 and 3.97 ns, respectively. The latter result is rationalized by considering appreciable Coulombic interactions between the species bearing opposite charges. Hence, transduction of energy from photoexcited porphyrin to MoS_2 in **7a** and WS_2 in **7b** occurs and the quenching rate constant k^S_q and quantum yield Φ^S_q of the singlet excited state were calculated to be 1.43 x 10^8 s^{-1} and 1.28 x 10^8 s^{-1}, and 0.57 and 0.54, for **7a** and 7**b**, respectively.

Moving on the electrostatic association of CDs with TMDs, Figure 8 shows the electronic absorption spectra of CDs **5** upon addition of incremental amounts of ammonium modified MoS_2 **3a**. Again, subtraction of the MoS_2 absorption background allowed a clear observation of the titration effects. Evidently, a progressive red-shift for the absorption of CDs **5** is observed, namely from 350 to 355 nm after the addition of 320 μL of **3a**. Moreover, an isosbestic point at 310 nm, consistent with strong electronic communication between the two species in the ground state, was developed. Notably, when blank titration assays were conducted, by employing the neutral MoS_2-based derivative **2a** instead of the positively charged **3**, none of the aforementioned results were observed (Figure 8b), thus, proving the beneficial role of attractive Coulombic forces not only in the establishment of the CDs/MoS_2 ensembles but also on the progression of effective interactions between MoS_2 and CDs.

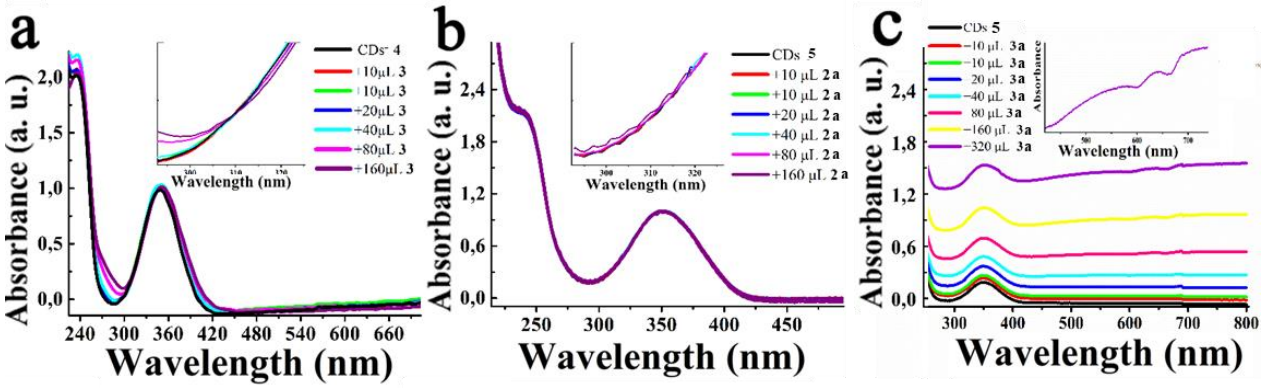

Figure 8. Absorption spectra of anionic CDs **5** upon incremental additions of (a) positively charged MoS_2-based material **3a**. Inset: Enlargement of the 300-320 nm region, where the isosbestic point is developed, (b) neutral MoS_2-based material **2a** with subtraction of MoS_2 signals. (c) Absorption spectra of anionic CDs **5** upon incremental additions of positively charged MoS_2-based material **3a**. Inset: Enlargement of the 450-720 nm region showing absorption bands due to MoS_2.

Meaningful insight on photoinduced electronic interactions between MoS_2 and CDs at the excited states was derived from photoluminescence measurements. Steady-state assays revealed that the 460 nm fluorescence emission of CDs **5**, upon excitation at 370 nm, was progressively quenched upon addition of the ammonium modified MoS_2-based material **3a** (Figure 9a), for samples possessing equal absorbance at the excitation wavelength. Notably, when blank assays were conducted, by incorporating the neutral MoS_2-based derivative **2a** instead of the positively charged **3a**, a lower quenching rate for the emission of CDs **5** was observed (Figure 9b), ascribed to the inner filter effect of MoS_2. These results suggest strong electronic interactions at the excited states between the positive and negative species within the CDs/MoS_2 ensemble. The photoluminescence quenching is supportive of photoinduced electron and/or energy transfer as the decay mechanism for the transduction of the singlet excited state of CDs.

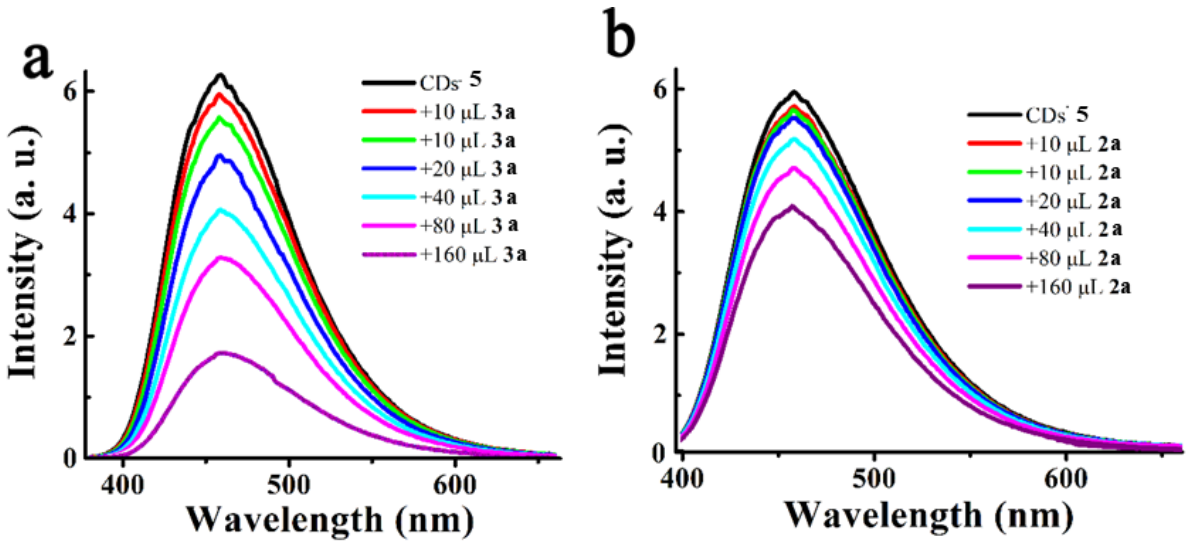

Figure 9. Emission titration assays of anionic CDs **5** (20 μg/mL) upon incremental additions of (a) positively charged MoS_2-based material **3**, and (b) neutral MoS_2-based material **2**. Measurements were conducted in water for samples possessing equal absorbance at the excitation wavelength of 370 nm.

Next, based on the time-correlated-single-photon-counting method, the fluorescence emission decay profiles for CDs **5** were acquired (Figure 10a). The analysis of the decay profiles at 460 nm (excitation at 376 nm) for the singlet excited state of CDs **5** was exclusively monoexponentially fitted with a lifetime of 14.0 ns. Addition of the positively charged MoS_2-based material **3** to the negatively charged CDs **5** resulted in biexponential fitting, giving rise to the identification of two components, namely, one with the same lifetime, attributed to non-interacting CDs and a faster new one with 3.0 ns lifetime, corresponding to the fluorescence quenching of the emission intensity of the singlet excited state of CDs within the CDs/MoS_2 ensembles. By comparing the lifetime of unbound CDs with the one attributed to the CDs/MoS_2 ensembles, the quenching rate constant k^S_q and the quenching quantum yield Φ^S_q were estimated to be 2.67×10^8 s^{-1} and 0.79, respectively. This is further confirmed upon examination of the fluorescence decay profile for the blank measurement employing neutral MoS_2-based derivative **2**, which remained monoexponentially fitted, following the lifetime of intact CDs **5** (Figure 10b).

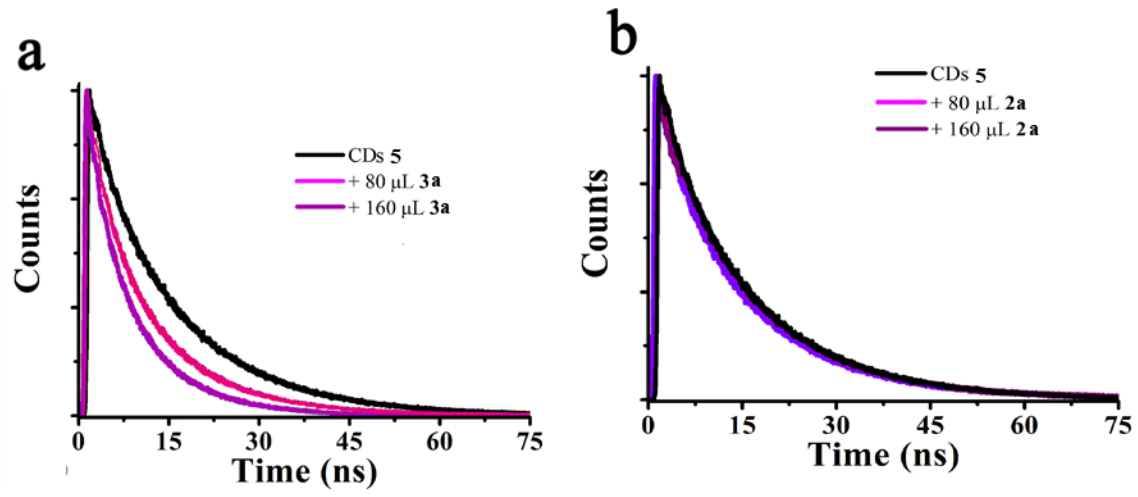

Figure 10. Decay profiles for **5** upon incremental additions of (a) positively charged MoS_2-based material **3a** and (b) neutral MoS_2-based material **2a**.

The electrocatalytic activity of CDs/MoS_2 **8** towards the hydrogen evolution reaction (HER) was examined by employing a rotating disc working glassy carbon electrode in a standard three-electrode glass cell at a scan rate of 5 mV/sec in 0.5 M H_2SO_4. In general, MoS_2 are promising materials for HER, based on the overpotential and Tafel slope values they exhibit.[46,47] In addition, the aqueous solubility of CDs together with the presence of surface functional groups contribute to draw hydrated protons, thus enhancing proton adsorption capacity,[48] Based on the above and considering that hydrogen binds too strongly to S, hence leaving as primary active site for MoS_2 the Mo edge, the performance of CDs/MoS_2 towards the HER was probed by linear sweep voltammetry. The polarization curve of CDs/MoS_2 along with those of individual CDs **5** and bare glassy carbon electrode for comparison are shown in Figure 16a. For a given potential, the cathodic current increased for CDs/MoS_2 as compared to that based on individual CDs **5** and the bare carbon glassy electrode. The evolution of gaseous hydrogen for CDs/MoS_2 was visualized as bubbles appearing at currents as small as 0.5 $\mu A/cm^2$, with enhanced rate at around -0.7 V vs RHE. Since the cathodic current density is proportional to the amount of hydrogen evolved, the latter result highlights the better catalytic activity for CDs/MoS_2 and prominent hydrogen evolution behavior exhibiting an onset overpotential near -0.5 V vs RHE, which is lower than the individual CDs **5** by around 150 mV. The better electro-catalytic activity of CDs/MoS_2 is mainly attributed to a synergic effect due to enhanced charge-transfer kinetics

owed to the intimate contact between the two species CDs and MoS_2 as well as the presence of active sites in MoS_2. Next, the linear regions of the Tafel plots (Figure 11b) were fit to the Tafel equation, $\eta = B \log j + a$, where η is the overpotential, j is the current density and B is the Tafel slope, to further characterize the fluent charge transport efficiency and the efficacy of the electro-catalytic reaction. Analysis of the Tafel slope helps to elucidate the possible HER mechanism and define the rate-limiting step. The Tafel slope for CDs/MoS_2 ensemble was found to be 22 mV/dec, smaller than that owed to CDs **5** by 4 mV/dec. Considering that smaller Tafel slope suggests that for the generation of an equivalent current only a lower overpotential is needed to apply, the electro-catalytic activity of individual CDs **5** is improved upon realization of the CDs/MoS_2 ensemble. The latter improvement in charge transport is attributed to good electrical contact between the two components in the donor-acceptor CDs/MoS_2 ensemble, in which charge-transfer phenomena prevail. Moreover, the small Tafel slope of CDs/MoS_2 manifests that the electrochemical desorption of adsorbed hydrogen atoms onto the modified electrode to generate hydrogen is the rate-limiting step – see equations 2 and 3 below. Based on the widely applied mechanisms for the HER, initially a proton is adsorbed onto the electrode surface via a reduction process (Volmer adsorption [Eq. (1)]) followed by either direct bonding of the adsorbed hydrogen atom with another proton and electron transfer from the electrode surface (Heyrovsky desorption [Eq. (2)]) or recombination of two hydrogen atoms adsorbed on the electrode surface (Tafel desorption [Eq. (3)]).

Volmer adsorption: $H^+ + e^- \rightarrow H^\bullet_{(ads)}$ (1)

Heyrovsky desorption: $H^\bullet_{(ads)} + H^+ + e^- \rightarrow H_2$ (2)

Tafel desorption: $H^\bullet_{(ads)} + H^\bullet_{(ads)} \rightarrow H_2$ (3)

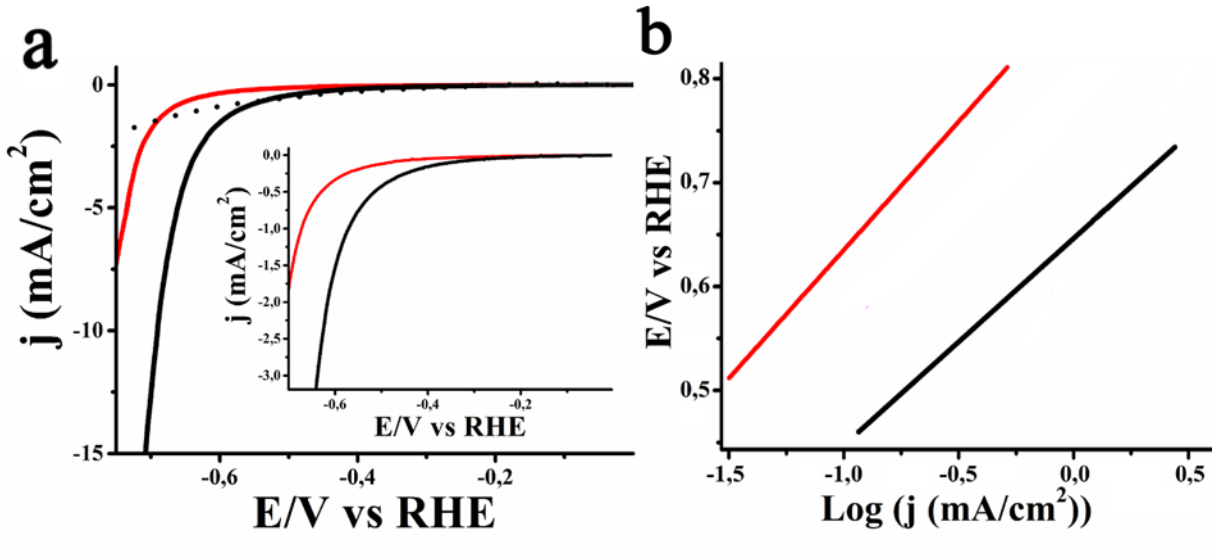

Figure 11. (a) Linear sweep voltammograms for the HER of CDs/MoS_2 **8** (black), individual CDs **5** (red) and bare glassy carbon electrode (dotted). Inset: enlarged region near the onset. (b) Tafel plots for CDs/MoS_2 (black) and individual CDs **5** (red) showing overpotential vs current density.

Next, focusing on the integration of poly (3-thiophene sodium acetate) **6** on TMDs, the formation of ensembles **9a** and **9b** was realized upon addition of aqueous **3a** and **3b** to water-soluble **6**, based on a series of titration assays, monitored by electronic absorption spectroscopy. In more detail, the UV-Vis spectrum of **6** exhibits a strong and broad absorption band around 400 nm due to π-π* transitions of the conjugated polymer backbone, corresponding to the non-aggregated amorphous polymer domains.[49] Upon incremental additions of **3a** and **3b**, the excitonic bands of MoS_2 at 629 and 687 nm and of WS_2 at 654 nm started to evolve (inset, Figure 12a-12b). Subtraction of the absorption background due to MoS_2 and WS_2 allowed a clear observation of the titration effect on the polymer's absorption features, during formation of **9a** and **9b**. Specifically, a blue-shift of 4 and 9 nm of the polymer's band after a total of 290 μL and 40 μL was observed for **9a** and **9b**, respectively (Figure 12a and 12b). This hypsochromic shift corresponds to conformational changes on the structure of **6**, as the long π-π conjugation system of the coplanar polythiophene breaks[50] due to the developed attractive electrostatic interactions with the modified TMDs **3a** and **3b**. In addition, the absorption band due to **6** was progressively decreased upon interaction with **3a** and **3b**. Considering that the unstacked carboxylate unit absorbs more light in intact polymer **6**, the latter decrease identified in the corresponding

absorption band of the ensembles **9a** and **9b** can be safely attributed to efficient interactions developed between the carboxylate units of **6** and the ammonium species of **3a** and **3b**, respectively. On the other hand, in blank titration assays performed by employing exfoliated MoS_2 and WS_2, neither a blue-shift nor a decrease in the polymer's absorption features were observed (Figure 11c and d), showcasing the role of modified MoS_2 and WS_2 with ammonium units for the effective Coulombic association with negatively charged **6**.

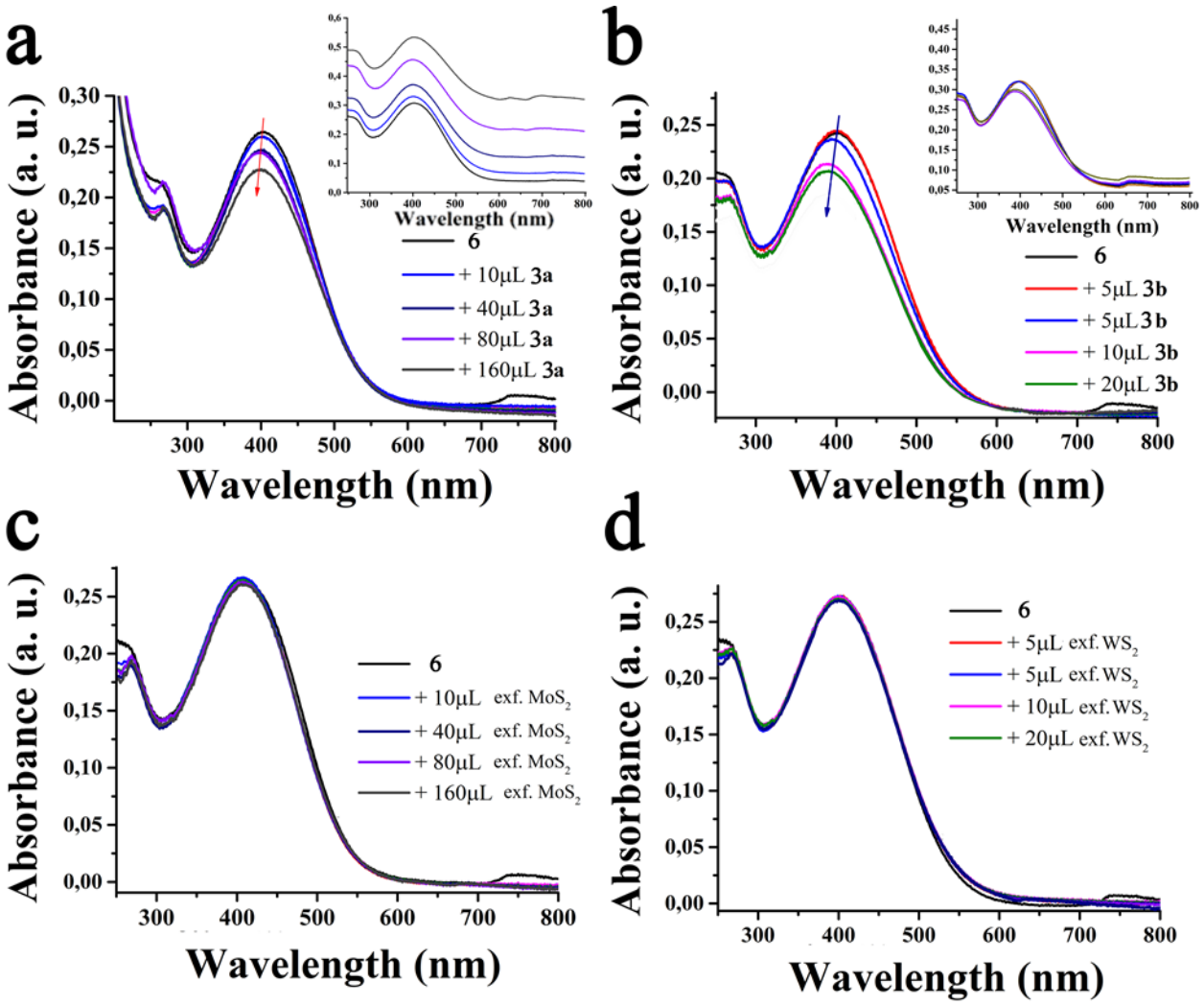

Figure 12. Absorption spectra of anionic **6** upon incremental additions of (a) positively charged MoS_2-based material **3a** with subtraction of MoS_2 signals (b) positively charged WS_2-based material with subtraction of WS_2 signals and Inset: UV-Vis absorption spectra of **6** upon incremental additions of ammonium modified (a) MoS_2-based material **3a** and (b) WS_2-based

material **3b**. Absorption spectra of anionic **6** upon incremental additions of (a) neutral MoS_2-based material **2a** and (b) neutral WS_2-based material with subtraction of WS_2 signals.

Photoluminescence spectroscopy measurements were carried out to elucidate possible interactions between **6** with **3a** and **3b** at the excited states. Aqueous **6** exhibits fluorescence emission centered at 555 nm, upon excitation at 395 nm. This photoluminescence band gradually decreases with increasing amounts of ammonium modified MoS_2 **3a** or WS_2 **3b** (Figure 13a and b), thereby leading to the realization of **9a** and **9b**, respectively. These outcomes prove the effective deactivation of the singlet-excited state of **6** to MoS_2 and WS_2, via energy and/or electron transfer as the decay mechanism. Besides, when blank assays were investigated, by incorporating exfoliated MoS_2 and WS_2 instead of the positively charged ones, a substantially lower quenching rate for the emission of **6** was observed (Figure 13c and d). The observation of intra-ensemble photo-induced processes from poly(3-thiophene sodium acetate) **6** to MoS_2 and WS_2 is consistent with the oxidation potential of the former, precisely the energy of the singlet excited state of **6**, that lies above the conduction band of MoS_2 and WS_2. The energy for the singlet excited state of **6** can be easily obtained from the crossing point of the corresponding absorption and emission spectra (Figure 14) and found to be 2.50 eV. On the other hand, the conduction band edges for MoS_2 and WS_2 were calcualted to be 4.27 and 3.96 eV below the vacuum level, respectively, as a result of the higher reactivity of Mo vs W.[51] Hence, photoexcited electron/energy transfer from **6** to both MoS_2 and WS_2 within **9a** and **9b** respectively, is an energetically favored process. Moreover, the degree of fluorescence emission quenching of **6** in the presence of WS_2 is more prominent than that registered by MoS_2. For instance, for the quantitative emission quenching of **6** (2 mL, 10 mM) addition of 290 μL of **3a** (0.33 mg/mL) is required, while only 40 μL of **3b** (0.33 mg/mL) produces similar result – see Figure 13a and b. This fact is attributed to the smaller energy difference between the singlet excited state of **6** and the conduction band of WS_2, calculated to be 1.46 eV, as compared to that of MoS_2 which is calculated to be 1.77 eV.

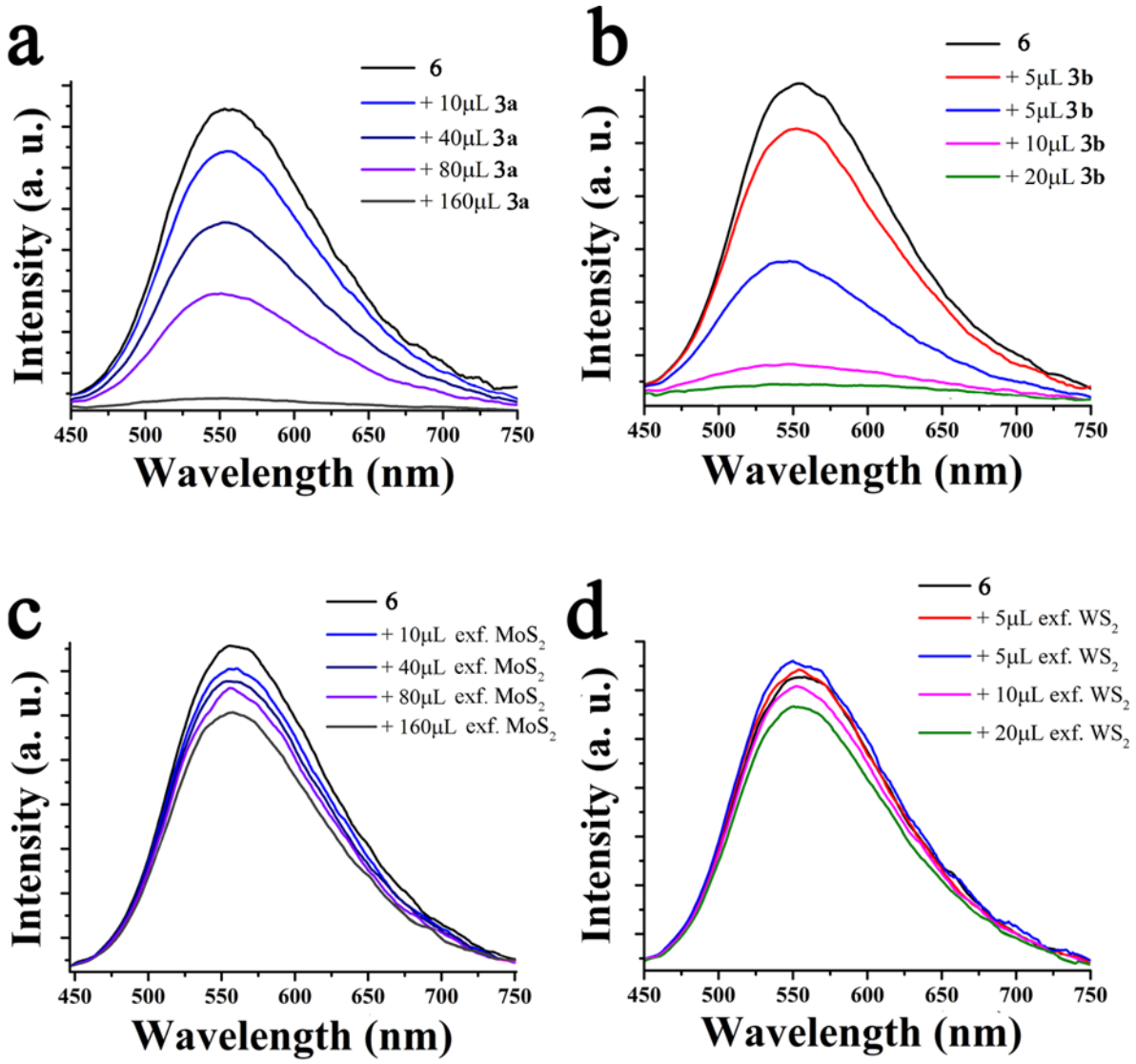

Figure 13. Emission titration assays of anionic **6** upon incremental additions of (a) positively charged MoS_2-based material **3a**, (b) positively charged WS_2-based material **3b**, (c) neutral MoS_2-based material **2a** and (d) neutral WS_2-based material **2b** respectively. Measurements were conducted in benzonitrile upon excitation at 395 nm.

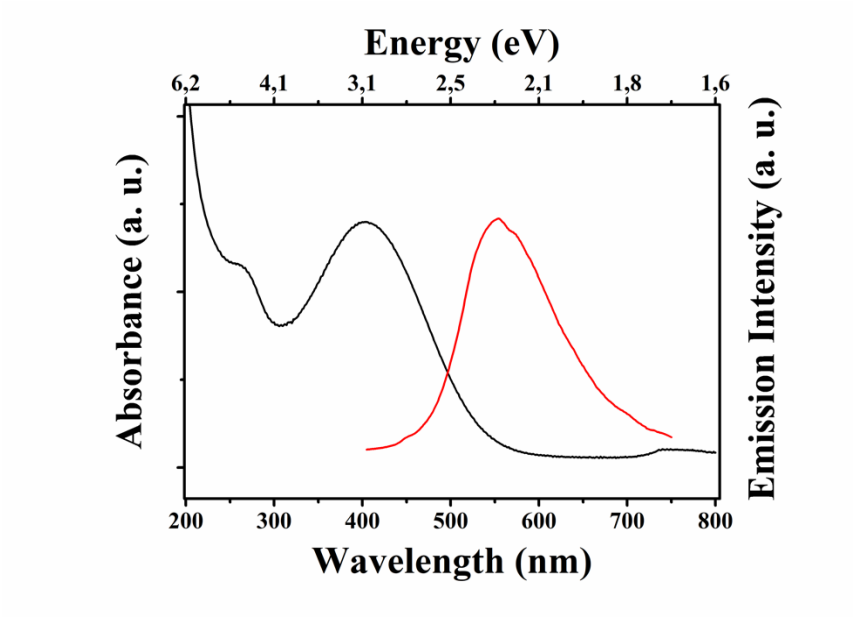

Figure 14. Absorption spectra and fluorescence emission spectra of anionic poly (3-thiophene sodium acetate) **6**. From the crossing point of the two spectra the energy of the singlet excited state of 1 is derived as 2.50 eV.

In order to get additional insight on the electronic communication between **6** with MoS_2 and WS_2, within **3a** and **3b**, time-resolved photoluminescence assays based on the time-correlated-single-photon-counting method were conducted. Polymer **6** shows a decay at 555 nm, which was monoexponentially fitted with a lifetime of 0.6 ns. On the other hand, ensembles **3a** and **3b** were better correlated with a biexponential fitting, which after analysis gave rise to lifetimes of 0.12 and 0.6 ns for **3a** and 0.14 and 0.6 ns for 3**b**. While the slow lifetimes were identical to those due to free polymer **6**, the faster new ones 0.12 and 0.14 ns, for **3a** and **3b**, respectively, correspond to the fluorescence quenching of the emission intensity of the singlet excited state of the polymer within the ensembles **3a** and **3b**. Then, the quenching rate constant and quenching quantum yield were estimated for both **3a** and **3b** are $6.67 \times 10^9$and 5.48×10^9 and 0.80 and 0.78 respectively.

To further investigate the interactions between **6** with modified MoS_2 and WS_2 within ensembles **9a** and **9b**, Raman measurements were carried out under on-resonance conditions (633 nm for MoS_2-based materials and 514 nm for WS_2-based materials) on drop-casted films of the materials. As far as ensemble **9a** concerns, on top of the aforementioned observations, an additional band at 1460 cm^{-1} after subtracting the intense fluorescence of **9** was observed (Figure

15a). The latter band is due to the C=C of the thiophene ring[52] and found to be red-shifted by 5 cm^{-1} as compared with the corresponding band registered for intact **6**. Similar is the situation with the Raman spectra due to WS_2-based materials. In this case, WS_2 the band due to the C=C of the thiophene in **9b** was red-shifted by 10 cm^{-1} centered at 1455 cm^{-1}, as compared to intact **6** (Figure 15b).

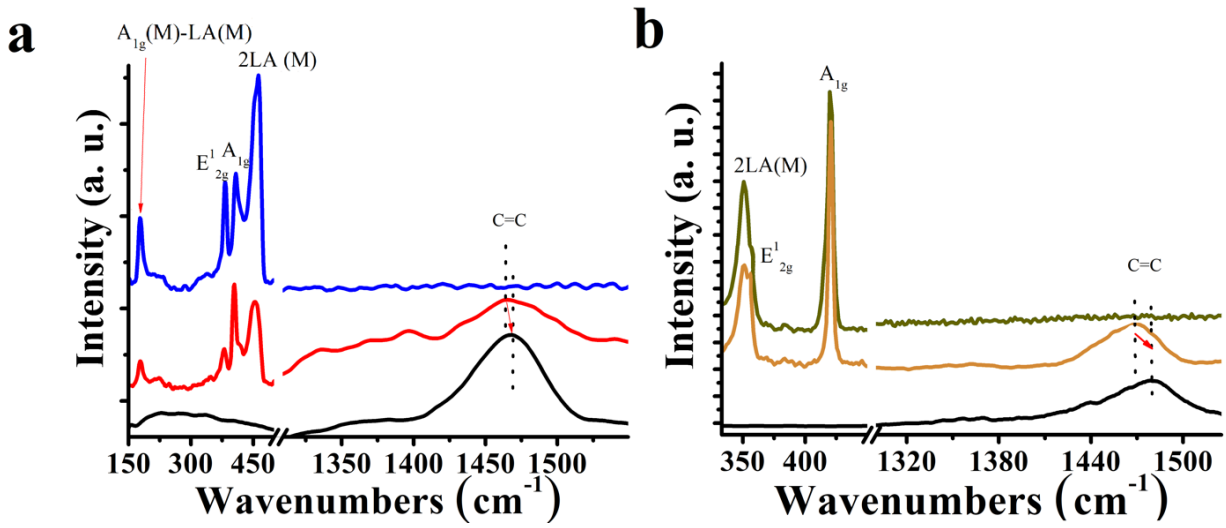

Figure 15. Raman spectra for (a) exfoliated MoS_2 (blue), ensemble **9a** (red), **6** (black), obtained upon 633 nm excitation, and (b) exfoliated WS_2 (olive), ensemble **9b** (brown) and **6** (black), obtained upon 514 nm excitation.

The morphology of the ensembles **9a** and **9b** was assessed by SEM imaging. The pictures are clearly different as compared with the previous images in Figure 16 for **3a** and **3b** materials, being clearly seen that MoS_2 and WS_2 are covered by soft organic matter due to the presence of polymer **6**. The latter is further corroborated due to the lack of crystallinity of the commonly observed flat structures of TMDs becoming wrinkled and roughen upon integration of the polymer.

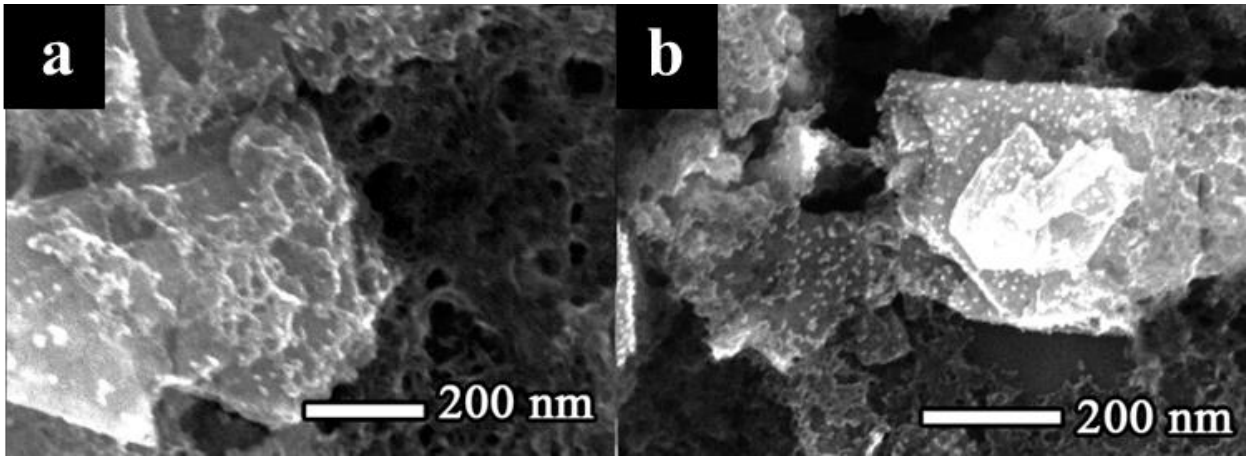

Figure 16. Representative FE-SEM images obtained for (a) MoS_2-based material **9a**, and (b) WS_2-based material **9b**, respectively.

In Figure 17, the general scheme for the non-covalent functionalization of TMDs with pyrene, in which the latter is physisorbed onto the 2D layered materials, is presented. The MoS_2/pyrene and WS_2/pyrene nanoensembles **11a** and **11b**, respectively, were obtained free of non-immobilized pyrene by filtering the reaction mixture over a PTFE filter (100 nm pore size) and subsequently washing the solid residue obtained onto the filter with dichloromethane. The process was followed by monitoring the electronic absorption spectrum of the filtrate until no signatures due to pyrene were observed.

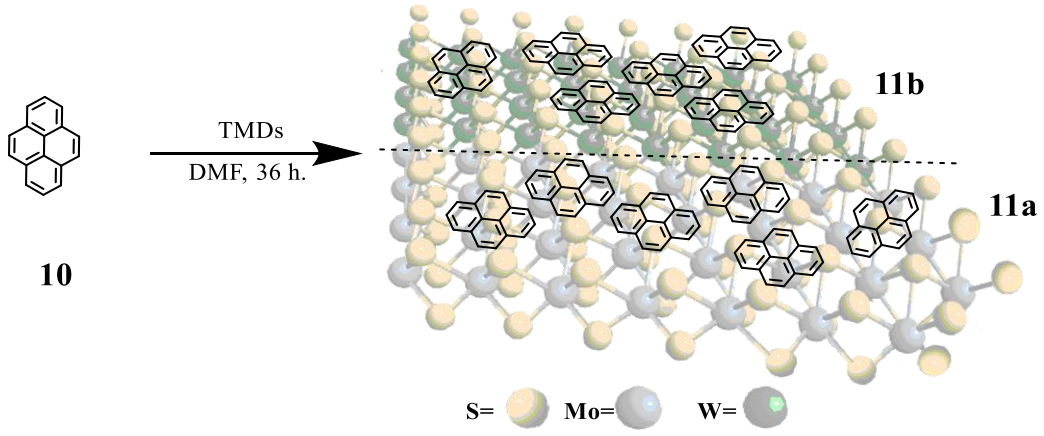

Figure 17. Non-covalent functionalization of exfoliated TMDs by physisorption of pyrene **10** onto 2H-MoS_2 and 2H-WS_2, furnishing **11a** and **11b** ensembles.

The solubility of **11a** and **11b** was calculated with the aid of UV-Vis spectroscopy by initially estimating the molar absorptivity as 3.24 L g^{-1} cm^{-1} at 400 nm for **11a**, 3.04 L g^{-1} cm^{-1} at 465 nm for **11b** and then applying the Beer-Lambert law. In general, **11a** and **11b** ensembles present the best solubility in DMF (100 μg/mL), while they disperse well in o-DCB (50 μg/mL), too.

Electronic absorption spectroscopy studies were performed in DMF and absorption bands of pyrene at 315, 330 and 345 nm were detected in both TMD-based **11a** and **11b** ensembles. Moreover, the typical signals owed to the semiconducting polytype of MoS_2 at 400, 500, 630 and 690 nm for **11a** (Figure 18a) and of WS_2 at 420, 465, 535 and 640 nm for **11b** (Figure 18b) were identified. Markedly, the aforementioned bands were found broadened and red-shifted as compared to the ones owed to the exfoliated 2H-MoS_2 and 2H-WS_2, implying the presence of ground state electronic interactions between pyrene and the TMDs.

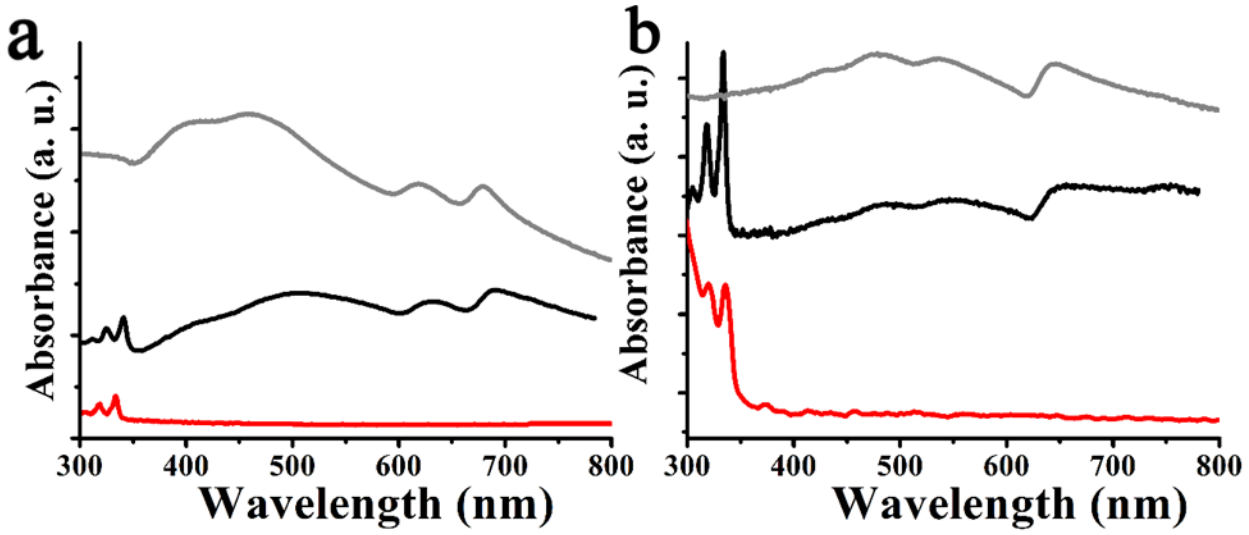

Figure 18. (a) UV-Vis spectra for free pyrene **10** (red) as compared with nanoensemble **11a** (black) and exfoliated MoS_2 of the semiconducting polytype (gray) and (b) UV-Vis spectra for free pyrene **10** (red) as compared with nanoensemble **11b** (black) and exfoliated WS_2 of the semiconducting polytype (gray), obtained in DMF.

The strong emission of pyrene was beneficial to employ it as convenient and sensitive probe for identifying intra-ensemble interactions at the excited states within ensembles **11a** and **11b**. Photoluminescence of monomeric pyrene with fine structure in the 370-430 nm region was observed for free pyrene **10** upon photoexcitation at 340 nm in DMF. Then, after adjusting the

optical concentration of **11a** and **11b** with that of **10** at the excitation wavelength, the photoluminescence was registered. It was found that the emission owed to pyrene was appreciably quenched in **11a** and **11b** as compared to that of **10** (Figure 19a and 19b, respectively). Evidently, the efficient quenching of fluorescence in **11a** and **11a** implies strong electronic interactions of non-covalently immobilized pyrene with MoS_2 and WS_2. In order to further support our results and get additional insight on the electronic communication between the individual species within ensembles **11a** and **11b**, time-resolved fluorescence measurements were performed by employing the time-correlated-single-photon-counting method. The time profile of the fluorescence decay at 396 nm for the singlet-excited state of free pyrene **10** was monoexponentially fitted with a lifetime of 9.66 ns. Notably, the corresponding fitting for **11a** and **11b** was biexponential, giving rise to two components, a faster one with lifetime 275 and 238 ps, respectively, ascribed to efficient interactions of pyrene with MoS_2 and WS_2, respectively, and a slower one with 5.36 ns attributed to non-interacting pyrene. The quenching rate constant k^S_q for the singlet excited state of pyrene was then calculated to be 3.53×10^9 and 4.14×10^9 s^{-1} for MoS_2/pyrene **11a** and WS_2/pyrene **11b,** respectively, while the corresponding quantum yield Φ^S_q was found to be 0.96 and 0.97, respectively.

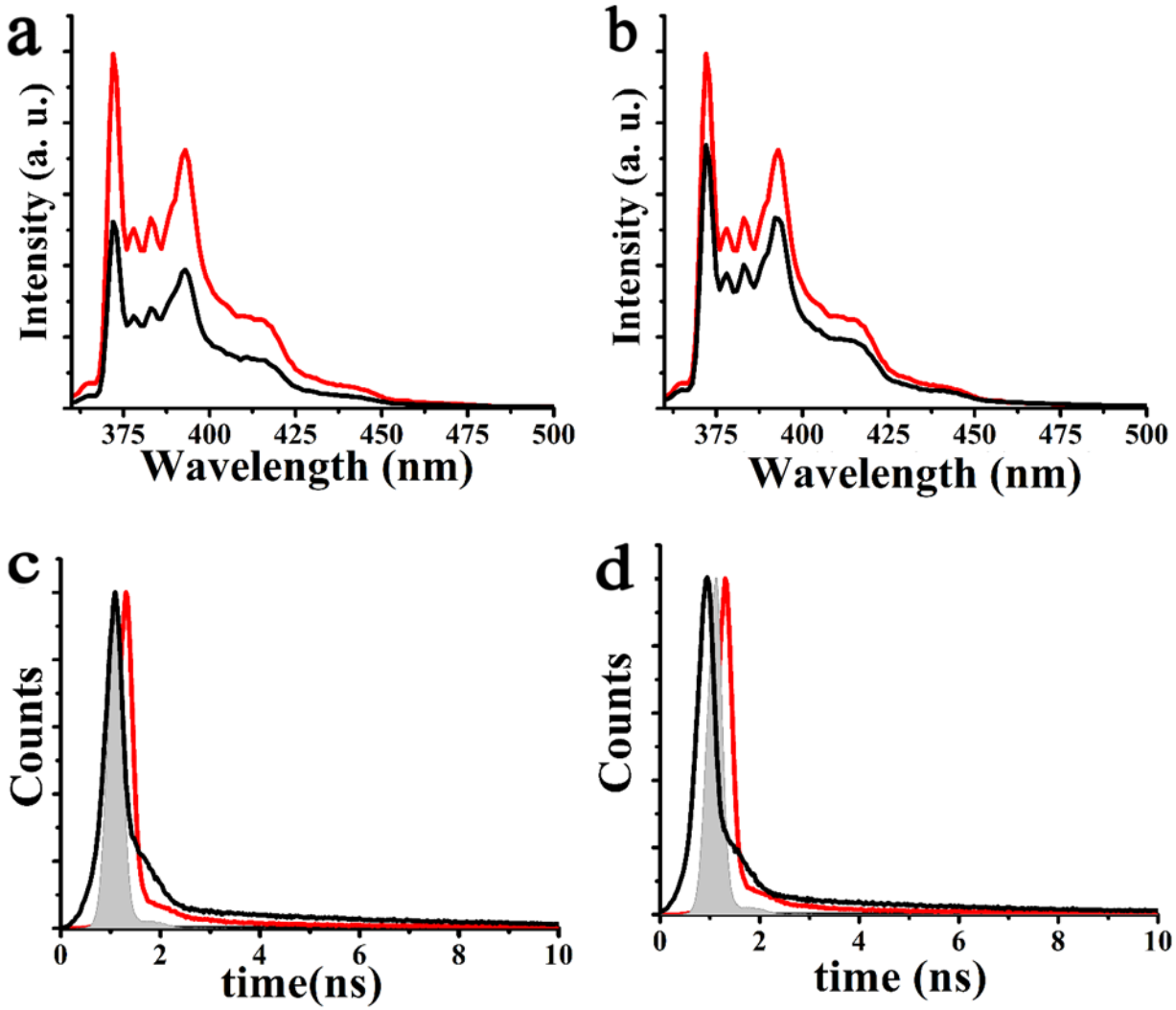

Figure 19. (a) Photoluminescence spectra for free pyrene **10** (red) as compared with nanoensemble **2a** (black), obtained in DMF upon excitation at 340 nm. (b) Photoluminescence spectra for free pyrene **1** (red) as compared with nanoensemble **11b** (black), obtained in DMF upon excitation at 340 nm. (c) Photoluminescence decay time profiles for free pyrene **10** (red) and nanoensemble **11a** (black). (d) Photoluminescence decay time profiles for free pyrene **10** (red) and nanoensemble **11** (black).

Regardless that pyrene **10** was only physisorbed onto MoS_2 and WS_2, thermogravimetric analysis (TGA) was performed to shed light on the amount of pyrene decorating the TMDs. In this context, an appreciable mass loss of 5.9 and 3.9%, under nitrogen in the temperature range 400-600 ºC, was observed for **11a** and **11b**, respectively (Figure 20). The aforementioned mass

loss, associated with the decomposition of the pyrene material, allowed us to calculate the immobilization of one pyrene unit per every 20 Mo atoms for **11a** and per every 27 W atoms for **11b**, respectively, representing a rather high coverage.

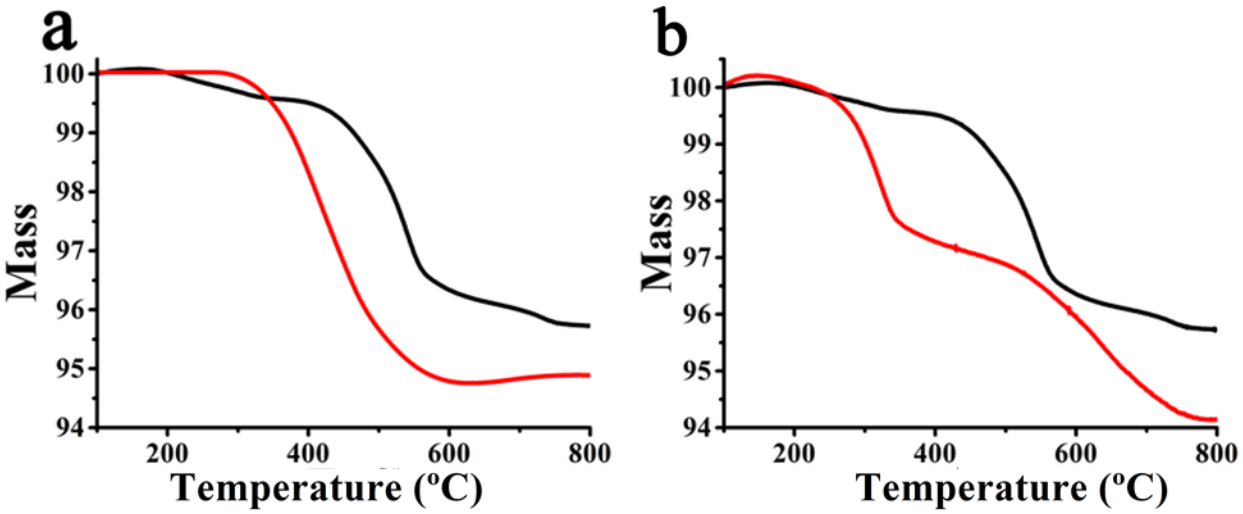

Figure 20. TGA of (a) **11a** (red) as compared with exfoliated MoS_2 of the semiconducting polytype (black), (b) and **11b** (red) as compared with exfoliated WS_2 of the semiconducting polytype (black) under nitrogen atmosphere.

Next, Raman spectroscopic study was performed in order to unveil important structural information for **11a** and **11b**. Exciting MoS_2 by 514 nm with less than 0.1 mW power at ambient conditions, MoS_2/pyrene **11a** and exfoliated MoS_2 materials, showed spectra with the same characteristics. Bands at 378, 405 and 446 cm^{-1} were distinguishable and related with the so-called E^1_{2g}, A_{1g} and 2LA(M), modes, respectively. The absence of the characteristic peaks from the metallic polytype, J_1, J_2 and J_3 at 150, 225 325 cm^{-1}, respectively, showcases the semiconducting properties of MoS_2 in the **11a** ensemble. However, the situation was dramatically changed for exfoliated MoS_2 once the power of laser irradiation was increased to 0.9 mW. New and strong Raman bands evolved located at both lower and higher energies and attributed to oxidized states of Mo. Specifically, the emergence of well-resolved bands centred at 843 and 859 cm^{-1} due to MoO_4 and MoO_6,[53] and at 948 cm^{-1} due to MoO_3[53] on top of the E^1_{2g}, A_{1g} and 2LA(M) modes, govern the spectrum of exfoliated MoS_2 (Figure 21). In addition, broad features with peaks at 151, 332 and 332 cm^{-1} attributed to MoO_3[53] were also observed, showing the quick photodegradation of the material upon light irradiation in ambient conditions.

Remarkably, when MoS_2/pyrene **11a** was subjected to the same exposure conditions (514 nm with 0.9 mW) no perturbation of the MoS_2 structure was observed as the corresponding Raman spectrum of **11a** retained its original features (Figure 21a). Similar was the situation with the Raman spectra for WS_2/pyrene **11b** and exfoliated WS_2. In brief, under on-resonance conditions with red laser illumination (514 nm, with less than 0.1 mW power at ambient conditions) three intense and distinguishable bands at 350, 355 and 418 cm^{-1}, due to the 2LA(M), E^1_{2g} and A_{1g} modes, respectively, were evident (Figure 21b). However, upon increasing the laser power to 0.9 mW, exfoliated WS_2 showed additional Raman peaks at 127 and 257 cm^{-1} related to WO_3 as well as a peak at 294 cm^{-1} associated with WO accompanied by two sharp peaks at 688 and 805 cm^{-1} linked to WO_2 species (Figure 21c).[54] All those bands associated to WO_x species were absent when WS_2/pyrene **11b** was exposed to light irradiation even at higher laser power conditions (Figure 21d). It should also be noted the proportional reduction of the MoS_2 and WS_2 characteristic modes E^1_{2g}, A_{1g} and 2LA(M), according to the degree of oxidation. Consequently, pyrene plays an important protecting role of MoS_2 and WS_2 from oxidation.

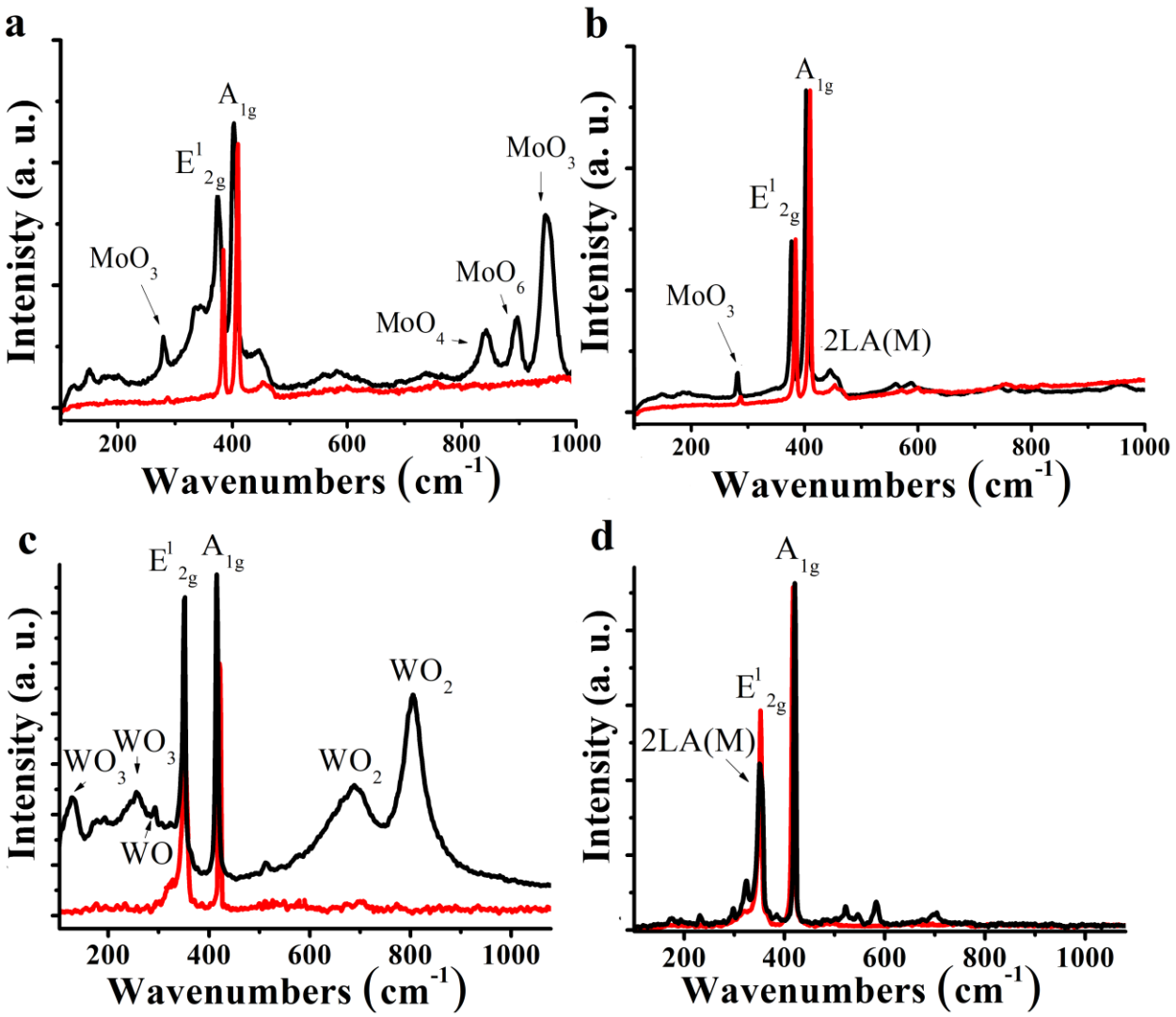

Figure 21. Raman spectra acquired at ambient conditions upon excitation at 514 nm with 0.1 mW (red) and 0.9 mW (black) laser power for (a) exfoliated MoS_2, (b) MoS_2/pyrene **11a**, (c) exfoliated WS_2, and (d) WS_2/pyrene **11b**.

In order to investigate more in detail and at the local scale the pyrene covering/functionalization of the TMDs materials, in particular MoS_2 flakes, we performed different TEM analyses. Indeed, such kind of analyses are required to have access to this structural and chemical information at the (sub-)nanometer level,[58]. Figure 22 shows the ensemble of these TEM results. Figure 22a and c correspond to two STEM high-angular annular dark-field (HAADF) images of two flakes of a pyrene functionalized MoS_2 sample (Figure 22a) and a pristine MoS_2 sample (Figure 22c). Both of the samples have followed the same light irradiation treatment at ambient conditions. Two

different EELS spectrum-line (SPLI) have been acquired following the two green lines that can be observed in these micrographs. For each of them, two different regions, marked as (i) and (ii) in each of the figures, have been selected. The two EELS spectra selected in Figure 22b show the S-$L_{2,3}$, Mo-$M_{4,5}$, C-K and Mo-$M_{2,3}$ edges. The Mo and S edges correspond to the MoS_2 flake and the carbon content confirms the presence of the pyrene moieties in the samples.[58] It is important to note that, even if we have examined close to 15 different areas of different flakes, oxygen has not been detected in this pyrene functionalized sample. This is not the case for the other pristine (no pyrene functionalized) sample that has also been irradiated. In fact, we have performed similar EELS on this sample (Figure 22c and d), and in this one, oxygen has been easily detected. This oxygen, (see Figure 22d-iii), corresponds to the oxidation of the flake, where a mix of molybdenum oxide and molybdenum disulfide can be observed in this region. This conclusion can be clearly inferred from the comparison of the S-$L_{2,3}$ edge in the two different selected regions of the SPLI of Figure 22c. The S-$L_{2,3}$ edge of the EEL spectrum marked as Figure 22d-iii is similar to this one obtained by other authors investigating a mixture of MoO_x-MoS_2 phases in nanomaterials.

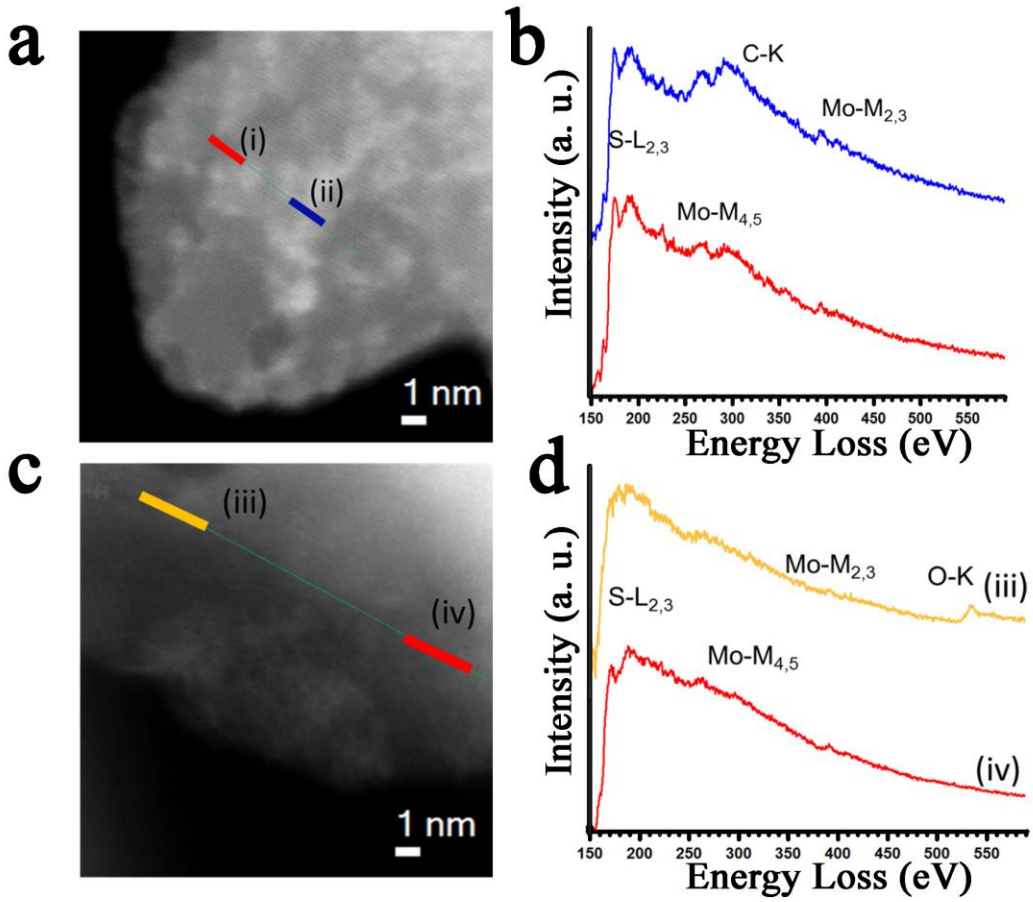

Figure 22. (a) and (c) HAADF-STEM micrographs of a pyrene functionalized MoS_2 flake and a pristine MoS_2 flake, respectively. Two EELS spectrum-lines have been recorded on these flakes, see the green lines marked in the Figure 22a and c. (b) 2 EELS spectra corresponding to the sum of 7 spectra recorded in each of the 2 areas highlighted in red (i) and blue (ii) in the Figure 22a, respectively. Carbon (corresponding to the pyrene), sulfur and molybdenum (associated to the MoS_2) are detected in these spectra. (d) 2 EEL spectra corresponding to the addition of 8 spectra collected in each of the 2 regions highlighted in orange (iii) and red (iv) in Figure. 22c, respectively. The presence of oxygen denotes the clear oxidation of this MoS_2 flake, see the text.

Shedding light on the oxidation mechanism, initially, oxygen from air is physisorbed onto the exfoliated MoS_2 and WS_2. In the next step, upon laser irradiation, the surface of TMDs is damaged, with defected sites created and stabilized by chemisorbed oxygen. At the same time, sulfur atoms may come out from the lattice and replaced oxygen ones, resulting in structural deformation. In fact, sulfur vacancies are thermodynamically favorable to be replaced by

substitutional oxygen species.[55] Localized heating, due to Raman laser irradiation conditions, further damages the chemisorbed TMDs surface, abundantly generating structural defects and etching the surface. Such transformations are evidenced in the Raman spectra of exfoliated MoS_2 and WS_2 after prolonged irradiation period, where not only new bands due to MoO_x and WO_x were evolved but also the intensity of the characteristic A_{1g}, E_{2g} and 2LA(M) modes was reduced.

Conversely, pyrene immobilized on the basal plane of TMDs by non-covalent interactions acts as barrier, insulating TMDs from the outer environment and avoiding physisorption of oxygen. This is evidenced by observing unaltered Raman spectra for **11a** and **11b** even after enhancing the laser power irradiation. Notably, materials stored under ambient conditions for more than two years remained structurally unaltered, showing that pyrene not only prevents the oxidation but also the aging of TMDs.[56]

6.3 EXPERIMENTAL SECTION

6.3.1 Materials

Instrumentation. ^{1}H and ^{13}C NMR spectra were recorded in a 300 MHz Varian instrument operated by Vjnmr software, with TMS used as internal standard and D_2O as solvent. Steady-state UV-Vis electronic absorption spectra were recorded on a PerkinElmer (Lambda 19) UV-Vis-NIR spectrophotometer. Steady-state emission spectra were recorded on a Fluorolog-3 JobinYvon-Spex spectrofluorometer (model GL3-21). Pico-second time-resolved fluorescence spectra were measured by the time-correlated-single-photon-counting (TCSPC) method on a Nano-Log spectrofluorometer (Horiba JobinYvon), by using a laser diode as an excitation source (NanoLED, 375 nm) and a UV-Vis detector TBX-PMT series (250-850 nm) by Horiba JobinYvon. Lifetimes were evaluated with the DAS6 Fluorescence-Decay Analysis Software. Mid-infrared spectra in the region 500−4500 cm^{-1} were obtained on a Fourier transform IR spectrometer (Equinox 55 from Bruker Optics) equipped with a single reflection diamond ATR accessory (DuraSamp1IR II by SensIR Technologies). A drop of the solution was placed on the diamond surface, followed by evaporation of the solvent, in a stream of nitrogen, before recording the spectrum. Typically, 100 scans were acquired at 2 cm^{-1} resolution. Micro-Raman scattering measurements were performed at room temperature in the backscattering geometry

using a RENISHAW inVia Raman microscope equipped with a CCD camera and a Leica microscope. A 2400 lines mm^{-1} grating was used for all measurements, providing a spectral resolution of ± 1 cm^{-1}. As an excitation source the Ar^+ laser (633 nm with less than 2.65 mW laser power) was used. Measurements were taken with 60 seconds of exposure times at varying numbers of accumulations. The laser spot was focused on the sample surface using a long working distance 50x objective. Raman spectra were collected on numerous spots on the sample and recorded with Peltier cooled CCD camera. The intensity ratio ID/IG was obtained by taking the peak intensities following any baseline corrections. The data were collected and analyzed with Renishaw Wire and Origin software. Thermogravimetric analysis was performed using a TGA Q500 V20.2 Build 27 instrument by TA in a nitrogen (purity >99.999%) inert atmosphere. X-ray photoelectron analysis (XPS) was performed with a Kratos AXIS Supra. The spectra were obtained using a monochromatized Al-Kα source at 1486.6 eV running at 15 kV and 10 mA. The survey spectrum was measured at 160 eV pass energy and for the individual peak regions, spectra were recorded with pass energy of 20 eV. The energy resolution was < 0.48 eV. The analysis of peaks was performed with the Casa XPS software, using a weighted sum of Lorentzian and Gaussian components curves after Shirley background subtraction. The binding energies were referenced to the internal C1s standard at 284.6 eV. High-resolution tranmission electron microscopy (HRTEM) was performed on an aberration-corrected (image corrector) FEI Titan Cube microscope, working at 80 keV. STEM imaging and EELS studies have been conducted using an aberration-corrected FEI Titan Low-Base microscope operated at 80 kV. This microscope is equipped with a Cs probe corrector and a Gatan Tridiem ESR 865 EELS spectrometer. The energy resolution was ~1 eV. The convergence and collection angles were 25 and 50 mrad, respectively. To increase the signal/noise ratio, the datasets were then de-noised with the open-source program Hyperspy by using principal component analysis routines.

The electrochemical experiments were performed with a AUTOLAB PGSTAT302N potentiostat. Cyclic voltammetry assays were carried out in a three-electrode cell employing a 0.1 M $NaClO_4$ in dry acetonitrile as supporting electrolyte at a scan rate of 20 mV/s were employed. Photoelectrochemical measurements were carried out on spray-coated samples on FTO substrates (covering area 1 cm^2) as working electrode, which were illuminated through a quartz window by a 150 W Xenon arc lamp (LOT-Oriel GmbH, Germany).

6.3.2 Synthesis

General procedure for the preparation of functionalized amonium-based nanohybrids. In a round bottom flask, exfoliated MoS_2 or WS_2 (20 mg) and **1** (10 mg) in DMF (10 mL) were stirred at 70 °C for 36 hours. After that period, the reaction mixture was filtered through a PTFE membrane (0.1 mm pore size), the solid residue was extensively washed with DMF and dichloromethane and then collected as a dispersion in dichloromethane obtaining **2a** or **2b**. In order to deprotect the BOC group, 5 mg of the material **2a** or **2b** were redisperse in dichloromethane and treated with gaseous HCl. The reaction mixture was left under stirring for 12 hours and then filtered through a PTFE membrane (0.2 μm pore size) to yield **3a** or **3b**.

Synthesis of carbon dots CDs 5. 2.0 g of citric acid monohydrate (9.5 mmol) were dissolved in 16 mL of ultrapure water. Upon addition of 0.64 mL of ethylenediamine (9.5 mmol) the solution was heated up through microwave irradiation. The mixture was irradiated in order to keep the temperature at 140°C for 6 minutes, after that the irradiation was stopped. This yields in a yellow, transparent solid product, highly soluble in water. The product was dissolved in ultrapure water and dialyzed against ultrapure water (MWCO = 0.5-1.0 KDa, 3 days, twice a day). The dry material CDs **5** was obtained by freeze-drying, with a yield in mass of 22 wt. %. Characterization data are shown in Figure 23.

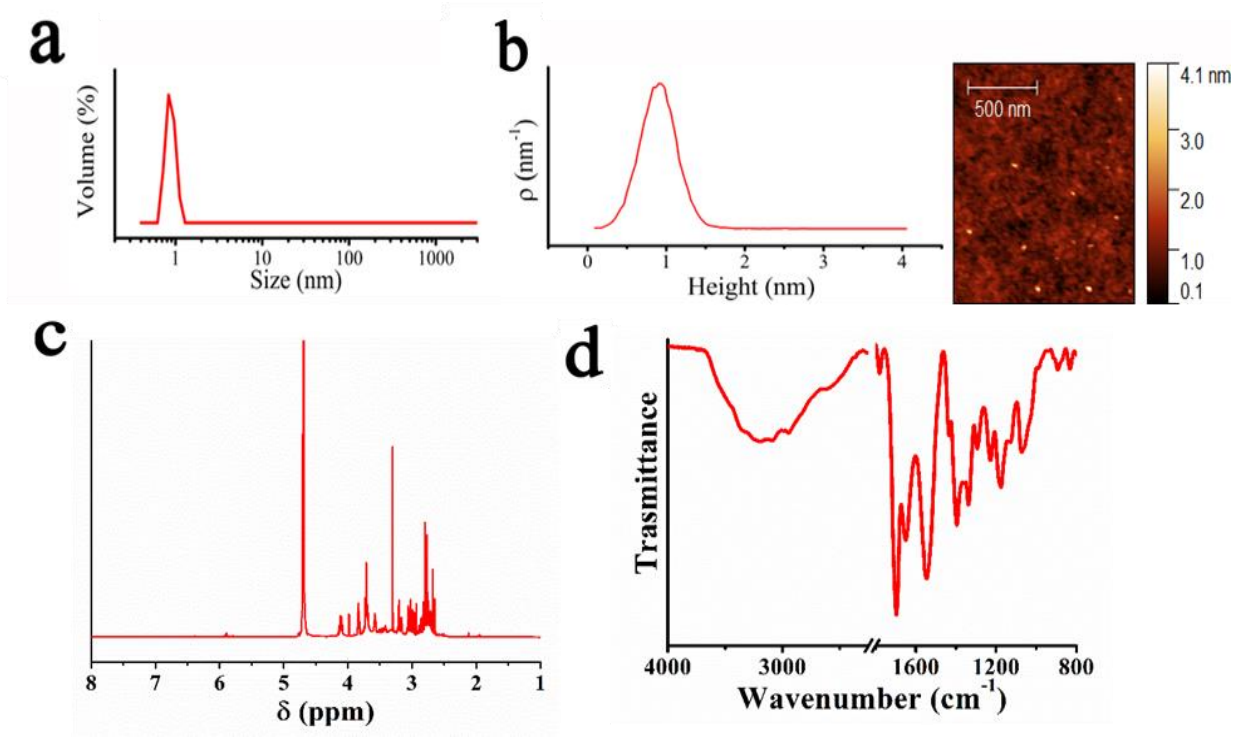

Figure 23. (a) Diameter distribution of CDs by dynamic light scattering. (b) AFM image and height distribution of CDs. (c) ^{1}H NMR spectrum of CDs in D_2O. (d) ATR-IR spectrum of CDs **5**.

Synthesis of 3-thiophene methyl acetate. Thiophene-3-acetic acid (1 g) in dry methanol (20 mL) with a 0.05 mL H_2SO_4 was refluxed for 24 hours. Then, the reaction poured onto the ultrapure water and extracted with dichloromethane. The organic phase was dried over magnesium sulfate and the solvent was evaporated to yield a pale-yellow liquid. Yield: 80 %.

Synthesis of poly (3-thiophene methyl acetate). The monomer 3-thiophene methyl acetate (2 mmol) was dissolved in 10 mL of dry chloroform and $FeCl_3$ (8 mmol) dissolved in 10 mL of chloroform was added dropwise under inert atmosphere. The reaction mixture was stirred at room temperature for 24 hours, then poured into methanol and the precipitate was filtered. The filtered polymer was washed with methanol and water several times to remove unreacted monomer and any $FeCl_3$ residue. The obtained poly (3-thiophene methyl acetate was dried at room temperature overnight.

Synthesis of poly (3-thiophene sodium acetate) 6. Poly (3-thiophene methyl acetate) (100 mg), deionized water (50 mL) and aqueous 2 M NaOH (10 mL) were placed in a double-neck flask and refluxed overnight. After that period, the reaction mixture was filtered and the supernatant

centrifuged at 4000 rpm for 5 min in order to remove any insoluble materials. The collected supernatant was transferred inside a dialysis tubing and dialyzed against deionized water for 3 days at room temperature. Subsequent evaporation of water by freeze-drying technique gave 1 as a reddish solid. Characterization data are shown in Figure 24.

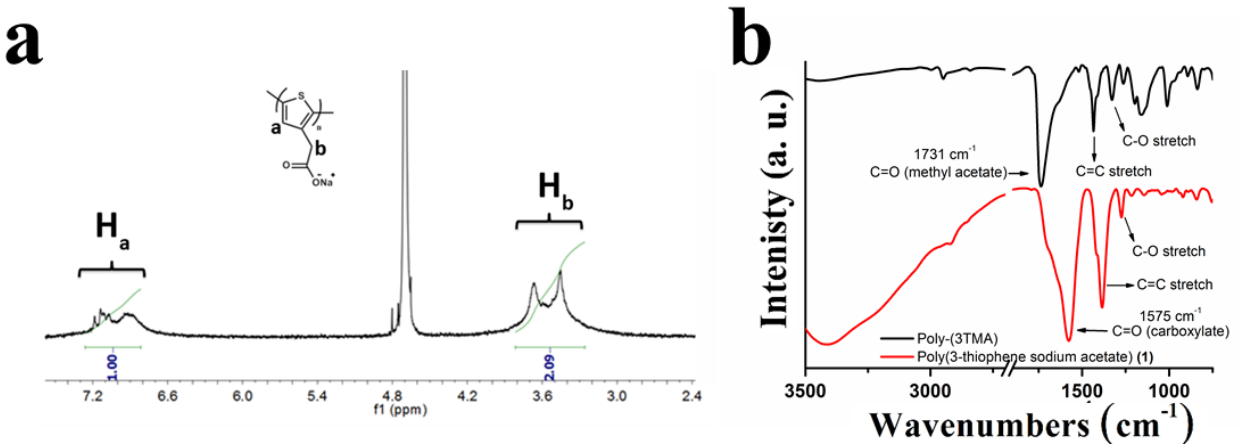

Figure 24. (a)^{1}H-NMR spectrum of poly (3-thiophene sodium acetate) **6** in D_2O. (b) FTIR spectra of poly (3-thiophene methyl acetate) (poly-(3TMA) and poly (3-thiophene sodium acetate) **9**.

Titration assays – preparation of 6-9. Aliquots of **3a** or **3b** (0.33 mg/mL) were added to diluted **4**, **5** or **6** (2 mL, 10 μM) and changes after each addition in the UV-Vis absorption and fluorescence were recorded.

General procedure for the preparation of functionalized TMDs/pyrene. In a round bottom flask, exfoliated MoS_2 or WS_2 (20 mg) and pyrene (10 mg) in DMF (10 mL) were stirred at 70 °C for 36 hours. After that period, the reaction mixture was filtered through a PTFE membrane (0.1 mm pore size), the solid residue was carefully washed with 1 ml of DMF 1 ml of dichloromethane and then collected as a dispersion in dichloromethane obtaining **11a** or **11b**. In order to deprotect the BOC group, 5 mg of the material **2a** or **2b** were redisperse in dichloromethane and treated with gaseous HCl. The reaction mixture was left under stirring for 12 hours and then filtered through a PTFE membrane (0.2 μm pore size) to yield **3a** or **3b**.

6.4 CONCLUSION

In summary, we accomplished via attractive Coulombic interactions the formation of nanosized ensembles featuring modified MoS_2 and WS_2 bearing positive charges, due to the incorporation of ammonium units, and a negatively charged porphyrin, carbon dots and poly (3-thiophene sodium acetate). The ensembles were fully characterized via spectroscopic (ATR-IR and Raman), thermal (TGA), and microscopic (SEM) means. Moreover, electronic absorption and photoluminescence titration assays unambiguously verified the formation of porphyrin/MoS_2, porphyrin/WS_2, CDs/MS_2, poly (3-thiophene sodium acetate)/MoS_2 and poly (3-thiophene sodium acetate)/WS_2 ensembles **7a**, **7b**, **8**, **9a** and **9b** respectively. In combination with time-resolved photoluminescence measurements, the transduction of energy from the photoexcited porphyrin, carbon dots and poly (3-thiophene sodium acetate) acting as an electron donor, to MoS_2 or WS_2, acting as acceptors, was revealed. Moreover, the electrocatalytic performance of CDs/MoS_2 was evaluated regarding the HER and found improved in comparison with that of the individual CDs species. Without a doubt, such CDs/MoS_2 ensembles performing in electron donor-acceptor schemes can be further exploited for managing charge-transfer processes as well as for electro- catalysis and may be useful for advancing the field of energy conversion in a wide range of technological and environmental applications. In addition, the supramolecular immobilization of pyrene via multiple π-S interactions with exfoliated MoS_2 and WS_2 sheets was accomplished and was found that pyrene protects MoS_2 and WS_2 by inhibiting oxidation.

6.5 REFERENCES

1. X. Huang, Z. Zenga and H. Zhang. Metal dichalcogenide nanosheets: preparation, properties and applications. *Chem. Soc. Rev*. **2013**, *42*, 1934-1946.
2. M. Pumera, Z. Soferb and A. Ambrosi. Layered transition metal dichalcogenides for electrochemical energy generation and storage. *J. Mater. Chem. A* **2014**, *2*, 8981-8987.
3. V. Nicolosi, M. Chhowalla, M. G. Kanatzidis, M. S. Strano and J. N. Coleman. Liquid Exfoliation of Layered Materials. *Science* **2013**, *340*, 1420-1424.
4. P. Miro, M. Audiffred and T. Heine. An Atlas of Two-Dimensional Materials. *Chem. Soc. Rev*. **2014**, *43*, 6537-6554.
5. Q. H. Wang, K. Kalantar-Zadeh, A. Kis, J. N. Coleman and M. S. Strano. Electronics and Optoelectronics of Two-Dimensional Transition Metal Dichalcogenides. *Nat. Nanotechnol* **2012**, *7*, 699-712.

6. K. Lee, R. Gatensby, N. McEvoy, T. Hallam and G. S. Duesberg. High-Performance Sensors Based on Molybdenum Disulfide Thin Films. *Adv. Mater.* **2013**, *25*, 6699-6702.

7. S. Rowley-Neale, C. Foster, G. Smith, D. Brownson and C. E. Banks. Mass-Producible, 2D-$MoSe_2$ Bulk Modified Screen-Printed Electrodes Provide Significant Electrocatalytic Performances Towards the Hydrogen Evolution Reaction. *Sustainable Energy Fuels* **2017**, *1*, 74-83.

8. D. K. Perivoliotis and N. Tagmatarchis. Recent Advancements in Metal-Based Hybrid Electrocatalysts Supported on Graphene and Related 2D Materials for the Oxygen Reduction Reaction. *Carbon* **2017**, *118*, 493-510.

9. T. Stephenson, Z. Li, B. Olsen and D. Mitlin. Lithium ion battery applications of molybdenum disulfide (MoS_2) nanocomposites. *Energy Environ. Sci*. **2014**, *17*, 209-231.

10. M. Xu, T. Liang, M. Shi and H. Chen. Graphene-Like Two- Dimensional Materials. *Chem. Rev.* **2013**, *113*, 3766-3798.

11. J. S. Ross, P. Klement, A. M. Jones, N. J. Ghimire, J. Yan, D. G. Mandrus, T. Taniguchi, K. Watanabe, K. Kitamura, W. Yao, D. H. Cobden and X. Xu. Electrically tunable excitonic light-emitting diodes based on monolayer WSe_2 p–n junctions. *Nat. Nanotechnol*. **2014**, *9*, 268-272.

12. G. Pagona, C. Bittencourt, R. Arenal and N. Tagmatarchis. Exfoliated semiconducting pure 2H-MoS_2 and 2H-WS_2 assisted by chlorosulfonic acid. *Chem. Commun*. **2015**, *15*, 12950-12953.

13. J. Zheng, H. Zhang, S. Dong, Y. Liu, C. T. Nai, H. S. Shin, H. Y. Jeong, B. Liu and K. P. Loh, High yield exfoliation of two-dimensional chalcogenides using sodium naphthalenide. *Nature Commun.* **2014**, *5*, 2995-2999.

14. Y. Yao, L. Tolentino, Z. Yang, X. Song, W. Zhang, Y. Chen and C.-P. Wong. High-Concentration Aqueous Dispersions of MoS_2. *Adv. Funct. Mater.*, **2013**, *23*, 3577-3583.

15. C. Lee, Q. Y. Li, W. Kalb, X. Z. Liu, H. R. Berger, W. Carpick and J. Hone. Frictional Characteristics of Atomically Thin Sheets. *Science* **2010**, *328*, 76-80.

16. H. S. S. R, Matte, A. Gomathi, A. K. Manna, D. J. Late, R. Datta, S. K. Pati and C. N. R. Rao. MoS_2 and WS_2 analogues of graphene. *Angew. Chem. Int. Ed*. **2010**, *49*, 4059-4062.

17. Z. Zeng, Z. Yin, X. Huang, H. Li, Q. He, G. Lu, F. Boey and H. Zhang. Single-Layer Semiconducting Nanosheets: High-Yield Preparation and Device Fabrication. *Angew. Chem. Int. Ed.* **2011**, *50*, 11093-11097.

18. D. Voiry, A. Goswami, R. Kappera, C. C. C. Silva, D. Kaplan, T. Fujita, M. Chen, T. Asefa and M. Chhowalla. Covalent functionalization of monolayered transition metal dichalcogenides by phase engineering. *Nat. Chem*. **2015**, *7*, 45-49. (b) K. C. Knirsch, N. C. Berner, H. C. Nerl, C. S. Cucinotta, Z. Gholamvand, N. McEvoy, Z. Wang, I. Abramovi, P. Vecera, M. Halik, S. Sanvito, G. S. Duesberg, V. Nicolosi, F. Hauke, A. Hirsch, J. N. Coleman and C. Backes. Basal-plane functionalization of chemically exfoliated molybdenum disulfide by diazonium salts. *ACS Nano*, **2015**, *9*, 6018-6030.

19. (a) S. S. Chou, M. De, J. Kim, S. Byun, C. Dykstra, J. Yu, J. Huang and V. P. Dravid. Ligand conjugation of chemically exfoliated MoS_2. *J. Am. Chem. Soc*. 2**013**, *135*, 4584-4587; (b) L. Zhou, B. He, Y. Yang, and Y. He. Facile approach to surface functionalized MoS_2 nanosheets. *RSC Adv.* **2014**, *4*, 32570-32578; (c) R. Anbazhagan, H.-J. Wang, H.-C. Tsai and R.-J. Jeng. Highly concentrated MoS_2 nanosheets in water achieved by thioglycolic acid as stabilizer and used as biomarkers. *RSC Advances* **2014**, *4*, 42936-42941; (d) J.-S. Kim, H.-W. Yoo, H. O. Choi and H.-T. Jung. Tunable volatile organic compounds sensor by using thiolated ligand conjugation on MoS_2. *NanoLett*. **2014**, *14*, 5941-5947; (e) T. Liu, S. Shi, C. Liang, S. Shen, L. Cheng, C. Wang, X. Song, S. Goel, T. E. Barnhart, W. Cai and Z. Liu. Iron Oxide Decorated MoS_2 Nanosheets with Double PEGylation for Chelator-Free Radiolabeling and Multimodal Imaging Guided Photothermal Therapy. *ACS Nano* **2015**, *9*, 950-960; (f) E. P. Nguyen, B. J. Carey, J. Z. Ou, J. van Embden, E. D. Gaspera, A. F. Chrimes, M. J. S. Spencer, S. Zhuiykov, K. Kalantar-zadeh and T. Daeneke. Electronic Tuning of 2D MoS_2 through Surface Functionalization. *Adv. Mater.* **2015**, *27*, 6225-6229; (g) K. Cho, M. Min, T.-Y. Kim, H. Jeong, J. Pak, J.-K. Kim, J. Jang, S. J. Yun, Y. H. Lee, W.-K. Hong and T. Lee, Electrical and Optical Characterization of MoS_2 with Sulfur Vacancy Passivation by Treatment with Alkanethiol Molecules. *ACS Nano*, **2015**, *9*, 8044-8053.

20. X. Chen, N. C. Berner, C. Backes, G. S. Duesberg and A. R. McDonald. Functionalization of two-dimensional MoS_2: On the reaction between MoS_2 and organic thiols. *Angew. Chem. Int. Ed*. **2016**, *55*, 5803-5808.

21. R. Canton-Vitoria, Y Sayed-Ahmad-Baraza, M. Pelaez-Fernandez, R. Arenal, C. Bittencourt, C. P. Ewels and N. Tagmatarchis. Functionalization of MoS_2 with 1,2-dithiolanes: toward donor-acceptor nanohybrids for energy conversion. *NPJ 2D Mater. Appl.* **2017**, *13*, 1-13.

22. (a) J. Choi, H. Zhang and H. J. Choi Modulating Optoelectronic Properties of Two-Dimensional Transition Metal Dichalcogenide Semiconductors by Photoinduced Charge Transfer. *ACS Nano* **2016**, *10*, 1671-1680; (b) E. P. Nguyen, B. J. Carey, C. J. Harrison, P. Atkin, K. J. Berean, E. D. Gaspera, J. Z. Ou, R. B. Kaner, K. Kalantar-zadeh and T. Daeneke. Excitation Dependent Bidirectional Electron Transfer in Phthalocyanine-Functionalised MoS_2 Nanosheets. *Nanoscale* **2016**, *8*, 16276-16283; (c) T. R. Kafle, B. Kattel, S. Lane, D. T. Wang, H. Zhao and W.-L. Chan. Charge Transfer Exciton and Spin Flipping at Organic-Transition-Metal Dichalcogenide Interfaces. *ACS Nano* **2017**, *11*, 10184-10192; (d) C. J. Benjamin, S. Zhanga and Z. Chen. Controlled Doping of Transition Metal Dichalcogenides by Metal Work Function Tuning in Phthalocyanine Compounds. *Nanoscale* **2018**, *10*, 5148-5153.

23. R. C. Selhorst, E. Puodziukynaite, J. A. Dewey, P. Wang, M. D. Barnes, A. Ramasubramaniam and T. Emrick. Tetrathiafulvalene-Containing Polymers for Simultaneous Non-Covalent Modification and Electronic Modulation of MoS_2 Nanomaterials. *Chem. Sci*. **2016**, *7*, 4698-4705.

24. A. J. Molina-Mendoza, L. Vaquero-Garzon, S. Leret, L. Juan-Fernández, E. M. Pérez and A. Castellanos-Gomez, Engineering the Optoelectronic Properties of MoS_2 Photodetectors Through Reversible Noncovalent Functionalization. *Chem. Commun*. **2016**, *52*, 14365-14368.

25. (a) G. Torre, G. Bottari, M. Sekita, A. Hausmann, D. M. Guldi and T. A. Torres. Voyage into the Synthesis and Photophysics of Homo- and Heterobinuclear Ensembles of Phthalocyanines and Porphyrins. *Chem. Soc. Rev.* **2013**, *42*, 8049-8105; (b) F. D. Souza, and K. M. Kadish. Handbook of Carbon Nano Materials: Synthesis and supramolecular systems; World Scientific: Singapore, **2011**.

26. G. Bottari, M. A. Herranz, L. Wibmer, M. Volland, L. Rodrıguez-Perez, D. M. Guldi, A. Hirsch, N. Martın, F. D'Souza and T. Torres. Chemical Functionalization and Characterization of Graphene-Based Materials. *Chem. Soc. Rev.* **2017**, *46*, 4464-4500; (b) G. Bottari, O. Trukhina, M. Ince and T. Torres, Towards Artificial Photosynthesis: Supramolecular, Donor−Acceptor, Porphyrin- and Phthalocyanine/Carbon Nanostructure Ensembles. *Coord. Chem. Rev.*, **2012**, *256*, 2453-2477; (c) N. Zhang, M. Q. Yang, S. and Liu, Y. Sun and Y. J. Xu. Waltzing with the

Versatile Platform of Graphene to Synthesize Composite Photocatalysts. *Chem. Rev.* **2015**, *115*, 10307-10377.

27. X. Xu, R. Ray, Y. Gu, H. J. Ploehn, L. Gearheart, K. Raker and W. A. Scrivens. Electrophoretic Analysis and Purification of Fluorescent Single-Walled Carbon Nanotube Fragments. *J. Am. Chem. Soc.* **2004**, *126*, 12736-12737.

28. J. Gu, D. Hu, J. Huang, X. Huang, Q. Zhang, X. Jia and K. Xi. One-pot synthesis and control of aqueous soluble and organic soluble carbon dots from a designable waterborne polyurethane emulsion. *Nanoscale* **2016**, *8*, 3973-3981.

29. (a) A. N. Emam, S. A. Loutfy, A. A. Mostafa, H. Awad and M. B. Mohamed. Cyto-toxicity, biocompatibility and cellular response of carbon dots–plasmonic based nano-hybrids for bioimaging. *RSC Advances* **2017**, *7*, 23502-23514; (b) Y. Sun, W. Cao, S. Li, S. Jin, K. Hu, L. Hu, Y. Huang, X. Gao, Y. Wu and X. J. Liang. Ultrabright and Multicolorful Fluorescence of Amphiphilic Polyethyleneimine Polymer Dots for Efficiently Combined Imaging and Therapy. *Sci. Rep.* **2013**, *3*, 3036-3042.

30. K. K. R. Datta, G. Qi, R. Zboril and E. P. Giannelis. Yellow emitting carbon dots with superior colloidal, thermal, and photochemical stabilities. *J. Mater. Chem. C,* **2016**, *4*, 9798-9803.

31. S. N. Baker and G. A. Baker. Luminescent carbon nanodots: emergent nanolights. *Angew. Chem. Int. Ed.* **2010**, *49*, 6726-6744.

32. (a) B. C. M. Martindale, E. Joliat, C. Bachmann, R. Alberto and E. Reisner. Clean Donor Oxidation Enhances the H_2 Evolution Activity of a Carbon Quantum Dot–Molecular Catalyst Photosystem. *Angew. Chem. Int. Ed.* **2016**, *55*, 9402-9440; (b) J. T. Margraf, F. Lodermeyer, V. Strauss, P. Haines, J. Walter, W. Peukert, R. D. Costa, T. Clark and D. M. Guldi. Using carbon nanodots as inexpensive and environmentally friendly sensitizers in mesoscopic solar cells. *Nanoscale Horiz.* **2016**, *1*, 220-226; (c) X. Li, M. Rui, J. Song, Z. Shen and H. Zeng. Adv. Carbon and Graphene Quantum Dots for Optoelectronic and Energy Devices: A Review. *Funct. Mater.* **2015**, *25*, 4929-4947; (d) B. C. M. Martindale, G. A. M. Hutton, C. A. Caputo and E. Reisner. Solar Hydrogen Production Using Carbon Quantum Dots and a Molecular Nickel Catalyst. *J. Am. Chem. Soc.* **2015**, *137*, 6018-6025; (e) W. Kwon, G. Lee, S. Do, T. Joo and S. W. Rhee. Size-Controlled Soft-Template Synthesis of Carbon Nanodots toward Versatile Photoactive Materials. *Small* **2014**, *10*, 506-513.

33. (a) V. Strauss, J. T. Margraf, T. Clark, and D. M. Guldi. A carbon–carbon hybrid-immobilizing carbon nanodots onto carbon Nanotubes. *Chem. Sci.* **2015**, *6*, 6878-6885; (b) T. Skaltsas, A. Stergiou, D. D. Chronopoulos, S. Zhao, H. Shinohara, and N. Tagmatarchis. All-Carbon Nanosized Hybrid Materials: Fluorescent Carbon Dots Conjugated to Multiwalled Carbon Nanotubes. *J. Phys. Chem. C* **2016**, *120*, 8550- 8558.

34. P. Yu, X. Wen, Y.-R. Toh, Y.-C. Lee, K.-Y. Huang, S. Huang, S. Shrestha, G. Conibeer and J. Tang. Efficient electron transfer in carbon nanodot–graphene oxide nanocomposites. *J. Mater. Chem. C*, **2014**, *2*, 2894-2901.

35. V. Strauss, J. T. Margraf, K. Dirian, Z. Syrgiannis, M. Prato, C. Wessendorf, A. Hirsch, T. Clark and D. M. Guldi. Carbon Nanodots: Supramolecular Electron Donor–Acceptor Hybrids Featuring Perylenediimides. *Angew. Chem. Int. Ed.* **2015**, *54*, 8292-8297.

36. F. Arcoudi, V. Strauss, L. Dordevic, A. Cadranel, D. M. Guldi and M. Prato. Porphyrin Antennas on Carbon Nanodots: Excited State Energy and Electron Transduction. *Angew. Chem. Int. Ed.* **2017**, *56*, 12097-12101.

37. (a) Y. Wang and A. Hu. Carbon quantum dots: synthesis, properties and applications. *J. Mater. Chem. C* **2014**, *2*, 6921-6939; (b) Y. Du and S. Guo. Chemically doped fluorescent carbon and graphene quantum dots for bioimaging, sensor, catalytic and photoelectronic applications. *Nanoscale* **2016**, *8*, 2532-2543.

38. T. A. Skotheim, J. R. Reynolds, eds., Handbook of Conducting Polymers; CRC Press: Boca Raton, **2007**, Chapter 9, 1-39.

39. P. Routh, S. Das, A. Shit, P. Bairi, P. Das and A. K. Nandi. Graphene Quantum Dots from a Facile Sono-Fenton Reaction and Its Hybrid with a Polythiophene Graft Copolymer Toward Photovoltaic Application. *ACS Appl. Mater. Interfaces* **2013**, *5*, 12672-12680.

40. C.-C. Cheng, W.-L. Lin, Z.-S. Liao, C.-W. Chu, J.-J. Huang, S.-Y. Huang, W.-L. Fan and D.-J. Lee. Water-Soluble Fullerene-Functionalized Polymer Micelles for Efficient Aqueous-Processed Conductive Devices. *Polym. Chem.* **2017**, *8*, 7469-7474.

41. (a) P. K. Chow, R. B. Jacobs-Gedrim, J. Gao, T.-M. Lu, B. Yu, H. Terrones and N. Koratkar. Defect-Induced Photoluminescence in Monolayer Semiconducting Transition Metal Dichalcogenides. *ACS Nano*, **2015**, *9*, 1520-1527; (b) S. Tongay, J. Zhou, C. Ataca, J. Liu, J. S. Kang, T. S. Matthews, L. You, J. Li, J. C. Grossman, and J. Wu. Broad-Range Modulation of

Light Emission in Two-Dimensional Semiconductors by Molecular Physisorption Gating. *Nano Lett*. **2013**, *13*, 2831-2836.

42. (a) C. Pritchard and J. W. Midgley. The Effect of Humidity on the Friction and Life of Unbonded Molybdenum Disulphide Films. *Wear* **1969**, *13*, 39-50; (b) Z. Wang, Y.-J. Zhang, M. Liu, A. Peterson and Hurt R. H. Oxidation Suppression During Hydrothermal Phase Reversion Allows Synthesis of Monolayer Semiconducting MoS_2 in Stable Aqueous Suspension. *Tribol. Lett*. **2014**, *53*, 329-336.

43. (a) M. Tagawa, M. Muromoto, S. Hachiue, K. Yokota, N. Ohmae, K. Matsumoto, and M. Suzuki. Hyperthermal Atomic Oxygen Interaction With MoS_2 Lubricants and Relevance to Space Environmental Effects in Low Earth Orbit-Effects on Friction Coefficient and Wear-Life. *Tribol. Lett*., **2005**, *18*, 437-443; (b) T. Liang, W. G. Sawyer, S. S. Perry, S. B. Sinnott, and S. R. Phillpot. Energetics of Oxidation in MoS_2 Nanoparticles by Density Functional Theory. *J. Phys. Chem. C*, **2011**, *115*, 10606-10616; (c) T. Liang, W. G. Sawyer, S. S. Perry, S. B. Sinnott, and S. R. Phillpot. First-Principles Determination of Static Potential Energy Surfaces for Atomic Friction in MoS_2 and MoO_3. *Phys. Rev. B*, **2008**, *77*, 104105.

44. (a) G.-H. Lee, X. Cui, Y. D. Kim, G. Arefe, X. Zhang, C.-H. Lee, F. Ye, K. Watanabe, T. Taniguchi, P. Kim and J. Hone. Highly Stable, Dual-Gated MoS_2 Transistors Encapsulated by Hexagonal Boron Nitride with Gate-Controllable Contact, Resistance, and Threshold Voltage. *ACS Nano* **2015**, *9*, 7019-7026; (b) S. Ahn, G. Kim, P. K. Nayak, S. I. Yoon, H. Lim, H.-J. Shin and H. S. Shin. Prevention of Transition Metal Dichalcogenide Photodegradation by Encapsulation with h-BN Layers. *ACS Nano* **2016**, *10*, 8973–8979; (c) S.-Y. Kim, J. Kwak, J. H. Kim, J.-U. Lee, Y. Jo, S. Y. Kim, H. Cheong, Z. Lee and S.-Y. Kwon. Substantial Improvements of Long-Term Stability in Encapsulation-Free WS_2 Using Highly Interacting Graphene Substrate. *2D Mater*. **2017**, *4*, 011007.

45. M. A. Pimenta, E. del Corro, B. R. Carvalho, C. Fantini and L. M. Malard. Comparative Study of Raman Spectroscopy in Graphene and MoS_2-type Transition Metal Dichalcogenides. *Acc. Chem. Res.* **2015**, *48*, 41-47.

46. A. Berkdemir, H. R. Gutierrez, A. R. Botello-Méndez, N. Perea- López, A. L Elías. C. I. Chia, B. Wang, V. H. Crespi, F. López- Uıás, J.-C. Charlier, H. Terrones and M. Terrones, Identification of Individual and Few Layers of WS_2 Using Raman Spectroscopy. *Sci. Rep.* **2013**, *3*, 1755-1763.

47. X. Chia, A. Y. S. Eng, A. Ambrosi, S. M. Tan and M. Pumera. Electrochemistry of Nanostructured Layered Transition-Metal Dichalcogenides. *Chem. Rev*. **2015**, *115*, 11941-11966.

48. T. F. Jaramillo, K. P. Jørgensen, J. Bonde, J. H. Nielsen, S. Horch and I. Chorkendorff. Identification of Active Edge Sites for Electrochemical H_2 Evolution from MoS_2 Nanocatalysts. *Science* **2007**, *317*, 100-102; (b) J. Kibsgaard, Z. Chen, B. N. Reinecke and T. F. Jaramillo. Engineering the surface structure of MoS_2 to preferentially expose active edge sites for electrocatalysis. *Nature Mater*. **2012**, *11*, 963-969; (c) Y. Li, H. Wang, L. Xie, Y. Liang, G. Hong and H. Dai. MoS_2 Nanoparticles Grown on Graphene: An Advanced Catalyst for the Hydrogen Evolution Reaction. *J. Am. Chem. Soc*. **2011**, *133*, 7296-7299; (d) D. Voiry, M. Salehi, R. Silva, T. Fujita, M. Chen, T. Asefa, V. B. Shenoy, G. Eda, and M. Chhowalla. Conducting MoS_2 Nanosheets as Catalysts for Hydrogen Evolution Reaction. *NanoLett*. **2013**, *13*, 6222-6227.

49. H. Li, J. Liu, S. J. Guo, Y. L. Zhang, H. Huang, Y. Liu and Z. H. Kang. Carbon dots from PEG for highly sensitive detection of levodopa. *J. Mater. Chem. B* **2015**, *3*, 2378-2387.

50. E. Istif, J. Hernández-Ferrer, E. P. Urriolabeitía, A. Stergiou, G. Fratta, N. Tagmatarchis, M. J. Large, A. B. Dalton, A. M. Benito and W. K. Maser. Conjugated Polymer Nanoparticles – Graphene Oxide Charge-Transfer Complexes. *Adv. Funct. Mat.* **2018**, 1707548.

51. B.-S. Kim, L. Chen, J. Gong and Y. Osada. Titration Behavior and Spectral Transitions of Water-Soluble Polythiophene Carboxylic Acids. *Macromolecules* **1999**, *32*, 3964-3969.

52. C. Gong, H. Zhang, W. Wang, L. Colombo, R. M. Wallace, and K. Cho. Band Alignment of Two-Dimensional Transition Metal Dichalcogenides: Application in Tunnel Field Effect Transistors. *Appl. Phys. Lett*. **2013**, *103*, 053513.

53. W. C. Tsoi, D. T. James, J. S. Kim, P. G. Nicholson, C. E. Murphy, D. D. C. Bradley, J. Nelson, and J.-S. Kim. The Nature of In-Plane Skeleton Raman Modes of P_3HT and their Correlation to the Degree of Molecular Order in P_3HT:PCBM Blend Thin Films. *J. Am. Chem. Soc.* **2011**, *133*, 9834-9843.

54. (a) L. Aleksandrov, T. Komatsu, R. Iordanova, and Y. Dimitriev. Study of Molybdenum Coordination State and Crystallization Behavior in MoO_3-La_2O_3-B_2O_3 Glasses by Raman spectroscopy. *J. Phys. Chem. Solids* **2011**, *72*, 263-268; (b) B.C. Windom, W.G. Sawyer, and

D.W. Hahn. A Raman Spectroscopic Study of MoS_2 and MoO_3: Applications to Tribological Systems. *Tribol. Lett*. **2011**, *42*, 301-310.

55. N. Huo, Q. Yue, J. Yang, S. Yang, and J. Li. Abnormal Photocurrent Response and Enhanced Photocatalytic Activity Induced by Charge Transfer Between WS_2 Nanosheets and WO_3 Nanoparticles. *ChemPhysChem*. **2013**, *14*, 4069-4073.

56. (a) K. C. Santosh, R. C. Longo, R. M. Wallace and K. Cho. Surface Oxidation Energetics and Kinetics on MoS_2 Monolayer. *J. Appl. Phys*. **2015**, *117*, 135301; (b) R. Addou, S. McDonnell, D. Barrera, Z. Guo, A. Azcat, J. Wang, H. Zhu, C. L. Hinkle, M. Quevedo-Lopez, H. N. Alshareef, L. Colombo, J. W. P. Hsu and R. M. Wallace. Impurities and Electronic Property Variations of Natural MoS_2 Crystal Surfaces. *ACS Nano*, **2015**, *9*, 9124-9133; (c) R. Addou, L. Colombo, and R. M. Wallace. Surface Defects on Natural MoS_2. *ACS Appl. Mater. Interfaces* **2015**, *7*, 11921-11929.

57. (a) J. Gao, B. Li, J. Tan, P. Chow, T.-M. Lu and N. Koratkar. Aging of Transition Metal Dichalcogenide Monolayers. *ACS Nano* **2016**, *10*, 2628–2635; (b) S.-Y. Kim, J. Kwak, J. H. Kim, J.-U. Lee, Y. Jo, S. Y. Kim, H. Cheong, Z. Lee and S.-Y. Kwon. Substantial Improvements of Long-Term Stability in Encapsulation-Free WS_2 Using Highly Interacting Graphene Substrate. *2D Mater*. **2017**, *4*, 011007.

58. (a) P. Ayala, R. Arenal, M. Rummeli, A. Rubio and T. Pichler. The doping of carbon nanotubes with nitrogen and their potential applications. *Carbon* **2010**, *48*, 575-586; (b) R. Arenal, X. Blasé and A. Loiseau. Boron-nitride and boron-carbonitride nanotubes: synthesis, characterization and theory. *Advances in Physics* **2010**, *59*, 101-179 (c) L. Alvarez, Y. Almadori, R. Arenal, R. Babaa, T. Michel, R. Leparc, J-L. Bantignies, P. Hermet and J-L. Sauvajol. Charge Transfer Evidence between Carbon Nanotubes and Encapsulated Conjugated Oligomers. *J. Physical Chem. C* **2011**, *115*, 11898-11905; (d) R. Arenal, L. De Matteis, L. Custardoy, A. Mayoral, M. Tence, V. Grazu, J.M. de la Fuente, C. Marquina and M.R. Ibarra. Spatially-Resolved EELS Analysis of Antibody Distribution on Biofunctionalized Magnetic Nanoparticles. *ACS Nano* **2013**, *7*, 4006-4013.